

**Reactive Species transport and surface structuring by  
short-pulsed laser irradiation for plasma catalysis**

**DISSERTATION**

zur

Erlangung des Grades

“Doktor der Naturwissenschaften”

an der Fakultät für Physik und Astronomie  
der Ruhr-Universität Bochum

von

Patrick Preissing

aus

Essen

Bochum 2023

1. Gutachter .....

2. Gutachter .....

Datum der Disputation .....

RUHR-UNIVERSITY BOCHUM



DOCTORAL THESIS

Experimental Physics II  
Faculty for Physics and Astronomy

---

**Reactive Species transport and surface structuring by  
short-pulsed laser irradiation for plasma catalysis**

---

*A thesis submitted in fulfillment of the requirements  
for the degree of Doctor of Natural Sciences*

*Submitted by:*  
Patrick Preissing  
born in Essen

Bochum, 2022



## Declaration of Authorship

I, Patrick PREISSING, declare that this thesis titled, "Reactive Species transport and surface structuring by short-pulsed laser irradiation for plasma catalysis" and the work presented in it are my own. I confirm that:

- This work was done wholly or mainly while in candidature for a research degree at this University.
- Where any part of this thesis has previously been submitted for a degree or any other qualification at this University or any other institution, this has been clearly stated.
- Where I have consulted the published work of others, this is always clearly attributed.
- Where I have quoted from the work of others, the source is always given. With the exception of such quotations, this thesis is entirely my own work.
- I have acknowledged all main sources of help.
- Where the thesis is based on work done by myself jointly with others, I have made clear exactly what was done by others and what I have contributed myself.

Signed:

---

Date:

---



*“Everybody is a genius. But if you judge a fish by its ability to climb a tree, it will live its whole life believing that it is stupid.”*

Unknown

*“Everyone you meet is fighting a battle you know nothing about. Be kind. Always.”*

Robin Williams



## Acknowledgements

An dieser Stelle möchte ich mich bei einigen Personen bedanken, die diese Arbeit ermöglicht haben. Vielen Dank an...

- ...*Volker Schulz-von der Gathen*. Nicht nur für die herausragend fachliche Betreuung und bedingungslose Unterstützung, sondern auch - oder sogar insbesondere - für sein offenes Ohr in privat schwierigen Situationen.  
Danke!
- ...*Marc Böke* für die herausragende Betreuung der Arbeit, die stetige Hilfe und das Korrekturlesen sowie anregende Diskussionen.
- ...*Achim von Keudell*, der mir diese Arbeit und meine Rückkehr überhaupt ermöglicht hat. Der aber außerdem ein Team mit fachlicher Expertise und harmonischer Arbeitsatmosphäre zusammengestellt hat, in welcher das Arbeiten jeden Tag Freude bereitet.
- ... *Judith Golda* für die Übernahme des Zweitgutachtens.
- ...*Alicia Gonzalez Fontela* für ihre Unterstützung bei allen organisatorischen Themen, für die lustigen Gespräche sowie zahlreiche Schoko-Cookies.
- ...*David Steuer, Robin Labenski, Alexander Böttinger* und *Sascha Chur* die mich bei vielen Messungen unterstützt haben und von denen ich außerdem auch noch einiges lernen durfte.
- ...*Ihor Korolov* und *Julian Schulze* für ihre fachliche Expertise, die vielen Hilfestellungen sowie Anregungen. Ihor Korolov gilt außerdem großer Dank für die vielen lustigen Stunden und Gespräche im Labor während der LIF Messungen.
- ...*Sebastian Dzikowski und Adrian Marcak* für morgendliche Diskussionen und Debatten im Büro sowie mittags in Mensa und Q-West. Ihr wart jeden Tag eines der vielen Highlights, die der Arbeitsalltag am Lehrstuhl mit sich brachte. Euch möchte ich folgendes mit auf euren Lebensweg geben: "Wenn eine kleine triste Taube in den Spiegel schaut und dort einen wunderschönen Pfau sieht, dann ist ihr Leben völlig in Ordnung."

- ...*Katharina Grosse*, die beste Büropartnerin. Danke für deine Freundschaft und die vielen schönen Erinnerungen! Und nicht zuletzt dafür, dass du mit mir zusammen im Bochumer Stadtpark die Bewerbungsmail ausformuliert hast, sodass du mit ein entscheidender Faktor dafür bist, dass diese Arbeit entstanden ist.
- ...*jeden einzelnen Mitarbeiter* des Lehrstuhls für Experimentalphysik II, für die tolle Atmosphäre und Hilfsbereitschaft.
- ...*meine ganze Familie*. Insbesondere meine Eltern *Ursula und Norbert Preissing*, meinen Bruder *Sven Preissing* sowie meine Oma *Ursula Dierks*. Danke für viele schöne gemeinsame Abende und sonnige Stunden im Garten, die einen Sorgen und Stress vergessen lassen.
- ...meine Ehefrau *Bianca Preissing*. Danke, dass du seit nun 11 Jahren an meiner Seite bist und mich unterstützt. Danke für jedes gemeinsame Lachen und jede gemeinsame Erinnerung. Ich freue mich auf alles, was wir noch gemeinsam erleben. Ich hätte niemand anderen lieber an meiner Seite als dich!

# Contents

<b>Declaration of Authorship</b>	<b>iii</b>
<b>Acknowledgements</b>	<b>vii</b>
<b>1 Introduction</b>	<b>1</b>
1.1 CRC1316 "Transient atmospheric plasmas - from plasmas to liquids to solids" . . . . .	1
1.2 Motivation . . . . .	2
1.3 Thesis outline - key questions . . . . .	7
<b>2 Fundamentals</b>	<b>11</b>
2.1 Non-equilibrium atmospheric pressure plasmas . . . . .	11
2.2 0-dimensional modeling of NO . . . . .	13
2.2.1 Model . . . . .	13
2.2.2 Chemical kinetics . . . . .	16
2.3 Laser Induced Fluorescence (LIF) . . . . .	18
2.3.1 Transition probabilities . . . . .	18
2.3.2 Rate equations - total number of LIF photons . . . . .	20
2.3.3 The $\gamma$ -band of NO ( $A^2\Sigma^+ \rightarrow X^2\Pi$ ) . . . . .	23
2.4 Laser Induced Periodic Surface Structures (LIPSS) . . . . .	27
2.4.1 Theories of LIPSS formation . . . . .	29
2.4.1.1 Classic interference theory . . . . .	29
2.4.1.2 Surface Plasmon Polaritons (SPP) . . . . .	30
2.4.1.3 Efficacy Factor Theory - Sipe's theory . . . . .	33
<b>3 Experimental</b>	<b>37</b>
3.1 Plasma source - COST-Jet . . . . .	37
3.2 Experimental setup - LIF . . . . .	39
3.2.1 Laser system . . . . .	39
3.2.2 Measurement of the laser focus . . . . .	39

3.2.3	Chamber and plasmajet setup for measurements in the free effluent . . . . .	41
3.2.4	Modifications of the setup for measurements in front of surfaces . . . . .	42
3.3	Experimental setup - Laser-surface experiments . . . . .	43
3.3.1	Laser system . . . . .	43
3.3.2	Chamber and optical setup . . . . .	43
<b>4</b>	<b>Reactive species distribution in the plasma effluent</b>	<b>47</b>
4.0.1	Linearity of LIF signal . . . . .	47
4.1	Determining parameters for maximum NO production . . . . .	47
4.1.1	Dependence of NO creation on N <sub>2</sub> /O <sub>2</sub> admixture ratio . . . . .	48
4.1.2	Calibration procedure . . . . .	51
4.1.3	Error estimation of the calibration procedure . . . . .	54
4.1.4	Dependence of NO creation on synthetic air admixture . . . . .	55
4.1.5	NO production in different plasma operation regimes . . . . .	56
4.2	Diffusion of air into the plasma effluent . . . . .	60
4.2.1	Quenching of NO(A <sup>2</sup> Σ <sup>+</sup> ) . . . . .	60
4.2.2	Air intrusion into plasma effluent . . . . .	64
4.3	2d and 3d density distributions at different operating atmospheres . . . . .	66
4.3.1	Expansion of NO into free effluent and coupling to feed gas flow . . . . .	66
4.3.2	Turbulence like behavior in air and transport by free diffusion . . . . .	76
4.3.3	Summary of LIF measurements in the free effluent . . . . .	90
4.4	NO distribution in front of surfaces . . . . .	93
4.4.1	Preliminary geometrical considerations . . . . .	93
4.4.2	Density profiles of NO in front of surfaces . . . . .	96
4.4.3	Summary of LIF measurements in front of surfaces . . . . .	105
<b>5</b>	<b>Laser-Surface interaction</b>	<b>107</b>
5.1	Laser energy measurements . . . . .	107
5.2	Profile of the laser on the surface . . . . .	108
5.3	LIPSS . . . . .	110
5.3.1	Analysis of the LSM/SEM images . . . . .	110

5.3.2	LIPSS on substrates under $\theta_i = 0^\circ$ incident irradiation . . . . .	111
5.3.3	Dependence of the LIPSS orientation on the polarization vector . . . . .	120
5.3.4	LIPSS on substrates for $\theta_i \neq 0^\circ$ incident irradiation . . . . .	123
5.3.5	Summary of the LIPSS experiments . . . . .	130
5.4	PLiD on Cu substrates . . . . .	130
5.4.1	Summary of PLiDs experiments . . . . .	139
<b>6</b>	<b>Summary and Further Research</b>	<b>141</b>
	<b>Bibliography</b>	<b>147</b>



# List of Figures

1.1	General aim and geometry of the B2 project within the CRC1316	2
1.2	Illustration of the different mechanisms during plasma assisted catalysis . . . . .	5
2.1	Sketch of the different regions of the used plasma source . . . . .	13
2.2	Typical setup of a LIF measurement . . . . .	18
2.3	Density of the upper state $n_u(t)$ after excitation with a laser pulse	22
2.4	Potential energy curves for the A and X state . . . . .	23
2.5	Spectrum of the NO X-A(0,0) . . . . .	25
2.6	Photomicrograph of the first detected LIPSS in 1965 . . . . .	27
2.7	Classification scheme of laser induced periodic surface structures	28
2.8	Geometry and vector diagram for the classical interference theory explaining LIPSS . . . . .	29
2.9	Schematic of the geometry used for Sipe's theory . . . . .	33
3.1	Sketch of the COST-Jet system showing the housing, the head and the effluent . . . . .	37
3.2	Knife-edge measurements in order to measure the focus width of the excitation laser . . . . .	40
3.3	Sketch of the experimental setup for the LIF measurements . . . . .	41
3.4	Geometry for the LIF experiments in front of a surface . . . . .	43
3.5	Experimental Setup for the LIPSS experiments . . . . .	44
4.1	Pulse energy variation . . . . .	48
4.2	Influence of the N <sub>2</sub> and O <sub>2</sub> admixture on the NO production . . . . .	49
4.3	Influence of the N <sub>2</sub> and O <sub>2</sub> admixture on the NO production . . . . .	50
4.4	Calibration curve for the determination of absolute NO densities	53
4.5	Influence of the absolute synthetic air admixture on the NO production . . . . .	55
4.6	Variation of the plasma power . . . . .	57

4.7	Voltage-density correlation . . . . .	59
4.8	Exponential fit in order to calculate the lifetimes of the NO( $A^2\Sigma^+$ state) . . . . .	61
4.9	Stern-Volmer plot exemplary shown for air . . . . .	63
4.10	Air diffusion into the plasma effluent . . . . .	66
4.11	2-dimensional $xz$ -maps in air and controlled He atmosphere . . . . .	67
4.12	1-dimensional density profiles and gradients . . . . .	69
4.13	Geometry for the determination of the boundary conditions for the solution of the differential equation for $x$ . . . . .	71
4.14	2-dimensional $xz$ -maps in air with the calculated trajectories . . . . .	73
4.15	absolute densities of NO extrapolated at $\vec{r} = (0,0,0)$ plotted against the residence time and the energy density . . . . .	76
4.16	$yz$ -maps of the NO distribution in the free effluent . . . . .	78
4.17	Transverse density widths and central positions of the Gaussian fit function for different axial distances . . . . .	79
4.18	Collision frequency between NO, air and helium particles . . . . .	81
4.19	$yz$ -maps of NO for different heights. . . . .	82
4.20	$yz$ -maps for NO in He and air atmosphere. . . . .	84
4.21	Density profiles of NO along $z$ from diffusion equation and measurements . . . . .	84
4.22	Pseudo 3d maps of NO in He and air atmosphere . . . . .	85
4.23	Initial 2d NO distribution for the solution of the 2d diffusion equation . . . . .	88
4.24	Comparison of $yx$ -maps obtained from experiment and from diffusion equation. . . . .	89
4.25	Geometry for the calculation of vignetting effects. . . . .	93
4.26	Example of a one-dimensional density measurement in order to determine the position of the surface . . . . .	95
4.27	Correction factor $\zeta$ for measurements close to the surface . . . . .	96
4.28	1d NO density profiles in front of different surfaces. . . . .	97
4.29	Spectral reflectance of different surface materials . . . . .	98
4.30	Geometry of the detection system . . . . .	99
4.31	Simulations results from the ray optics simulation of the reflectance . . . . .	101
4.32	Comparison of 2d experimental results and simulation in front of surface . . . . .	104

4.33 Comparison of 3d experimental results and simulation in front of surface . . . . .	105
5.1 Power transmission curve of the Glan-Taylor attenuator. . . . .	108
5.2 Laser profile of the interaction laser . . . . .	108
5.3 LSM image of a surface-laser spot interaction profile . . . . .	109
5.4 2d FFT analysis scheme of the LSM images . . . . .	111
5.5 Magnitude spectrum of LIPSS in Fourier space . . . . .	112
5.6 LIPSS periodicities induced by $\theta_i = 0^\circ$ irradiation. . . . .	113
5.7 SEM and LSM images of LIPSS induced on a Ti layer for $\lambda_L = 1064$ and $532$ nm . . . . .	114
5.8 Coordinate for the efficacy maps . . . . .	118
5.9 Maximum of the efficacy factor depending on the filling factor and the geometrical shape factor . . . . .	119
5.10 Efficacy factor maps for $\theta_i = 0^\circ$ . . . . .	121
5.11 Evaluation of LIPSS orientation and polarization of the laser. . . . .	122
5.12 Orientation of the LIPSS against the orientation of the polarization vector of the laser. . . . .	123
5.13 Type $c$ and type $s^-$ LIPSS induced on a 20 nm thick Ti substrate with $\theta_i = 55^\circ$ irradiation. . . . .	124
5.14 Efficacy factor maps for $\theta_i \neq 0^\circ$ . . . . .	126
5.15 Efficacy factor $\eta$ of the $c$ -type LIPSS for different incidence angles $\theta_i$ onto a 20 nm thick Ti layer. . . . .	127
5.16 LIPSS periodicities $\Lambda_{\text{LIPSS}}$ plotted against the incident angle $\theta_i$ . . . . .	127
5.17 LSM image of $s^+$ and $s^-$ LIPSS induced on a Si wafer. . . . .	128
5.18 Periodicity $\Lambda_{\text{LIPSS}}$ plotted against the incident angle $\theta_i$ for $\pi$ -polarized light. . . . .	129
5.19 PLiD on a 10 nm thick Cu layer . . . . .	131
5.20 Initial stages of the dewetting process on a Cu sample . . . . .	132
5.21 Spacings of the spinodal net structure on the 10 nm thick Cu layer from experiment and the linear TFH theory. . . . .	133
5.22 Nanoparticles created on a 10 nm thick Cu layer . . . . .	136
5.23 SEM image of PLiDs with two different morphologies with the according histogram. . . . .	137
5.24 Comparisons of the experimental observed PLiDs with the TFH theory. . . . .	138

5.25 Circular structures induced on a 10 nm thick Cu layer irradiated by a  $\pi$ -polarized laser of the wavelength of  $\lambda_L=532$  nm. . . 139

## List of Tables

S1	Measured quenching rate coefficients and calculated (see equation 4.18) cross sections for the $\text{NO}(A^2\Sigma^+ v' = 0)$ state. Shown are the values observed in this study compared with literature values ( $T_g = 300 \text{ K}$ ). . . . .	65
S2	Flow dependencies of NO densities in air and He + 0.5 % synthetic air atmosphere. Shown are the respective fit parameters extracted from a fit function of the form $n_{\text{NO}}(z) = n_0 \exp\{-z/L\} + n_{\text{off}}$ . . . . .	70
S3	Ratios of the maximum densities that develop in front of the surface, $\hat{n}_j$ , and the undisturbed densities, $n_0$ . Furthermore, the spectral reflectances (+1) of the respective materials at the fluorescence wavelength and the integrated densities from the point of deviation ( $z = 3$ ) up to the surface $z = S_b$ are shown. . . . .	100
S4	Reactions taking into account the relevant surface kinetics for the NO production at surfaces. Here $S_v$ and $F_v$ denote vacant active chemi- and physisorption sites. . . . .	102
S1	LIPSS periodicities $\Lambda_{\text{LIPSS}}$ on different surface materials induced by perpendicular irradiation ( $\theta_i = 0^\circ$ ) of the fundamental $\lambda_L = 1064 \text{ nm}$ and the SHG $\lambda_L = 532 \text{ nm}$ . . . . .	115
S2	Optical constants of the investigated materials. The refractive index of a material is given by $n(\lambda) = \tilde{n}(\lambda) + i\kappa(\lambda)$ and $\epsilon_r(\lambda) = \epsilon_r(\lambda)' + i\epsilon_r(\lambda)'' = n(\lambda)^2$ . . . . .	116

S3	Comparisons of the theoretical calculated values of the LIPSS periodicities, $\Lambda_t$ , with the experimental observed values, $\Lambda_{exp}$ . The last column shows the deviations between the experimental and the theoretical value of the respective theory $\Delta\Lambda =  \Lambda_{exp} - \Lambda_t $ . Different theories are evaluated here, according to the Classical Interference theory (CI), the Surface Plasmon Polariton theory (SPP) and Sipe's theory (Sipe). . . . .	117
----	---	-----

# List of Abbreviations

<b>μAPPJ</b>	Micro Atmospheric Pressure Plasma Jet
<b>APPJ</b>	Atmospheric Pressure Plasma Jet
<b>CCP</b>	Capacitively Coupled Plasma
<b>CI</b>	Classical Interference
<b>COST-Jet</b>	European Cooperation in Science and Technology-Jet
<b>CRC</b>	Collaborative Research Center
<b>EEDF</b>	Electron Energy Distribution Function
<b>FFT</b>	Fast Fourier Transform
<b>FWHM</b>	Full Width of Half Maximum
<b>HSFL</b>	High Spatial frequency LIPSS
<b>LIF</b>	Laser Induced Fluorescence (Spectroscopy)
<b>LIPSS</b>	Laser Induced Periodic Surface Structures
<b>LSFL</b>	Low Spatial frequency LIPSS
<b>LSM</b>	Laser Scanning Microscope
<b>MBMS</b>	Molecular Mass Beam Spectroscopy
<b>PLiD</b>	Pulsed Laser induced Dewetting
<b>PLTE</b>	Partial Local thermal Equilibrium
<b>RF</b>	Radio Frequency
<b>SEM</b>	Scanning Electron Microscope
<b>SEW</b>	Surface Electromagnetic Waves
<b>SHG</b>	Second Harmonic Generation
<b>SNR</b>	Signal to Noise Ratio
<b>SPP</b>	Surface Plasmon Polaritons
<b>TALIF</b>	Two photon Absorption Laser Induced Fluorescence (Spectroscopy)
<b>TFH</b>	Thin Film Hydrodynamic (theory)
<b>VOC</b>	Volatile Organic Compounds



# Chapter 1

## Introduction

### 1.1 CRC1316 "Transient atmospheric plasmas - from plasmas to liquids to solids"

In plasma assisted catalysis a material with catalytic properties is combined and often brought in contact with a gaseous discharge. This combination can trigger synergisms and generate outcomes that would not be possible with the single components separately. Concerning the discharge types, the focus has shifted towards non-thermal atmospheric pressure plasmas, taking advantage of the non-equilibrium character of different plasma sources. The non-equilibrium character can be controlled and adjusted by many different parameters, such as large gas flows, short pulsed plasma sources or mixed frequency excitation. This assures strong cooling mechanisms and varies, for example, the exciting electric fields to generate a variety of kinetic mechanisms and desired plasma chemistry. The non-thermal character of these sources, makes them ideal devices for any application of thermal sensitive samples, such as biological systems. To establish the commercial use of those sources for certain applications, fundamental knowledge and understanding of the discharges is crucial. Furthermore, the transport and the subsequent interaction with liquid or solid targets needs to be investigated in detail. From this, fundamental questions arise, such as chemical non-equilibrium routes of new materials, the energy occurrence and species transfer on the ns timescale and many more. Answering these questions is extremely challenging since the discharges operate in atmospheric pressures, e.g., due to the small dimensions of the discharges and the accessibility via laser diagnostics. The plasma chemistry in those discharges is very complex, due to strong and fast quenching mechanisms of the excited species. There are many more complexities

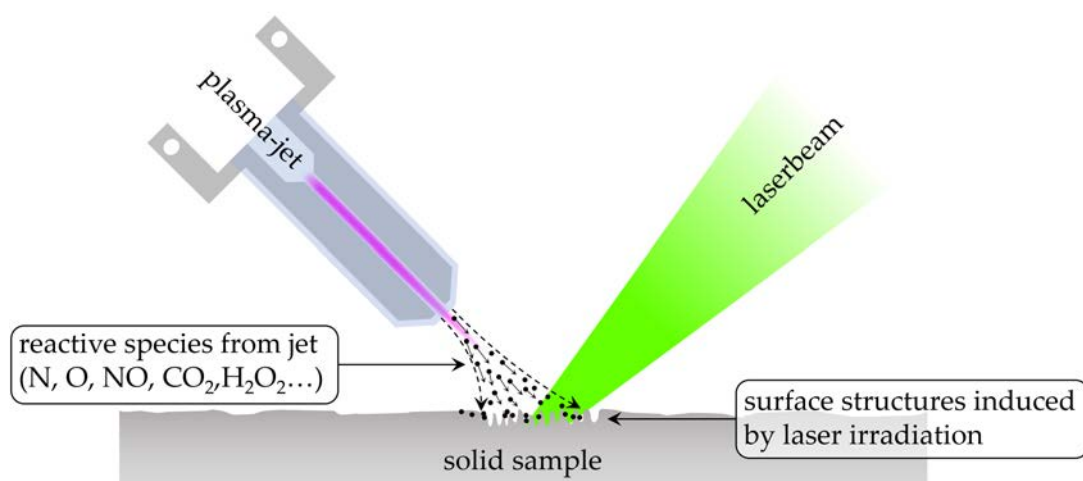


**Figure 1.1.** General geometry for the setup of the experiments within the subproject B2 within the CRC1316. This setup is used to investigate the simultaneous interaction between plasma generated reactive species and laser induced surface structures.

and questions to be answered to be able to control and tailor these discharges for surface applications. In this context a Collaborative Research Center was founded, namely the CRC1316 “Transient atmospheric plasmas - from plasmas to liquids to solids”. Clarifying and answering the afore mentioned questions is the CRC’s mission.

This thesis is part of a subproject of the CRC, namely the B2. This subproject in particular, deals with the simultaneous interaction of a laser beam, inducing surface modifications and reactive species that are generated in a plasma-jet and subsequently transported to the surface. These interactions might lead to synergisms at the surface interaction region, enhancing the catalytic activity. A sketch of the schematic geometry, to investigate this topic is shown in figure 1.1.

## 1.2 Motivation

Although many people are not familiar with the term plasma in a physical context, almost every person is dealing with objects in their everyday life that consist of components which have been plasma processed during their

manufacturing cycle. The plasma source that is applied for the various applications can vary in numerous plasma parameters, such as pressure, temperature, density of various species and many more. One of the common classification parameter is the operating pressure that can range from  $p \sim 1$  mbar for low pressure plasmas up to several hundred bars in high pressure discharges.

Among all different discharge types, atmospheric pressure plasma jets (APPJs) have gained significant attention over the last decades. This is owed to their unique physical properties and their technical simplicity as e.g., no need for complex vacuum systems as compared to the low pressure counterparts. Their strong non-equilibrium character offers the possibility of creating hot electrons and therefore complex chemical kinetics in the plasma bulk, where a cocktail of reactive species is formed (ions, electrons, excited (metastable) species, radicals or neutral molecules). These reactive species are eventually transported into the effluent with the feed gas flow, leading to many chemical reactive species with a narrow directed flow. While the electrons are effectively heated, the heavy species (that eventually interact with any sample) remain cold, i.e., near room temperature. This feature of the APPJs opens the door to a wide field of possible applications. This field covers material processing, such as treatments of polymers in order to e.g., increase the adhesion, the hydrophobic/hydrophilic characteristics of the surface or the etching [1, 2, 3]. Biomedical applications such as dentistry [4, 5], acceleration of wound healing on human skin [6, 7] or even agricultural applications like the decontamination and processing of wastewater [8, 9] to name a few.

However, nowadays in times of climate change, environmental issues are being studied more and more intensively beside the above-mentioned technical or medical applications. One central aspect in this scope are catalysis processes. Catalysis refers to chemical reactions whose reaction rate is increased by catalysts. Catalysts are substances that lower the activation energy of the reaction but do not change the chemical equilibrium and are not consumed in the process.

The (unknown) use of inorganic catalysts traces back to the year 1575, when Valerius Cordus catalyzed the conversion of alcohol to ether via sulfuric acid. [10]. Therefore, catalysis itself is a long known ancient phenomenon, even though not so its chemical or physical theory and fundamentals. However,

the terminology *catalysis* was later established in 1835, where it was first proposed by the Swedish physician and chemist Jöns Jakob Berzelius [11]. Over the decades many catalytic reactions in different fields have been experimentally investigated and used but it was only in 1909 when Wilhelm Ostwald received the Nobel Prize for his pioneering theoretical explanation and his work on catalysis, chemical equilibria and reaction velocities [12]. Nowadays, catalytic processes are well studied and frequently used. One of the most prominent processes is the conversion of hydrocarbons ( $C_mH_n$ ), carbon-monoxide (CO) and nitric oxides ( $NO_x$ ) into carbon-dioxides ( $CO_2$ ), water ( $H_2O$ ) and nitrogen ( $N_2$ ) by reduction or oxidation (cite some.).

About three decades ago researchers around the world started to investigate plasma assisted catalysis. One of the earliest publications concerning the interaction of a catalyst and a plasma goes back to the year 1986, where Gicquel et al. reported on nitric oxide synthesis from molecular oxygen and nitrogen and the decomposition of ammonia during the combination of a low pressure plasma and a tungsten oxide surface ( $WO_3$ ) [13]. While plasma assisted catalysis had its start in the low pressure field, it was six years later that the first work was published by Mizuno et al. about the usage of an atmospheric pressure plasma source with a catalyst in order to induce the synthesis of methanol ( $CH_3OH$ ) from methane ( $CH_4$ ) and  $CO_2$  in a dielectric barrier discharge [14]. This was followed by a rapid increase in the 1990s leading to the state of the art that is present today concerning this topic. The non-equilibrium character of the plasma offers several advantages over the classical thermal catalysis operation. Due to the different temperatures of the species, i.e., the low temperature of heavy particles, this offers an opportunity of chemical transformations into application specific desired products without the kinetic and thermodynamic limitations. Another beneficial feature of non-equilibrium plasmas that is of particular interest is the vibrational temperature that is typically in the range of a few 1000 K. These temperatures allow vibrationally excited states to participate in chemical reactions that in turn can lead to enhanced reactivity at the surface of a catalyst, due to the lower dissociation barriers. Indeed, the temperature concept is one of the central reasons for the paradigm shift towards plasma assisted catalysis. In conventional catalysis the processes and reactions are thermally driven

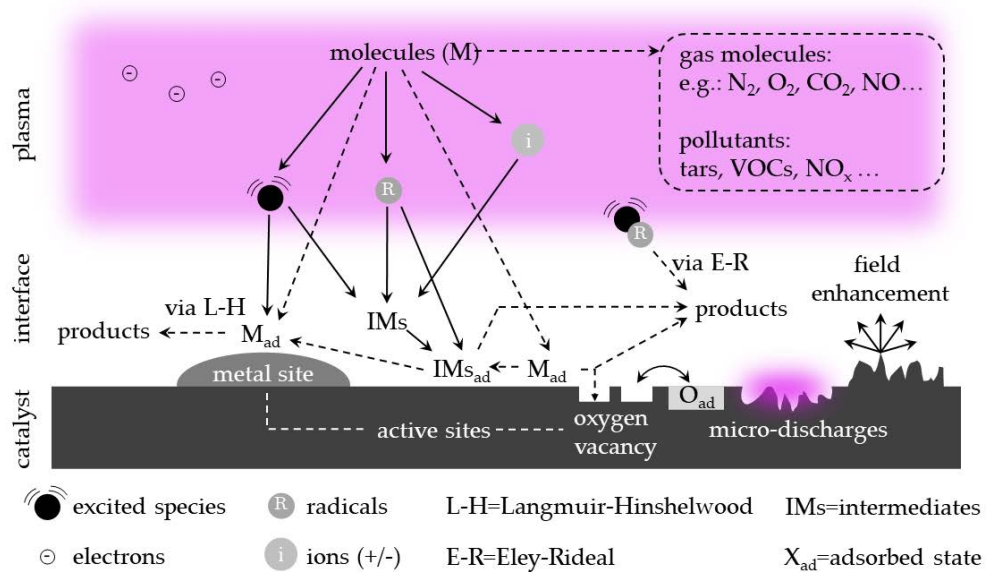


**Figure 1.2.** Illustration of the most important key mechanisms during plasma assisted catalysis. Modified image inspired by [16].

- hence, by nature the energy distribution is non-selective and equally distributed among all degrees of freedom, as shown by the equipartition theorem [15]. This is very different in plasma assisted catalysis. Here the reactions are partly driven non-thermally, which offers the possibility to direct the energy selectively into a single desired reaction coordinate, in order to tailor the kinetics for a given application. The aforementioned advantages are only a few of many more complex possibilities that have become accessible by the use of plasma. There are, however, many more processes that can be beneficial for catalysis originating from plasma processes. This may be the change of the oxidation state at the surface, the change of the morphology on the nanoscale in order to create reactive sites, the change of surface reactions due to surface charges and many more. An overview sketch to illustrate the different key mechanisms is shown in figure 1.2. A detailed overview about plasma catalysis can be found in [16]. While conventional catalysis has evolved over more than 100 years to its current state and its industrial usage, plasma assisted catalysis is in the very beginning and an intense ongoing field of research.

However, the highly complex dynamics of non-equilibrium plasma systems

are both - boon and bane in a sense. While the characteristics offer the described benefits, the plasma sources are difficult to operate to assure a high selectivity towards a desired species. Furthermore, the modeling of those discharges is very complex and time-consuming due to the high number of reactive species and the even higher number of chemical reactions that can occur in different discharge types. It is therefore crucial to experimentally measure the different plasma parameters, such as the density of reactive species, in order to gain control and fundamental knowledge to optimize the processes for the desired application and compare them to models to reveal the chemical and physical mechanisms.

The fact that the efficiency of a catalytic surface is, among other parameters, strongly dependent on the morphology, gives rise to the use of laser sources. Surface modifications by laser irradiation is a long known field. Nowadays e.g., laser cutting or laser welding are well established techniques commonly used in the industry [17, 18]. Over the last decades a relatively new phenomenon was observed that was referred to as *Laser Induced Periodic Surface Structures*, abbreviated LIPSS. The very beginning of these structures leads back to the year 1965, where it was described as a surface defect [19]. It was then only in the last two decades that the publications about LIPSS have rapidly taken off and experimental and theoretical data have been collected [20]. Nevertheless, it is still an ongoing controversial discussion, which of the several proposed theories is the most adequate description of the phenomenon. One of the special features when it comes to LIPSS is the tuneability of the induced structures. The periodicity, orientation, height and other properties can be tuned by the excitation laser parameters, such as pulse energy, angle of incidence or wavelength to name a few. This offers the possibility of tailoring the structures depending on the needs of various applications. The increase of the effective surface area, due to LIPSS formation, might change the catalytic activity of a sample by inducing - and hence increasing - the accessible active sites as compared to flat polished surfaces. This was, among others, investigated by Lange et al. [21] and Neale et al. [22] for picosecond pulses onto platinum and nickel electrodes, where the electrochemical activity could be significantly improved. Beside the LIPSS, another known feature of surface morphology modification, which also increases the

effective surface area is the creation of nanoparticles by, e.g., *Pulsed Laser induced Dewetting* formation, abbreviated PLiD - or PLiDs. Nanoparticle formation on surfaces is also known to improve the catalytic activity, see.e.g. [23, 24]. Nanoparticle formation via dewetting is also a tuneable mechanism, depending on laser and surface parameters, as e.g. the film thickness or the deposited energy onto the surface.

In this context the simultaneous interaction of plasma treatment of the surface, more precisely the reactive species that are transported and laser irradiation that induces the before mentioned tailored structures can lead to new synergisms that need to be investigated and controlled. This might be the incorporation of species into the surface, changing the chemical compound. The general field of plasma catalysis will certainly not replace the well explored field and established classical catalysis. But it certainly offers new possibilities and chemical transformations that can beneficially supplement conventional catalysis.

### 1.3 Thesis outline - key questions

Atmospheric pressure plasma jets provide a huge number of different reactive species. One of the crucial parts is to know and, if possible, being able to control and tailor the absolute number of different species to gain full control of the surface treatment process and to avoid endangering, e.g., biological materials by exceeding harmful limit densities. To have comparable results around the labs of the world in 2016 the COST-Reference Jet was introduced by Golda and Schulz-von der Gathen et al. [25]. Over the years a lot of data, both experimentally and theoretically, have been collected revealing the absolute densities of several species and their forming mechanisms (see e.g., [26, 27, 28, 29]). However, extending data for various species to have a benchmark is still a central point. Furthermore, while biomedical applications are usually performed in an open, reactive air atmosphere, technological applications are often performed under a closed inert atmosphere to have clear defined conditions and suppress interactions with reactive molecules in the surrounding atmosphere. This is also important for fundamental studies, such as modeling density distributions. Therefore, significant differences of the densities with

the jet operated in different atmospheres can occur. Nitric Oxide has shown to be an important molecule, especially for biomedical applications since it triggers many biological processes and can act as an extracellular messenger.

***Key question I***

*What is the 3-dimensional density distribution of Nitric Oxide in the effluent of the COST-Reference Jet in different atmospheres and what are the formation and transport mechanisms?*

The benchmarking of the reactive species density distribution in the free effluent is one central aspect for the characterization of a reference source. From those data the fundamental chemical kinetics, creation, and loss mechanisms can be derived and a fundamental knowledge can be obtained. However, during sample treatments, the reactive species that arrive at the surface are, on the one hand, subject to pure fluid-solid state interactions that will deflect the species from its original trajectory and, on the other hand, are undergoing further chemical reactions that can significantly change the densities as compared to those measured in the free effluent. Those chemical reactions and the dynamics can be significantly different depending on the surface material.

***Key question II***

*What is the 3-dimensional density distribution of Nitric Oxide species in front of surfaces using different materials and how does it compare to the distributions in the free effluent?*

The main aim of the project that this thesis is part of is to investigate the simultaneous interaction between reactive species coming from the plasma jet and short pulsed laser irradiation and to find possible synergisms concerning the catalytic activity of the surface. However, different mechanisms must first be investigated independently of each other to have control and full knowledge of the final interplay between the involved processes. The interaction of laser pulses and surfaces have been investigated for decades. However, it has only been in the last twenty years that the number of publications concerning LIPSS and the formation of nanoparticles via PLiD has steeply risen. The concrete physical mechanism, that creates the structures is still a controversial

discussion in the field. It is in this context crucial to perform further experiments, to verify which of the relevant theories is applicable and whether the structures can be induced and controlled with laser and surface parameters on the materials of interest for catalytic processes.

***Key question III***

*Can periodic structures be induced via short pulsed laser irradiation, under conditions that are suitable for plasma catalysis? If so, what is the physical mechanism and which theory is applicable? Can those induced structures be tailored by changing laser or surface parameters?*



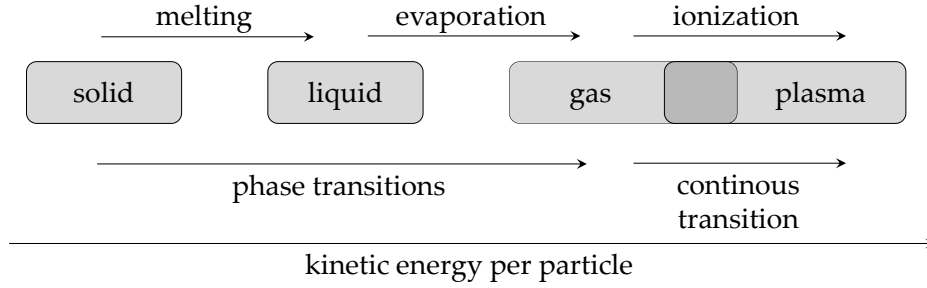
## Chapter 2

# Fundamentals

In this section physical fundamentals are explained. This contains for the sake of completeness a brief description of the term plasma and the underlying physical and chemical mechanisms, as well as the used diagnostics in this study.

### 2.1 Non-equilibrium atmospheric pressure plasmas

Matter in the universe can exist in a variety of stable forms. For most non-scientific people the classification of those states of matter is limited to three: the solid state that, can be transferred into a liquid by adding energy to the system and raising the temperature beyond the melting point and eventually the gas state that is reached when adding further energy and the atoms have sufficient energy to desorb. These are commonly known as the three states of matter. However, a fourth state can be distinguished by adding further energy into the gaseous system and ionizing the neutral atoms or molecules, hence the state contains charged particles and is conducting. Irving Langmuir firstly described this state as the *plasma state* [30]. Therefore, a plasma is often called the fourth state of matter, although the transition from the gas to the plasma state is continuous, whereas for the other transitions a phase transition with involved latent heat takes place. And even though the plasma state is not familiar to many people, the common assumption is that  $\approx 99\%$  of the visible matter, both by mass and volume, in the universe is in this state.



In order to call a state in the plasma state typically three criteria need to be fulfilled. These criteria are connected with two characteristic plasma parameters. Those are namely the *Debye length* ( $\lambda_D$ ), which is the length at which a plasma shields an electric potential. and secondly the *plasma frequency*,  $\omega_p$ , which is the frequency at which an electron oscillates when being replaced out of its position in rest in front of a constant and static ion background.

- $L > \lambda_D = \sqrt{\frac{\epsilon_0 k_B T_e}{n_e e^2}}$  The length of the plasma needs to be bigger than the Debye length in order to guarantee quasi neutrality
- $N_D \gg 1$  The number of particles in the Debye sphere  $N_D$ , a volume of the sphere with radius  $\lambda_D$ , needs to be large in order to guarantee collective behavior
- $\omega_p \tau_c = \sqrt{\frac{n_e e^2}{\epsilon_0 m_e}} \tau_c \gg 1$  The product of plasma frequency and collision time with a neutral needs to be large in order to guarantee the dominance of electrostatic forces over the conventional gas kinetics dominated by collisions

Within the state of a plasma the different parameters, such as temperature or density, can vary over a wide range. For these concrete properties, this may differ like  $k_B T_e \approx 0.1$  eV and  $n_e \approx 1 \times 10^1$  cm<sup>-3</sup> for interstellar space plasmas up to  $k_B T_e \approx 10^5$  eV and  $n_e \approx 10^{16}$  cm<sup>-3</sup> for controlled fusion experiments ( $k_B$  is Boltzmanns constant). Those plasmas are then categorized into thermal and non-thermal plasmas according to high or low temperatures.

In this thesis the focus will be on a non-thermal, non-equilibrium atmospheric pressure plasma jet that is operated at radio frequency (RF). The non-equilibrium nature of the discharge originates from the external alternating field that is induced by the RF generator. A detailed sketch of the source and the parameter can be found in section 3.1. Due to the large mass difference between the electrons and the heavy particles, for example ions ( $m_e/m_i \approx 1/2000$ ), the relation between the external excitation frequency and the plasma frequency of

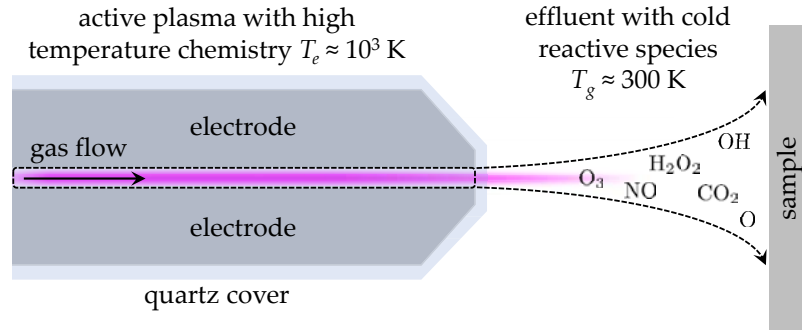


**Figure 2.1.** Sketch of the different regions of the used plasma source. The active plasma region is located in between the electrodes. This region is characterized by high electron temperatures and build up of high amounts of different reactive species. The reactive species are eventually carried into the effluent by the gas flow, where they first interact with the surrounding atmosphere and finally arrive at the surface of the treated sample where different mechanisms can be triggered.

the respective species reads  $\omega_{p,e} > \omega_{RF} > \omega_{p,i}$  and therefore the electrons are effectively heated by several mechanisms ( $T_e \approx 10^3$  K), while the heavy particles remain cold near room temperature ( $T_h \approx 300$  K). This is an important aspect, since the high electron temperature can trigger strong temperature dependent reactions and chemistry, while the thermal stress for a treated sample remains low. A sketch of the different regions and the distinct properties can be seen in figure 2.1.

## 2.2 0-dimensional modeling of NO

To compare the experimental observed densities of NO with theoretical predictions, a zero dimensional model was developed. This is also important to reveal the chemical kinetics and reactions that are significantly responsible for the creation or destruction of the respective species. In this thesis only the fundamentals of the model are briefly explained. A detailed description of the model and the simulation efforts can be found in [31].

### 2.2.1 Model

For the model the species and electron balance equation are incorporated and the effective electron temperature,  $T_e$ , is derived from the mean energy of

a non-Maxwellian EEDF as is used in [32, 33]. The electron density is obtained from the quasi neutrality implementation [34]. The gas temperature,  $T_g$ , is measured in the experiments and used for the simulations. The non-Maxwellian EEDFs are calculated using the open source solver LoKI-B.

The species that are considered for the simulations are reported in [31]. The volume averaged particle balance equation is given by

$$\frac{dn_i}{dt} = \sum_j \Xi_{ij} R_i^j \Big|_V + \sum_j \Xi_{ij} R_i^j \Big|_W \quad (2.1)$$

where  $n_i$  is the respective volume averaged species,  $\Xi$  is the net stoichiometric coefficient for either a gain or loss mechanism denoted by  $j$  and  $R_i^j$  is the reaction rate. Here  $W$  describes the flux source term which includes interactions and reactions with the walls and  $V$  stands for processes inside the plasma bulk. In the plasma volume it is:

$$R_i^j \Big|_V = k_j \prod_l n_l^{\nu_{lj}}, \quad (2.2)$$

where  $k^j$  is the reaction coefficient and  $n_l$  the respective reactant density with  $\nu_{lj}$  the forward stoichiometric coefficient.

The flow in and the flow out rate are given respectively as

$$R_{in}^s = \frac{c p_{atm}}{V k_B T_{in}} \Phi_s \quad R_{out}^i = \frac{c p_{atm} T_g n_i}{V p T_{in}} \Phi_s. \quad (2.3)$$

Here  $i$  and  $s$  denotes the respective species, i.e., in this case  $s \hat{=} \text{He, N}_2$  or  $\text{O}_2$ .  $\Phi_s$  is the partial mass flow rate,  $p$  and  $p_{atm}$  the plasma and the atmospheric pressure, respectively  $T_{in}$  the feed gas temperature and  $c$  the conversion factor.

The ion and neutral wall flux to the surfaces perpendicular to the flow field is neglected due to the negligible small area as compared to the surfaces parallel to it ( $\leq 2\%$ ). The loss to the surfaces parallel to the flow field is implemented as

$$R_i^+ \Big|_W = \left( u_{iB} \frac{2h_{ix}^+ A_y}{V} + u_{iB} \frac{2h_{iy}^+ A_y}{V} \right) n_i. \quad (2.4)$$

where  $u_{iB}$  is the Bohm velocity,  $V$  and  $A$  are the volume and the areas in  $x$ -respective  $y$ - directions and  $h$  is the ion edge to center ratios. The  $h$  values in the collisional regime are calculated as in [34, 35]. The reaction rate due to diffusion of a neutral particle to the walls and the resulting reaction is given as:

$$R_i^{diff} = \left( \frac{\Lambda_0^2}{D_i} + \frac{2V(2 - \gamma_i)}{2(A_x + A_y)\langle v_i \rangle \gamma_i} \right)^{-1} n_i \quad (2.5)$$

where  $\Lambda_0$  is the effective diffusion length,  $D_i$  the classical diffusion coefficient and  $\langle v_i \rangle$  the mean velocity.  $2(A_x + A_y)$  is the total surface area and  $\gamma_i$  the wall reaction probability. The net volume averaged energy balance equation for the electrons in order to describe the energy gains and losses is described by:

$$\frac{d}{dt} \left( \frac{3}{2} n_e T_e \right) = Q_{abs} - \sum_k Q_k \quad (2.6)$$

where  $k$  is the sum over all losses. It is assumed that the energy provided by the generator is mainly absorbed by the electrons and subsequently released to the plasma volume by different processes. Hence, the absorbed power  $Q_{abs}$  is simply described by  $Q_{abs} = \beta P_{RF}/V$ , where  $\beta$  is the transfer efficiency and  $P_{RF}$  is the generator power. The losses and therefore the distribution to the plasma volume, on the other hand, are ascribed to three mechanisms:

I the energy loss due to chemical reactions according to

$$Q_{che} = \sum_j \mathcal{E}_j R_e^j \Big|_V, \quad (2.7)$$

where  $\mathcal{E}_j$  is the net energy absorbed or released during the reaction and  $R_e^j$  is the reaction rate

II the energy loss due to the flux towards the walls as

$$Q_W = \sum_{i \in \text{ions}} (\Phi_p + \Phi_{sh} + \mathcal{E}_e) R_i^+ \Big|_W. \quad (2.8)$$

Here  $\Phi$  is the plasma and the sheath potential, respectively and  $\mathcal{E}_e = 2T_e$  is the mean energy loss for an electron crossing the sheath to the wall

III the elastic losses in the plasma. Assuming the electron temperature to be much bigger than the neutral gas temperature the elastic loss can be calculated via

$$Q_{ela} = 3n_e T_e \sum_j \frac{n_j}{m_j} k_{ej}^{ela} \quad (2.9)$$

where  $k_{ej}^{ela}$  is the elastic rate coefficient.

Hence, the losses are described as  $\sum_k Q_k = Q_{che} + Q_W + Q_{ela}$ .

## 2.2.2 Chemical kinetics

In this study only a gas mixture containing He/N<sub>2</sub>/O<sub>2</sub> is measured. The species, the reactions, and the elastic collision sets that are taken into account in this model and a detailed description of the kinetics and the respective references can be found in [31]. However, it should be stated here that certain modifications of the production channels as compared to the existing literature needed to be applied to match the experimental data. These modifications in the He/N<sub>2</sub>/O<sub>2</sub> mixture concerning the NO production are as follows:

- I A rate coefficient of  $10^{-17} \text{ m}^3 \text{ s}^{-1}$  [36] instead of  $10^{-19} \text{ m}^3 \text{ s}^{-1}$  as used in [37, 38, 39] is applied for the reaction



This rate coefficient had to be adjusted, to fit the experimental data. This might be an indication that this reaction is much more pronounced in the COST-Jet, as compared to the existing sources in the literature, where the smaller coefficient is applied.

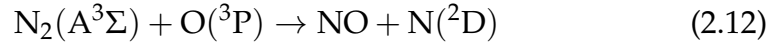
- II For kinetic models in the low pressure regime the NO wall formation due to adsorption of O(<sup>3</sup>P) and N(<sup>4</sup>S) is typically neglected [40]. However, at atmospheric pressure those effects are not necessarily negligible and they are taken into account in this model as



This mechanism requires a sufficient concentration of adsorbed O(<sup>3</sup>P) atoms which is reasonable, due to its much higher concentration in the

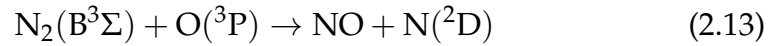
discharge channel as measured in previous studies (see e.g., [41, 42, 43, 44])

III For the reactive quenching mechanism of the A state according to



there is a well accepted value in the literature of  $7 \times 10^{-18} \text{ m}^3 \text{ s}^{-1}$  (see e.g. [37, 45, 46]). However, this value is only valid for the vibrational ground state  $\text{N}_2(\text{A}^3\Sigma, v = 0)$ . For higher vibrational quantum numbers a much larger coefficient is found [47, 48, 49, 50]. Here also the vibrational excited species,  $\text{N}_2(\text{A}^3\Sigma, v > 0)$  are calculated in the model and their influence on the NO formation is attributed by a larger rate coefficient of  $7 \times 10^{-15} \text{ m}^3 \text{ s}^{-1}$

IV The reactive quenching of the B state according to



is neglected in many chemical kinetic studies. However, there are studies who take this quenching mechanism into account with a rate coefficient for the vibrational ground state of  $3 \times 10^{-16} \text{ m}^3 \text{ s}^{-1}$  [51, 52]. Again it is observed that for higher vibrational quantum numbers larger values are measured. Thus, the same coefficient as presented in III is taken into account for this reaction.

Implementing these modifications in the base chemical kinetic set, an excellent agreement is found between the simulated and the measured NO densities. This agreement is much more pronounced for high powers as compared to lower powers, which is an indication that vibrationally excited nitrogen molecules  $\text{N}_2(v \geq 13)$  contribute to NO formation in this regime.

## 2.3 Laser Induced Fluorescence (LIF)

Laser Induced Fluorescence is the effect of (spontaneous) emission from atoms or molecules that were excited to upper states by interaction with a laser radiation field. However, the process of induced fluorescence was first discussed back in 1905 by R.W. Wood more than 50 years before the invention of the first laser in 1960. The invention of the first laser and its ongoing progression offered new possibilities and deeply influenced the experimental research in many scientific topics.

When an atom or molecule that is exposed to the radiation field of a laser resonantly absorbs a photon it is left in an unstable excited state that has a finite lifetime typically in the order of ns. After this time the state will de-excite spontaneously to a lower energetic state emitting a photon. This process is called induced fluorescence. To describe the underlying processes quantitatively and calculate absolute densities, as done in this thesis, the relevant light-matter interactions are described in the following.

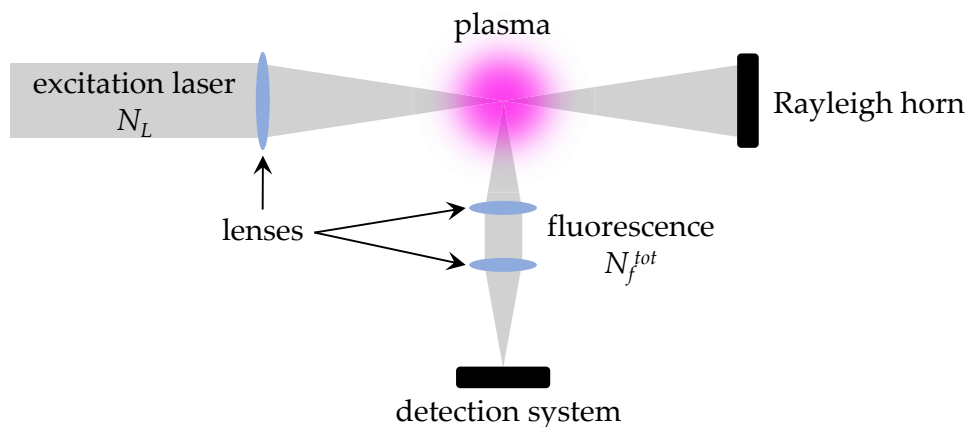


**Figure 2.2.** Typical optical setup for a LIF measurement with a two lens detection system. Especially seen here is the excitation laser with number of photons  $N_L$  and the fluorescence signal with a total number of photons  $N_f^{tot}$

### 2.3.1 Transition probabilities

In order to detect a fluorescence signal from the molecule of interest it is necessary that it undergoes a transition  $|i\rangle \rightarrow |k\rangle$ , i.e., the eigenstates change in

time. Therefore, the system is described by the time dependent Schrödinger equation that can be solved using Dirac's time dependent perturbation theory. The solution yields a wave function of the form (for a state  $m$ ):  $\psi(\vec{r}, t) = \psi_m(\vec{r}) \exp\{-iE_m t/\hbar\}$ , where  $E_m$  is the energy of the state  $m$ . However, usually the solution is written as a linear combination of wave functions according to

$$\psi_m(\vec{r}, t) = \sum_n c_{mn}(t) \psi_n(\vec{r}) \exp\{-iE_n t/\hbar\}, \quad (2.14)$$

where  $c_{mn}(t)$  are time dependent coefficients and  $\psi_n(\vec{r})$  are time independent wave functions of the unperturbed system, i.e., in the absence of any external field. The coefficients  $c_{mn}$  reflect the probability to find the particle in the respective state and hence  $\sum_n |c_{mn}(t)|^2 = 1$ .

When substituting into the Schrödinger equation and solving the set of differential equations one can deduce an important quantity that reads [53]:

$$\vec{D}_{ik} := q \langle \psi_k | \vec{r} | \psi_i \rangle = q \int d^3r \psi_k^*(\vec{r}) \vec{r} \psi_i(\vec{r}), \quad (2.15)$$

where  $q$  is the charge of the particle. This is the so-called transition dipole moment. This quantity determines the way how the system will interact with an electromagnetic wave. The transition probabilities (in units of  $s^{-1}$ ) for an electron with charge  $|q| = e$  can then be expressed in terms of this moment [54]:

$$A_{ki} = \frac{4e^2 \omega_{ki}^3}{3\hbar c^3} |\langle \psi_k | \vec{r} | \psi_i \rangle|^2 \quad (\text{spontaneous emission}) \quad (2.16)$$

$$R_{ik} = \sigma_{exc} g(\Delta\nu) \frac{I_L(\vec{r}, t)}{h\nu_L} \quad (\text{absorption rate}) \quad (2.17)$$

$$R_{ki} = \frac{g_i}{g_k} R_{ik} \quad (\text{induced emission rate}) \quad (2.18)$$

$$\Gamma_k = \frac{I_L(\vec{r}, t)}{h\nu_L} \int d\nu \sigma_i(\nu + E_e/h) g_L(\nu) \quad (\text{photoionization rate}) \quad (2.19)$$

Here  $g_{i,k}$  are the statistical weights of the respective states,  $I_L$  is the laser intensity,  $E_e$  the average energy of the laser photons,  $\sigma_i$  the ionization cross section and  $\nu_L$  the frequency of the laser. Furthermore,  $\sigma_{exc}$  is the excitation cross

section that is defined as

$$\sigma_{exc} = \frac{2\pi^2\nu_{ki}}{c\epsilon_0\hbar} |\langle \psi_k | \vec{r} | \psi_i \rangle|^2 \quad (2.20)$$

and  $g(\Delta\nu)$  is the excitation line profile. This can be calculated as the convolution of the absorption profile  $g_{ik}$  and the spectral profile of the excitation laser  $g_L$ :

$$g(\Delta\nu) = g_{0u} \otimes g_L = \int d\nu g_{0u}(\Delta\nu - \nu) \cdot g_L(\nu). \quad (2.21)$$

The calculation of the convolution of these profiles in general is difficult, due to the unknown laser profile, as well as several broadening mechanisms of the transition in the plasma.

### 2.3.2 Rate equations - total number of LIF photons

Here is given a short derivation for the expression of the absolute number of fluorescence photons coming from a solution of the rate equation for the upper state to calculate the densities. A more detailed procedure of the solutions and approximations for different regimes can be found in [54].

Taking into account the different possible interactions of the radiation and matter, the rate equations for the different states, where  $n_0$  is the density of the ground state,  $n_u$  is the density of the upper excited state and  $n_i$  is the ion density of the investigated species

$$\frac{dn_u}{dt} = R_{0u}(\vec{r}, t)n_0 - n_u \left( \Gamma_u + A_{u0} + R_{u0} + \sum_j n_j k_{q,j} \right) \quad (2.22)$$

$$\frac{dn_0}{dt} = -R_{0u}(\vec{r}, t)n_0 + n_u (R_{u0} + A_{u0}) \quad (2.23)$$

$$\frac{dn_i}{dt} = \Gamma_i n_u \quad (2.24)$$

where the quantities  $R$ ,  $A$  and  $\Gamma$  are the rate coefficients as introduced and  $Q_u = \sum_j n_j k_{q,j}$  is the quenching rate due to collisions. In this case only the solution for the upper state is important since the decay from this state emits the photons that are essential in order to perform the LIF technique. Taking

into account a rectangular shaped laser pulse of the form  $I = I_0$  during the pulse ( $t \in [0, \tau_L]$  where  $\tau_L$  is the length of the pulse and 0 else wise), the differential equations can be solved using the following boundary conditions:

$$n_u(0) = 0, \quad n_0(0) = \hat{n}_0, \quad n_i(0) = 0. \quad (2.25)$$

The solution for the upper excited state during the excitation phase then reads:

$$n_u(t) = \hat{n}_0 R_{0u} \frac{\exp\{-\lambda_2 t\} - \exp\{-\lambda_1 t\}}{\lambda_1 - \lambda_2} \quad (2.26)$$

where  $\lambda_{1,2}$  are characteristic rates according to

$$\lambda_{1,2} = \frac{R_{0u} + \Gamma_u + R_{u0} + A_{u0} + Q_u}{2} \pm \sqrt{\left(\frac{R_{0u} + \Gamma_u + R_{u0} + A_{u0} + Q_u}{2}\right)^2 - R_{0u}(\Gamma_u + Q_u)}. \quad (2.27)$$

where  $Q_u = \sum_j n_j k_{q,j}$  is the quenching rate. During the relaxation phase  $t > \tau_L$  the solution simplifies to

$$n_u(t) = n_u(\tau_L) \exp\left\{- (A_{u0} + Q_u)(t - \tau_L)\right\} \quad (2.28)$$

Those are general solutions for the upper state taking into account all the interactions from 2.16, 2.17, 2.18, 2.19. However, in the discharge and the laser LIF regime applied in this thesis several effects can be neglected. This constitutes ionization, since the photon energy of the laser is only about  $5 \text{ eV} < E_{i,\text{NO}} \approx 9.26 \text{ eV}$  [55] which is smaller than the ionization energy of NO from the ground state. Furthermore, it is assumed that at room temperature the ground state is strongly overpopulated according to the PLTE and corona equilibrium, hence  $n_0(t) \approx \hat{n}_0$ . Then the induced emission can also be neglected, i.e., ( $R_{u0} = \Gamma_u = 0$ ). In this case the rate equations can be simplified and solved. The solutions in the excitation and the relaxation phase then read:

$$n_u(t) = \begin{cases} \hat{n}_0 \int_0^\infty d\tilde{t} R_{0u} \exp\{-(A_{u0} + Q_u)(t - \tilde{t})\} & \text{for } t \in [0, \tau_L] \\ n_u(\tau_L) \exp\{-(A_{u0} + Q_u)(t - \tau_L)\} & \text{for } t > \tau_L \end{cases} \quad (2.29)$$

Since for every transition one photon is emitted, multiplication of the upper state with the Einstein coefficient for spontaneous emission and subsequent integration over the interaction volume  $V$  of length  $L$ , yields an expression for the total number of fluorescence photons,  $N_{tot}^f$ , emitted from particles that were excited by a weak laser pulse with  $N_L$  photons:

$$N_{tot}^f = A_{u0} \int_V \int_0^\infty dt dV n_u(t) \quad (2.30)$$

$$= \frac{A_{u0}}{A_{u0} + Q_u} n_0 \sigma_{exc} g(\Delta\nu) \int_V \int_0^\infty dt dV \frac{I(t)}{h\nu_L} \quad (2.31)$$

$$= \frac{A_{u0}}{A_{u0} + Q_u} n_0 \sigma_{exc} g(\Delta\nu) L N_L \quad (2.32)$$

From equation 2.32 it can be seen that the total number of fluorescence photons emitted, which is recorded as the LIF signal by a photomultiplier is directly proportional to the number of the particles in the ground state  $n_0$ .

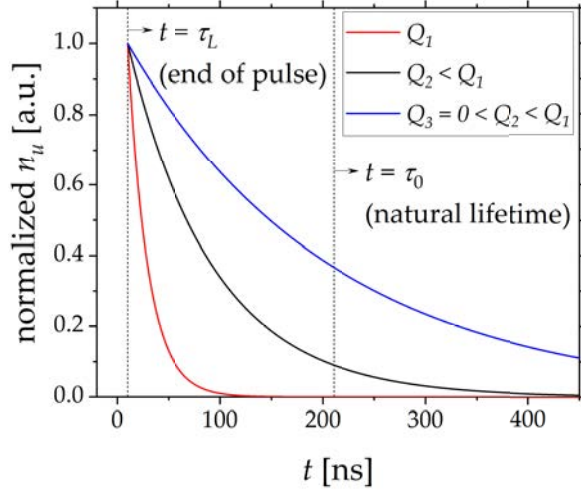


**Figure 2.3.** Density of the upper state  $n_u(t)$  in the relaxation phase, according to equation 2.29. Shown are three different regimes of quenching. One with no quenching which results in the natural lifetime (blue), one with moderate (black) and one with strong quenching (red).

Furthermore, the signal is not dependent on the actual laser pulse shape but only on the number of photons per pulse. It can also be seen that the number of emitted fluorescence photons is strongly dependent on the quenching, i.e., the factor  $Q_u$ . The population of the upper state  $n_u(t)$  is displayed in figure 2.3. Seen here is the relaxation phase in three different environments. One without quenching that gives the natural lifetime of the state, one with moderate and one with

strong quenching. It can be seen that the lifetime is significantly decreased by this inelastic collision process. This needs to be accounted for when performing LIF measurements and calculations. The concrete procedure is discussed

in section 4.2.1.

### 2.3.3 The $\gamma$ -band of NO ( $A^2\Sigma^+ \rightarrow X^2\Pi$ )

The electronic spectrum of Nitric Oxide was one of the first spectra observed by spectroscopists already in the early 20<sup>th</sup> century [56]. In this context the  $\gamma$ - and the  $\beta$ -system have been extensively studied and are well understood [57, 58]. Figure 2.4 shows the three electronic levels, the vibrational and schemat-

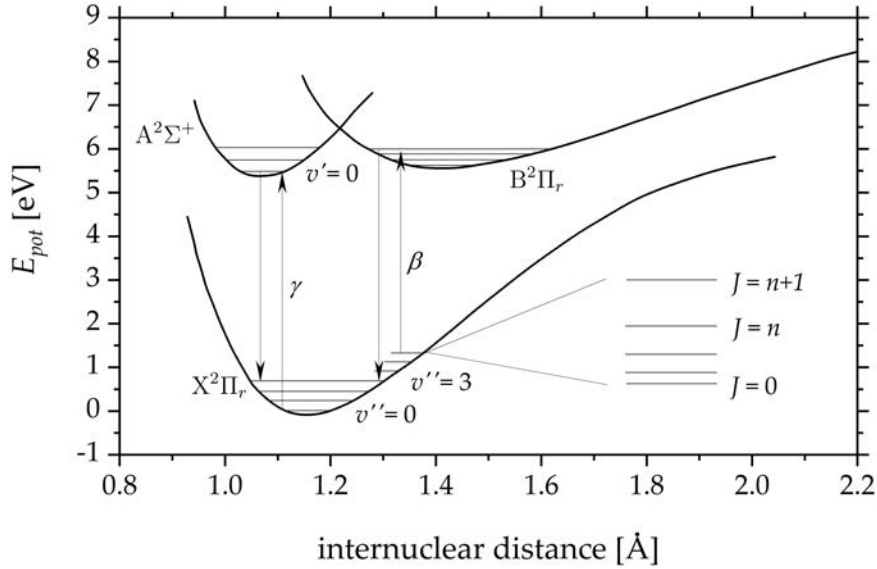


**Figure 2.4.** Potential energy curves for the ground and first excited electronic states of NO whose transition is observed for the LIF measurements in this thesis. The excitation takes place from  $X^2\Pi(v'' = 0) \rightarrow A^2\Sigma^+(v' = 0)$ , which equals a wavelength of  $\lambda_{exc} \approx 226.9$  nm, while the fluorescence photons are emitted during the transition  $A^2\Sigma^+(v' = 0) \rightarrow X^2\Pi(v'' = 3)$  at a wavelength of  $\lambda_F \approx 259$  nm. The energy curves are taken and modified from [59].

ically the rotational states corresponding to the transitions forming the bands - here the  $\gamma$ - and the  $\beta$ - bands are shown. The total energy of the state can then be described by a sum according to

$$E_{tot}(n, v, J) = E_{el}(n) + E_{vib}(v) + E_{rot}(J) \quad (2.33)$$

where  $E_{vib}$  and  $E_{rot}$  are the vibrational and the rotational energy respectively. They are obtained from the analytical solution of the Schrödinger equation

according to [60]:

$$E_{vib}(v) = \hbar\omega_0 \left( v + \frac{1}{2} \right) - \underbrace{\frac{\hbar^2\omega_0^2}{4E_D} \left( v + \frac{1}{2} \right)^2}_{\text{anharmonicity}} \quad (2.34)$$

$$E_{rot}(J) = \frac{J(J+1)\hbar^2}{2\mu R_e^2} - \underbrace{\frac{J^2(J+1)^2\hbar^4}{2k\mu^2 R_e^6}}_{\text{centrifugal distortion}} + \mathcal{O}(J^3) \quad (2.35)$$

here  $v$  and  $J$  are the vibrational and rotational quantum numbers, respectively,  $\mu$  is the reduced mass of the atoms,  $E_D$  is the dissociation energy and  $R_e$  is the location of the potential minimum, hence the equilibrium distance. For small vibrational and rotational quantum numbers the deviation anharmonicity of the potential and the centrifugal distortion can be neglected and considering the approximations the energy terms strongly simplify.

In this thesis the band of choice to measure the NO densities will be the  $\gamma$ -band. The excitation takes place from the vibrational ground level of the X state to the ground level of the A state  $X^2\Pi(v'' = 0) \rightarrow A^2\Sigma^+(v' = 0)$  at a wavelength of  $\lambda_{0,0} = 226.94$  nm, while the fluorescence signal is recorded for another transition into the third excited vibrational level according to  $A^2\Sigma^+(v' = 0) \rightarrow X^2\Pi(v'' = 3)$  and a wavelength of  $\lambda_{0,0} = 259.57$  nm [61]. The detection at another wavelength is chosen in order to minimize stray-light from the excitation wavelength. Furthermore the line for the detection was intense and well separated from other lines so that no line wings or other effects from neighbor lines should influence the signal. A spectrum of the ro-vibrational band can be seen in figure 2.5. The lifetime of the upper excited state of the  $\gamma$ -band is measured in the scope of this thesis. However the natural lifetime can also be calculated theoretically, according to

$$\frac{1}{A_{v',v''}} = \frac{m_e c_0}{8\pi^2 e^2 f_{v',v''} \tilde{\nu}^2} \frac{g_2}{g_1} \quad (2.36)$$

where  $A_{v',v''}$  and  $f_{v',v''}$  are the Einstein coefficients and the  $f$  value for the respective band and  $\tilde{\nu}$  is an average wavenumber.  $g_1$  and  $g_2$  are the degeneracies of the state. The electronic absorption oscillator strength was measured

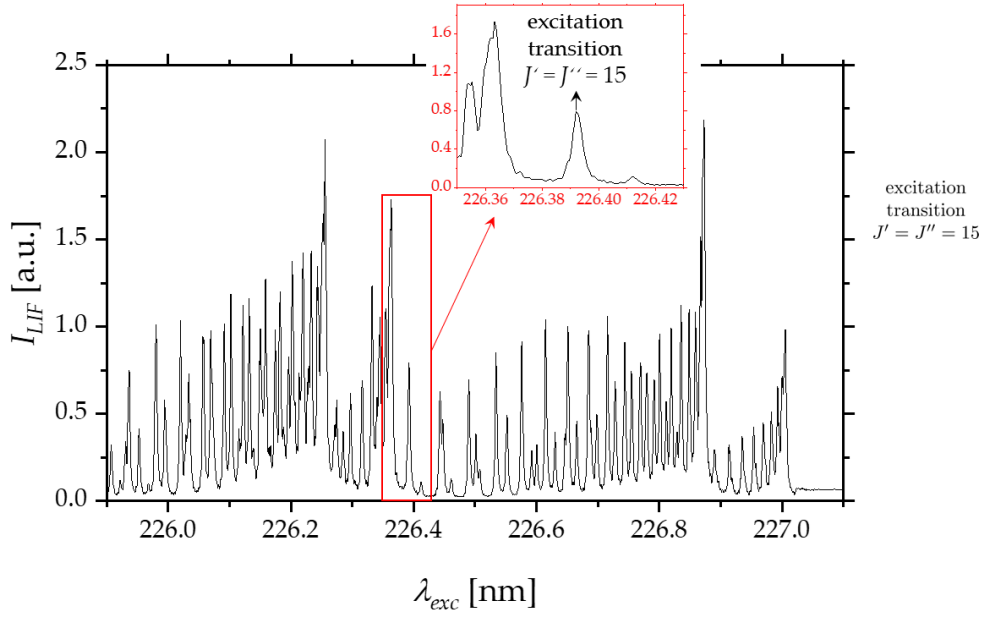


**Figure 2.5.** Measured NO spectrum of the  $\gamma$ -band. In the zoomed area the transition chosen for the LIF excitation is shown. It is chosen due to its relatively high intensity and its spectral position to be as good isolated from the neighbour lines as possible.

by Bethke et al. to be  $3.99 \times 10^{-4}$  [62]. This is connected to the  $f$ -value via

$$f_{el} = \frac{f_{v',v''} \tilde{\nu}}{q(v',v'') \nu_{v',v''}^3} \quad (2.37)$$

where  $q(v',v'')$  is the Franck Condon factor for the  $\gamma$ -band and  $\tilde{\nu}$  is an average wavenumber,  $\tilde{\nu} = 48.082 \text{ cm}^{-1}$ . The radiative lifetime of a state can then be calculated:

$$\tau_{v',v''} = \frac{1}{A_{v',v''}} = \frac{8\pi^2 e^2 f_{el} g_1}{m_e c \tilde{\nu} g_2} q(v',v'') \nu_{v',v''}^3 \quad (2.38)$$

$$= 0.66 \times 10^{-7} q(v',v'') \nu_{v',v''}^3 \quad (2.39)$$

With the Franck-Condon factors taken from [58] the radiative lifetime for  $v' = 0$  results in  $\tau_{0,v''} \approx 217 \text{ ns}$ .

Those are the fundamentals of the diagnostic to measure and calculate absolute densities of reactive species, more precise NO in this thesis. The plasma and the reactive species generated within is one of the main components of

the project this thesis is part of. The final aim is to investigate the simultaneous interaction of those reactive species with pulsed laser irradiation onto a solid sample. This pulsed laser irradiation induces periodic structures on the surface, that is intensively during the last twenty years. This phenomenon is called Laser Induced Periodic Surface Structures, abbreviated (LIPSS). The change of the morphology combined with the interaction of reactive species might be beneficial for the incorporation of reactive species and change the chemical bonds within. This in turn might be beneficial for a catalysis process.

In the following section the different theoretical approaches to describe the formation of these structures are briefly explained.

## 2.4 Laser Induced Periodic Surface Structures (LIPSS)

Laser Induced Periodic Surface Structures, in the following abbreviated as LIPSS, is a phenomenon that occurs on solid surfaces upon radiation with short, intense, polarized laser beams. LIPSS emerge on the surfaces as periodic structures that show a strong and clear correlation to the laser properties, such as polarization, fluence, wavelength, number of pulses or the pulse duration that can range from cw laser operation down to only a few femtoseconds. The dependence of the structures on the mentioned properties and many more offer a wide parameter space to be studied for the formation and the theoretical explanation of LIPSS.

The discovery of periodic structures on a polished germanium single crystal surface irradiated by a ruby laser goes back to the year 1965 by Birnbaum et al. [19] who first declared it as a "surface damage [...] a regular system of parallel straight lines" on the material caused by the intense laser exposure.

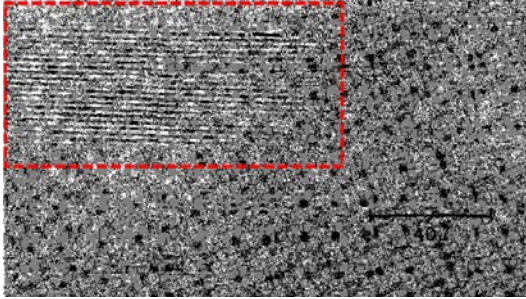


**Figure 2.6.** Photomicrograph of the surface damage of a (111) face of the germanium sample used in the publication of Birnbaum. The image is taken from the original publication in the year 1965 [19]. The red dashed area shows the early formation of LIPSS.

He attributed the patterns to be a result of diffraction patterns caused by the focus lens onto the surface. He deduced an equation for the pattern formation according to maxima and minima of the intensity distribution to be

$$\Lambda = 2\lambda_L \left(\frac{f}{a}\right)^3 \quad (2.40)$$

where  $\lambda_L$  is the laser wavelength,  $f$  is the focal length of the lens and  $2a$  is the lens aperture. However, it turned out that the theory was not applicable for further experiments and observa-

tions of the structure formation. A couple of years later in 1973, Emmony et al. suggested that the ripple formation is a consequence of interference between the incoming laser light and surface scattered wave [63]. In the following years many theories on the formation mechanism have been suggested, yet it is not fully understood.

Although the discovery of the phenomenon dates back to the early 60's, the number of publications on the topic, referred to as LIPSS introduced by Sipe et al. [64], only significantly increased during the last 20 years. This is also attributed to the discovery of a new LIPSS type, where the periodicity of the structures,  $\Lambda$ , is much smaller than the irradiation laser wavelength. These LIPSS are referred to as *high spatial frequency LIPSS*, abbreviated *HSFL*. They must be clearly separated from the classical observed LIPSS due to different physical creation mechanisms. The classical LIPSS, for which  $\Lambda \approx \lambda_L$  are referred to as *low spatial frequency LIPSS (LSFL)*.

Over the years many different patterns of these structures have been observed and classified into different types of LIPSS. This classification scheme can be seen in figure 2.7. From a theoretical point of view a controver-

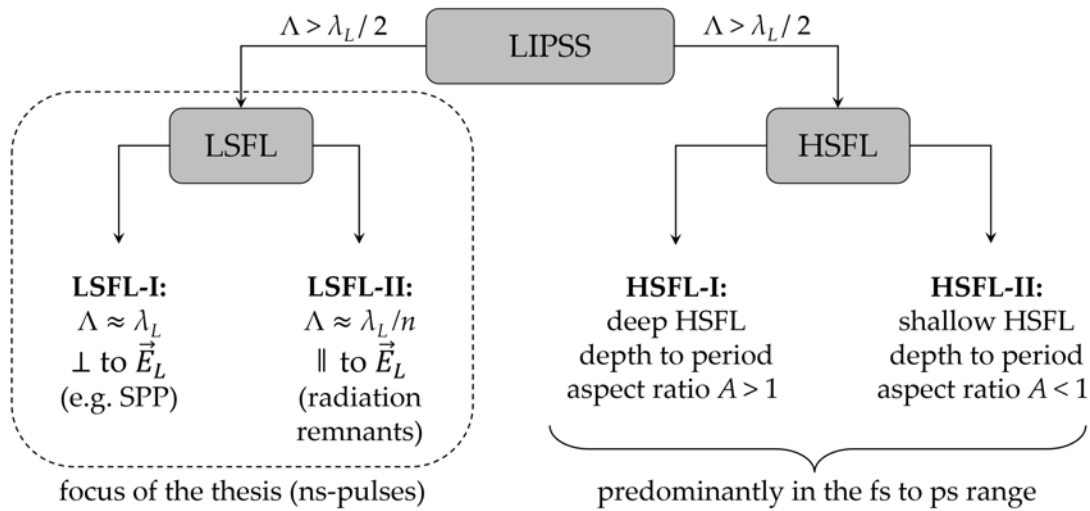


**Figure 2.7.** Classification scheme of laser induced periodic surface structures. Modified image from [20]

sial debate has emerged whether LIPSS are a consequence of electromagnetic effects or a cause of feedback mechanisms and matter reorganization. The fact that the LIPSS organization is a function of so many parameters ( $\Lambda = f(\lambda_L, E_p, \tau_p, \hat{P}, \bar{P}, \vec{E}, \vec{B}, \epsilon_r, \theta \dots)$ ) makes it difficult to simulate and predict results for certain applications and environments in theory and at the same time the experimental parameter space is so big that a verification for any given configuration is hard. In the following section the most relevant theories for the creation of LIPSS are introduced.

## 2.4.1 Theories of LIPSS formation

### 2.4.1.1 Classic interference theory

The first ansatz to explain the formation of periodic structures on the surface is given by classic interference theory. In this theory the incident laser light, with wave vector  $\vec{k}_i$ , interferes with the scattered wave along the surface. This scattered wave, with wave vectors  $k_{\parallel}^{s,a}$ , can be affected by microscopic roughnesses, defects or local spatial variations of the dielectric constant,  $\epsilon_r$ . This interference causes an inhomogeneous energy input at the surface that can in turn, together with other mechanism lead to a periodic surface modulation. Here the solid is characterized by a uniform dielectric constant with

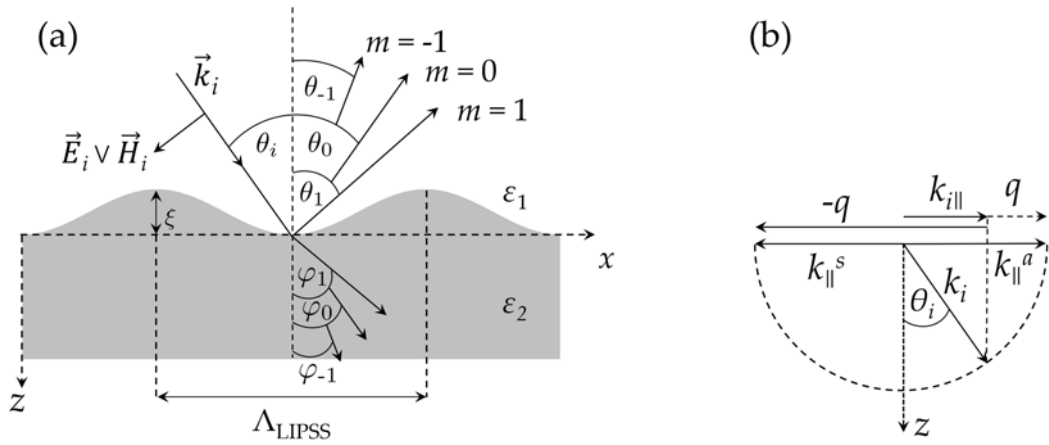


**Figure 2.8.** Schematic of the (a) reflected and diffracted wave at the rough surface and (b) a vector diagram for the scattered wave along the surface.  $\vec{k}_i$  is the wave vector of the incident laser beam and  $\vec{k}_{i\parallel}$  the respective projection onto the surface.  $\vec{q}$  is the Fourier component, i.e. the grating vector of the rough surface. The scattered wave can then have the resulting wave vectors according to  $\vec{k}_{\parallel}^s = \vec{k}_{i\parallel} - \vec{q}$  which is referred to as the Stokes wave and  $\vec{k}_{\parallel}^a = \vec{k}_{i\parallel} + \vec{q}$ , as the anti-Stokes wave. Modified image taken from [65].

$\epsilon = \epsilon' + i\epsilon''$ . The surface modulation is caused by the scattering of the incident laser light,  $\vec{E}_i = \Re\{\vec{E}_0 \exp[i(\vec{k}_i \cdot \vec{r} - \omega t)]\}$ , by the Fourier component of the surface corrugation, which is characterized by the vector  $\vec{q}$ . In general,  $\vec{q}$  is randomly oriented and the surface roughness can have a non-periodic arbitrary shape. In this case, for simplicity the surface roughness is described by a cosine profile according to  $z(\vec{r}) = \xi \cos(\vec{q} \cdot \vec{r} + \delta)$  and  $\vec{q}$  is directed in the  $x$  direction (see figure 2.8). Here  $\xi$  is a (complex) amplitude and  $|\vec{q}| = 2\pi/\Lambda$ .

The incoming wave can either be  $\sigma$ -polarized ( $\vec{E}_i \parallel y$ ) or  $\pi$ -polarized ( $\vec{H}_i \parallel y$ ). The scattered waves are given by the grating equation according to

$$\vec{k}_{\parallel}^{s,a} = \vec{k}_{i\parallel} \pm m\vec{q} \quad (2.41)$$

where  $m$  is the order of diffraction. For the specific simplified case that  $\vec{q} \parallel \vec{k}_{i\parallel}$  the grating equation reads:

$$k_i \sin(\theta_m) = k \sin(\varphi_m) = k_i \sin(\theta_i \pm m\varphi), \quad (2.42)$$

where  $\vec{k}_{\parallel}^{s,a}$  are the surface components of the scattered Stokes (+) and the anti-Stokes (-) waves and  $\theta, \varphi$  are the angles of the reflected and transmitted waves. The wave vector is given by  $|\vec{k}_i| = n\omega/c$ , where  $n = \sqrt{\epsilon}$  is the refractive index of the material. The z-components can be obtained by the Helmholtz equations,  $k_{\parallel}^2 + k_z^2 = \epsilon k_i^2$ . Considering the most important situation for ripple formation, where the scattered waves are either along the  $x$ - or  $y$ -axis ( $\vec{k}_{\parallel}^{s,a} \parallel \vec{e}_x \vee \vec{e}_y$ ), the resulting periodicity can be calculated as

$$\Lambda(\lambda, \theta_i) = \begin{cases} \frac{\lambda}{1 \pm \sin(\theta_i)} & \text{for } \vec{q} \parallel \vec{k}_{i\parallel} \parallel x \quad (\pi\text{-pol}) \\ \frac{\lambda}{\cos(\theta_i)} & \vec{q} \perp \vec{k}_{i\parallel}, \text{ i.e., } \vec{q} \parallel y \quad (\sigma\text{-pol}) \end{cases} \quad (2.43)$$

$$(2.44)$$

### 2.4.1.2 Surface Plasmon Polaritons (SPP)

Another widely accepted theory involves the excitation of surface electromagnetic waves (SEW) and surface plasmon polaritons (SPP). Plasmons were first discussed back in 1952 by Pines and Bohm [66] who described a quantized bulk plasma oscillation to explain the energy loss of energetic electrons passing through metal foils. However the term surface plasmon was first used by Ritchie et al. in 1957 [67]. Surface plasmons are quantized excitations of electron oscillations at the interface between two media, one of them usually being a metal with a positive permittivity and the other a dielectric, such as vacuum or air. For this purpose a classical model approach is used considering two semi-infinite media with dielectric functions  $\epsilon_{1,2}$ , respectively. The media are separated by a planar interface located at  $z = 0$  (see figure 2.8

(a)). The space and time dependence of the quantities causing these oscillations, namely the electric and magnetic field vector  $\vec{E}$  and  $\vec{H}$ , respectively, is described by Maxwell's equation (in case of no external sources):

$$\nabla \cdot \epsilon_i \vec{E} = 0 \quad (2.45)$$

$$\nabla \cdot \vec{H}_i = 0 \quad (2.46)$$

$$\nabla \times \vec{E}_i = -\frac{1}{c} \frac{\partial \vec{H}_i}{\partial t} \quad (2.47)$$

$$\nabla \times \vec{H}_i = \frac{\epsilon_i}{c} \frac{\partial \vec{E}_i}{\partial t} \quad (2.48)$$

For the separating interface, boundary conditions that restrict the electromagnetic fields at  $z = 0$  need to be given in a form of continuity equations. Considering  $\vec{n}_{12}$  to be the unit vector of a infinite small area of the interface between media 1 and 2, the two important ones for the description of the periodicity read [68]:

$$\vec{n}_{12} \times (\vec{E}_2 - \vec{E}_1) = 0 \quad (2.49)$$

$$\vec{n}_{12} \cdot (\vec{D}_2 - \vec{D}_1) = \hat{\rho} \quad (2.50)$$

where  $\vec{D} = \epsilon_i \vec{E}$  is the electric displacement with the dielectric function in medium  $i$  and  $\hat{\rho}$  is the surface charge induced by the wave. From equation 2.50 it can be seen that the incident wave needs to have a component perpendicular to the surface to induce a surface charge. Hence, a surface charge can only be created by the incidence of a  $\pi$ -polarized wave, since in the  $\sigma$ -polarized case the normal component of the electric field is missing and  $\vec{n}_{12} \cdot \delta \vec{D}_i = 0$ . The  $\pi$ -wave on the contrary will automatically induce time dependent polarization charges at the surface. Furthermore, independent from the concrete form of the surface wave it has to satisfy the wave equation in the two media. The solutions of Maxwell's equations for  $\vec{E}_i$  and  $\vec{H}_i$ , choosing the  $x$ -direction as the propagation direction, yield:

$$\vec{E}_i = (E_{ix}, 0, E_{iz}) \exp \{ -k_i |z| \} \exp \{ i(q_i x - \omega t) \} \quad (2.51)$$

$$\vec{H}_i = (0, E_{iy}, 0) \exp \{ -k_i |z| \} \exp \{ i(q_i x - \omega t) \} \quad (2.52)$$

where  $q_i$  is the magnitude of a wave vector parallel to the surface and the index  $i$  again represents the different media. Inserting those solutions (equations 2.51 and 2.52) into Maxwell's equations one finds that

$$k_i = \sqrt{q_i^2 - \epsilon_i \left(\frac{\omega}{c}\right)^2}. \quad (2.53)$$

Furthermore it can be deduced from the boundary conditions and the necessity of the continuation of the electric and magnetic fields parallel to the surface that the following relation has to be fulfilled:

$$\frac{\epsilon_1}{k_1} + \frac{\epsilon_2}{k_2} = 0 \quad (2.54)$$

which is the dispersion relation for surface plasmon polaritons. Taking into account the boundary conditions and the continuity of the 2d wave vector  $\vec{q}$ , the dispersion relation can also be expressed as:

$$q(\omega) = \frac{\omega}{c} \sqrt{\frac{\epsilon_1 \epsilon_2}{\epsilon_1 + \epsilon_2}} \quad (2.55)$$

where  $\frac{\omega}{c}$  is the magnitude of the light wave vector. The periodicity can eventually be calculated by

$$\Lambda_{SPP} = \frac{2\pi}{\Re\{q(\omega)\}} = \lambda \Re\left\{\sqrt{\frac{\epsilon_1 + \epsilon_2}{\epsilon_1 \epsilon_2}}\right\} \quad (2.56)$$

A more detailed derivation can inter alia be found in [68, 69, 70, 71].

However, this holds only for  $\pi$ -polarized light. Several approaches have been made to expand the SPP model to include  $\sigma$ -polarized light and non-perpendicular irradiation, e.g. found in [72, 65]. The periodicity can then be described by the equations:

$$\Lambda^{(\pi)} = \frac{\lambda}{\Xi \pm \sin(\theta_i)} \approx \frac{\lambda}{1 \pm \sin(\theta_i)} \quad (2.57)$$

$$\Lambda^{(\sigma)} = \frac{\lambda}{\sqrt{\Xi^2 - \sin^2(\theta_i)}} \approx \frac{\lambda}{\cos(\theta_i)} \quad (2.58)$$

where  $\Xi^2 = |\Re\{\epsilon_i\}| / (|\Re\{\epsilon_i\}| - 1)$ . The approximations hold for strong absorbing and plasmonic active materials, where  $\Re\{\epsilon_i\} \ll -1$  and, within the

approximation, yields the same results as obtained from the classic interference theory.

### 2.4.1.3 Efficacy Factor Theory - Sipe's theory

One of the most widely accepted theories on LIPSS formation was already developed during the early 80's by the group of Sipe and van Driel. They combined the excitation of SEWs, in particular SPPs and the interference with the incident radiation and developed a detailed mathematical accurate electromagnetic theory combined with experimental series [73, 74, 75, 76, 77].

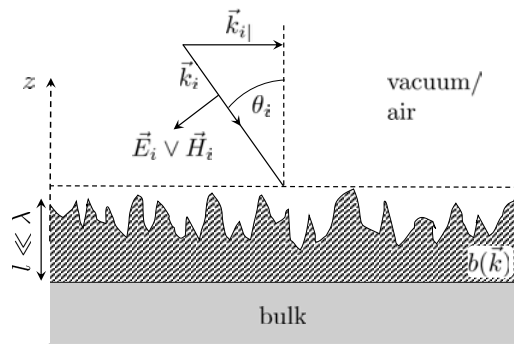


**Figure 2.9.** Schematic of the geometry used for Sipe's theory. The incident laser beam hits a surface, whose roughness is described by the function  $b(\vec{k})$ .

They claimed that due to the independency of  $I(\vec{k})$  on the initial surface roughnesses it might be more powerful to study the modifications in the  $\vec{k}$ -space rather than local damages in the real space. To do so, an infinite plane wave with wave vector  $\vec{k}_i$  is assumed to hit a rough surface under an angle  $\theta_i$ . The corrugation is located at  $z \in [0, l]$ , where  $l/\lambda \ll 1$ . For an ideal surface with no corrugations only a refracted beam with wave vector  $\vec{k}_{i\parallel} = \vec{k}_i \sin(\theta_i)$  would appear in the bulk. However, due to an existing Fourier component of the surface at  $\vec{k}$ , scattered fields can appear in the bulk according to  $\vec{k}_{\pm} = \vec{k}_{i\parallel} \pm \vec{k}$ . These interfere with the refracted and the incident beam and lead to inhomogeneous energy absorption at  $z = 0$  with a wave vector  $\vec{k}$  parallel to the surface. Neglecting feedback processes and considering damage only in the bulk region below the rough area, the inhomogeneous absorption is described by

$$I(\vec{k}) \propto \eta(\vec{k}, \vec{k}_{i\parallel}) \left| b(\vec{k}) \right| \quad (2.59)$$

where  $\eta(\vec{k}, \vec{k}_{i\parallel})$  is a response function describing the efficacy with which the surface corrugations lead to an inhomogeneous energy absorption at  $\vec{k}$  and

$b(\vec{k})$  describes the amplitude of the surface roughness. A schematic geometry of the situation can be seen in figure 2.9. Starting from Maxwell's equations and using Green's formalism, 14 complex valued equations are derived to straightforwardly calculate  $\eta$  for a given wavelength and polarization of the laser beam under a certain incident angle and permittivity of the surface. Furthermore two roughness parameters  $s$  and  $f$  are introduced that encode the roughness characteristics. The set of equations is presented here since it is used for the calculation of  $\eta$  presented in the results section. According to Sipe the efficacy factor can be calculated according to [74]:

$$\eta(\vec{k}, \vec{k}_{i\parallel}) = 2\pi \left| v(\vec{k}_+) + v^*(\vec{k}_-) \right| \quad (2.60)$$

where the complex functions for  $\sigma$ - and  $\pi$ -polarized light are given as

$$v^{(\sigma)}(\vec{k}_{\pm}) = \left[ h_{ss}(k_{\pm})(\vec{k}'_{\pm} \cdot \vec{e}_y)^2 + h_{kk}(k_{\pm}) \times (\vec{k}'_{\pm} \cdot \vec{e}_x)^2 \right] \gamma_t \left| t_s(\vec{k}_{i\parallel}) \right|^2 \quad (2.61)$$

$$\begin{aligned} v^{(\pi)}(\vec{k}_{\pm}) = & \left[ h_{ss}(k_{\pm})(\vec{k}'_{\pm} \cdot \vec{e}_x)^2 + h_{kk}(k_{\pm}) \times (\vec{k}'_{\pm} \cdot \vec{e}_y)^2 \right] \gamma_t \left| t_x(\vec{k}_{i\parallel}) \right|^2 + h_{kz}(k_{\pm}) \\ & \times (\vec{k}'_{\pm} \cdot \vec{e}_y) \gamma_z \epsilon t_x(\vec{k}_{i\parallel}) t_z(\vec{k}_{i\parallel}) + h_{zk}(k_{\pm}) \times (\vec{k}'_{\pm} \cdot \vec{e}_y) \gamma_t t_x(\vec{k}_{i\parallel}) t_z^*(\vec{k}_{i\parallel}) \\ & + h_{zz}(k_{\pm}) \gamma_z \epsilon \left| t_z(\vec{k}_{i\parallel}) \right|^2 \end{aligned} \quad (2.62)$$

with the according inner products  $(\vec{k}'_{\pm} \cdot \vec{e}_y) = (\sin(\theta_i) \pm \kappa_y) / \kappa_{\pm}$  and  $(\vec{k}'_{\pm} \cdot \vec{e}_x) = \kappa_x / \kappa_{\pm}$ . Here it is used  $\kappa_{\pm} = \sqrt{\kappa_x^2 + (\sin(\theta_i) \pm \kappa_y)^2}$ . Furthermore all the lengths have been normalized by  $\lambda / (2\pi)$ , so that the LIPSS wave vector becomes dimensionless resulting in  $\kappa = k \times \lambda / (2\pi) = \lambda / \Lambda$  and  $\epsilon$  is the dielectric function of the material. The  $h$  and  $t$  functions are expressed as

(equations not enumerated)

$$\begin{aligned}
 h_{ss}(\kappa_{\pm}) &= \frac{2i}{\sqrt{1 - \kappa_{\pm}^2} + \sqrt{\epsilon - \kappa_{\pm}^2}} & h_{zz}(\kappa_{\pm}) &= \frac{2i\kappa_{\pm}^2}{\epsilon\sqrt{1 - \kappa_{\pm}^2} + \sqrt{\epsilon - \kappa_{\pm}^2}} \\
 h_{kz}(\kappa_{\pm}) &= \frac{2i\kappa_{\pm}\sqrt{\epsilon - \kappa_{\pm}^2}}{\epsilon\sqrt{1 - \kappa_{\pm}^2} + \sqrt{\epsilon - \kappa_{\pm}^2}} & h_{zk}(\kappa_{\pm}) &= \frac{2i\kappa_{\pm}\sqrt{1 - \kappa_{\pm}^2}}{\epsilon\sqrt{1 - \kappa_{\pm}^2} + \sqrt{\epsilon - \kappa_{\pm}^2}} \\
 h_{kk}(\kappa_{\pm}) &= \frac{2i\sqrt{(\epsilon - \kappa_{\pm}^2)(1 - \kappa_{\pm}^2)}}{\epsilon\sqrt{1 - \kappa_{\pm}^2} + \sqrt{\epsilon - \kappa_{\pm}^2}} & t_x(\vec{k}_{i\parallel}) &= \frac{2\sqrt{\epsilon - \sin^2(\theta_i)}}{\epsilon|\cos(\theta_i)| + \sqrt{\epsilon - \sin^2(\theta_i)}} \\
 t_s(\vec{k}_{i\parallel}) &= \frac{2|\cos(\theta_i)|}{\epsilon|\cos(\theta_i)| + \sqrt{\epsilon - \sin^2(\theta_i)}} & t_z(\vec{k}_{i\parallel}) &= \frac{2\sin(\theta_i)}{\epsilon|\cos(\theta_i)| + \sqrt{\epsilon - \sin^2(\theta_i)}}
 \end{aligned}$$

The corrugation of the surface is included in the  $\gamma$  parameters which implicitly include the numerical  $s$  and  $f$  factors according to

$$\begin{aligned}
 \gamma_t &= \frac{\epsilon - 1}{4\pi \left\{ 1 + 0.5(1 - f)(\epsilon - 1) [F(s) - R \times G(s)] \right\}} \\
 \gamma_z &= \frac{\epsilon - 1}{4\pi \left\{ \epsilon(1 - f)(\epsilon - 1) [F(s) - R \times G(s)] \right\}}
 \end{aligned}$$

where  $R = (\epsilon - 1)/(\epsilon + 1)$ ,  $F(s) = \sqrt{s^2 + 1} - s$  and  $G(s) = 0.5(\sqrt{s^2 + 4} + s) - \sqrt{s^2 + 1}$  are scalar functions. With this set of equations the efficacy factor can be calculated for the specific radiation and material input parameters  $\eta(\lambda, \sigma/\pi, \theta_i, \epsilon)$ . From the back-transformation into the real space, the periodicity, and the orientation of the induced LIPSS can be deduced and eventually be compared to the experimental results. A precisely detailed mathematical derivation can be found in [74].



## Chapter 3

# Experimental

### 3.1 Plasma source - COST-Jet

The plasma source used in this work is a micro atmospheric pressure plasma jet ( $\mu$ APPJ) that was designed to act as a reference jet for laboratories across the world. It is based on the design of Schütze et al. [78] and was then modified by a team of scientists and eventually published by Golda et al. [25]. This jet is referred to as the *COST Reference Microplasma Jet* or in short *COST-Jet*.

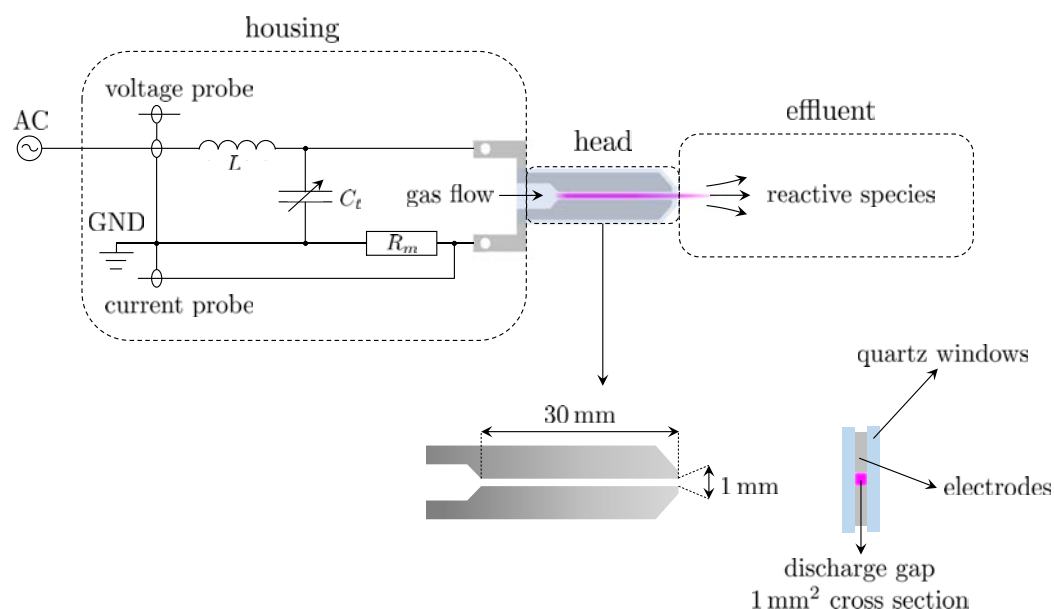


**Figure 3.1.** Sketch of the COST-Jet used for the experiments in this thesis. Seen is an overall sketch of the system containing the housing with the internal LC circuit and the current and voltage probes, the head of the jet where the plasma is ignited and the effluent region where the created reactive species eventually interact with a sample. On the bottom the geometry of the head is shown in more detail.

It is a capacitively coupled plasma (CCP), that is operated at atmospheric pressure. The jet is driven by a sinusoidal waveform at an RF frequency of 13.56 MHz and typically He is used as feed gas with flows in the range of  $\Phi_{\text{He}} = 0.2 - 2$  slm. To create reactive species and extend the operation ranges of the jet, a reactive gas admixture (e.g.  $\text{N}_2$ ,  $\text{O}_2$ ,  $\text{CO}_2$ ...) of about 0.5-2% is added to the feed gas.

The jet itself consists of two main components, namely the housing and the head. A sketch of the plasma source can be seen in figure 3.1. The housing comprises an internal voltage and current probe and an LC circuit with a tunable capacitor  $C_t$  and an inductance  $L = 9.6 \mu\text{H}$ . The capacity can be varied to bring the circuit into resonance and optimize the power coupling ( $C_t \approx 0.8 - 8 \mu\text{F}$ ). The integrated LC circuit has a Q-factor of about 30, so that a power supply capable of around 15 V is enough to provide the necessary breakdown voltage of around 150-300 V, mainly depending on the gas mixture used for operation. The discharge current,  $I_d$ , is calculated via the voltage that drops over the shunt resistor  $R_m = 4.7 \Omega$  and the termination resistance  $R_t = 50 \Omega$  via Ohm's law:

$$I_d = V_{\text{RMS}} \frac{R_t + R_m}{R_t R_m}, \quad (3.1)$$

where  $V_{\text{RMS}} = \hat{V}/\sqrt{2}$  is the root-mean-square of the voltage amplitude delivered by the power supply,  $\hat{V}$ . With the calculated current and the voltage, the dissipated plasma power,  $P_d$  can be calculated via the known relation:

$$P_d = \frac{1}{T} \int_{t_0}^{t_0+T} dt P(t) \quad (3.2)$$

$$= I_d V_{\text{RMS}} \cos(\phi - \phi_{\text{ref}}) \quad (3.3)$$

$$= \frac{\hat{V}^2}{2} \frac{R_t + R_m}{R_t R_m} \cos(\phi - \phi_{\text{ref}}). \quad (3.4)$$

Here  $\phi$  is the measured phase shift between voltage and current during the operation of the jet and  $\phi_{\text{ref}}$  is a reference phase recorded without plasma discharge i.e. the electrodes act as a capacity and the phase shift equals  $\pi/2$ .

While in older versions of the jet the power always referred to the generator power without further information on the real power dissipated in the discharge, in the COST-Jet the power is always assigned to the dissipated plasma power measured by the internal probes. Detailed information on the

procedure can be found in [79]. Hence, in this study, the given power always refers to the plasma power.

The head consists of two stainless steel electrodes that are arranged in a plain parallel configuration. The discharge channel is 30 mm long and the discharge gap has a square cross section of  $1 \times 1 \text{ mm}^2$ , resulting in a discharge volume of  $30 \text{ mm}^3$ . The electrodes are stacked between two quartz windows in order to confine the plasma and guarantee broadband optical access for diagnostic purposes.

The reactive species that are created in the strong non-equilibrium plasma are eventually transported into the effluent by the feed gas stream, where they finally interact with a sample.

## 3.2 Experimental setup - LIF

### 3.2.1 Laser system

The laser system used for the experiments consists of a dye laser (Narrowscan, RadiantDyes Laser GmbH) and an Nd:YAG laser (Spotlight Compact DPSS, InnoLas Laser GmbH). The dye laser is pumped by the frequency tripled YAG laser at  $\lambda_{3\omega} = 355 \text{ nm}$  and a repetition frequency of 100 Hz. The dye laser is operated with Coumarin-47, that has a spectral tuning range of 442 – 479 nm, with its maximum efficiency at 460 nm. The emitted wavelength of the dye laser is eventually frequency doubled by a BBO crystal yielding a final wavelength of the laser light of  $\lambda_{2\omega, dye} = \lambda_L \approx 226 \text{ nm}$ , to investigate the  $\gamma$ -band of the NO molecule. The final laser pulses reach maximum energies of up to  $E_p \approx 150 \text{ }\mu\text{J}$  at pulse lengths of about  $\tau_p \approx 5 \text{ ns}$  and a spectral line width (FWHM) of  $\Delta k \approx 0.05 \text{ cm}^{-1}$ . The initial laser beam that is emitted by the laser system has a diameter of about  $d \approx 2 \text{ mm}$ .

### 3.2.2 Measurement of the laser focus

One central parameter during the LIF measurements is the size of the laser focus, since it is one of the parameters that determines the spatial resolution, as well as the intensity that is coupled to the absorption processes in the plasma.

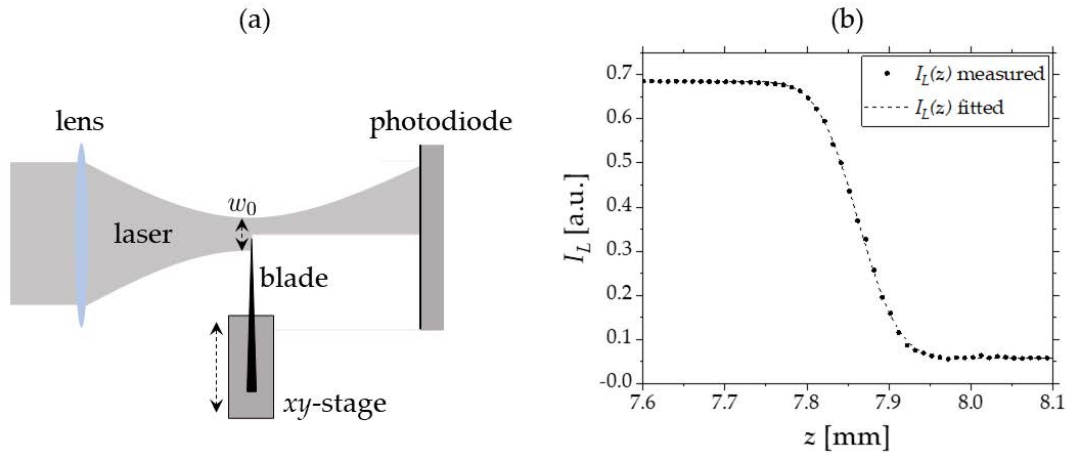


**Figure 3.2.** (a): Experimental setup of the knife-edge method in order to measure the laser profile. (b): data points of the measured profile of the excitation laser used for the experiments with the corresponding fit function according to equation 3.6.

To measure the width of the laser profile in the focus, the *knife-edge method* is used [80]. The measured profile as well as a sketch of the experimental setup can be seen in figure 3.2,

By assuming a Gaussian laser beam shape of the form

$$I_L(x, y) = I_0 \exp \left\{ -\frac{(x - x_0)^2 + (y - y_0)^2}{w_0^2} \right\} \quad (3.5)$$

where  $I_0$  is the intensity in the center of the beam located at  $(x_0, y_0)$  and  $x$  and  $y$  are the respective Cartesian coordinates, usually an error function is fitted to obtain the beam waist  $w_0$ . However, Araujó et al. have shown that an alternative fitting function delivers more accurate results [81]. The fitting function is given as:

$$I_L(x) = \left[ 1 + \exp \left\{ \sum_{j=0}^m c_j \left( \frac{\sqrt{2}(x - x_0)}{w_0} \right)^j \right\} \right]^{-1}. \quad (3.6)$$

Here  $c_j$  are polynomial coefficients obtained from a least-square analysis and  $w_0$  is the laser beam waist in the focus. Usually for this fitting procedure  $m = 3$ . The measured profile as well as the corresponding fitting function

according to equation 3.6 can be seen in figure 3.2 (b). From the fitting procedure, a laser beam waist of  $w_0 \approx 80 \mu\text{m}$  was deduced.

### 3.2.3 Chamber and plasmajet setup for measurements in the free effluent

The LIF measurements are performed in a cylindrical vacuum chamber of 40 cm diameter and height. A sketch of the setup can be seen in figure 3.3. The

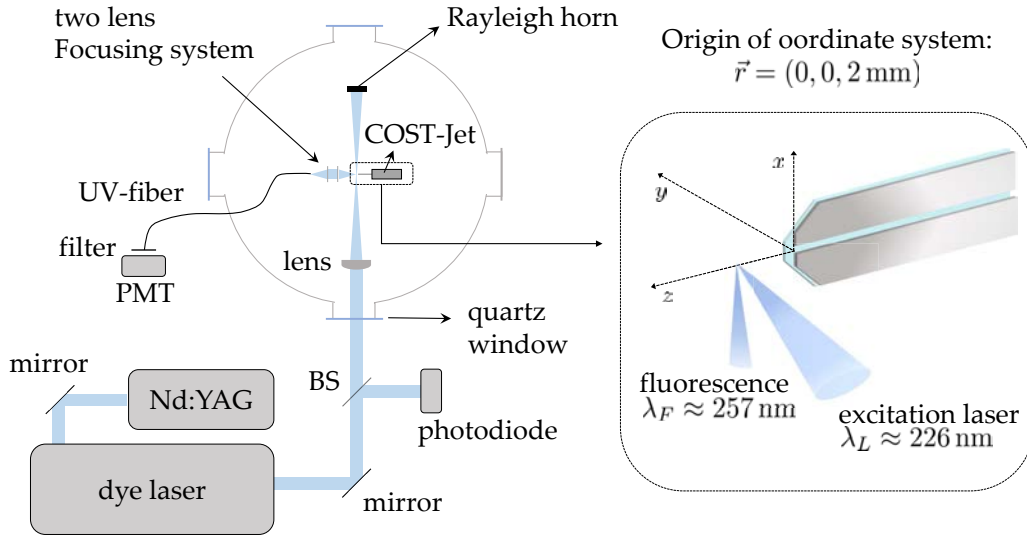


**Figure 3.3.** Sketch of the experimental setup for the LIF measurements. Shown is the vacuum chamber with the laser path and the optical setup and a zoomed view of the interaction region with the associated three-dimensional Cartesian coordinate system. The origin of the coordinate system is located at the center of the electrodes and the quartz windows at the end of the electrode tip.

COST-Jet is mounted in the center of the chamber onto a vacuum compatible motorized  $xyz$ -stage (Standa ltd.). This stage allows a fully three-dimensional scan of the density distribution with a step resolution of  $2.5 \mu\text{m}$ . The Cartesian coordinate system is chosen such that the origin is located in the center of the quartz windows and the electrodes at the end of the electrode tips. However, it should be noted that the quartz windows exceed the electrode tips by 1 mm as a safety gap, in order to minimize danger for the experimentalist by the powered electrode. Additional distance from the windows to

avoid reflection or inducing fluorescence inside the quartz lead to a first accessible measurement point approximately 2 mm into the effluent region at  $\vec{r} = (0, 0, 2 \text{ mm})$ . A sketch of the coordinate system can be seen in figure 3.3.

Two operation modes of the chamber are used in this study. First the cover lid is open and the NO density is measured with the jet expanding into lab atmosphere i.e. air. Second the chamber is closed, pumped down and operated into a controlled gas He/ synthetic air atmosphere. The chamber is pumped by a turbo molecular pump down to a base pressure of  $p_b \approx 5 \times 10^{-5}$  mbar, while the leakage rate of the system is estimated below  $5 \times 10^{-7}$  slm. Subsequently, the chamber is filled by the jet with a gas mixture of He+0.5% synthetic air up to a pressure near the lab atmosphere of  $\approx 970$  mbar. However, it is kept well below the actual lab pressure in order to avoid overpressure and leakage of the gas mixture. During the operation and the measurements, the pressure is kept constant by a PID controller (Pfeiffer RVC 300), a capacitance transmitter (Pfeiffer CMR 371) and a scroll pump (Edwards nxDS6i).

The NO density distributions are measured in either of these atmospheres to observe the influence of the surrounding environment of the reaction kinetics and the resulting distribution. The measurements in ambient air are particularly important for biomedical treatments of e.g., human skin, where treatment in controlled atmosphere is not possible. The measurements in controlled atmosphere are rather important for surface modifications, where the sample can be placed in such a controlled atmosphere to avoid the influence of unknown surrounding parameters such as humidity and other impurities that can be dependent on space and time. Furthermore, the measurements in a controlled atmosphere are important for the modeling community, where a well defined mixture of the surrounding is necessary to get reliable results.

### 3.2.4 Modifications of the setup for measurements in front of surfaces

The chamber used for the experiments is the same as described in the setup for the measurements in the free effluent (see section 3.2.3). Since the final geometry for the experiments is set up with the laser and the jet hitting the surface under an angle of  $45^\circ$  (see figure 1.1), the treated samples in this study are fixed under the respective angle. Therefore, a self built construction mount for the plasma-jet was developed that can be seen in figure 3.4.

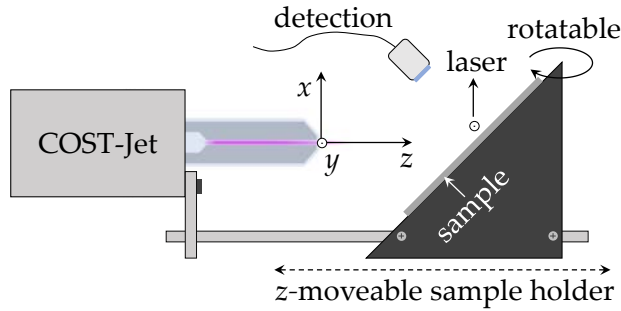


**Figure 3.4.** Geometry for the experiments in order to measure the NO densities in front of different surfaces.

The two rods of a microbank rail are attached to the housing of the COST-Jet. The 3D-printed sample holder can then be slid onto the rods and be tightened with two screws to guarantee a constant treating distance during the measurements. The sample holder can be moved along the  $z$ -axis to vary the sample distance and can also be rotated around the  $x$ -axis to assure a parallel beam path of the diagnostic laser relative to the surface. The sample is glued onto the surface and can easily be exchanged to investigate the influence of different materials. The direction of the diagnostic laser is as before in the  $\vec{e}_y$  direction.

The two rods of a microbank rail are attached to the housing of the COST-Jet. The 3D-printed sample holder can then be slid onto the rods and be tightened with two screws to guarantee a constant treating distance during the measurements. The sample holder can be moved along the  $z$ -axis to vary the

### 3.3 Experimental setup - Laser-surface experiments

#### 3.3.1 Laser system

The laser system used for the LIPSS experiments is a Nd:YAG laser by Continuum. It is mainly operated at the fundamental  $\lambda = 1064 \text{ nm}$  and the second harmonic (SH)  $\lambda_{2\omega} = 532 \text{ nm}$  wavelength. The maximum output energy per pulse is  $E_{1064} \approx 1800 \text{ mJ}$  at the fundamental and  $E_{532} \approx 900 \text{ mJ}$  at the SH. It has a pulse width of  $\tau_p \approx 7 \text{ ns}$  with a standard line width of  $\Delta k = 1 \text{ cm}^{-1} = 30 \text{ GHz}$ . The unfocused beam diameter is about  $d \approx 9 \text{ mm}$ .

#### 3.3.2 Chamber and optical setup

Figure 3.5 shows a sketch of the experimental setup used for the LIPSS experiments. The Nd:YAG laser, as described in section 3.3.1 is guided onto the polarizer, where the polarization of the laser light is determined. This is important for the surface experiments, since the interaction between the laser and the interface are dependent on whether the laser light is in  $\pi$ - or  $\sigma$ -polarization. After the polarizer the laser beam passes a Glan-Taylor prism.

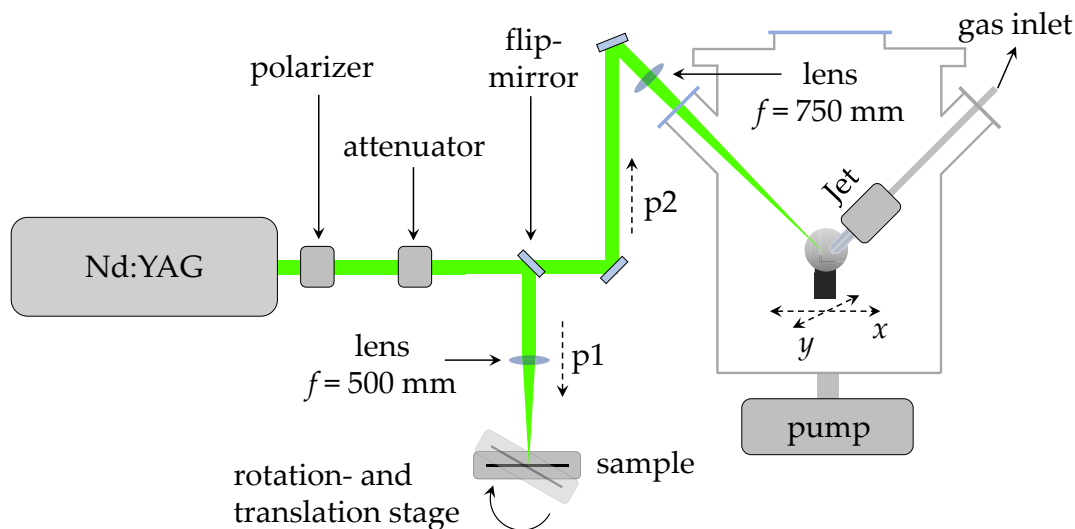


**Figure 3.5.** Experimental setup for the LIPSS experiments. The flip mirror can either be flipped up (path p1) so that the beam is focused onto the sample that is mounted on a 1d translational stage with a rotating device so that the angle of incidence can be adjusted. If the flip mirror is dismounted the laser beam is guided into the interaction chamber onto the sample under  $45^\circ$ , where it can simultaneously interact with the surface and the reactive species coming from the plasma jet (path p2).

This prism can be used as an attenuator to adjust the laser energy, hence the fluence, which is an important parameter for the LIPSS formation. The flip mirror can either be inserted or retracted. If it is inserted (path 1) the laser beam is directly focused onto the sample via a lens with a focal length of  $f = 500$  mm. The sample in this configuration is mounted on a 1-dimensional translational stage. The sample holder has a rotational axis to tune the incident angle  $\theta_i$ . Path 1 is used for the laser-surface experiments independent of the plasma source. If the flip mirror is retracted the laser beam is traveling along path 2. Here it is reflected via two mirrors and focused into the interaction chamber with a  $f = 750$  mm lens, where it eventually hits the sample under an angle of  $45^\circ$  with respect to the normal. The sample has several holders to adjust the angle of incidence from  $\theta_i = 0 - 60^\circ$  with respect to the surface normal. At the same time, the COST-Jet is also mounted inside the chamber under the same angle. In this configuration, laser-surface-plasma experiments can be performed. Furthermore, the interaction chamber is connected to a pump system consisting of a rotary- and a turbo pump. The rotary pump pumps the chamber down to a pressure of  $p \approx 10^{-1}$  mbar. Afterwards

---

the turbopump supports the evacuation and the chamber is finally pumped down to a base pressure of  $p_b \approx 5 \times 10^{-4}$  mbar. By that the measurements in the chamber can be performed in two different ways. Either the chamber is left open and it is measured in ambient air, or the chamber is pumped down and subsequently filled with the gas flow of the jet (He/synthetic air mixture) to measure in a controlled atmosphere. This is the same procedure as already described in section 3.2.3, except for the fact that no automated control pressure by a PID controller was installed. Instead, the pressure was manually controlled by gradually closing a valve until the pump rate is equal to the inflow rate, hence a constant pressure in the chamber.



## Chapter 4

# Reactive species distribution in the plasma effluent

### 4.0.1 Linearity of LIF signal

The energy of the single pulses of the excitation laser can be tuned by varying the pulse energy of the pump laser by adjusting the Pockels cell delay. Bigger pulse energies generate a higher fluorescence signal, hence a better signal-to-noise ratio. However, it has to be ensured that the pulse energy does not exceed a certain threshold, so that the excited state of the measured species becomes saturated. To investigate the saturation behavior of the measurements, the fluorescence signal at the same parameters, of plasma power and gas admixture, was analyzed. These measurements were performed for the ratio of maximum NO production found in section 4.1.1, namely an admixture of synthetic air. The results can be seen in figure 4.1: It can be seen that the LIF signal is linear, according to equation 2.32 and therefore not saturated over the whole possible energy range of the excitation laser. For this study typically energies of about  $E_p \approx 50 \mu\text{J}$  were used. This relatively low energy was chosen to realize a longer stable operation of the dye laser, while maintaining a large enough LIF signal to ensure a good signal-to-noise ratio of  $\text{SNR} \approx 200$ .

## 4.1 Determining parameters for maximum NO production

In this section, distributions and absolute densities of NO are presented. The distributions are measured in the free effluent, while the jet is operated in

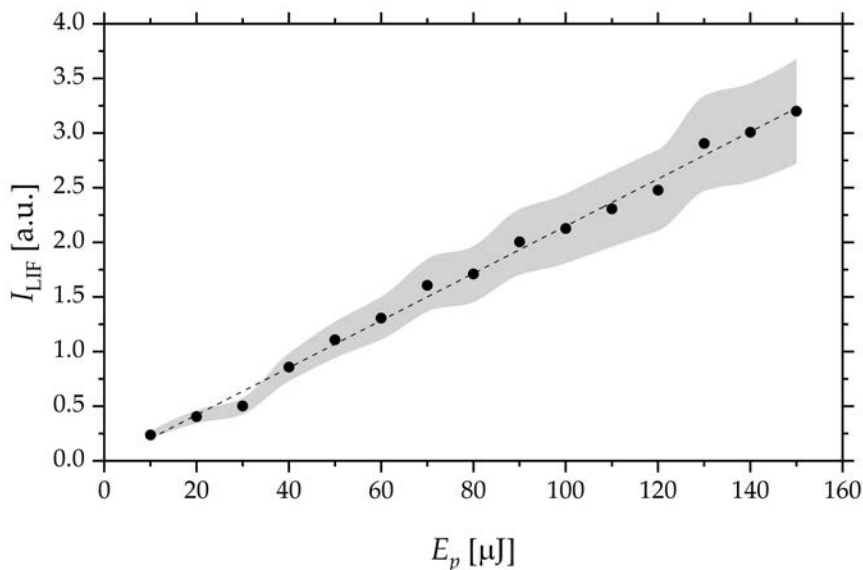


**Figure 4.1.** Variation of the pulse energy of the excitation laser and the according LIF signal. The measurements were performed for a helium flow of 1 slm and 0.5% admixture of synthetic air. The grey shaded area represents the 15% error band (see subsection 4.1.3.)

normal air atmosphere and on the other hand in controlled He/synthetic air atmosphere. Subsequently, different surfaces are placed in the effluent to investigate the influence of the respective materials onto the density distribution.

As preliminary measurements, different operation regimes of the jet with different  $N_2/O_2$  admixtures and different plasma powers are investigated to find the optimum NO production and the most stable operation of the device.

#### 4.1.1 Dependence of NO creation on $N_2/O_2$ admixture ratio

For many applications, in particular for biological samples, the efficiency of the production of any desired reactive species is of great importance. This is due to the heat sensitivity of the treated surfaces resulting in a limitation of the applied plasma power.

Thus, the NO density should be maximized for any given plasma power. However, at first the most efficient admixture of the  $N_2/O_2$  admixture must be identified. To do so, the  $N_2$  and  $O_2$  admixtures are systematically varied,

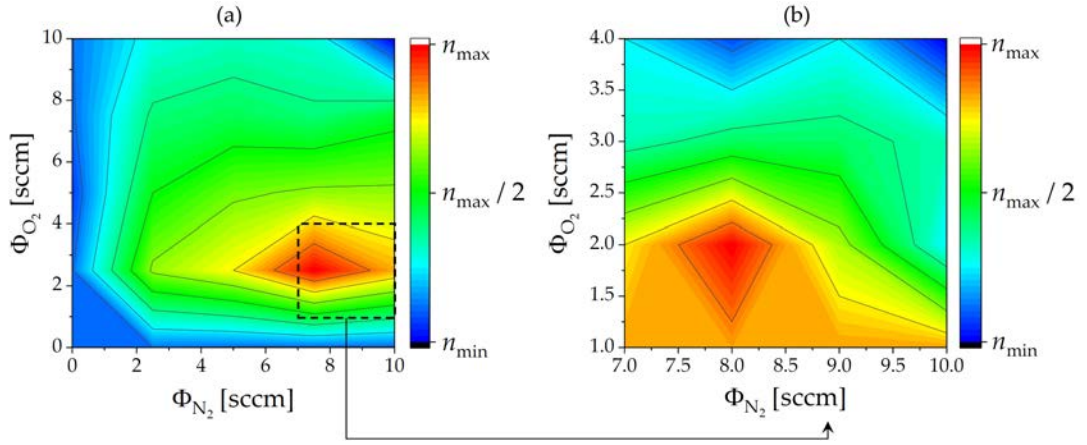


**Figure 4.2.** (a) Overview of the normalized NO density recorded at  $\vec{r} = (0, 0, 2)$  mm in the effluent of the plasma jet of the possible  $N_2/O_2$  ratios. (b) Zoomed view into the maximum region obtained from (a). The densities are plotted as a function of the  $N_2$  and  $O_2$  admixtures with a constant helium flow of  $\Phi_{He} = 1$  slm and a plasma power of  $P = 0.5$  W.

while the helium flow, as well as the applied plasma power are kept constant. The jet is operated in ambient air and the NO LIF signal is recorded as close as possible to the jet nozzle to avoid influence of the surrounding air (for example, due to quenching). This position is located 2 mm away, i.e.,  $\vec{r} = (0, 0, 2)$  mm.

Two parameter scans are performed. One to cover the full range of possible  $N_2/O_2$  admixtures with a step width of  $\Delta\Phi_{N_2,N_2} = 2.5$  sccm, according to a set of the reactive gas flows  $\Phi_{O_2,N_2} \in \{0, 2.5, 5, 7.5, 10\}$  in sccm as seen in figure 4.2 (a). The second scan focuses on the region of maximum NO production, as observed from the first scan, to explore this region more precisely with a smaller step width of  $\Delta\Phi_{N_2,N_2} = 1$  sccm according to  $\Phi_{N_2} \in \{7, 8, 9, 10\}$  in sccm and  $\Phi_{O_2} \in \{1, 2, 3, 4\}$  in sccm displayed in figure 4.2 (b). The helium flow is set to be at  $\Phi_{He} = 1$  slm and the plasma power as  $P_{diss} = 0.5$  W. From the measurements, it can be seen that the production of NO is most efficient with an admixture ratio of  $N_2/O_2 = 8/2$ , which can be considered synthetic air. Hence, for all the measurements presented in the following the feed gas is admixed with a commercially available synthetic air mixture, if not stated otherwise ( $\Phi_{tot} = \Phi_{He} + \Phi_{syn}$ ).

The measurements shown in figure 4.2 are performed with a constant plasma

power of  $P_{diss} = 0.5$  W. However, when operating the jet with different reactive gas mixtures, different maximum plasma powers can be applied before the discharge transits into a constricted arc like mode. This mode is to be avoided, since it can destroy the jet device and additionally can thermally threaten the treated sample. The different operation regimes are due to different power consumption mechanisms when higher amounts of molecular species are present in the plasma volume. To investigate the operation regimes according to the admixtures as depicted in figure 4.2, for each admixture the maximum stable power  $P_{max}$  and the corresponding maximum densities,  $n_{max}$ , are recorded.

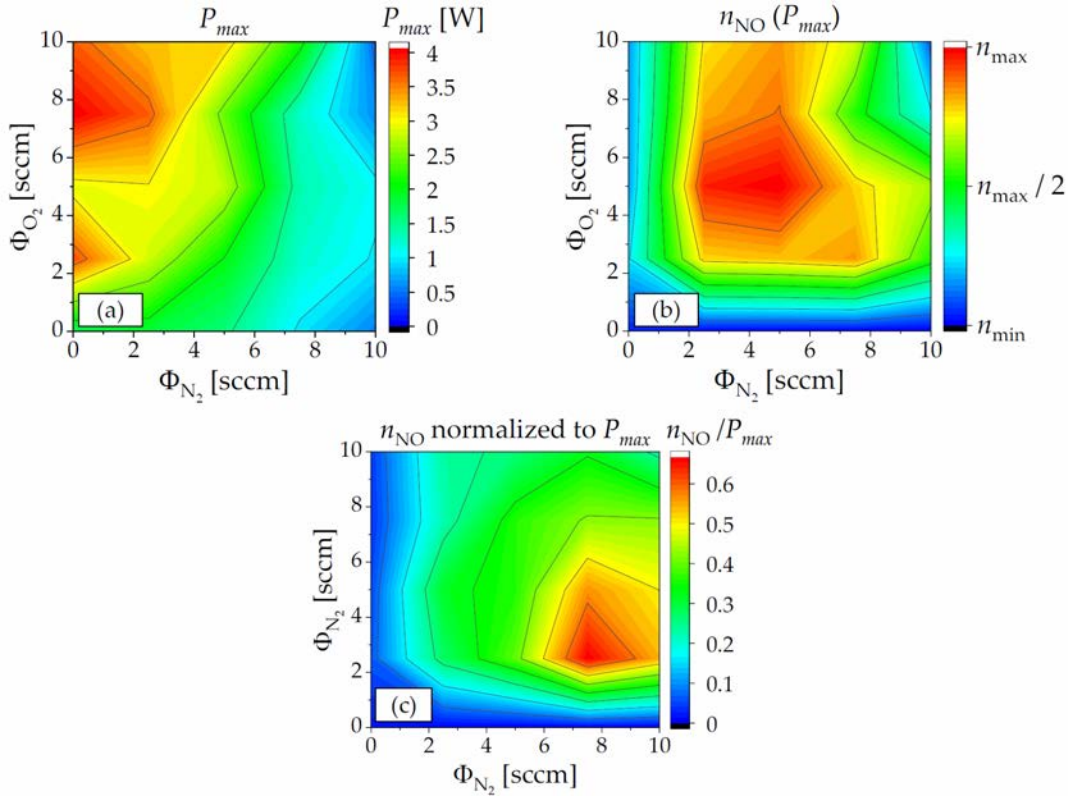


**Figure 4.3.** (a): maximum sustainable plasma power before the discharge transits into a constricted mode. (b): corresponding NO densities recorded at the maximum powers displayed in (a). (c): Normalized NO densities calculated from the ratio (b)/(a), according to  $n_{NO}(P_{max})/P_{max}$  recorded at  $\vec{r} = (0, 0, 2)$  mm in the effluent of the plasma jet. The densities and powers are plotted as a function of the  $N_2$  and  $O_2$  admixtures with a constant helium flow of  $\Phi_{He} = 1$  slm and a plasma power of  $P = 0.5$  W.

The results are shown in figure 4.3. It can be seen that the maximum reachable

power for a stable operation with a synthetic air admixture ( $P_{max} \approx 1.4 \text{ W}$ ) is considerably lower as compared to the one that can be operated when for example a high amount of oxygen is added e.g.,  $\Phi_{\text{O}_2} = 10 \text{ sccm}$  and  $\Phi_{\text{N}_2} = 0 \text{ sccm}$ , where  $P_{max} \approx 4 \text{ W}$ . This is caused by the electronegative character of  $\text{O}_2$ , with a dissociative attachment energy of about 4.7 eV that tends to form negative ions in the discharge, lowering the electron density and therefore a higher plasma power is necessary to sustain the discharge. Furthermore,  $\text{O}_2$  has several low-lying metastable molecular states that can be easily excited [82]. However, in those high power regimes N atoms and  $\text{N}_2$  molecules are missing to form NO, hence the NO production is low. It is observed that the highest absolute amount of NO is created when the flow is about  $\Phi_{\text{N}_2} = \Phi_{\text{O}_2} = 5 \text{ sccm}$  and the dissipated power about  $P_{diss} \approx 2.7 \text{ W}$  (figure 4.3 (a) and (b)). However, the most efficient production admixture for NO should be obtained again upon normalizing the maximum NO density by the maximum power that can be applied to the plasma without transitioning into the constricted mode. This is shown in figure 4.3 (c) with an operation at  $P_{diss} = 0.5 \text{ W}$ . It can be seen that the most efficient production is again found with an admixture ratio of  $\text{N}_2/\text{O}_2 = 8/2$ , which is the same as found in figure 4.2. This confirms that indeed synthetic air is the most efficient way to form NO, nevertheless, if the thermal sensitivity of the sample is not such a limiting factor and high amounts of NO are desired for a specific application, other admixtures may be preferable that can be looked up in figure 4.3 (b). Based on those results all the measurements in the following are performed with a synthetic air admixture and a plasma power of  $P_{diss} = 0.5 \text{ W}$  to ensure stable operation.

### 4.1.2 Calibration procedure

For the prior LIF measurements only relative values, i.e., emission intensities are recorded and displayed. Those intensities are directly proportional to the density of the respective state. However, to obtain absolute values, a calibration procedure is needed. This is done by pumping down the chamber and gradually filling up the chamber with a known mixture that contains NO. In this case it was a commercially available mixture by Air Liquide (He + 5 vol. % NO). The concrete procedure is as follows: first the chamber is pumped down to a base pressure of  $p_b \approx 5 \times 10^{-5} \text{ mbar}$  as already mentioned in

section 3.2.3. Subsequently, the chamber is filled with the NO mixture to a pressure of  $p_{cal}$  which was typically in the order of  $p_{cal} \approx 10$  mbar. The NO density for the calibration,  $n_{cal}$ , in the chamber can then be calculated via the idea gas law as:

$$n_{cal}k_B T_g = 0.05p_{cal} \Leftrightarrow n_{cal} = 0.05 \frac{p_{cal}}{k_B T_g} \quad (4.1)$$

where  $T_g = 293.15$  K is the normal gas temperature inside the chamber. Afterwards the chamber is filled up to  $\approx 950$  mbar with pure helium. Here it is important to keep the pressure well below the lab pressure, to avoid overpressure inside the chamber that might be a danger to the windows or lead to leaking of NO that would cause errors in the calculation of  $n_{cal}$  via the ideal gas law. After a LIF signal of the corresponding NO density is recorded, the chamber is pumped down to  $\approx 500$  mbar and filled up again with pure helium. In this way the NO density is iteratively diluted and the LIF signals corresponding to the known absolute NO densities are recorded. In this way a connection between the LIF signal and the NO density  $I_{LIF}(n_{NO})$  is deduced that follows equation (4.3), hence a linear correlation is obtained. The NO(X) ground state density can then be calculated via:

$$\frac{I_{LIF}}{\tau_q E_L} = \frac{\zeta I_{cal}}{E_{cal} n_{cal} \tau_{cal}} n_{NO} \quad (4.2)$$

$$\Leftrightarrow n_{NO}(I_{LIF}) = \frac{E_{cal} n_{cal} \tau_{cal}}{\zeta I_{cal}} \frac{I_{LIF}}{E_L \tau_q} \quad (4.3)$$

where  $\zeta$  is a constant taking into account the efficiency of the detection, e.g., coupling of fluorescence light into the fibre,  $E_{cal}$ ,  $I_{cal}$  and  $E_L$ ,  $E_{cal}$  are the laser pulse energies and the LIF intensities during the calibration and the measurements, respectively.  $\tau_q$  and  $\tau_{cal}$  are the decay times, i.e., the lifetime of the states during the measurements and during the calibration to account for different quenching mechanisms in the different environments. The radiative lifetime of the electronic vibrational state undergoing a spontaneous transition  $(u, v') \rightarrow (l, v'')$  with and without quenching in general is given by [46]:

$$\tau_{cal} = (A_{v'}^u)^{-1} = \left( \sum_l \sum_{v''} A_{v'v''}^{ul} \right)^{-1} \quad (4.4)$$

and

$$\tau_q = (A_{v'}^u + Q_u)^{-1} = \left( \sum_l \sum_{v''} A_{v'v''}^{ul} + \sum_j n_j k_{uj} \right)^{-1} \quad (4.5)$$

where  $A_{v'}$  and  $A_{v'v''}^{ul}$  are the Einstein coefficients for the transition from the upper state  $u$  and the vibrational level  $v'$  to all lower vibrational levels  $v''$  and lower electronic states  $l$ . The lifetimes can be directly deduced from the time resolved LIF signals by performing an exponential fit. One example graph of a calibration procedure is shown in figure 4.4. The LIF technique used here

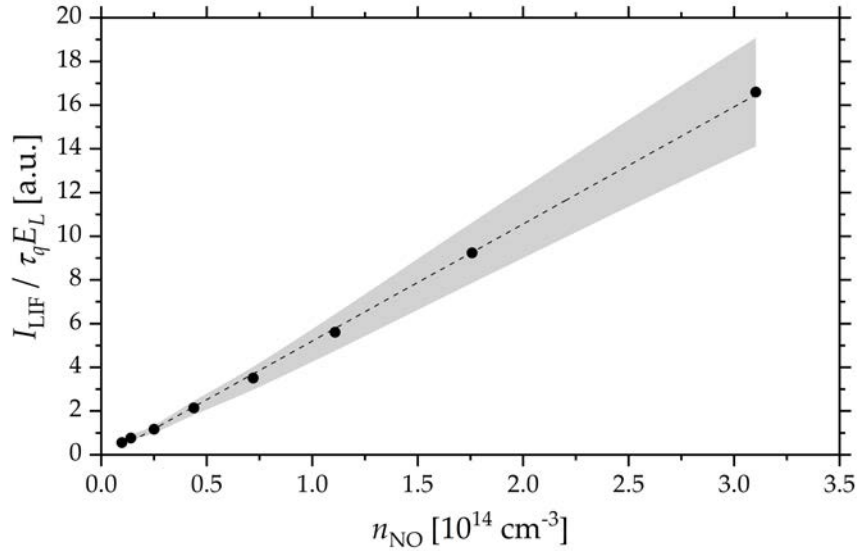


**Figure 4.4.** Calibration curve for the determination of absolute NO densities during the measurements. This calibration contains all the physical mechanisms as well as the optical properties of the detection system

is only sensitive to the vibrational ground state of NO. Golda et al. measured the gas temperature in the effluent of the COST-Jet at  $\vec{r} = (0, 0, 2)$  mm to be  $T_g \approx 310$  K for operation at  $P_{diss} = 0.4$  W in a 99.5% He/0.5% O<sub>2</sub> discharge [83]. The lifetime of the NO( $X^2\Pi$ ) state is considered to be long enough for the particles to reach vibrational equilibrium. In this case the distribution can be described by a Boltzmann distribution according to

$$f(v, T_{vib}) = \frac{1}{Z_{vib}} \exp \left\{ -\frac{E_v}{k_B T_{vib}} \right\} \quad (4.6)$$

where  $Z_{vib} = \prod_k \sum_v \exp \{ -E_{k,v} / k_B T \}$  is the vibrational partition function,  $E_{k,v}$  is the energy of the  $k$ -th mode with vibrational number  $v$ . This function

cancels out for relative expressions. With the approximation of a harmonic oscillator this energy is calculated via

$$E_v = \omega_n \left( v + \frac{1}{2} \right). \quad (4.7)$$

Here  $\omega_n$  is the vibrational constants for the different levels. In this case  $\omega_A = 2374 \text{ cm}^{-1}$  and  $\omega_X = 1904 \text{ cm}^{-1}$ , according to [84]. Taking into account these values and an estimated vibrational temperature of  $T_{vib} = 310 \text{ K}$  the ratio of the excited species to the ground state of the investigated species is calculated according to equation 4.6:

$$\frac{n_{v=1}}{n_{v=0}} = \exp \left\{ \frac{E_0 - E_1}{k_B T} \right\} \approx 1.1 \times 10^{-5}. \quad (4.8)$$

Therefore it is justified to assume that all the species are in the vibrational ground state and calculate the absolute NO density from the density in this state. From this point on the calibration procedure was performed and absolute numbers of NO are presented.

### 4.1.3 Error estimation of the calibration procedure

Due to the fact, that the calibration is performed with the investigated gas itself and not with an auxiliary gas as for example krypton when performing TALIF measurements on oxygen, one of the biggest error sources, the uncertainty in the two-photon cross sections, completely disappears. The potential error sources during the calibration in this case are the density during the procedure,  $n_{cal}$ , which in turn is dependent on the gas temperature  $T_g$  and the calibration pressure,  $p_{cal}$ . In both cases the fluctuations are assumed to be small. The pressure device (Pfeiffer CMR371) has a relative error of  $\Delta p_{cal} \approx 0.15\%$  (see datasheet). The temperature fluctuations in the lab are also assumed to be small in the range of a couple of K, which results in a relative error of  $\Delta T_g \approx 2\%$ . The deviations of the pulse energies are within the limit of  $\Delta E_{cal,L} < 0.5\%$  (see datasheet SpitLight Compact DPSS). Here the error in the energy rather occurs due to fluctuations of the diode signal. During the experiments these fluctuations were measured to be in the range of 5%. The largest fraction of the resulting error is due to the detection of the LIF signal using the two-lens system, hence in the optical constant  $\zeta$ . Here it

was observed that the fluctuations of the signal can be up to  $\Delta I_{\text{LIF}} \leq 10\%$ . Therefore, the resulting error of the absolute NO densities is assumed to be in the range of  $\Delta n_{\text{NO}} \approx 15\%$  for all measurements presented in this thesis. The error interval is indicated by shaded regions around the data points in the plots.

#### 4.1.4 Dependence of NO creation on synthetic air admixture

In section 4.1.1 the influence of different  $\text{N}_2/\text{O}_2$  ratios on the NO production was investigated and it was found that the admixture of synthetic air yields the optimum NO production. In this section the influence of different absolute admixtures of the synthetic air is presented. The helium flow is again kept constant at  $\Phi_{\text{He}} = 1$  slm and the amount of synthetic air is varied from 0.1 – 1.1 %.

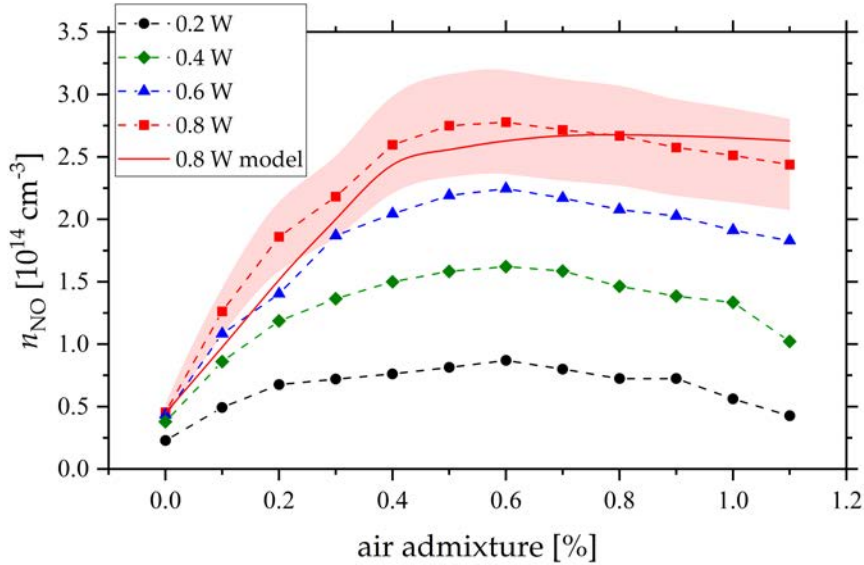


**Figure 4.5.** NO density as a function of the absolute synthetic air admixture measured at  $\vec{r} = (0, 0, 2)$  mm. The measurements are performed with a helium flow of  $\Phi_{\text{He}} = 1$  slm and the plasma power is varied as  $P_{\text{diss}} \in \{0.2, 0.4, 0.6, 0.8 \mid \text{in W}\}$ . The solid line shows the results from the model for  $P = 0.8$  W.

The LIF signals are then recorded as close as possible to the nozzle, as mentioned in the section before at  $\vec{r} = (0, 0, 2)$  mm. The results are displayed in figure 4.5. It can be seen that even without any external input of synthetic air a small amount of NO ( $n_{\text{NO}} \approx 0.25 - 0.5 \times 10^{14} \text{ cm}^{-3}$  depending on the power)

is formed. This is due to impurities from the gas lines and bottles, that is sufficient to build up NO. Subsequently, the NO density rises monotonously until an admixture of 0.5 – 0.6 % is reached, where it exhibits a maximum. This finding is independent of the plasma power as can be seen from the different curves. From there on the NO density decreases. These results are similar to the findings of Ellerweg et al., Willems et al. and Knake et al. who measured the dependency of the atomic oxygen density on the molecular oxygen admixture in older versions of the jet by molecular beam mass spectroscopy and TALIF, respectively and also found the maximum to be at 0.5 – 0.6 % [85, 44, 43]. Kelly et al. numerically modeled the dependency for a plasma jet device and also found the maximum to be at 0.4 – 0.8 %. Here, the decrease for higher admixtures of O<sub>2</sub> is purely attributed to the power consumption of the negative ions and the resulting lower electron density [86]. Pipa et al. measured the NO production rate in the kINPen jet as a function of the synthetic air admixture and found the maximum rates at 0.2 % and 0.07 % for gas flows of  $\Phi_{\text{Ar}} = 5 \text{ slm}$  and  $\Phi_{\text{Ar}} = 15 \text{ slm}$ , respectively [87, 88].

The trend observed and shown in figure 4.5 can be explained by different physical and chemical processes. For low admixtures the electron energy distribution function (EEDF) is hardly affected by the molecules. The NO production is low due to the lack of N<sub>2</sub> and O<sub>2</sub> molecules and their dissociative products N and O which are key players for the NO production kinetics. With increasing admixtures of the synthetic air, the dissociation probability increases and as a consequence N and O densities increase and at some point the optimum point for NO production is reached. For higher admixtures the EEDF is significantly influenced by the high amount of molecules present in the plasma. Its high energy tail is depleted due to the high number of inelastic collisions [89, 90]. This leads to fewer electrons energetic enough to dissociate the molecules and form the atomic components. Furthermore, due to the electronegative character of O<sub>2</sub> the electron density is decreased and dissociation by electron impact is further reduced.

#### 4.1.5 NO production in different plasma operation regimes

In this section, the influence of the dissipated plasma power on NO production is investigated. Therefore, the power is varied from the lowest possible

point where the discharge ignites and is in a stable regime up to the power where the discharge transitions and a constricted mode occurs. The dependencies are investigated for two different flows, while the synthetic air admixture is kept constant at 0.5%. The results can be seen in figure 4.6. 4.6 (a)

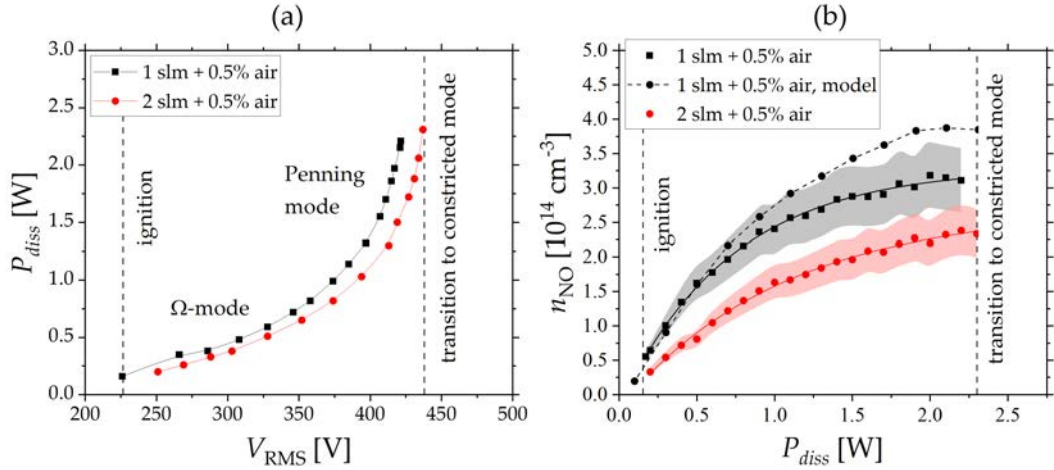


**Figure 4.6.** (a): voltage-power characteristic of the COST-Jet, (b): power dependencies of the NO densities with the corresponding fit functions measured at  $\vec{r} = (0, 0, 2)$  mm. The helium flow is varied while the synthetic air admixture is kept constant at 0.5%.

shows the voltage power characteristic of the COST-Jet. For low voltages the curve follows a rather linear correlation that turns into a non-linear behavior for higher voltages. This is owed to different operation modes of the jet with distinct differences in the electron power absorption for different values of the dissipated power: the  $\Omega$ -mode for lower powers and the Penning mode in the higher power regimes. In the  $\Omega$ -mode the ionization mainly occurs inside the bulk by electrons that are accelerated up to high energies in a strong ambipolar electric field. In the Penning-mode on the other side the ionization happens due to electrons that are generated inside the sheaths by Penning ionization but also due to the secondary electrons that are emitted from the electrodes when the positive ions impinge onto the surface. These modes and the physical mechanisms behind were investigated in detail by Bischoff et al. by simulations and experiments [91]. The non-linearity of the voltage power characteristic is also an important aspect for the LIF measurements. At high powers small fluctuations of the voltage by the RF generator can lead to high deviations in the absorbed power and hence the plasma dynamics. It is therefore preferable to measure in the  $\Omega$ -mode to keep the deviations small and

assure reproducible operation parameters as possible.

Figure 4.6 (b) shows the NO dependency on the dissipated power. The first data-points correspond to the first possible measurements after which the plasma ignites for the adjusted flows and is in a stable operation mode. The last data-points correspond to the power where the jet is just prior to the transition into the constricted mode. For both flows a strictly monotonous increase of the densities is observed. For a helium flow of 1 slm the density rises from  $n_{\text{NO}}(\Phi_{\text{He}} = 1 \text{ slm}) : 0.6 \times 10^{14} \text{ cm}^{-3} \rightarrow 3.2 \times 10^{14} \text{ cm}^{-3}$  and for the 2 slm flow  $n_{\text{NO}}(\Phi_{\text{He}} = 2 \text{ slm}) : 0.3 \times 10^{14} \text{ cm}^{-3} \rightarrow 2.4 \times 10^{14} \text{ cm}^{-3}$ . In both cases the synthetic air admixture was kept constant. For high powers the NO density seems to evolve into an equilibrium like state where creation and loss mechanisms cancel out. We therefore fit a function of the form

$$n_{\text{NO}}(P_{\text{diss}}) = n_{\text{lim}} \left( 1 - \exp \left\{ -\frac{P_{\text{diss}}}{P_{\text{char}}} \right\} \right) \quad (4.9)$$

where  $P_{\text{char}}$  is the power depending on the discharge conditions where the density has increased up to a value of  $n_{\text{lim}}(1 - 1/e) \approx 0.63n_{\text{lim}}$ . The smaller the parameter  $P_{\text{char}}$ , the steeper the slope and the faster the steady state for the NO density is reached. As a consequence it can be found by a limit consideration that

$$\lim_{P_{\text{diss}} \rightarrow \infty} \left[ n_{\text{NO}}(P_{\text{diss}}) = n_{\text{lim}} \left( 1 - \exp \left\{ -\frac{P_{\text{diss}}}{P_{\text{char}}} \right\} \right) \right] = n_{\text{lim}}. \quad (4.10)$$

Indeed the NO density converges towards a stable value of  $n_{\text{lim}}$ . In the cases investigated here these values are:

$$n_{\text{lim}}(\Phi_{\text{He}}) = \begin{cases} 3.4 \times 10^{14} \text{ cm}^{-3} & \text{for } \Phi_{\text{He}} = 1 \text{ slm} \\ 2.8 \times 10^{14} \text{ cm}^{-3} & \text{for } \Phi_{\text{He}} = 2 \text{ slm} \end{cases}$$

and

$$P_{\text{char}} = \begin{cases} 0.80 \text{ W} & \text{for } \Phi_{\text{He}} = 1 \text{ slm} \\ 1.30 \text{ W} & \text{for } \Phi_{\text{He}} = 2 \text{ slm} \end{cases}$$

It can be seen that higher NO densities are observed for the lower flow under otherwise identical discharge conditions. The physical reason for that behavior is explained later in this thesis. When evaluating the results presented in

figure 4.6 (a) and (b), it is interesting to show the voltage-density correlation. This is shown in figure 4.7. As already assumed from the analytical shape of the fit functions a linear dependency of the NO density on the voltage is

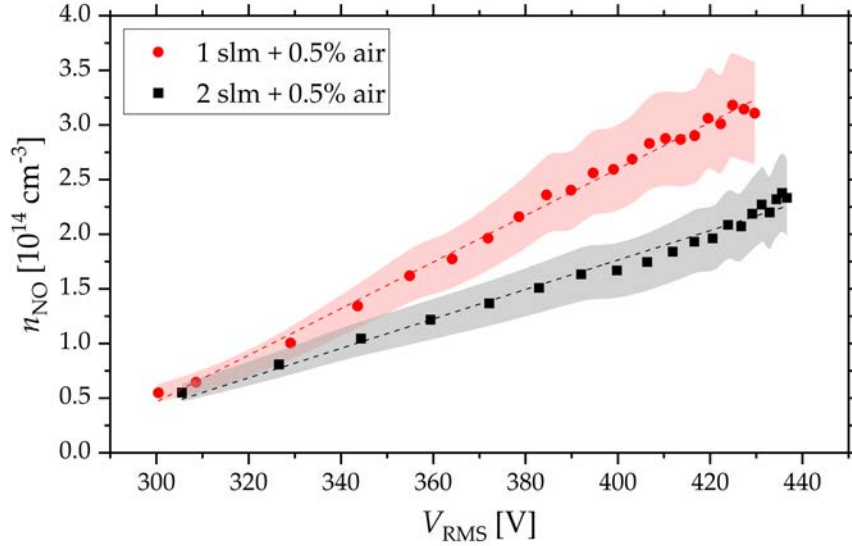


**Figure 4.7.** Voltage-density correlation of the NO density measured at  $\vec{r} = (0, 0, 2)$  mm. The data-points show the results for two different helium flows, while the synthetic air admixture is kept constant.

observed over the whole power operation range of the jet, i.e., in the  $\Omega$ -mode as well as in the Penning mode. The same linear trend was observed for the atomic oxygen density depending on the molecular oxygen admixture that was measured by Willems et al. [44]. In the case of the NO dependency the linear fit for  $\Phi_{\text{He}} = 1$  slm yielded a slope of  $dn_{\text{NO}}/dV = 2.13 \times 10^{12} \text{ V}^{-1} \text{ cm}^{-3}$  and in the  $\Phi_{\text{He}} = 2$  slm case  $dn_{\text{NO}}/dV = 1.29 \times 10^{12} \text{ V}^{-1} \text{ cm}^{-3}$ . In case of the COST-Jet with a high reproducibility and stable voltage-power characteristics the linear dependency on the voltage seems reasonable. By this relation the NO density can be more easily tuned for certain applications by adjusting the voltage and taking into account the linear voltage dependency as compared to power adjustments, where a more complex analytic behavior is observed (see figure 4.6 (b)).

## 4.2 Diffusion of air into the plasma effluent

### 4.2.1 Quenching of NO(A $^2\Sigma^+$ )

Due to the large number of collisions in atmospheric pressure plasmas, quenching is a common process that needs to be taken into account. This is a radiationless de-excitation process triggered by inelastic collisions. Due to the non-radiative character, this reduces the LIF signal and its time constant and can lead to significant errors in the density determination, if not taken into account. The measurements up to now were performed close to the plasma nozzle at  $\vec{r} = (0, 0, 2)$  mm where the species are well shielded from the surrounding air and quenching does not play a major role. However, if measuring further away in the effluent ambient atmosphere will diffuse into the effluent and quenching will occur. To investigate the influence of the air intrusion, the time resolved LIF signal, hence the effective lifetime of the NO(A  $^2\Sigma^+$ ) state is monitored and systematically scanned throughout the effluent region. By this it is possible to gain quantitative information about the quenching properties of the surrounding gas. Figure 4.8 shows two exemplary waveforms of the LIF signal in two different regions in the effluent. The first one shows a slow decay with a lifetime of  $\tau_q \approx 200$  ns, which is close to the natural lifetime, i.e., almost no quenching is affecting the lifetime and another narrow LIF signal with a lifetime of  $\tau_q \approx 6$  ns that corresponds to a strong quenching regime. From those waveforms, the lifetimes are determined throughout the effluent. Neglecting photochemical reactions, the rate equation for the excited state can be written as follows:

$$\frac{\partial n_u}{\partial t} = A_{0u}n_0 - n_u \left( A_{u0} + \sum_j k_{uj}n_j \right) \quad (4.11)$$

where  $n_u$  and  $n_0$  correspond to the excited and the ground state respectively,  $A_{0u}$  is the excitation rate,  $A_{u0}$  the Einstein coefficient for spontaneous emission and  $k_{uj}$  and  $n_j$  the quenching coefficient and the quencher density of the  $j$ -th species. In the presented results the population of the excited state is mainly caused by the absorption of the photons of the excitation laser. Since the fluorescence signal is only recorded after the laser pulse (red shaded area

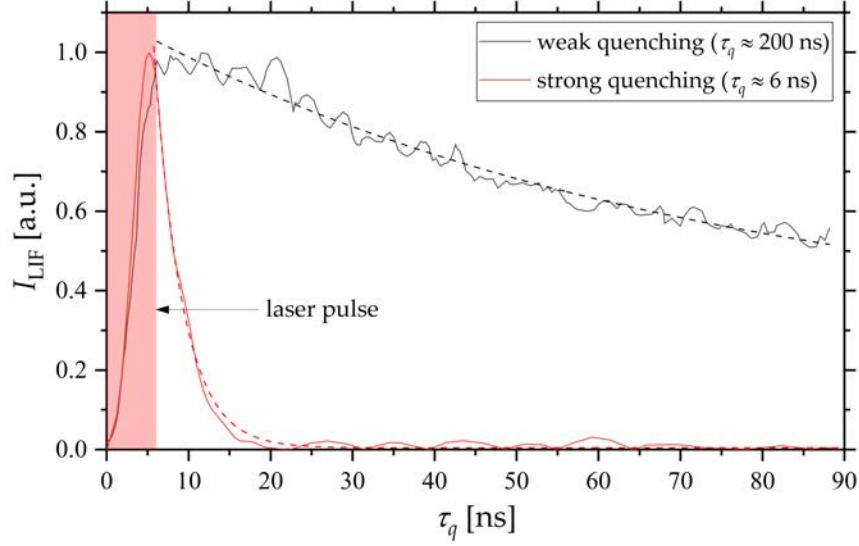


**Figure 4.8.** Two fluorescence waveforms and the according exponential fits in order to calculate the  $\text{NO}(A^2\Sigma^+)$  lifetime. The two waveforms correspond to a strong quenching regime with a calculated lifetime of  $\tau_q \approx 6$  ns and a weak (no) quenching regime with a lifetime of  $\tau_q \approx 200$  ns. By this method the lifetimes in different regions of the effluent are calculated in order to investigate the quenching properties.

in 4.8) one finds that  $A_{0u}n_0 = 0$  and the differential equation 4.11 can be written as:

$$\frac{\partial n_u}{\partial t} = -n_u \left( A_{u0} + \sum_j k_{uj}n_j \right) \quad (4.12)$$

This differential equation can then be solved by separating the variables and integrating from the time when the laser pulse ends ( $\tau_e$ ) until an arbitrary time  $t$ :

$$- \int_{n_u(\tau_e)}^{n_u(t)} \frac{\partial \tilde{n}_u}{\tilde{n}_u} = \left( A_{u0} + \sum_j k_{uj}n_j \right) \int_{\tau_e}^t d\tilde{t} \quad (4.13)$$

$$\Rightarrow n_u(t) = n_u(\tau_e) \exp \left\{ - \left( A_{u0} + \sum_j k_{uj}n_j \right) (t - \tau_e) \right\} \quad (4.14)$$

$$= n_u(\tau_e) \exp \left\{ - \frac{t - \tau_e}{\tau_q} \right\} \quad (4.15)$$

where  $\tau_q = \left( A_{u0} + \sum_j k_{uj}n_j \right)^{-1}$  is the effective lifetime of the state including quenching effects. Furthermore, the Einstein coefficient is linked to the natural lifetime as  $A_{u0} = \tau_0^{-1}$ . The relation of the effective lifetime and the natural lifetime can then be written as:

$$\frac{1}{\tau_q} - \frac{1}{\tau_0} = \sum_j k_{uj}n_j \quad (4.16)$$

This is a linear correlation between the inverses of the natural and the effective quenched lifetime and the quencher density and its properties, namely the quenching coefficient. Hence, by recording the quenched lifetime via LIF and looking up the natural lifetime in the literature it is possible to deduce the quenching coefficient by adding a known amount of quenching species and plot  $1/\tau_q - 1/\tau_0$  against  $n_j$ . Equation 4.16 and the corresponding plot are called the *Stern-Volmer equation* and *Stern-Volmer plot*.

Before the quenching coefficient of the state by air is investigated, the influence of the carrier gas itself, namely helium must be measured. In order to do so the interaction chamber was pumped down and subsequently filled up with a commercially available He/NO mixture up to a small pressure of about  $\approx 5$  mbar. By gradually introducing a little more amount of helium into the chamber and measuring the lifetime after each pressure increase, it was found that the lifetime of the state does not change, hence the quenching of NO(A  $^2\Sigma^+$ ) by helium is very weak. A linear fit according to equation 4.16 yields a quenching coefficient for helium of  $k_{u,\text{He}} \leq 10^{-14} \text{ cm}^3 \text{ s}^{-1}$ . However, this coefficient is only an upper limit, since the quenching induced by the impurities from the gas bottle and gas lines is at some point more pronounced than quenching by helium itself. This small quenching coefficient for helium justifies to neglect any quenching by helium in all the measurements, including the determination of the quenching coefficient of air. Therefore, the measured lifetime in the helium atmosphere,  $\tau_{\text{He}} = 200(\pm 10) \text{ ns}$ , is considered to be close to the natural lifetime of the state. This is verified by comparison with literature values of the natural lifetime that vary from values of e.g.,  $\tau_0 = 215(\pm 20) \text{ ns}$ ,  $\tau_0 = 209(\pm 10) \text{ ns}$  or  $\tau_0 = 192.5(\pm 5) \text{ ns}$  [92, 93, 94].

Quenching by air is investigated following the same procedure as before in the helium case, except for the fact that now synthetic air is introduced in each

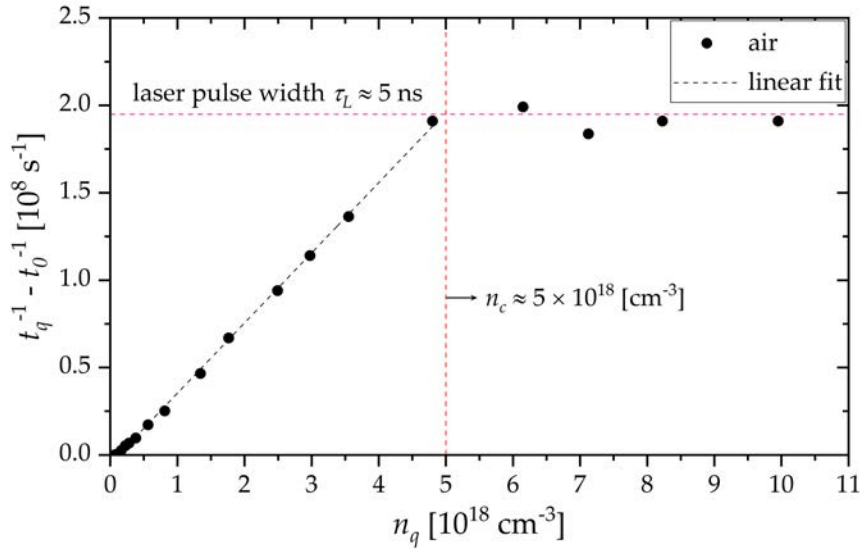


**Figure 4.9.** Stern-Volmer plot for the determination of the quenching coefficient of the  $\text{NO}(A^2\Sigma^+)$  state. In this case one example for air as quencher is shown. The red dotted lines indicate the laser pulse width, for which the lifetime of the state becomes shorter than the pulse itself (horizontal line) and the corresponding air density, indicated as  $n_c$  (vertical line)

iteration step. The same was done for the single constituents of air, namely  $\text{N}_2$  and  $\text{O}_2$ . The results can be seen in figure 4.9. For all three measured species, a linear dependency of the inverse lifetimes and the quencher density is observed. In the case of synthetic air, a plateau is reached that is linked to the FWHM of the excitation laser pulse of  $\tau_L \approx 5$  ns. This is the lower detection limit. From the linear fits of the plots, the quenching coefficients for the different species are obtained as:

$$k_{u,j} = \begin{cases} 4.02 \times 10^{-11} \text{ cm}^3 \text{ s}^{-1} & \text{for air} \\ 2.14 \times 10^{-14} \text{ cm}^3 \text{ s}^{-1} & \text{for N}_2 \\ 2.07 \times 10^{-10} \text{ cm}^3 \text{ s}^{-1} & \text{for O}_2 \\ 4.01 \times 10^{-10} \text{ cm}^3 \text{ s}^{-1} & \text{for CO}_2 \\ 2.29 \times 10^{-10} \text{ cm}^3 \text{ s}^{-1} & \text{for NO} \end{cases}$$

By taking into account the relation of the absolute quenching coefficient and the coefficients of the single constituents, the measurements can be cross checked

according to

$$k_{eff}n_{eff} = \sum_j \xi_j k_j n_j^{\text{air}} \stackrel{\text{air}}{=} \sum_{j=\text{N}_2, \text{O}_2} = 0.8k_{\text{N}_2} + 0.2k_{\text{O}_2} = 4.1 \times 10^{-11} \text{ cm}^3 \text{ s}^{-1} \quad (4.17)$$

where a pure synthetic air atmosphere is assumed, and quenching only occurs with  $\text{N}_2$  and  $\text{O}_2$ , hence  $n_{\text{N}_2}/n_{\text{O}_2} = 2/8$  and  $\xi_{\text{N}_2} + \xi_{\text{O}_2} = 1$ . Comparing the quenching coefficient for air calculated from the single components as in equation 4.17 with the measured quenching coefficient obtained from the linear fit in figure 4.9 it can be seen that they agree very well. This confirms the applicability of the method in our case to determine the quenching properties. Furthermore, the same method is used to determine the quenching coefficients for NO and  $\text{CO}_2$ . From the quenching coefficient, the quenching cross section can be calculated assuming a Maxwellian distribution function:

$$\sigma_{u,j} = \frac{k_{u,j}}{\langle v_{ij} \rangle} \quad \text{where} \quad \langle v_{ij} \rangle = \sqrt{\frac{8k_B T_g}{\pi \mu_{ij}}} \quad \text{and} \quad \mu_{ij} = \frac{m_i m_j}{m_i + m_j}. \quad (4.18)$$

Here  $\langle v_{ij} \rangle$  is the mean velocity between two colliding partners of the species  $i$  and  $j$ ,  $T_g$  the gas temperature parameter of the Maxwellian distribution,  $k_B$  the Boltzmann constant and  $\mu_{ij}$  the reduced mass. The results are eventually verified against data from other studies (see table S1 those values have been measured with various different diagnostics).

## 4.2.2 Air intrusion into plasma effluent

As shown in 4.9, besides the absolute and calibrated LIF signal, also an exponential decay function is fitted from which the lifetimes of the respective states are deduced. From those measured lifetimes, the air diffusion into the plasma effluent can be calculated. This is done by assuming a gas composition only consisting of helium and air. The measured lifetime,  $\tau_q$  is then given as:

$$\tau_q(\xi_{\text{He}}, \xi_{\text{air}}) = \left( \frac{\xi_{\text{He}}}{\tau_{\text{He}}} + \frac{\xi_{\text{air}}}{\tau_{\text{air}}} \right)^{-1} \quad \text{with} \quad \xi_{\text{He}} + \xi_{\text{air}} = 1. \quad (4.19)$$

Here  $\xi_{\text{He}}$  and  $\xi_{\text{air}} \in [0, 1]$  are the fractions of helium and air, respectively.  $\tau_{\text{He}}$  is the lifetime in pure helium measured during the calibration (close to the

TABLE S1: Measured quenching rate coefficients and calculated (see equation 4.18) cross sections for the NO( $A^2\Sigma^+ v' = 0$ ) state. Shown are the values observed in this study compared with literature values ( $T_g = 300$  K).

Ref.	$k_{u,j}$ [ $10^{-10}$ cm <sup>3</sup> s <sup>-1</sup> ]				$\sigma_{u,j}$ [ $\text{\AA}^2$ ]			
	N <sub>2</sub>	O <sub>2</sub>	NO	CO <sub>2</sub>	N <sub>2</sub>	O <sub>2</sub>	NO	CO <sub>2</sub>
our	$2.14 \times 10^{-3}$	2.07	2.29	4.01	0.032	32.3	35.2	42
[94]	$4.6 \times 10^{-3}$	1.79			0.007	28.5	41.4	
[95]	$9.1 \times 10^{-4}$	1.41		3.6		21.3		
[96]					0.014	30	40	61
[97]	$<1 \times 10^{-3}$	1.46	2.67	4.30		22		73
[98] <sup>b</sup>	-					22	29	65
[99]	$7.8 \times 10^{-4}$		2.3					-
[100]					$<0.01$	21	37	-
[101]		1.44	2.81	3.58		22.6	43.5	60.3
[102]					$\leq 0.01^a$	$26.9^a$	$38.6^a$	$68.4^a$

<sup>a</sup> measured at  $T_g = 294$  K

<sup>b</sup> obtained by emission intensity ratios  $\Phi_0/\Phi$  instead of lifetime ratios

natural lifetime without any quenching) and  $\tau_{\text{air}} = 0.96$  ns is the lifetime in pure air that is obtained from the extrapolation of the linear fit of the inverse lifetimes shown in fig. 4.9. The fraction of air can then be calculated from equation 4.19 as:

$$\xi_{\text{air}}(\tau_q) = \frac{\tau_{\text{air}}(\tau_{\text{He}} - \tau_q)}{\tau_q(\tau_{\text{He}} - \tau_{\text{air}})} \quad (4.20)$$

The results for air intrusion into the plasma effluent can be seen in figure 4.10. Shown are the effective lifetimes of the NO( $A^2\Sigma^+$ ) state that are obtained by an exponential decay fit of the time resolved LIF signals (a) and the air fraction calculated via equation 4.20. The black dotted line in (b) shows the equidensity line, ( $n_{\text{air}} = n_c$  see figure 4.9), at which the effective lifetimes become shorter than the laser pulse width ( $\approx 5$  ns), corresponding to the detection limit. The outlet of the plasma jet is located at  $x \in [-0.5, 0.5]$  and  $z = 0$ . It can be seen that the gas stream is well shielded from the surrounding air up to approximately  $z \approx 10$  mm. This leads to rather long lifetimes and less pronounced quenching. Once the axial distance exceeds this value, the lifetime rapidly drops, indicating a more pronounced quenching and therefore also an indication of the diffusion of air into the helium stream expanding

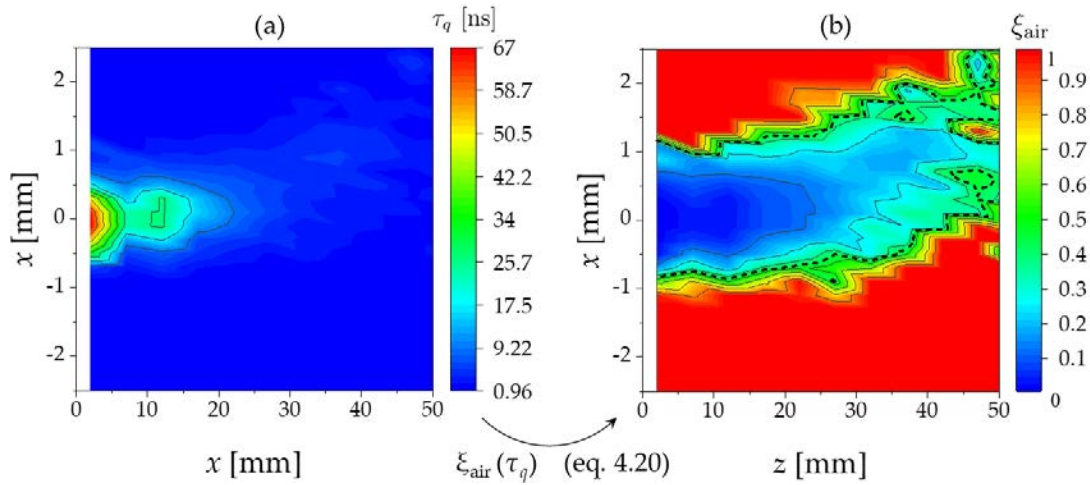


**Figure 4.10.** (a): quenched lifetimes of the NO(A  $^2\Sigma^+$ ) state obtained from the time resolved LIF signal, (b): fraction of air diffusing into the plasma effluent calculated via the quenched lifetimes plotted in (a) and equation 4.20. The dotted line represents the density, (see  $n_c$  in figure ??), at which the lifetime becomes shorter than the laser pulse width, hence the detection limit. The example shown here is operated at  $\Phi_{\text{He}} = 1 \text{ slm}$ ,  $\Phi_{\text{syn}} = 5 \text{ sccm}$  and  $P_{\text{diss}} = 0.5 \text{ W}$

from the jet. This is also an important finding for any application of the jet for surface treatments. When operating the jet at a distance to the sample within  $z \approx 15 \text{ mm}$ , the atmosphere is rather clean because the helium stream shields it from possible distortions. However, when moving further away it must be taken into account that the surrounding atmosphere is significantly diffusing into the effluent influencing the chemistry and hence the products that reach and interact with the surface.

### 4.3 2d and 3d density distributions at different operating atmospheres

#### 4.3.1 Expansion of NO into free effluent and coupling to feed gas flow

In this section, 2d density distributions of NO in the free effluent are presented. The jet is operated in two different atmospheres. First it is operated in an air environment and is then compared to the operation in a controlled helium atmosphere, to which 0.5% of synthetic air is admixed. According to

figure 3.3, the  $z$ -coordinate corresponds to the axial distance from the nozzle of the jet and the  $x$ -coordinate gives the inter-electrode distance, where the electrodes are located at  $x = -0.5$  mm and  $x = 0.5$  mm. A comparison for three feed gas flows, where the jet is operated in two different atmospheres is shown in figure 4.11

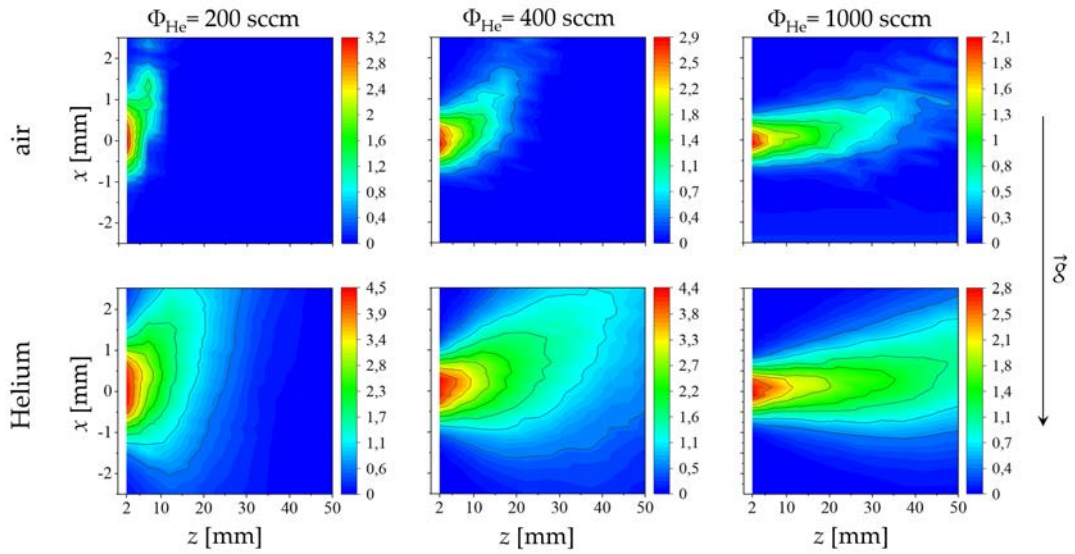


**Figure 4.11.** 2-dimensional density maps of NO in the  $xz$ -plane of the effluent. The top row shows the jet operated in ambient air, whereas the bottom row shows distributions where the jet is operated in a controlled He/ syn. air atmosphere. The associated coordinate system can be seen in figure 3.3. The different columns correspond to different feed gas flows as follows  $\Phi_{\text{He}} \in \{200, 400, 1000 \mid \text{in sccm}\}$ , while the power is kept constant at  $P_{\text{diss}} = 0.6$  W. The color scale bars are in units of  $10^{14} \text{ cm}^{-3}$  and the vector represents the direction of gravity.

Here the top row shows the distributions for the jet operated in ambient air, while the bottom row shows the distribution operating in a controlled He/ synt. air atmosphere.

The first striking feature when comparing the different flows is the fact that NO expands much further into the ambient for higher flows. This is as expected due to the increased initial velocity that can be calculated as  $v_{\text{gas}}(\Phi_{\text{He}}) = \Phi_{\text{He}}/A_d$ , where  $A_d = 1 \text{ mm}^2$  is the cross section of the channel. The initial velocities for the investigated flows vary from  $v_{\text{gas}}(200 \text{ sccm}) = 3.3 \text{ m s}^{-1}$  up to  $v_{\text{gas}}(2000 \text{ sccm}) = 33 \text{ m s}^{-1}$ . Furthermore, it can be seen that the NO also expands further in the controlled He atmosphere as compared to pure air. This

is observed not only in the axial  $z$ -direction but also in  $x$ -direction.

To study this different expansion behavior, 1-dimensional axial profiles of the NO density and the corresponding gradients are investigated to deduce density drops and appropriate distances for certain applications. To account for buoyancy, that is clearly observed for the density distributions in figure 4.11, one must not take the on axis values ( $x = 0$ ). Therefore, the measured data are transformed into bigger matrices via the Renka-Cline interpolation [103]. By this method the resulting images consist of  $51 \times 51$  matrices. To obtain the 1-dimensional density profile and taking into consideration the buoyancy, the maximum value of each column is extracted and put into an array. An analytic function is fitted, and the derivative is calculated. From those functions the decay length and the gradients can be calculated, respectively. The fit function and its derivative are of the form:

$$n_{\text{NO}}(z) = \hat{n} \exp \left\{ -\frac{z}{L} \right\} + n_{\text{off}} \quad \text{and} \quad \nabla_z n_{\text{NO}} = \frac{\partial n_{\text{NO}}}{\partial z} = -\frac{\hat{n}}{L} \exp \left\{ -\frac{z}{L} \right\} \quad (4.21)$$

Here  $\hat{n}$  is the maximum density at the first data point at  $\vec{r} = (0, 0, 2)$ ,  $L$  is the decay length at which the density has dropped to  $\hat{n}/e$  and  $n_{\text{off}}$  is a possible density offset. One exemplary evaluation of this data treatment is shown in figure 4.12. Here the  $\Phi_{\text{He}} = 200$  sccm case from figure 4.11 is chosen. This evaluation is performed for all investigated flows and the results are presented in table S2. It is observed that the first measured absolute densities are higher in the controlled helium atmosphere as compared to the air environment (see figure 4.12 (a)). This can be understood by the fact that these values are already measured 2 mm in the effluent, where the NO particles have already interacted with the surrounding atoms or molecules. As already seen in section 4.2.1 helium is a very slow quencher, hence the NO particles are not destroyed so quickly as compared to air, where  $\text{O}_2$  quenches quite fast. By extrapolating the data to  $z = 0$  comparable values are observed. This is reasonable, since at this point, the surrounding atmosphere should only have minor impact on the NO generation by back-diffusion into the channel. By looking at the gradients  $\partial n_{\text{NO}}/\partial z$ , that determine how fast NO is destroyed, it is clearly visible how strong the ambient gas influences the expansion of the reactive species into the effluent. While at  $z = 0$ , the gradient is almost three times higher in the air environment ( $\nabla_{z=0,\text{air}}/\nabla_{z=0,\text{He}} = 1.05/0.39$ ), even at  $z = 2$  the gradient is still more than two times higher ( $\nabla_{z=2,\text{air}}/\nabla_{z=2,\text{He}} =$

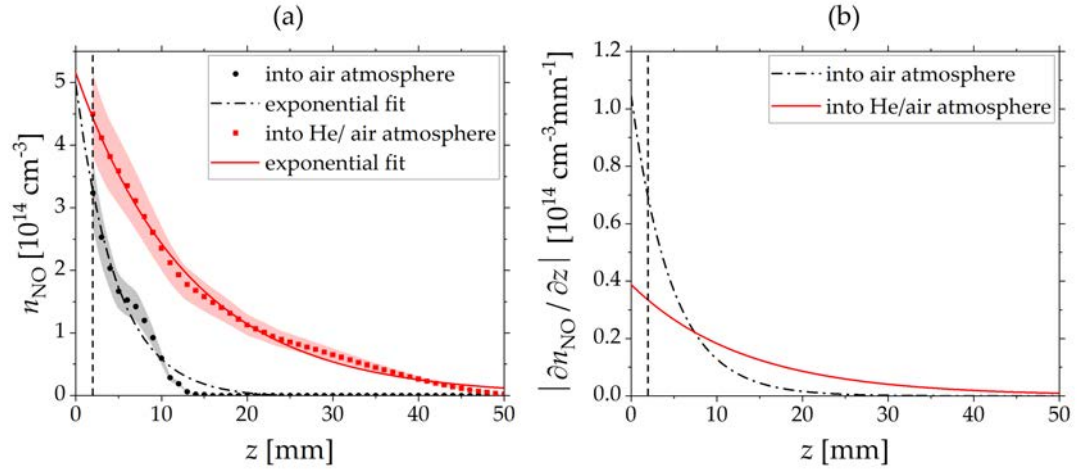


**Figure 4.12.** (a) NO density profiles along the axial  $z$ -axis and the corresponding exponential fit in air and He/ synthetic air atmosphere and (b) the corresponding absolute values of the gradients  $\nabla_z n_{\text{NO}} = |\partial n_{\text{NO}} / \partial z|$  calculated from the fit. Here  $\Phi_{\text{He}} = 200$  sccm and the power is kept constant at  $P = 0.6$  W. The vertical dotted line shows the first measurable point at  $\vec{r} = (0, 0, 2)$ . Data left to this line are extrapolated from the exponential fit.

0.7/0.3). The same behavior can be seen when evaluating the decay lengths  $L$ . For 200 sccm e.g., the decay length in the air environment is almost three times smaller as compared to the helium environment, ( $L_{\text{air}} / L_{\text{He}} = 4.8 / 13.3$ ). All those parameters are important for any treatment applications, since they are crucial for the determination of treatment parameters and also show the limitations or possibilities for different distances of operation and the resulting densities of reactive species that interact with the surface. The different evolution of NO in the effluent in the different atmospheres can be explained by taking into account the reaction kinetics concerning NO destruction and creation channels. One key player to create NO is atomic oxygen. However, prior studies by Knake et al. and Ellerweg et al. showed a fast destruction of O in the effluent with a strong exponential decay within the first millimeters [85, 43]. Predominantly this occurs due to the reaction of  $\text{O} + \text{O}_2 + \text{M} \rightarrow \text{O}_3 + \text{M}$  and  $\text{O} + \text{O}_3 \rightarrow \text{O}_2 + \text{O}_2$  [104]. This destruction of O and subsequently creation of  $\text{O}_3$  in turn, favors the destruction of NO, since the rate coefficient of the reaction  $\text{NO} + \text{O}_3 \rightarrow \text{O}_2 + \text{NO}_2$  is two orders of magnitude larger than the corresponding creation channel involving  $\text{O}_3$  according to  $\text{N} + \text{O}_3 \rightarrow \text{NO} + \text{O}_2$ . This will not happen in a helium atmosphere, since helium is an inert gas and does not react with the reactive species in the plasma effluent. Here the transport

TABLE S2: Flow dependencies of NO densities in air and He + 0.5 % synthetic air atmosphere. Shown are the respective fit parameters extracted from a fit function of the form  $n_{\text{NO}}(z) = n_0 \exp\{-z/L\} + n_{\text{off}}$ .

$\Phi_{\text{He}}$ [sccm]	$\hat{n}_{z=0}^{a,b} \mid \hat{n}_{z=2}^b$		$L$ [mm]		$\left  \frac{\partial n_{\text{NO}}}{\partial z} \right _{z=2}^c$	
	air	He/ air	air	He/ air	air	He/ air
200	4.99   3.3	5.13   4.5	4.8	13.3	1.04	0.3
400	3.62   2.87	4.54   4.34	11.1	19.3	0.3	0.31
600	3.06   2.67		17.4		0.16	
800	2.38   2.12		21.9		0.09	
1000	2.16   2.01	2.91   2.81	24.5	30.3	0.08	0.06
1200	1.75   1.61		26.9		0.06	
1600	1.51   1.31		21.1		0.06	
2000	1.12   1.04		23.2		0.03	

<sup>a</sup> obtained from the extrapolation of the exponential fit

<sup>b</sup>  $\hat{n}$  in units of  $10^{14} \text{ cm}^{-3}$

<sup>c</sup>  $\left| \frac{\partial n_{\text{NO}}}{\partial z} \right|$  in units of  $10^{14} \text{ cm}^{-3} \text{ mm}^{-1}$

of reactive species is mainly driven by free diffusion as shown later in this thesis in section 4.3.2.

Another effect that can be clearly seen in figure 4.11 is the fact that NO is strongly affected by buoyancy. This is not intuitive when comparing the densities of NO and air for standard conditions, where  $\rho_{\text{NO}} = 1.250 \text{ kg/m}^3 > \rho_{\text{air}} = 1.204 \text{ kg/m}^3$ . Hence, due to gravitational effects the NO stream might be expected to be directed downwards in the direction of  $\vec{g}$ . As this is not the case, the NO must be coupled to a stream of different density. Here the feed gas used for the operation of the jet is helium. Since  $\rho_{\text{He}} = 0.179 \text{ kg m}^{-3} \ll \rho_{\text{air}}$  the NO trajectory might be coupled to the helium gas flow. An approximation of the trajectories of the helium particles in air can be calculated via

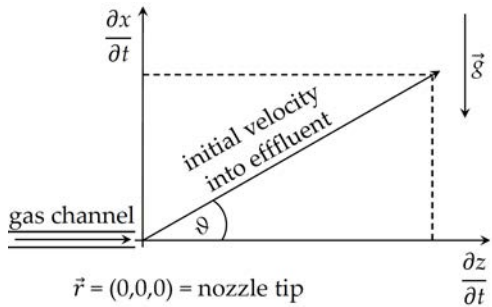
looking at the single particle trajectories when taking into account Stokes friction. The equations of motion for the different components can then be written as:

$$m \frac{\partial^2 x(t)}{\partial t^2} = g \left( \frac{\rho_{air}}{\rho_{He}} - 1 \right) - \beta \frac{\partial x(t)}{\partial t} \quad (4.22)$$

$$m \frac{\partial^2 y(t)}{\partial t^2} = 0 \quad (4.23)$$

$$m \frac{\partial^2 z(t)}{\partial t^2} = -\beta \frac{\partial z(t)}{\partial t} \quad (4.24)$$

where  $m$  is the mass,  $g = 9.81 \text{ m s}^{-2}$  is the gravitational acceleration,  $\beta = 6\pi r\eta$  is the Stokes friction coefficient with the dynamic viscosity  $\eta$ ,  $r$  the radius of a spherical particle and  $\rho$  the density of the respective media at  $T = 293.15 \text{ K}$ . Since no force is acting on the particles in the  $y$ -direction only the differential equations for the  $x$ - and  $z$ -component are solved. Therefore, the following boundary conditions are applied:



$$\frac{\partial x(t=0, \vartheta)}{\partial t} = \frac{\Phi_{He}}{A_d} \sin(\vartheta) \quad (4.25)$$

$$\frac{\partial z(t=0, \vartheta)}{\partial t} = \frac{\Phi_{He}}{A_d} \cos(\vartheta) \quad (4.26)$$

$$x(t=0) = z(t=0) = 0 \quad (4.27)$$

**Figure 4.13.** Geometry for the determination of the boundary conditions for the initial velocity in the velocity space. The angle  $\vartheta$  accounts for small angles of the gas stream when leaving the jet nozzle.

The geometry for the determination of the boundary conditions can be seen in figure 4.13. In this case  $\vartheta$  is the angle to account for either small horizontal misalignment of the jet itself or small angles that occur due to turbulence or other hydrodynamic effects during the escape of the gas from the jet nozzle. However, during the fitting procedure it was found that the angles are small in the range of  $\vartheta \in [0, 2]$ . This is reasonable, since especially for small flows the back diffusion of the surrounding gas is more pronounced as compared to higher flows, which

causes mixing of the different gases at the tip of the nozzle and small turbulences, that may lead to a velocity component with small azimuth angles,  $\vartheta > 0$ , with respect to the horizontal  $\vartheta = 0$ . Solving the differential equations for the single components and combining the solution in order to get an expression of the form  $x(z, \Phi_{\text{He}}, \vartheta)$  eventually yields an equation that reads:

$$\begin{aligned} x(z, \Phi_{\text{He}}, \vartheta, \Lambda) = & -\Omega\Lambda^2 \ln \left[ 1 - \frac{1}{\Lambda} \frac{zA_d}{\Phi_{\text{He}} \cos(\vartheta)} \right] + \Lambda \left( \Omega\Lambda - \frac{\Phi_{\text{He}} \sin(\vartheta)}{A_d} \right) \\ & \times \left( 1 - \frac{1}{\Lambda} \frac{zA_d}{\Phi_{\text{He}} \cos(\vartheta)} \right) + \Lambda \left( \frac{\Phi_{\text{He}} \sin(\vartheta)}{A_d} - \Omega\Lambda \right) \end{aligned} \quad (4.28)$$

where  $\Omega = g(\rho_{\text{air}}/\rho_{\text{He}} - 1)$  is the effective acceleration of a particle in the  $x$ -direction due to buoyancy and gravity without any influence of friction,  $\Lambda = m/\beta$  in units of s is used as a fitting parameter that accounts for Stokes friction and  $A_d$  is the cross section of the discharge channel (here  $A_d = 1$  mm). During the fitting procedure it was found that an excellent agreement is obtained keeping the fitting parameter constant as  $\Lambda = 3.5 \times 10^{-3}$  s for all investigated flows. The resulting trajectories according to the different flows, calculated by equation 4.28 are shown amongst the two-dimensional density plots in figure 4.14 as the black dotted line. Due to this agreement, this is a strong indication that the NO is closely coupled to the helium flow. However, it should be kept in mind that this calculation is based on a single particle picture, while the expansion of the gas flow is a fluid problem. These calculations are an approximation.

Based on that model another important parameter can be derived from the single solution in the  $z$ -component that is

$$z(t, \Phi_{\text{He}}, \vartheta, \Lambda) = \frac{\Lambda\Phi_{\text{He}} \cos(\vartheta)}{A_d} \left( 1 - \exp \left\{ -\frac{t}{\Lambda} \right\} \right). \quad (4.29)$$

From the limit at large times, an expression of the value  $D_z$  is derived as:

$$D_z(\Phi_{\text{He}}, \vartheta, \Lambda) := \lim_{t \rightarrow \infty} z(\Phi_{\text{He}}, \vartheta, \Lambda) = \frac{\Lambda\Phi_{\text{He}} \cos(\vartheta)}{A_d} = \frac{mv_0 \cos(\vartheta)}{\beta} = \frac{p_z}{\beta'}, \quad (4.30)$$

with  $\Phi_{\text{He}}/A_d = v_0$  as the initial velocity of the gas leaving the jet nozzle and

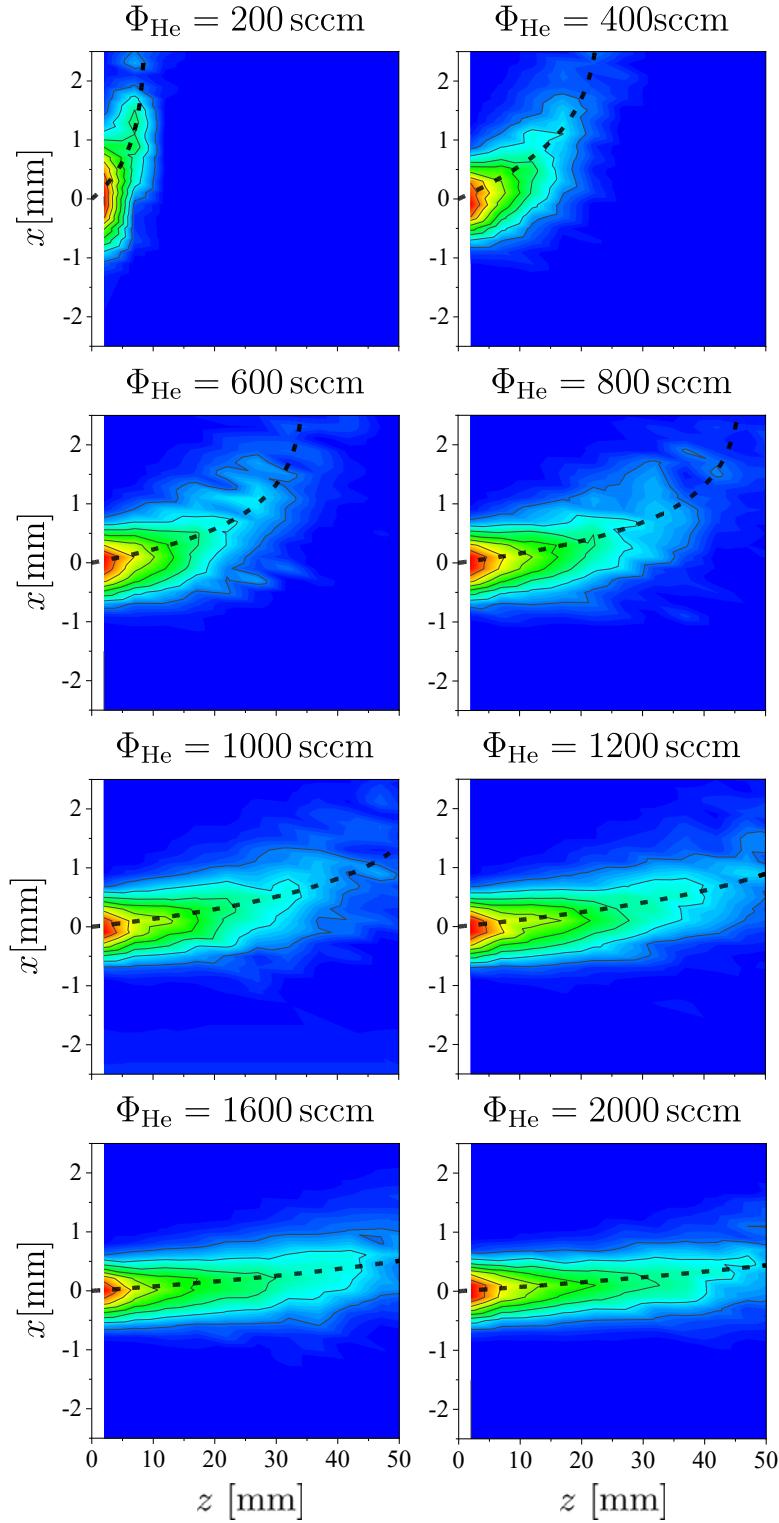


**Figure 4.14.** 2-dimensional density distributions in the  $xz$ -plane of the effluent. The jet is operated into air atmosphere. The associated coordinate system can be seen in figure 3.3. The different images correspond to different helium flows according to  $\Phi_{\text{He}} \in \{200, 400, 600, 800, 1000, 1200, 1600, 2000\}$  in sccm, while the synthetic air admixture was kept constant at 0.5% and the plasma power for all the measurements was  $P_{\text{diss}} = 0.6$  W. The black dotted lines are the calculated trajectories for taking into account Stokes friction according to equation 4.28.

$p_z$  the initial momentum in the z-component. This expression of  $D_z$  yields an upper limit of the maximum axial distance, for samples to be treated in the effluent for a given flow and therefore the maximum distance at which a sample can be placed. It scales linearly with the feed gas flow  $\Phi$ . From the mathematical expression 4.28, 4.29 and 4.30 it can be seen that the trajectory and the parameter  $D_z$ , for a given feed gas flow is solely dependent on the environment, that the jet is expanding into. In this case, the fact is described by the dependency of the expressions on  $\Lambda = f(\beta)$  and  $\Omega = f(\rho_{env})$ , where both parameters are dependent on properties of the environment, such as density,  $\rho_{env}$ , and the Stokes friction coefficient,  $\beta$ . The maximum treating distance  $D_z$  is solely described by the degree of friction between the gas escaping the channel and the environment. Additionally, a prediction of the point of intersection with a sample placed in the effluent is possible.

As already seen and listed in table S2 the maximum densities scale inversely with the feed gas flow. This fits to the findings of Douat et al. [105], who investigated the NO production in an older version of the jet used in this thesis via laser absorption spectroscopy and Iseni et al. [106], who investigated the NO production in the kINPen via molecular beam mass spectrometry (MBMS) and LIF. Generally, for given flow rates, the residence time of single gas particles inside the gas channel in the active plasma region can be calculated via

$$\tau_R = \frac{V_d}{\Phi_{He}} \quad (4.31)$$

where  $V_d$  is the discharge volume and  $\Phi_{He}$  the feed gas flow. If the gas remains in the active plasma region longer, there is more time to dissociate the molecules and build up atomic species such as N and O. Those atomic species are crucial to form NO. This might lead to a higher NO density inside the channel and a faster build up for lower flows. It should be noted, however, that the power during the experiments is kept constant at  $P_{diss} = 0.6$  W. This results in a lower dissipated energy per molecule for higher flows according to

$$w = \frac{P_{diss}}{\Phi_{He}}. \quad (4.32)$$

This means, that for higher energy densities there is more energy available per

unit volume per electron to trigger chemical reactions, such as the aforementioned dissociation of molecules. To correlate these quantities to the measured NO densities, the densities are plotted against the energy density and the residence time. This can be seen in figure 4.15. In figure 4.15 (a) the residence time of the single particles in the active plasma region is plotted. Since the volume is constant, this is simply a  $1/x$ -function. Furthermore, the measured NO density is displayed. These values are obtained from the extrapolation to the origin at  $\vec{r} = (0, 0, 0)$  from the exponential fits according to the example shown in figure 4.12 (a). It can be seen that the dependence of the densities on the feed gas flow resembles the one of the residence time. This supports the assumption that the residence time of the particles in the jet plays a decisive role in the build up of NO. The plot of the NO density against the energy density shows a similar trend as the dependency on the power (see figure 4.6) (b) and indeed a similar function can be fitted, i.e., the density saturates at higher specific energy densities. By this it can be concluded that the density dependence is a combination of longer residence times in the jet and an enhanced specific energy per molecule.

Additionally, the NO density depending on the feed gas flow is simulated in a zero-dimensional model that contains 138 species and 11799 reactions. Details on the model can be found in [31]. The results are shown in figure 4.15 (a). In this case, to match the simulations with the measured values, four distinct features needed to be modified compared to the basic chemical model that seemed to have major impact on the results:

- The rate coefficient for the reaction  $\text{O}(^3\text{P}) + \text{N}_2(v \geq 13) \rightarrow \text{NO} + \text{N}(^4\text{S})$  is set two orders of magnitude larger ( $\sim 10^{-17} \text{m}^3 \text{s}^{-1}$ ) as compared to existing literature.
- The interaction of the atomic species O and N with the wall and the resulting NO formation are taken into account by the reaction  $\text{N}(^4\text{S}) + \text{wall} \rightarrow \text{NO}$ , whereas in other models this reaction is neglected.
- For the NO formation channel via the A state, according to  $\text{N}_2(\text{A}^3\Sigma) + \text{O}(^3\text{P}) \rightarrow \text{NO} + \text{N}(^2\text{D})$  vibrationally higher excited species are taken into account, hence a larger rate coefficient of  $7 \times 10^{-15} \text{m}^{-3} \text{s}^{-1}$  is applied.

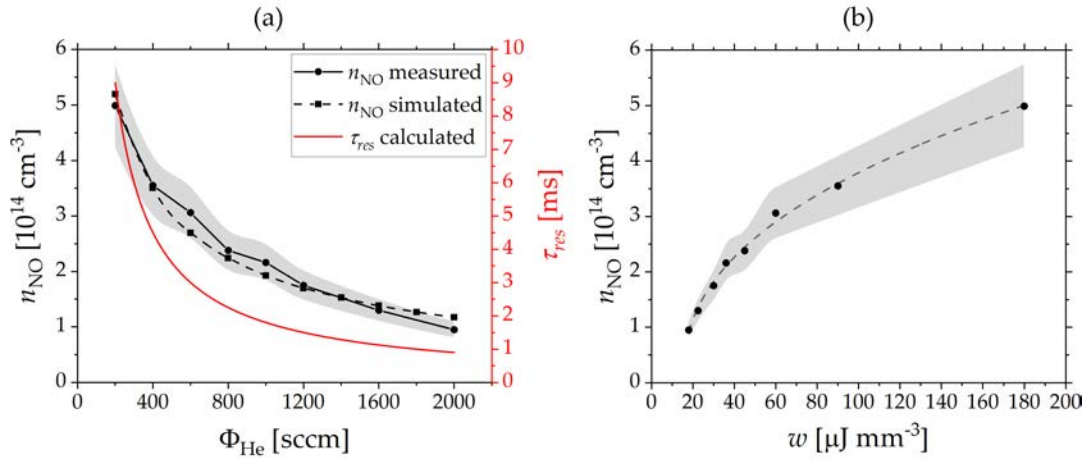


**Figure 4.15.** Absolute densities of NO measured and extrapolated at  $\vec{r} = (0,0,0)$  and obtained from the model for different flows plotted against (a) the residence time calculated by equation 4.31. Additionally, the simulated NO density from a zero-dimensional model from [31] is displayed against the measured values and (b) plotted against the energy density in the jet calculated by equation 4.32.

- The same rate coefficient is used for the NO formation via the B channel, according to  $\text{N}_2(\text{B}^3\Sigma) + \text{O}(\text{P}) \rightarrow \text{NO} + \text{N}(\text{D})$ . This reaction is completely neglected in many existing studies.

Inserting these modifications to the base chemical kinetic set, an excellent agreement is found between the simulated and the measured NO densities. The agreement with the hypothetical values is much more pronounced for high power regimes as compared to lower powers, which is an indication that the vibrational excited nitrogen molecules  $\text{N}_2(v \geq 13)$  to NO formation gain more significance for higher applied powers.

### 4.3.2 Turbulence like behavior in air and transport by free diffusion

In this section two-dimensional density maps in the  $yz$ -plane are presented. This is a top view of the NO distribution with the gravitational vector pointing into the paper plane. Figure 4.16 shows the  $yz$ -maps for  $x = 0$ . The associated coordinate system can be found in figure 3.3. The outlet of the plasma channel reaches from  $-0.5$  mm to  $0.5$  mm in the  $y$ -direction. The maximum NO density in both atmospheres is detected at the central position of the outlet at  $\vec{r} = (0,0,0)$ . In air, the density is measured to be  $n_{\text{NO}} = 2.3 \times 10^{14} \text{ cm}^{-3}$ ,

while in helium it is  $n_{\text{NO}} = 2.8 \times 10^{14} \text{ cm}^{-3}$ . This fits well to the densities measured above (see 4.5, 4.6, 4.15). The density in axial direction drops to about  $1.1 \times 10^{14} \text{ cm}^{-3}$  at  $z = 20 \text{ mm}$  according to the gradient calculated in table S2. However, it should be noted that the maps are only recorded in the  $x = 0$  plane, while the profiles for the gradient calculations have been corrected to account for the buoyancy, due to the coupling to the helium. The left column of figure 4.16 shows the density maps of NO and the right column shows the transverse profiles for different axial distances extracted from the density maps. It can be seen that the NO distributes in the transverse direction according to a Gaussian function. To investigate the behavior of the NO distribution a Gaussian function is fitted to each of the transverse profiles, according to

$$n_{\text{NO}}^T(y, \sigma, \mu) = \frac{1}{\sqrt{2\pi}\sigma} \exp \left\{ -\frac{(x - \mu)^2}{2\sigma^2} \right\}. \quad (4.33)$$

Here  $n^T$  is the transverse density profile,  $\mu$  the center coordinate of the distribution and  $\sigma$  the standard deviation. The results can be seen in figure 4.17. For small distances it can be seen that the width of the distribution,  $\sigma$  is close to 1 mm which is the width of the discharge channel. This can be seen for both atmospheres, which is reasonable, since at close distances the environment should not influence the distribution much except for the interaction of the back-diffusion from the surrounding into the channel. As the axial distance is increased, an increase of  $\sigma$  is also observed. This increase is slightly more pronounced in the helium atmosphere. However, as a certain distance is reached ( $z = 35 \text{ mm}$ ) the distribution in the air environment tends to become turbulent, which can be seen from the large error bars of the Gaussian fit, while the distribution in helium stays quite laminar in Gaussian shape. At  $z > 35 \text{ mm}$  in air environment, a Gaussian fit is no longer converging and the distribution becomes turbulent, while the error of the fit in helium is still small and the width of the distribution steeply increases for great axial distances. Concerning the  $\mu$  parameter of the distributions another difference is visible. While in air the distribution is distorted from the original center of the nozzle from  $z = 25 \text{ mm}$  onwards, it stays very close to zero in the helium atmosphere for all measured axial distances, i.e. the NO particles are not significantly deflected from its original path. Iseni et al. [106] and Reuter et al. [107] also observed a transition into a turbulent behavior. In their publications

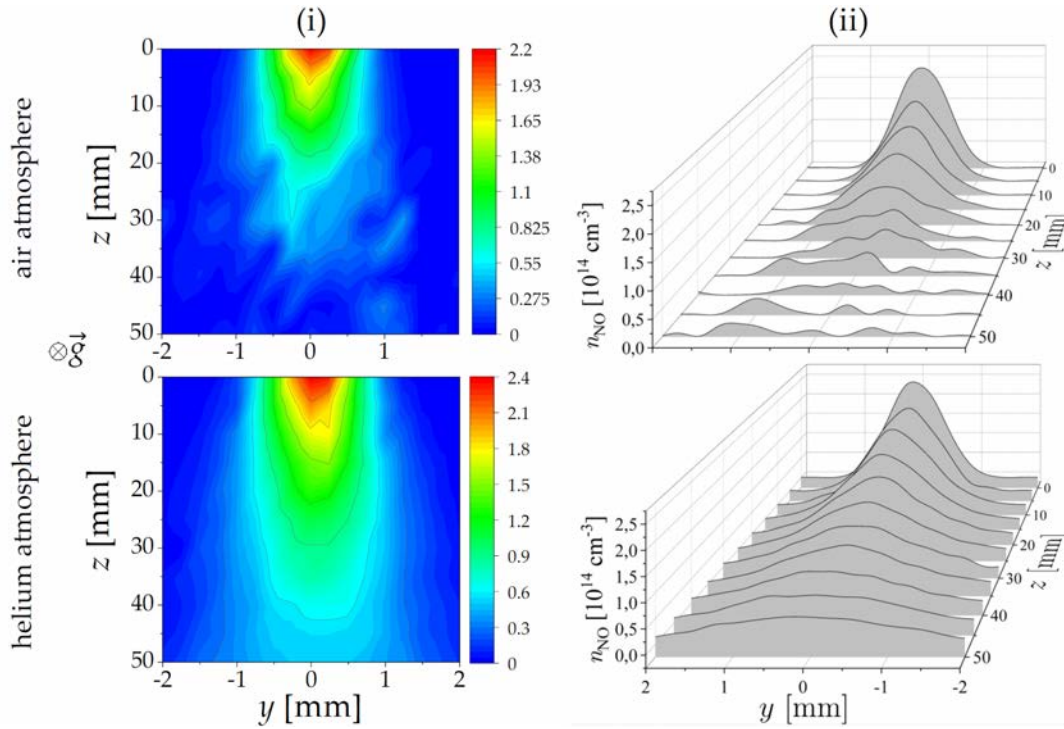


**Figure 4.16.** Column (i):  $yz$ -maps of the density distribution measured in air atmosphere (top row) and in helium (bottom row). Column (ii) shows the according transverse density profiles extracted from (i) for different axial distances. The parameter of the Gaussian fits to these profiles can be seen in figure 4.17.

they accounted this to an excess of the critical Reynolds number of

$$Re = \frac{\rho u L}{\eta} \quad (4.34)$$

where  $\rho$  is the fluid density,  $u$  the fluid velocity,  $L$  the discharge channel diameter and  $\eta$  the dynamic viscosity. In this case the Reynolds number of the highest investigated flow is  $Re(2000 \text{ sccm}) = 575 < Re_c \approx 2300$ , which is well below the critical Reynolds number. Hence, the excess of the Reynolds number and a resulting turbulence formation due to different fluid velocities or directions can be excluded.

Instead, the deviation from a Gaussian shape is explained by two mechanisms: one is static and dynamic quenching that either converts NO into other species or just de-excites NO without any radiation process making it invisible to the LIF technique, the other mechanism is collisions between helium,

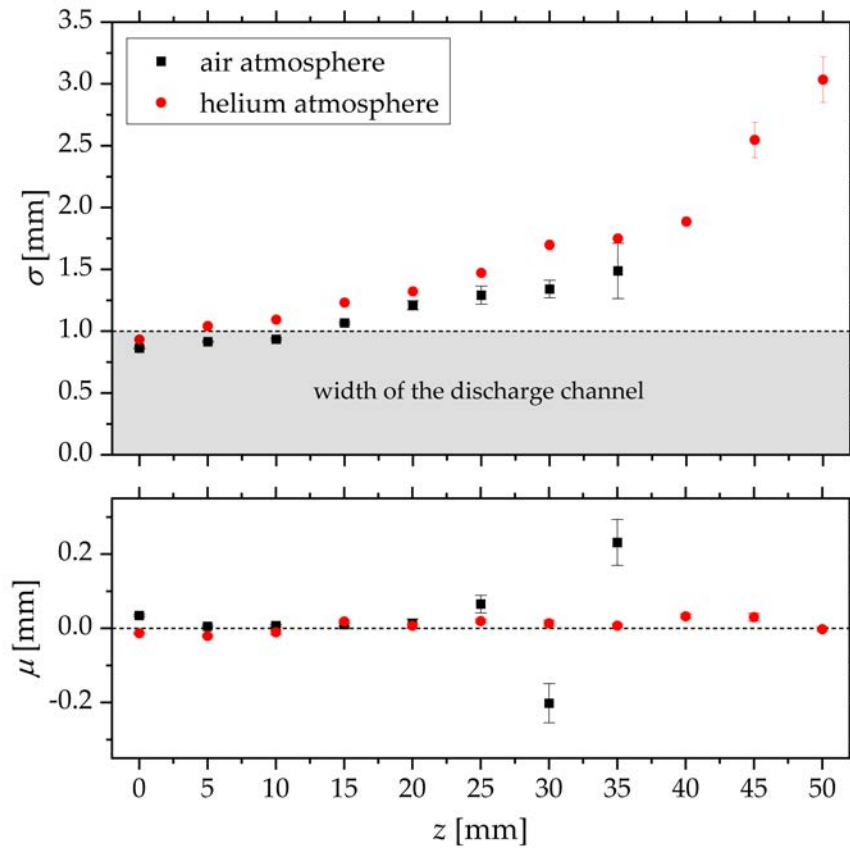


**Figure 4.17.** Different parameters of the Gaussian fit function according to equation 4.33. The function is fitted to the distributions shown in figure 4.16. The parameter  $\sigma$  represents the width of the Gaussian distribution, i.e., how far the NO expands transverse to the gas flow in  $y$ -direction, and  $\mu$  gives a transverse shift of the central position of the distribution with respect to the center of the discharge channel  $y = 0$ . The dotted line in the upper graph represents the width of the electrode gap of the jet and in the bottom graph the zero line with respect to the center of the outlet.

NO and other surrounding particles contained in air. In section 4.3.1 it was concluded that NO particles are closely coupled to the helium flow. Hence, a deflection of the helium particles from their original path would also lead to deviation of NO from the Gaussian shaped distribution. A deflection happens due to momentum transfer during an elastic collision between two partners  $A$  and  $j$ . The collision frequency of two particles according to the hard sphere model and classical collision theory can be written as

$$v_c^{Aj} = \sum_A n_A n_j \sigma_{Aj} \sqrt{\frac{8k_B T}{\pi \mu_{Aj}}} \quad \text{with } \sigma_{Aj} = \pi(r_A + r_j)^2 \quad (4.35)$$

where  $n_A$ ,  $n_j$ ,  $r_j$  and  $r_A$  are the densities and the radii of the collision partners,  $k_B$  is the Boltzmann constant and  $\mu_{Aj} = \frac{m_A m_j}{m_A + m_j}$  is the reduced mass of particles  $A$  and  $j$ . In air, the main collision partners are  $N_2$  and  $O_2$ . The radii of these species were estimated by *G. Barrow* from their co-volume to be  $r_{O_2} \approx 1.47 \text{ \AA}$  and  $r_{N_2} \approx 1.57 \text{ \AA}$  [108], while the van der Waals radius of a helium atom is estimated to be  $r_{He} \approx 1.069 \text{ \AA}$  [109]. From equation 4.35 it can be seen that the collision frequency is a function of the density of both collision partners and the radii of the respective species. This means, that as soon as a significant amount of air diffuses into the gas stream, the collision frequency with  $N_2$  and  $O_2$  molecules increases and the NO particles are deflected from its trajectory causing a deviation from the original Gaussian shape when leaving the jet nozzle. The calculated normalized collision frequency can be seen in figure 4.18. The normalized collision frequency is calculated based on the density profiles obtained by the data shown in figure 4.10 for the density of helium and air particles and from figure 4.11 for the NO density along the axis. From figure 4.10 it was already concluded that the gas stream is well shielded from the surrounding air up to  $z \approx 15 \text{ mm}$ . Hence, in this region the atmosphere mainly consists of helium and NO with a directed flow and the collision frequency remains small, resulting in well-defined NO distribution with a Gaussian shape in transverse directions (see figure 4.16). Beyond this point a notable amount of air diffuses into the gas stream and the collision frequency of helium and NO with air increases. Considering a particle of the surrounding atmosphere in rest, the fraction of energy that is transferred

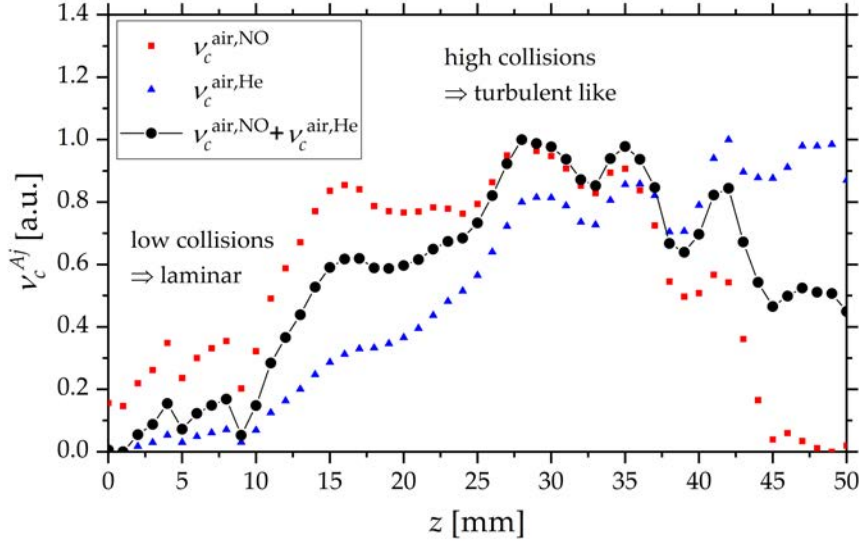


**Figure 4.18.** Calculated and normalized collision frequency along the  $\vec{r} = (0, 0z)$  axis, between air and NO (red squares), air and helium (blue triangles) and eventually the sum of both, i.e., the total collision between air and the species contained in the gas stream (black dots with B-Spline interpolation).

between two collision partners  $A$  and  $j$  can be calculated via

$$\eta(m_A, m_j, \Phi) = \frac{4m_A m_j}{(m_A + m_j)^2} \cos^2(\Phi) = \Theta_{Aj} \cos^2(\Phi) \quad \text{where } \Phi \in [0, \pi/2] \quad (4.36)$$

where  $m_A$ ,  $m_j$  are the masses of the two collision partners and  $\Phi$  is the angle of deflection after the collision. The decisive factor  $\Theta_{Aj}$ , a ratio of the masses of the two interaction partners can be calculated by taking into account the density of species and the above-mentioned radii, assuming spherical particles, with a mass of  $m_j = \rho_j \frac{4}{3} \pi r_j^3$  and the factor  $\Theta_{Aj}$  can then be described by the known properties according to

$$\Theta_{Aj} = \frac{16\pi}{3} \frac{\rho_j r_j^3 \rho_A r_A^3}{(\rho_j r_j^3 + \rho_A r_A^3)^2}. \quad (4.37)$$

From this equation the transfer factor can be calculated for collisions between the different species, and it can be concluded that the deflection of NO and helium air can be very effective, while for collisions with helium the deflection is not as pronounced and the shape stays rather laminar. Furthermore,

the quenching in air is much faster, as was shown in section 4.2.1.

Figure 4.19 shows density distributions in the  $yz$ -plane for different heights, hence showing 3-dimensional maps. The scale of each image is set with re-

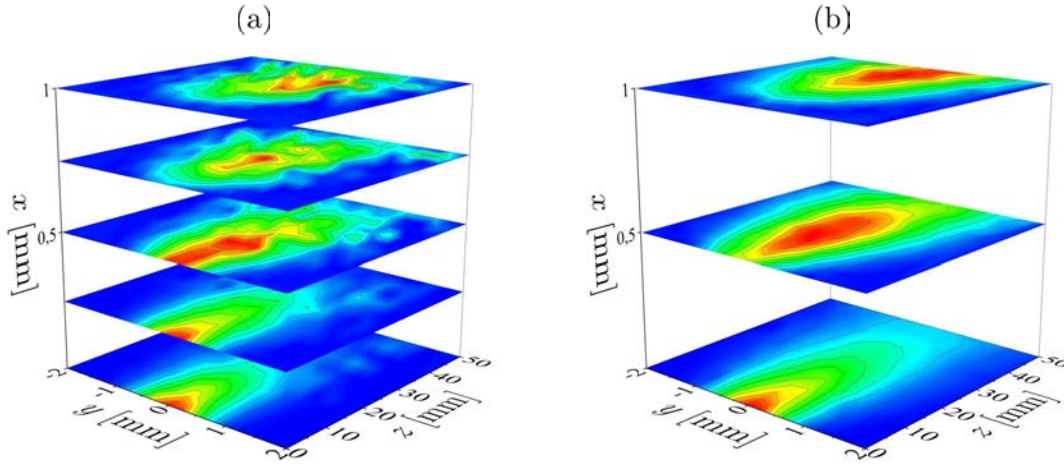


**Figure 4.19.** Density distributions of NO in the  $yz$ -plane for different heights ( $z$ 's) operating the jet into (a) air atmosphere and (b) the controlled helium atmosphere. The jet is operated at a power of  $P_{diss} = 0.6\text{ W}$  and the example shown here is for a helium flow of 1 slm.

spect to its own maximum, to emphasize the distributions over the absolute densities. Figure 4.19 (a) shows five different heights of the maps for the jet operated in air according to the  $x$ -coordinates being  $x \in \{0, 0.25, 0.5, 0.75, 1\}$  in mm} and three different slices for the jet operated in helium according to  $x \in \{0, 0.5, 1\}$  in mm}. The center of the discharge channel is located at  $\vec{r} = (0, 0, 0)$  and reaches up to  $x = 0.5$  mm. In this region reactive species are effectively created inside the plasma channel and are transported out into the effluent by the feed gas flow. Beyond this point  $x \geq 0.5$  mm the transport is mainly driven by diffusion, buoyancy, and inertia of the particles. As already seen in prior comparisons of the two atmospheres the NO distributions becomes rather turbulent for large axial distances and heights as already explained, due to collisions and quenching. The height at which the turbulence like behavior occurs, fits well to the measured data shown in figure 4.10, where it can be seen that up to a height of  $x \approx 0.5$  mm the gas stream is well shielded from the surrounding atmosphere. This prevents the particles from collision and quenching processes and the distribution stays laminar. For larger heights, a significant amount of air enters the region and the mixing

and collisions occurs. This is not observed in helium, where the elastic and inelastic collisions are not as efficient in disturbing the NO and helium particles from their initial path. The streamlines stay very laminar even for  $x = 1$  mm. As shown in figure 4.16, the distributions expand in the transverse directions for all measured heights and the maximum of the distributions moves along the  $z$ -axis according to the fluid velocity of the gas stream.

Usually, to model the density distributions, the diffusion-reaction equation needs to be solved. This equation has the form

$$\frac{\partial}{\partial t} n_{\text{NO}}(\vec{r}, t) = D\Delta n_{\text{NO}}(\vec{r}, t) + f(n_1 \dots n_{i-1}, n_i) \quad (4.38)$$

where  $f(n_1 \dots n_{i-1}, n_i)$  is a function that accounts for all chemical reactions that influence the NO density, with reaction partners,  $n_1 \dots n_i$ . This equation is difficult to solve often due to lack of information about densities of reaction partners in the environment or the reactions itself. However, due to the fact, that NO particles are closely coupled to the helium flow and helium is an inert gas and a slow quencher, as shown in section 4.2.1, one can use the approximation, that in the controlled helium atmosphere the radial transport is purely driven by diffusion of NO, while the axial transport is driven by the velocity of the helium gas-flow leaving the jet. To investigate this correlation the reaction function  $f(n)$  in the reaction diffusion equation is neglected and the problem is reduced to one dimension. Then equation 4.38 can be simplified and reduces to the 1-dimensional diffusion equation, according to

$$\frac{\partial n_{\text{NO}}(y, t)}{\partial t} = D\Delta n_{\text{NO}}(y, t) = D \frac{\partial^2 n_{\text{NO}}(y, t)}{\partial y^2}, \quad (4.39)$$

where  $D$  is the diffusion coefficient for NO in helium,  $D_{\text{NO,He}} = 62.4 \text{ cm}^2 \text{ s}^{-1}$ . In this case, the initial condition is a Gaussian profile with the initial density extracted from the exponential fits shown in figure 4.12. The solution to the diffusion equation then reads

$$n_{\text{NO}}(y, t) = \frac{1}{\sqrt{4\pi Dt}} \exp \left\{ -\frac{(y - y_c)^2}{4Dt} \right\} \quad (4.40)$$

where  $y_c$  is the center position of the Gaussian profile. The time according to each axial position in the effluent can be calculated from the model and

equation 4.29 and reads

$$t(z) = -\Lambda \ln \left( 1 - \frac{zA_d}{\Lambda\Phi_{\text{He}} \cos(\vartheta)} \right). \quad (4.41)$$

Applying equations 4.40 and 4.41 the density profile for each position  $z$  in the effluent can be calculated. The results of the measured map and the map calculated by diffusion can be seen in figure 4.20.

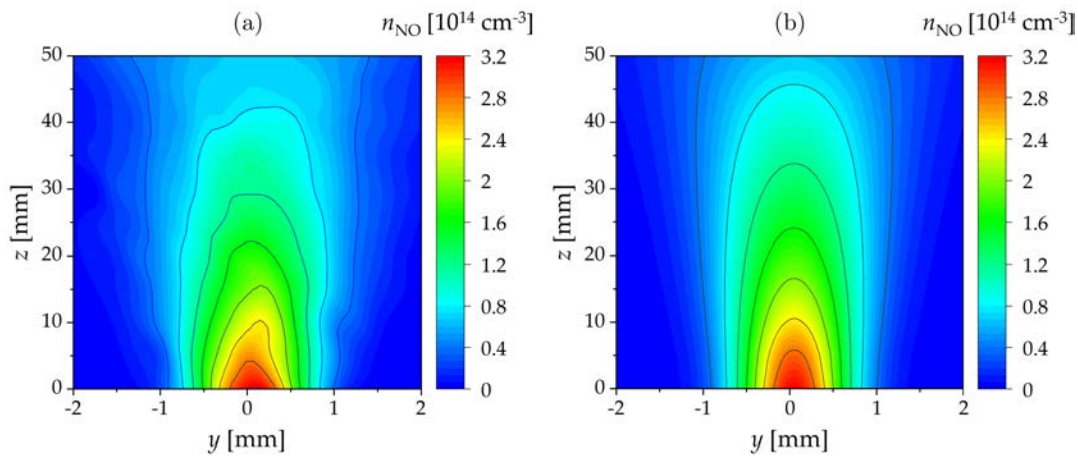


**Figure 4.20.** 2-dimensional density plots for  $\Phi_{\text{He}} = 1$  slm and 0.5% synthetic air admixture in the controlled helium atmosphere (a) obtained from the experiment (b) obtained from the solution of the diffusion equation (equations 4.40 and 4.41).

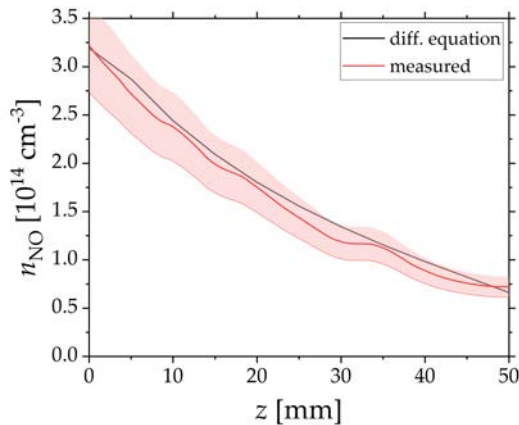


**Figure 4.21.**  $z$ -profiles extracted from figure 4.20 on the  $y = 0$  axis.

It can be seen that the extracted profiles from the 2d

It can be seen that good agreement is achieved by the solution of the diffusion equation without the implementation of any chemical reactions. This is a verification that in the controlled inert atmosphere the transport of NO in axial direction is purely governed by the gas velocity of the helium gas stream leaving the jet and by diffusion in radial direction. This becomes even more visible when plotting the axial density profiles for the maximum density extracted from figure 4.20 (a) and (b).

contour-plots (see lines) agree excellently. This is an indication that in the controlled helium atmosphere the reaction term in the diffusion reaction equation can be neglected and the atmosphere is indeed inert. The transport of NO particles in the transverse directions is then purely determined by the diffusion, whereas the transport in axial direction is determined by the gas velocity of the helium leaving the jet. Furthermore, this agreement is a verification of the approximation of the single particle model, owing to the fact that the axial positions are determined by the expression  $t(z)$  (equation 4.41) that is derived from the Stokes friction in the effluent. Hence, it is reasonable that also the axial velocity of the gas stream  $\partial z(t)/\partial t$  and the acceleration  $\partial^2 z(t)/\partial t^2$  can be adequately described by the model.

The last investigated orientation is the  $xy$ -plane which is located perpendicular to the gas stream escaping the jet. While the images shown in the sections before ( $xz$ - and  $yz$ -planes correspond to images from the side and the top respectively, the orientation shown here corresponds to a front view of the NO distribution. The results for different axial distances ( $z \in \{0, 20, 40\}$  in mm), are shown in figure 4.22. Here the jet is operated at  $\Phi_{\text{He}} = 1$  slm and 0.5% admixture of synthetic air while the power is kept constant at  $P_{\text{diss}} = 0.6$  W. The dashed square in the  $z = 0$  plane indicates the dimensions of the jet

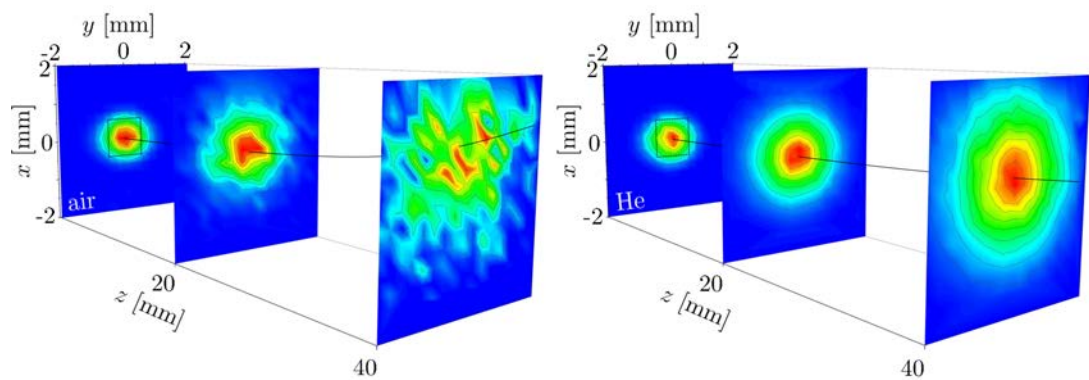


**Figure 4.22.** Density distributions of NO in the  $xy$ -plane for different axial distances ( $z$ ), operating the jet into air and helium atmosphere (see labels in the respective images). The jet is operated at a power of  $P_{\text{diss}} = 0.6$  W and the example shown here is for a helium flow of 1 slm.

nozzle. The lines along the gas stream indicate the trajectories of the NO particles to guide the eye. The distributions of NO appear to be quite similar

close (keep in mind that the origin of the coordinate system is located two millimeters in the effluent) to the outlet which is reasonable due to the shielding of the gas stream from the surrounding air as found and plotted in figure 4.10. The interaction with the surrounding is not much pronounced, hence the distribution when escaping the jet is significantly determined by the NO production inside the jet which is independent of the environment except for the back diffusion into the channel which can have minor influences on the reaction kinetics in the last couple of millimeters. The distributions close to the nozzle have a radial symmetric structure with Gaussian shapes in both,  $x$ - and  $y$ -direction (see figure 4.24). The rectangular shape of the nozzle exit is not visible which can be understood by the fast destruction of higher radial modes that would be necessary to build up a rectangular profile.

The measured distances at  $z = \{0, 20, 40\}$  are important. From figure 4.10 it can be seen that around  $z = 15 - 20$  mm the air intrusion into the channel becomes significant and hence the NO is deflected from its original path, causing strong deviations from the original Gaussian profile when leaving the jet. In the air atmosphere at  $z = 20$  mm it can be seen that slight turbulence like behavior sets in and the equidensity lines are not as laminar as close to the nozzle.

However, a pronounced maximum is still visible and clearly located in the center of the radial pattern. That behavior has changed when moving further away from the jet nozzle to  $z = 40$  mm. Here the distribution is strongly perturbed due to collisions and diffusion. No clear pronounced maximum is visible. Comparing the distributions to the ones measured in the helium atmosphere clear differences are visible. In this atmosphere, the pattern stays very similar at great axial distances compared to the one when leaving the jet. The distribution expands radially mainly due to diffusion but the maximum is still located clearly at the center and the equidensity lines are laminar. As evaluated in section 4.3.2, the radial transport in helium is mainly driven by the diffusion of NO particles. For the plots shown in 4.20, the diffusion equation was solved in one dimension with a Gaussian distribution as the initial condition, while the times of the position in  $z$ -direction was calculated by the stream velocity and Stokes friction (see equation 4.41), hence this calculations produce 2d maps at different  $z$ -positions resulting in a pseudo 3d distribution

with a plug flow like mechanism. However, for the density maps in the  $xy$ -plane the diffusion equation can be solved numerically in 2 dimensions with the same time steps in  $z$ -direction as before, to obtain a pseudo 3d profile and compare that with the measurements. In order to do so, the 2-dimensional diffusion equation according to

$$\frac{\partial}{\partial t} n_{\text{NO}}(x, y, t) = D \left( \frac{\partial^2}{\partial x^2} n_{\text{NO}}(x, y, t) + \frac{\partial^2}{\partial y^2} n_{\text{NO}}(x, y, t) \right). \quad (4.42)$$

The equation can then be numerically solved by discrete functions according to  $x = i\Delta x$ ,  $y = j\Delta y$  and  $t = k\Delta t$  and applying a finite difference approximation as (for convenience purpose we will write  $n := n_{\text{NO}}(x, y, t)$ )

$$\frac{n_{i,j}^{(k+1)} - n_{i,j}^{(k)}}{\Delta t} = D \left[ \frac{n_{i+1,j}^{(k)} - 2n_{i,j}^{(k)} + n_{i-1,j}^{(k)}}{(\Delta x)^2} + \frac{n_{i,j+1}^{(k)} - 2n_{i,j}^{(k)} + n_{i,j-1}^{(k)}}{(\Delta y)^2} \right] \quad (4.43)$$

and from that the state of the density system at the next time step  $k + 1$ , the expression  $n_{i,j}^{(k+1)}$  can be calculated by

$$n_{i,j}^{(k+1)} = n_{i,j}^{(k)} + D\Delta t \left[ \frac{n_{i+1,j}^{(k)} - 2n_{i,j}^{(k)} + n_{i-1,j}^{(k)}}{(\Delta x)^2} + \frac{n_{i,j+1}^{(k)} - 2n_{i,j}^{(k)} + n_{i,j-1}^{(k)}}{(\Delta y)^2} \right]. \quad (4.44)$$

and here it can be shown that the maximum time step we can apply in order to keep the process stable is given by

$$\Delta t = \frac{1}{2D} \frac{(\Delta x \Delta y)^2}{(\Delta x)^2 + (\Delta y)^2}. \quad (4.45)$$

The numerical treatment of the diffusion equation allows the investigation of different initial distributions of the NO density. In this case two were investigated. Firstly a top hat distribution. This means that the NO distribution is constant  $n = \hat{n}$  across the jet nozzle. However, applying this condition, it was found that the circular Gaussian distribution measured at  $z = 2$  mm, which is the first measurement distance (see figure 4.11), could not be reproduced by pure diffusion within the first 2 mm. Therefore, a 2-dimensional Gaussian

distribution function is chosen as the initial condition that reads

$$n(x, y, t = 0) = \hat{n} \exp \left\{ \frac{(x - x_c)^2 + (y - y_c)^2}{c^2} \right\} \quad (4.46)$$

with the initial density,  $\hat{n}$ , obtained from the extrapolation of the exponential 1d fits performed in figure 4.12 and the width of the distribution that was estimated by the cross section of the jet nozzle and former spatial resolved measurements of the atomic oxygen distribution as  $c = 0.5$  [110]. The diffusion coefficient for NO in helium is again taken as  $D_{\text{NO,He}} = 62.4 \text{ cm}^2 \text{ s}^{-1}$ . The initial distribution is shown in figure 4.23. Furthermore, Dirichlet boundary conditions are applied, hence  $\forall (x, y) \in \partial\Omega : n(x, y) = 0$  where  $\partial\Omega : x, y \in [-4, 4]$ . The domain is chosen to be bigger as the experimental investigated area to avoid suppression of the densities near the borders of the domain due to the boundary conditions. The results and the comparison of the calculated and

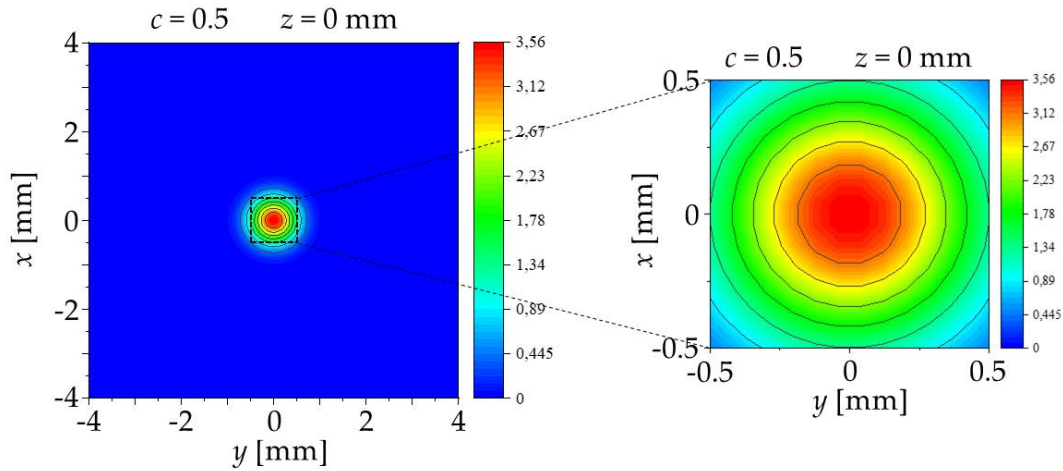


**Figure 4.23.** Initial NO distribution applied for the solution of the 2d diffusion equation. The left image shows the whole modelling domain with the boundary  $\partial\Omega$ , whereas the right image is a zoomed view according to the cross section of the jet nozzle.

the experimental profiles can be seen in figure 4.24 (i) and (ii), respectively. The movement of the particles in  $x$ -direction is accounted for by the buoyancy obtained from equation 4.24. Very good agreement is found between experiment and simulation for all axial distances. The distributions in the radial directions are in good agreement with the Gaussian distributions obtained from the diffusion equation, both when it comes to absolute densities and the width of the distribution. The experimental distributions show

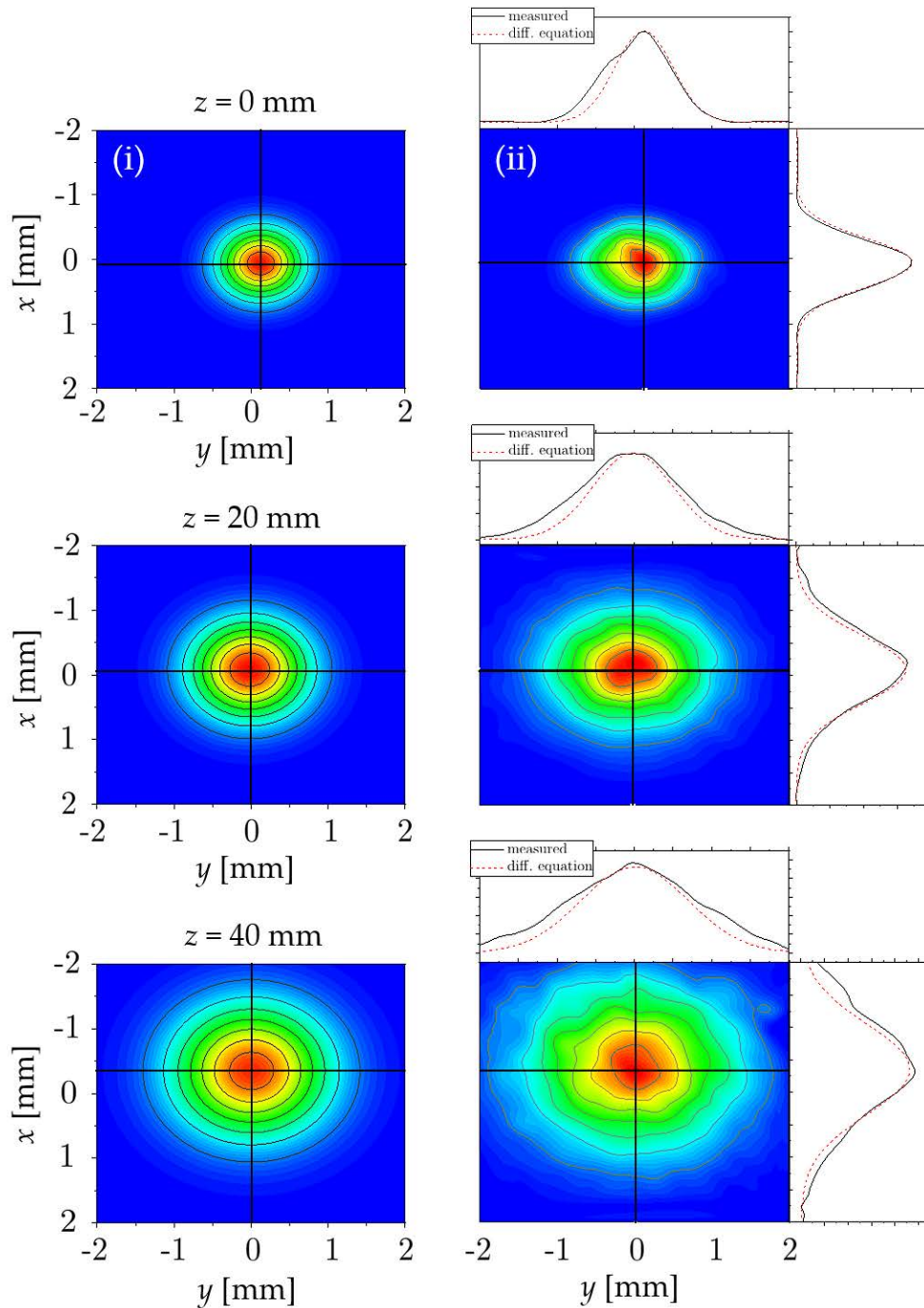


**Figure 4.24.** 2-dimensional density plots obtained from (i) the solution of the diffusion equation and (ii) the experiment, where the jet is operated in a controlled helium atmosphere. Attached are the radial profiles in  $x$ - and  $y$ -direction from all plots extracted along the lines shown in the respective images. Here the red dashed lines show the results from the simulation, while the black line is the extraction from the experimental data.

slightly higher FWHMs in  $y$ -direction. This is owed to the fact that this is the direction of the propagation of the excitation laser. Hence, in this direction the spatial resolution is not as good as in the  $x$ -direction, because the NO molecules can be excited from the whole Rayleigh length, which can be a few cm. Then, the spatial resolution is purely defined by the optical detection system. This behavior is completely different in the air atmosphere, as observed in figure 4.22.

While in air at small axial distances, the initial distribution is equal to the one in helium, where Gaussian profiles are observed in both radial directions, at greater axial distances the behavior changes. In air, a pure random distribution is measured where no Gaussian profiles can be seen, while in the helium atmosphere still a Gaussian profile is apparent with wider FWHM. This is also plotted in figure 4.17 for the  $y$ -direction where one can clearly see the widening of the Gaussian profiles with increasing axial distance that is now also seen in the  $x$ -direction. This is an important finding for applications of the COST-Jet. If treating a sample it is crucial to have knowledge about the absolute densities and their respective distribution in order to avoid any damage due to an excess of certain reactive species for a given sample. Therefore, if treating, for example biological samples in an open ambient air environment, the experimentalist should keep in mind that for large axial distances, a turbulent behavior sets in and the treated spot is not treated with a sharp local maximum of given absolute values but rather with a random distribution as seen in figure 4.22. In the controlled helium atmosphere in contrast, where non-biological surfaces can be modified, even at larger axial distances, the surface is treated with a well defined Gaussian distribution of NO particles with a sharp maximum in the center of the radial symmetric distribution.

### 4.3.3 Summary of LIF measurements in the free effluent

In the previous sections, LIF was used to determine absolute densities of NO and the density distributions with 3-dimensional spatial resolution. The experiments were performed in two distinct atmospheres (i) the jet is operated into open air, i.e., the environment consists of air in the lab and (ii) the chamber was pumped down and filled up by the jet so that the experiments were performed in He+0.5% synthetic air admixture at a constant pressure of

around  $p \approx 980$  mbar. The optimum admixture for maximum NO production was found to be a 0.5% air admixture with a ratio of  $N_2/O_2=8/2$  which is commonly considered as synthetic air. However, the maximum absolute NO densities were found for a different admixture of  $\Phi_{N_2} = \Phi_{O_2} = 5$  sccm. This is owed to a different power consumption and different stability regimes of the plasma source, where higher powers can be sustained without the jet transitioning into an arc like mode that can thermally destroy the jet. Those insights provide the opportunity to tailor the NO densities depending on the application the jet is used for.

From the time resolved LIF signal the natural lifetime of the  $NO(A^2\Sigma^+)$  state was measured and compared to a theoretical calculated lifetime. From this measured natural lifetime and measured lifetimes in different atmospheres with different quenching molecules the quenching coefficients for different molecules were determined. Furthermore, based on these measurements it was calculated how much air diffuses into the helium gas stream escaping the jet which leads to a destruction of NO.

3-dimensional density maps of NO were measured in the different atmospheres and a strong buoyancy of NO was observed. Since  $\rho_{NO} > \rho_{air}$  this is contra-intuitive and suggests a coupling of NO to the helium flow. This was verified by a simple model, by calculating the helium trajectories in an air taking into account Stokes friction and comparing them with the ones of NO. Excellent agreement was found. The elastic and inelastic collisions in the air atmosphere were found to affect the NO distributions significantly by deflecting and destroying them from their original Gaussian distribution that is observed at small axial distances when the NO particles just leave the jet. This is different in the helium atmosphere, since the density of helium is much smaller as compared to air and therefore NO particles are less deflected from their original path. Additionally, helium is a much slower quencher than oxygen that is contained in the air atmosphere. The breakup of the Gaussian distribution to a random one is not attributed to an excess of the critical Reynolds number, since for all investigated flows it stays well below the critical value of  $Re < Re_c \approx 2300$ , but to collisions and momentum transfer that is much more pronounced in air. The occurrence of turbulence like behavior and the breakup of the Gaussian distribution is an important finding for any

application. If a biological sample is treated, it is usually not possible to do it in a controlled atmosphere. The experimentalist must be aware of the fact that in air environment turbulence like patterns evolve and a certain axial distance should not be exceeded in order to have a well defined treating spot on the surface.

Knowledge about the species distribution and the possibilities to tailor it is an important aspect for possible applications. However, jets are most often used to treat some type of samples, such as solids. The interaction with the samples might induce chemical reactions that modify the distribution as compared to the free effluent. Therefore, it is important to have both, the measurements in the free effluent and subsequently the measurements in front of the surface to reveal the influence that the surface has on the density dynamics. In this context, certain materials are more interesting over others, due to their physical properties, being beneficial for catalytic processes. Here the materials, that are investigated are therefore chosen to be Ti, Cu, Al, Fe, and Au [111, 112, 113, 114, 115]. The samples are created with a magnetron plasma source, in a High Power Impulse Magnetron Sputtering process onto a 1 mm thick silicon wafer. The deposition rate was measured via a Quartz Crystal Microbalance and by that the film thicknesses were tailored by varying the sputtering time.

## 4.4 NO distribution in front of surfaces

### 4.4.1 Preliminary geometrical considerations

In section 4.1 NO densities were measured in the free effluent. Since the aim of the thesis is the simultaneous interaction between the COST-Jet, the laser and the surface, it is necessary to first investigate the sole interaction between the reactive plasma species and the sample. Therefore, the setup is modified according to figure 3.4. The surface normal of the sample is oriented with  $45^\circ$  towards the initial gas stream leaving the jet, to set it up close to the final geometry. When measuring reactive species close to the target, it is crucial to know the exact position of the surface. From equation 2.32 one can see that the total number of detectable fluorescence photons is directly proportional to the number of laser photons in the volume,  $N_{tot}^f \propto N_L n_0$ . Close to the surface, the vignetting of the laser sets in, hence the number of fluorescence photons in the laser focus reduces. This in turn leads to a decrease of the LIF signal, that needs to be compensated for in the evaluation of the experimental data. Therefore, some geometrical considerations are made in the following. The laser diameter of the excitation laser is about  $d_L \approx 2$  mm. The lens used for surface measurements has a focal length of  $f = 200$  mm and the targets have diameters of  $1'' = 25.4$  mm. A sketch of the geometry is shown in figure 4.25.

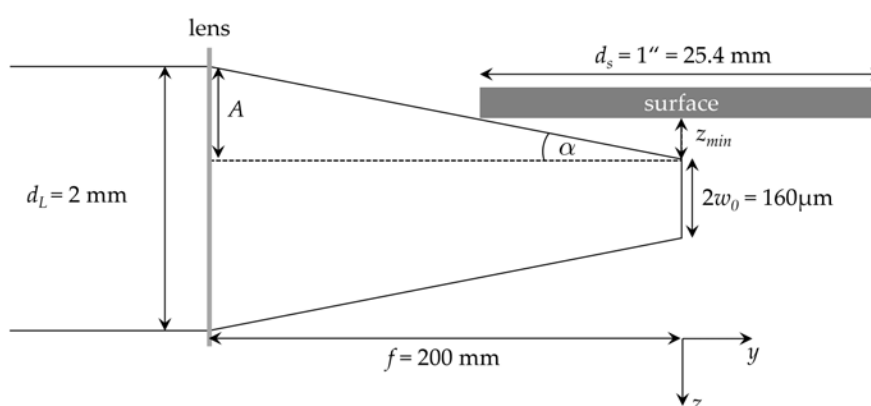


**Figure 4.25.** Geometry for the calculation of the minimum distance  $z_{min}$ , before the laser is cut by the surface for the measurements of the reactive species close to the sample (the geometry is not true to scale and is only for the calculation and visualization purpose).

The focus of the laser was adjusted, so that it is located at the center of the investigated sample at  $y = 0$ . With those assumptions, and assuming a symmetric focusing of the lens, the property  $A$ , which is the outer fraction of the laser beam that is first blocked, can obviously be calculated as

$$A = \frac{1}{2}(d_L - w_0) = \frac{1}{2}(2 \text{ mm} - 80 \text{ }\mu\text{m}) = 0.96 \text{ mm} \quad (4.47)$$

Therefore the angle  $\alpha$  can be calculated via

$$\tan(\alpha) = \frac{A}{f} \quad (4.48)$$

$$\Leftrightarrow \alpha = \arctan\left(\frac{A}{f}\right) = \arctan\left(\frac{0.96}{200}\right) \approx 0.27^\circ \quad (4.49)$$

Finally, the minimum distance,  $z_{min}$ , at which the surface starts obstructing the laser as it approaches the surface, is

$$\tan(\alpha) = \frac{2z_{min}}{d_s} \quad (4.50)$$

$$\Rightarrow z_{min} = \frac{d_s}{2} \tan(\alpha) = \frac{25.4 \text{ mm}}{2} \tan(0.27^\circ) \approx 60 \text{ }\mu\text{m} \quad (4.51)$$

The exact position of the surface can then be determined by considering the first point where the laser is completely blocked by the surface, hence  $I_{LIF} = 0$ . This point is denoted as  $z_0$  and subtracting the beam radius,  $z_0 - w_0$ , yields the exact position. An example for the determination of the position of the surface for a one-dimensional density distribution is given in figure 4.26. The point where the laser is completely covered by the surface is determined by the first point on the  $z$ -axis, where the LIF intensity drops to zero (i.e.,  $n_{NO} = 0$  in the graph), taking into account the background noise. From this point the sum of the minimum distance that the laser can be adjusted close to the surface without getting cut, by the geometrical considerations shown in figure 4.25,  $z_{min}$  and the beam diameter  $2w_0$ , obtained from the measurements shown in figure 3.2 are subtracted. This in turn means, that for all measurement points in the interval  $z \in [z_c, z_s]$ , where  $z_s$  is the position of the surface and  $z_c$  is the first position where the surface starts to obstruct the laser, a correction factor needs to be multiplied to compensate for the blocking of the laser and the resulting decrease in the number of photons that contribute

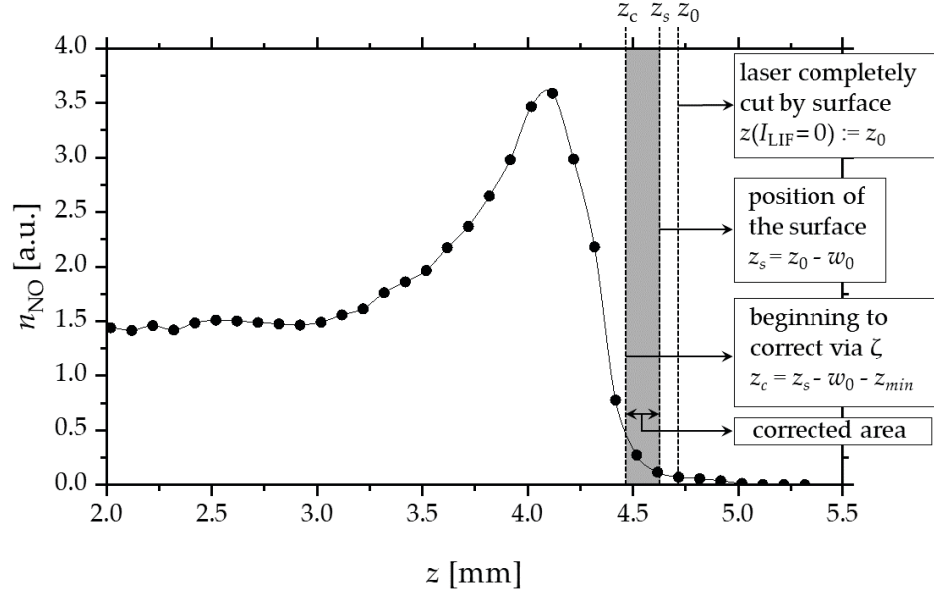


**Figure 4.26.** One-dimensional NO distribution in front of a surface. The exact position is determined by geometrical thoughts according to figure 4.25.

to the LIF signal. The correction factor can be calculated, assuming a circular excitation laser cross section that is obstructed by the surface. The factor,  $\zeta(z)$ , to compensate for the photon loss by the vignetting of the laser can be calculated by a circular segment according to [116]

$$\zeta = \left\{ 1 - \underbrace{\left[ w_0^2 \cdot \arccos \left( 1 - \frac{z}{w_0} \right) - (w_0 - z) \sqrt{2w_0z - z^2} \right]}_{:=A_c} \right\}^{-1} \quad (4.52)$$

where  $z$  is the distance of the fraction of the circle that is being blocked by the surface and  $A_c$  is the area being blocked. Before evaluating and calculating the correction factor this area needs to be normalized. Figure 4.27 shows a plot of the correction factor for the  $z$ -interval where the factor is needed. In this interval the LIF signal needs to be corrected according to  $I_{\text{LIF}} = \zeta \cdot I_{\text{LIF}}^{\text{meas}}$ , where  $I_{\text{LIF}}^{\text{meas}}$  is the measured signal in the experiment. This correction is done for all the following data in front of the surface that are presented in this thesis. However, one should keep in mind that the considerations made here are only valid for a top hat laser beam profile.

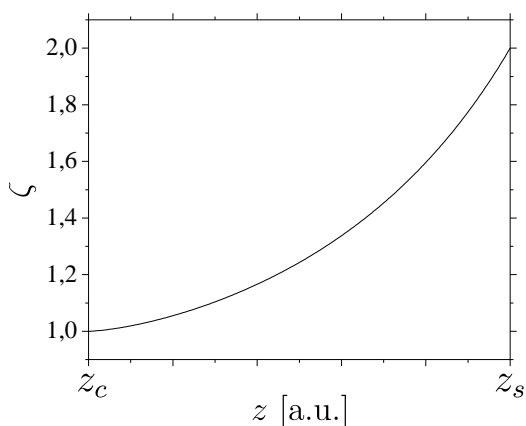


**Figure 4.27.** Correction factor  $\zeta$  used for the correction due to the cutting of the laser for measurements close to the surface.

Hence, this correction factor is an approximation towards the real situation, where the laser beam profile is ideally Gaussian, although in experiments often strong deviations from a Gaussian laser profile are found. These calculations are just preliminary geometrical considerations to prepare the data for evaluation of the density distributions in front of the surfaces and correct for vignetting effects that occur during the measurements.

#### 4.4.2 Density profiles of NO in front of surfaces

In this section 1-dimensional density profiles of NO in front of different surfaces are presented. The jet was operated at a power of  $P_{diss} = 0.6$  W. The investigated samples were mounted onto the holder as shown in figure 3.4, and then slightly moved towards the jet until the sample touched the quartz glass covers. Subsequently, the sample was removed a couple of mm by hand and the distance was then determined by the method described in section 4.4.1. A stopper was mounted onto the metal rods, so that the sample holder was at the exact same position for all measurements performed after the first distance calibration. The position of the surface was determined at  $z = 4.9$  mm.

Results of the 1-dimensional density profiles in front of the surface for different materials are shown in figure 4.28. It can be seen that up to approximately  $z \approx 3$  mm the surface does not influence the density distribution at all and the profile of the reactive species resembles the distribution in the free effluent. However, when  $z > 3$  mm the densities start to deviate from the original distribution. It is observed that in the case of an Al target the density starts to rise monotonously up to a local maximum that is located approximately 0.5 mm in front of the surface. For all other materials the increase of the density starts less steep and also the absolute density in the local maximum is not as pronounced as in the Al case. The double peak structure in the

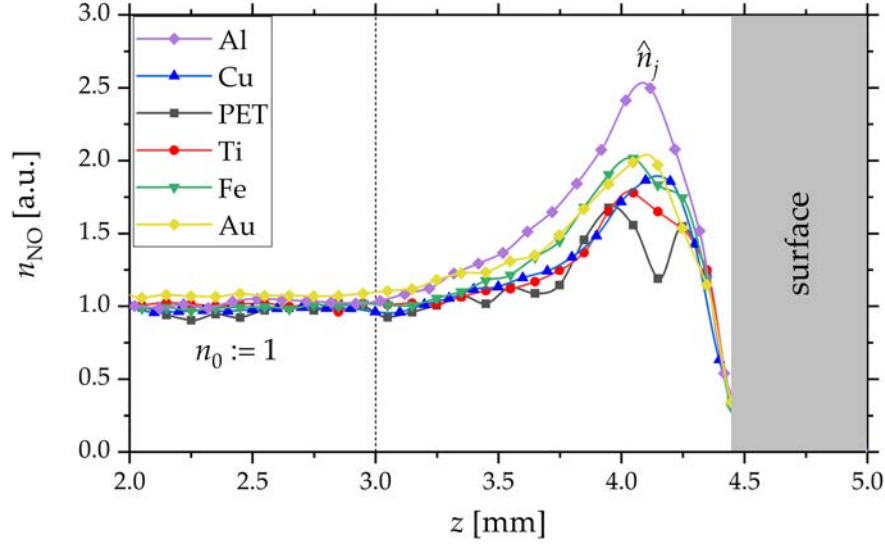


**Figure 4.28.** 1-dimensional density profiles of NO in front of different surface materials.  $n_0$  denotes the base density where it is not affected by the surface and  $\hat{n}_j$  is the maximum density close to the surface. The dotted line shows the point where the deviation begins.

PET case is most probably an artifact arising from the fluorescence emitted by the PET substrate itself. Therefore, a background signal is subtracted from the original signal that might induce this artifact structure.

However, the fluorescence of the respective transition is radiated into the whole solid angle,  $4\pi$ . This in turn means, that as the laser approaches the surface, there is a possibility that the fluorescence light is reflected from the surface and is then recorded by the detection system. This would lead to an additional signal and apparent higher densities. To account for this effect the reflectance of the different materials is shown in figure 4.29. The spectral reflectance is calculated using Fresnel's equation [117]:

$$R_\lambda(n, \kappa) = \frac{(n-1)^2 + \kappa^2}{(n+1)^2 + \kappa^2} \quad (4.53)$$

where  $n = n(\lambda)$  and  $\kappa = \kappa(\lambda)$  are the wavelength dependent optical constants of the materials. The  $n$  and  $\kappa$  values are taken from [118, 119, 120, 121]. It is striking that the spectral reflectance of Al is more than two times higher compared to all the other investigated materials.

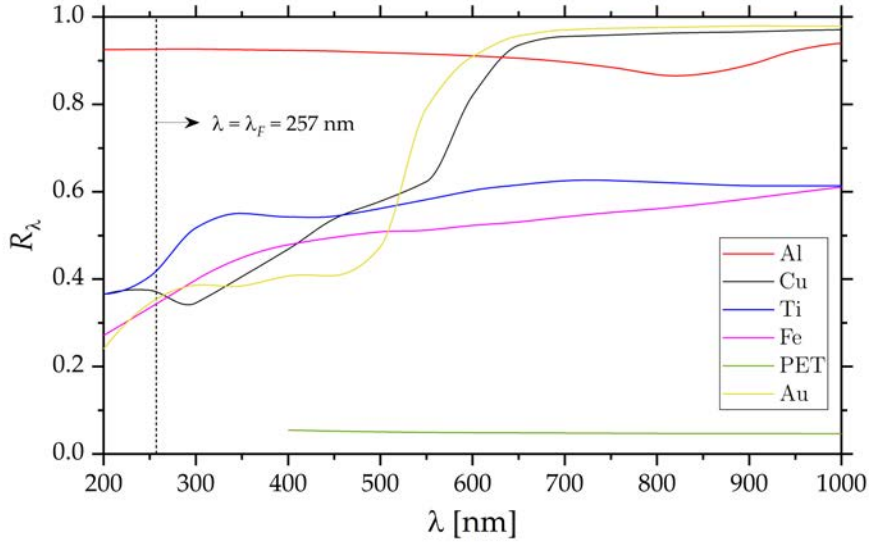


**Figure 4.29.** Spectral reflectance,  $R_\lambda$  for the different investigated surface materials calculated from equation 4.53. The fluorescence wavelength that is detected in the experiments is shown as a dotted vertical line at  $\lambda_F = 257$  nm.

The reference density unaffected by the surface for  $z \in [2, 3]$  mm is denoted as  $n_0$ , which is equal for all materials and was here defined as  $n_0 [\text{a.u.}] := 1$ , to easily compare the rise to the reference density. The maximum density at the peak for each material is denoted as  $\hat{n}_j$ . By evaluating the ratio  $n_0/\hat{n}_j$  (where the index  $j$  stands for the different materials) one obtains the fractional increase of the density in front of the surface. Table S3 shows the different values for  $n_0/\hat{n}_j$  depending on the materials. To account for the possible artifact of reflection from the surface the geometry of the setup with a focus on the detection system is shown in figure 4.30. Here  $d_A$  is the aperture of the detection lens,  $f_{det}$  is the focal length of the detection system used for the surface experiments and  $z_S$  is the distance of the laser and the detection focus in  $z$ -direction, hence the LIF source, from the surface. Due to the spectral reflectance of the different materials,  $R_\lambda$ , the fluorescence light that is emitted from the laser focus is reflected and the reflected light is then detected by the system.

The effect of this reflectance is calculated using a ray optics simulation tool [122]. In these simulations two approximations are made: Due to the fact that

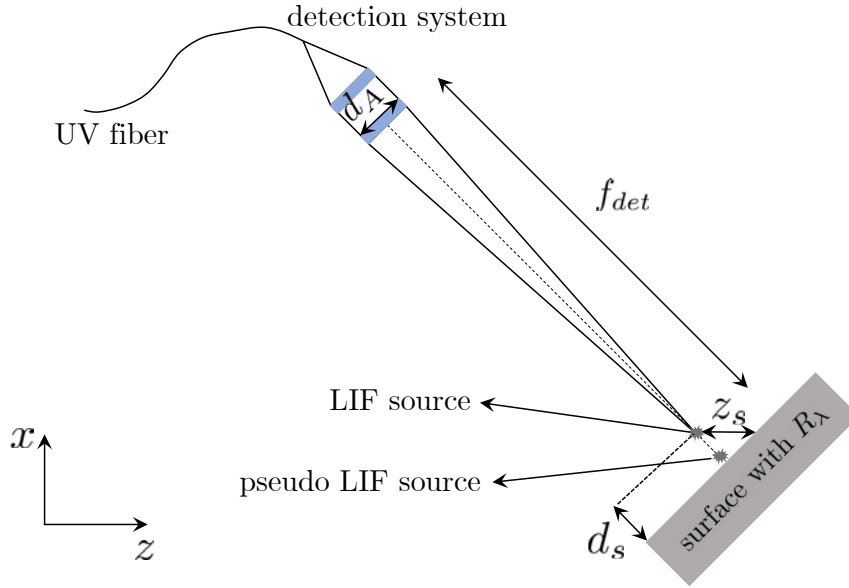


**Figure 4.30.** Zoomed view of the geometry of the detection system used for the surface experiments. Shown is the two lens detection system with a focal length of  $f_{det} = 48$  mm and an aperture of  $d_A = 10$  mm. The distance of the focus of the detection system and the excitation laser, hence the LIF source, from the surface with spectral reflectance in  $z$ -direction  $R_\lambda$  is denoted as  $z_s$  and the axial distance from the surface as  $d_s$

the focal length of the detection system ( $f_{det} = 48$  mm) is much larger as compared to the axial distance from the surface ( $d_s = (\sqrt{2}/2) \cdot z_s \approx 2$  mm), hence  $f_{det} \gg z_s$ , the reflected signal from the surface is assumed to be an additional point source. Due to the same fact, the imaging error due to defocusing of the pseudo LIF source (reflected signal from the surface) is neglected. However, it should be noted that this artifact exists and the real intensity that is detected by the system will be slightly lower than the one calculated in the simulations. The values for the reflectance at the fluorescence wavelength  $\lambda_F = 257$  nm are calculated according to equation 4.53. For the simulations they are:  $R_{Al} = 0.93$ ,  $R_{Cu} = 0.37$ ,  $R_{Ti} = 0.42$ ,  $R_{Fe} = 0.34$  and  $R_{Au} = 0.36$ . The simulations for the PET target are not performed since the reflectance is negligible small. Furthermore, PET is known to exhibit transitions that can lead to fluorescence from the material itself and the peak in front of the surface is most likely caused by this effect. If the increase of the density is a pure artifact of the reflection of the fluorescence light from the surface into the detection system, then the ratio of the maximum to the base density should obey the

TABLE S3: Ratios of the maximum densities that develop in front of the surface,  $\hat{n}_j$ , and the undisturbed densities,  $n_0$ . Furthermore, the spectral reflectances (+1) of the respective materials at the fluorescence wavelength and the integrated densities from the point of deviation ( $z = 3$ ) up to the surface  $z = S_b$  are shown.

mat. ( $j$ )	$R_\lambda(257 \text{ nm}) + 1$	$\hat{n}_j/n_0$	$\int_3^{S_b} dz [n(z) - n_0] [\text{m}^{-2}]$
Al	1.93	2.52	523±9
Cu	1.37	1.94	1054±16
Ti	1.42	1.81	519±16
Fe	1.34	2.00	1067±8
PET	≈ 1	1.69	512±21
Au	1.36	1.91	1054±32

following relation:

$$\frac{\hat{n}_j}{n_0} \approx R_\lambda(257 \text{ nm}) + 1 \quad \text{for } z_s \ll 1. \quad (4.54)$$

Furthermore it should also be noted that even under the ideal approximations mentioned above the ratio of the maximum to the base density can never exceed 2, therefore

$$\frac{\hat{n}_j}{n_0} \leq 2. \quad (4.55)$$

Figure 4.31 shows the results from the simulations. It can be seen that due to the approximations of a perfect image and an additional pseudo point source at the surface, for  $z_s = 0$  the results of  $\hat{n}_j/n_0$  follow equation 4.54. As the distance gets larger, the ratio  $\hat{n}_j/n_0$  decreases. However, it is observed, that even at  $z_s = 5 \text{ mm}$  the value is only about 7% lower as compared to the value at  $z_s = 0 \text{ mm}$ . Comparing these results against the measurements shown in figure 4.28 it can be deduced that the reflection of the LIF signal from the surface into the detection system can increase the signal by a factor  $R_\lambda(257 \text{ nm}) + 1$ , nevertheless it cannot explain solely the steep increase of the measured densities in front of the surface. This is also summarized in table S3.

Furthermore, it can be seen that the ratio exceeds a factor of 2 in the case of

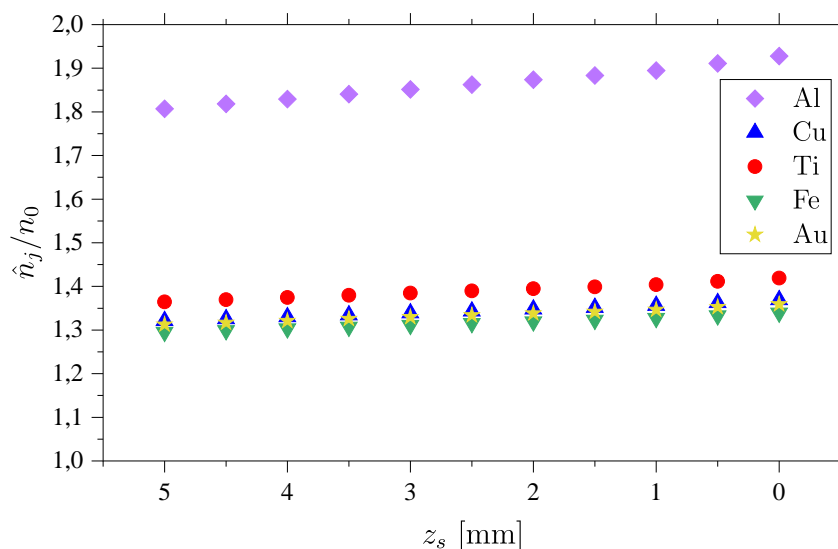


**Figure 4.31.** Results of the ray optics simulation for the reflection of the LIF signal from the surface. Shown are the results of the different materials and the fraction of the maximum density in front of the surface to the undisturbed base density solely caused due to a “pseudo LIF source” by reflection at the surface for different distances (see figure 4.30).

an Al target. This cannot be explained solely by reflection, since the reflection cannot be larger than the light source itself. Therefore, inequality 4.55 is violated and the result non-physical. This means that the reflection may partly explain the maximum in front of the surfaces but it is not the sole reason.

To properly investigate the density distributions in front of the surface a proper model is needed that takes into account the complex dynamics of molecule surface interactions, more precisely spoken the whole interaction between the gas phase species and the surface. However, such a model is not available at this time. So in the following qualitative mechanisms to produce NO at a surface are presented. If a reactive particle approaches a surface, in general three mechanisms are possible.

- It might either be reflected from the surface and travel back into the bulk with a probability  $r$
- it might stick to the surface where it can react with surface atoms and molecules to form chemical bonds and undergo chemical reactions with

a sticking probability  $s$

- it might react at the surface and form volatile products with a probability  $\beta$

where the relation  $r + s + \beta = 1$  holds. If the latter two events happen and the particle either sticks to the surface or forms products that desorb back into the gas phase the particle is lost. This loss is described by the surface loss probability  $\gamma$  that can then be written as  $\gamma = \beta + s = 1 - r$ .

In order to accurately evaluate and investigate the density distributions in front and on the surface, a kinetic model for surface processes would be needed. Gordiets et al. developed a kinetic model that includes the most relevant reactions involving nitrogen and oxygen species that are relevant for NO chemistry [123]. They took into account the reactions as shown in table S4. In this table the index  $f$  and  $s$  denote physisorbed and chemisorbed particles, respectively.

TABLE S4: Reactions taking into account the relevant surface kinetics for the NO production at surfaces. Here  $S_v$  and  $F_v$  denote vacant active chemi- and physisorption sites.

no.	reaction
1	$N + S_v \rightleftharpoons N_s$
2	$N_f + O_s \rightarrow (NO)_s + F_v$
3	$N_s + O_f \rightarrow (NO)_s + F_v$
4	$O + N_s \rightarrow (NO)_s$
5	$NO + S_v \leftrightarrow (NO)_s$
6	$(NO)_s + O \rightarrow (NO_2)_s$
7	$(NO)_s + O_f \rightarrow (NO_2)_s + F_v$
8	$NO + O_s \rightarrow (NO_2)_s$

At this point, due to the complexity of the surface kinetics, it is rather hard to make any predictions without an appropriate model. The typical mechanisms that occur are the interaction between chemisorbed  $N_s$  and  $O_s$  atoms and gas phase species of O, N and NO, which is the Eley-Rideal mechanism

or they can react with physisorbed  $N_f$  and  $O_f$ , the Langmuir-Hinshelwood path. The reactions, however, are not independent from each other, but are a coupled system, where one reaction can increase or decrease the reactivity of another. One of the many possible reactions that could lead to the increase of NO in front of surfaces is the pathway of chemisorbed  $NO_s$  that either directly desorbs and increases the gas phase density or it can react with O and  $O_f$  via reactions 6, 7 and 8. The created  $(NO)_2$  in turn can effectively desorb and eventually create gas phase NO via the reactions  $O+NO_2 \rightarrow NO+O_2$  and  $N+NO_2 \rightarrow NO+NO$ . However, this is just one possibility of many possible reaction pathways. The reaction probability of surface reactions can be expressed as

$$K_i = D_M K_i^0 \exp \left\{ -\frac{E_i}{T_W} \right\} \quad (4.56)$$

where  $K_i^0 \in [0, 1)$  are dimensionless steric factors,  $D_M$  the surface diffusion coefficients,  $E_i$  [K] the activation energies of the respective chemical processes and  $T_W$  the wall temperature. Furthermore, the reactions depend on the density of the reaction partners, hence the wall losses of the gas phase species. This in turn is strongly dependent on the wall loss probabilities  $\gamma_j$ . To adequately investigate the kinetics, a model with the above described parameters is needed.

Figure 4.32 shows (a) a side view of the 2-dimensional density distribution of NO in front of a Ti surface compared to (b) the pure helium flow, without plasma discharge, expanding from the nozzle towards the surface. The NO distribution is measured in a 1 slm He+0.5% gas mixture with  $P_{diss} = 0.6$  W in air environment. The pure He flow is modeled without plasma discharge, simply by the expansion of 1 slm pure helium into air. This is done by numerically solving the Navier-Stokes equation via COMSOL. It can be seen that the NO particles are not reflected by the surface but stick close to it, streaming upwards the 45° tilted Ti target. The maximum in front of the surface can be seen as shown in the 1-dimensional density profiles in figure 4.28. As discussed, this maximum is partly caused by reflection of the LIF signal into the detector. The high signal is not only visible at the impinging point of the species on the  $x = 0$  axis but remains high along the surface until it eventually decreases. Neglecting the absolute signal and just comparing the shape of the distribution with the fraction of helium calculated by the model it can be seen

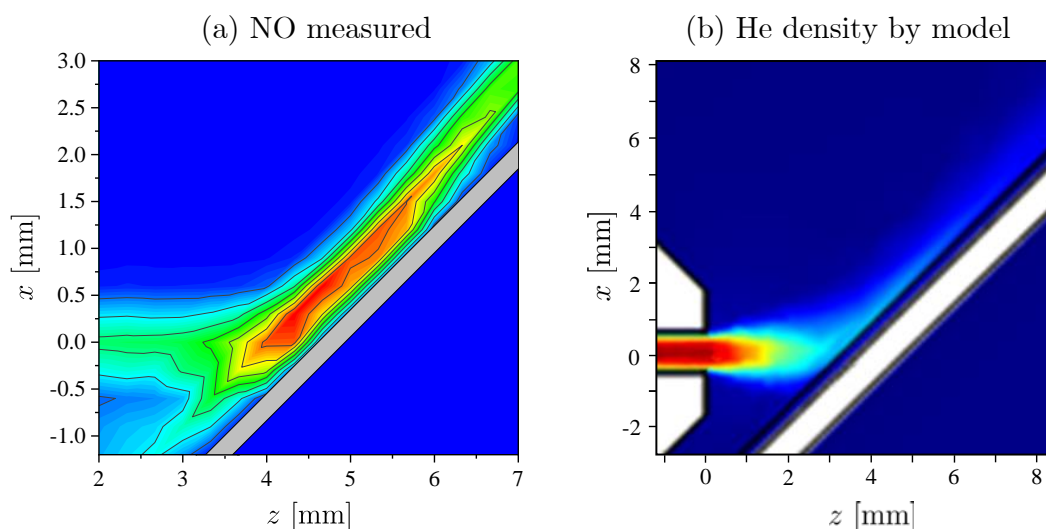


**Figure 4.32.** (a) 2-dimensional NO distribution in front of a Ti surface compared to (b) the fraction of helium in the effluent as modeled. The NO is measured in a 1 slm He+0.5% gas mixture, while the flow in the model shows the pure helium flow coming from the nozzle to the surface. The density is scaled with a colormap according to blue for low density to red with the highest density.

that both look very similar. This is a verification that not only in the free effluent the NO particles are coupled to the helium flow, but this coupling also persists at the surface.

This can also be seen in a pseudo 3-dimensional NO distribution that was also measured in front of a Ti target and is also compared to the He fraction modeled by COMSOL. This can be seen in figure 4.33. The experimental parameters are the same as those of the measurements shown in figure 4.32 which is also the case for the helium fraction results from the model. As observed in the 2-dimensional case shown in figure 4.32, the NO distribution at the surface resembles the helium distribution calculated by the model. It should be taken into account that the different slice images shown in 4.33 (a) are normalized to the maximum value of each respective slice in the image. However, it can be seen that the NO particles radially expand as they flow upwards the sample, just as the helium does. The fact that the trajectories of NO is closely coupled to the helium flow, not only in the free effluent but also in front of the sample is an important finding. By this, the distributions, where the reactive particles interact with the surface, can be deduced

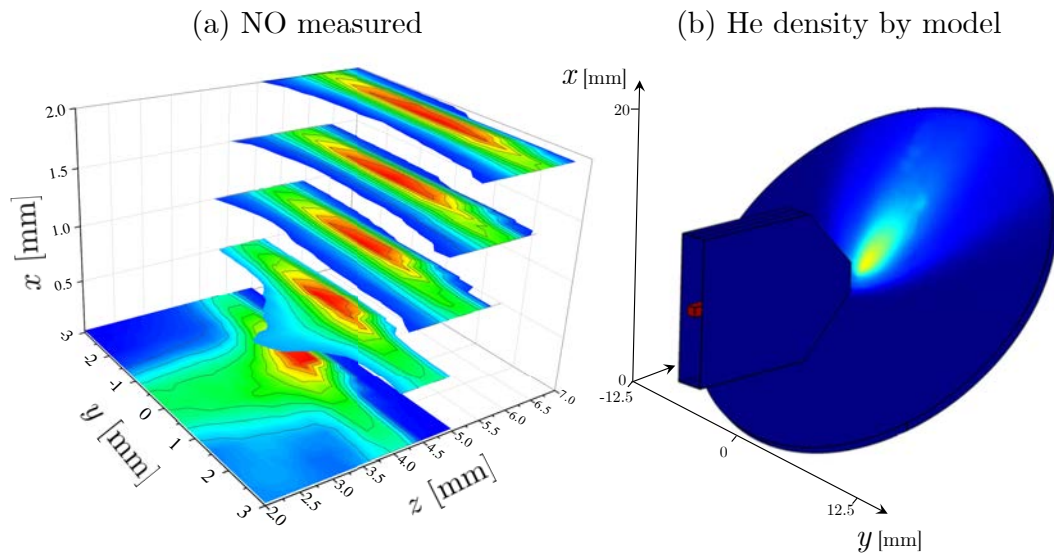


**Figure 4.33.** (a) Pseudo 3-dimensional distribution of NO in front of a Ti surface. (b) Helium fraction in front of the surface as calculated by the COMSOL model.

by modeling just the helium distribution towards the surface, neglecting any chemical reactions. This is possible with much less computational time and effort. However, it should be taken care of the fact that this only gives an approximation of the interaction area. The absolute densities, however, need to be measured or calculated with an accurate more complex model, to avoid damage of the sample by an excess of a critical density value.

#### 4.4.3 Summary of LIF measurements in front of surfaces

The (non calibrated) relative density distributions of NO have been determined in front of different surfaces of different materials. It was found that a significant maximum evolves millimeters in front of the surface that is dependent on the material. For aluminum this maximum is much more pronounced as for all other materials. This might be an effect of the reflection of the LIF signal from the surface itself, which is detected by the two-lens system, acting as a second pseudo LIF source that increases the signal. The spectral reflectance of aluminum at the detected wavelength is more than two times higher as compared to the other investigated materials. However, the increase is larger than twice the signal in the free effluent, which is impossible

to be caused by reflection only. Therefore, the increase cannot be explained solely by the reflectance of the surface. The detailed mechanism that causes the increase must be revealed by a kinetic model and further measurements that can deliver important input parameters for the model as for example the wall loss probabilities for the different materials.

The findings that the NO is closely coupled to the helium flow in the free effluent could also be verified and still holds at the surfaces. This was revealed by pseudo 3-dimensional NO measurements in the experiments that are compared to 3-dimensional models of the helium fraction in pure helium flow that expands from the nozzle towards the surface without any discharge ignited. The distributions are similar to each other and the NO as well as the helium stick close to the surface without being reflected.

## Chapter 5

# Laser-Surface interaction

The aim of the project is to investigate the simultaneous interaction between laser irradiation onto a surface and the reactive species expanding from the plasma jet. Therefore, it is important to understand the individual mechanisms first and bringing both parts together afterwards. While the former chapters dealt with distribution of nitric oxide in the free effluent and in front of surfaces, hence the plasma-surface interaction, in this chapter the focus will be on the laser-surface interaction independent from the plasma source.

### 5.1 Laser energy measurements

For laser-surface experiments it is important to know the energy of the laser pulse, since this is a crucial physical property that determines the result of the interaction and laser induced surface morphology. The laser energy is adjusted by the Glan-Taylor prism, that can be rotated  $360^\circ$  with an electrical controlled stage. The transmitted intensity according to Malus law is then given by

$$I(\alpha) = I_0 \cos^2(\alpha + \varphi) \quad (5.1)$$

where  $\alpha$  is the angle of the prism and  $\varphi$  an arbitrary phase. The power curve depending on the angle is shown in figure 5.1. The angle position to obtain the best LIPSS on the surface was found to be at  $230^\circ - 260^\circ$ . Here the average power is  $P_L = 30 - 120$  mW which, for a 20 Hz laser system equals a pulse energy of 1.5 – 6 mJ. For pulse lengths of  $\tau_p = 7$  ns the peak power during a pulse can be calculated as  $\hat{P}_L = E_p / \tau_p \approx 0.8$  MW.

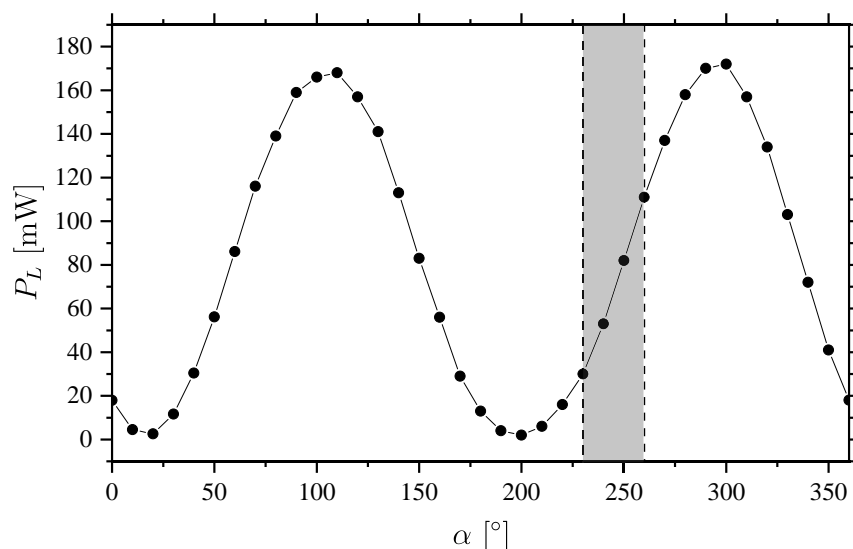


Figure 5.1. Power transmission curve of the Glan-Taylor attenuator.

## 5.2 Profile of the laser on the surface

One of the main parameters, when inducing structures on the surface is the intensity. The power is measured via a power-meter as shown in figure 5.1. However, this is the average power or, by knowledge of the frequency and pulse duration, the energy stored in a laser pulse. The intensity, however, is dependent on the spatial laser intensity distribution.

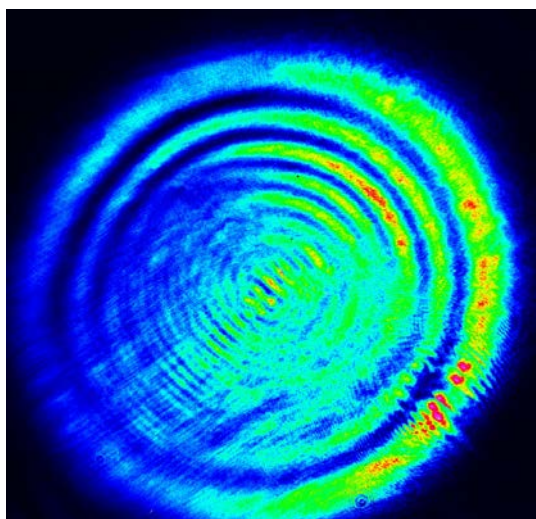
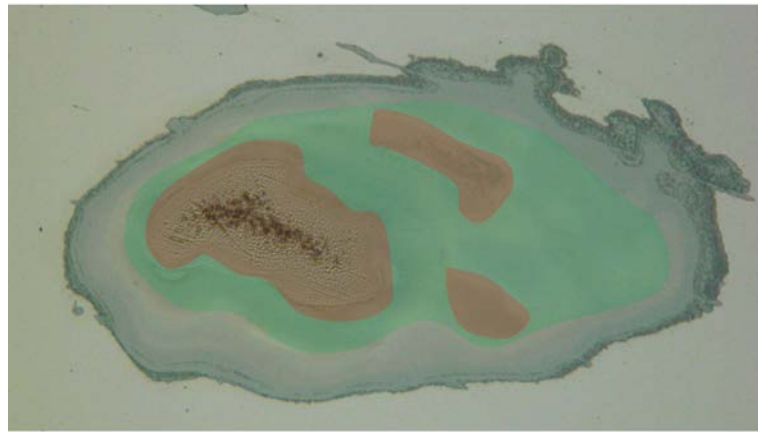


Figure 5.2. Profile of the Nd:YAG laser beam measured before the interaction with the sample. A strong inhomogeneity is observed.

Since no laser profiler was available during the experiments, the pattern that is induced on the surface gives a first indication on the laser beam profile. An example of such a typical pattern that was measured by the laser profiler, available after the experiments, is shown in figure 5.2. From this patterns it can be clearly seen that the profile shows a strong inhomogeneity. With such a profile the energy that is stored within one laserpulse is not equally deposited on the surface throughout the spot. The

energy is rather strongly localized in a small fraction of the spot and furthermore strong gradients along the interaction region on the surface will occur. This in turn leads to inhomogeneous heating of the surface and eventually inhomogeneous formation of the LIPSS patterns. This is a very important finding, since from those patterns it can be deduced that the intensity and, therefore, the temperature distribution can be significantly different at different locations inside the laser spot. This in turn is crucial for the development of the structures, since, for example, the temperature should not exceed beyond the melting point of the substrate to allow the formation of LIPSS.



**Figure 5.3.** Exemplary (colored) LSM image of a 20thick Ti surface exposed to 200 laser pulses. It can be seen that the shape is elliptic and different regimes of intensity are present. Red area: regime of high power, melting temperature exceeded and no detection of LIPSS. Green area: regime of proper intensity for LIPSS, LIPSS are detected

Figure 5.3 shows a spot of the surface that was irradiated under an angle of  $\theta_i = 45^\circ$ , hence the elliptical shape. It can be seen from the morphological properties in the LSM image that areas of different intensities are present. The different areas are indicated in the image by different colours. In the red area, an area of high intensity according to the right side of the laser distribution seen in figure 5.2, it can be seen that the intensity is so high that the melting temperature of the material is exceeded. In this area the material is melted and macroscopic unevenness evolve during the liquification and solidification processes with no LIPSS on the surface. The green area shows a proper

intensity for the LIPSS development, since in this area LIPSS are found and can be evaluated. The inhomogeneous intensity distribution on the surface might not solely be attributed to the characteristics of the laser itself, since the distribution can significantly differ from sample to sample, figure 5.3 only showing one example. Therefore, this might also be partly dependent on the initial state of the surface.

## 5.3 LIPSS

### 5.3.1 Analysis of the LSM/SEM images

The treated samples with the induced surface structures are analyzed via a Laser Scanning Microscope (LSM) or via Scanning Electron Microscopy (SEM). By these methods, the induced structures are visible and can be saved as an image. There are two different ways the images were analyzed subsequently. The first one is to transform the images into frequency space via a 2d Fast Fourier Transform (FFT) and then analyze the frequencies to obtain the information about the periodicity of the LIPSS. Furthermore, by back transforming into real space and applying filters to sort out certain frequencies the LIPSS can be separated from the background. An exemplary scheme of the analysis is shown in figure 5.4. To quantify the periodicity it is necessary to further investigate the spectrum in the Fourier space. By evaluating the intensities through the origin of the frequency domain and the distinct maxima, originating from the periodic structures in the real space, a plot of the form shown in figure 5.5 can be obtained. The periodicity of LIPSS can then be calculated by the relative distance of the frequency peaks

$$\Lambda_{\text{LIPSS}} = \frac{1}{d_{+1} - d_0}. \quad (5.2)$$

This method is well applicable when clear LIPSS were induced over a fairly large area and the peaks are clearly visible in Fourier space. This method yields a global information about all LIPSS that were induced in the investigated image. Therefore, if possible, this method is always preferred. However, it might be that LIPSS are only hardly visible on a small area. In this case the spectrum in Fourier space can be quite noisy and it can be difficult to obtain information about the LIPSS periodicity. In this case the evaluation of

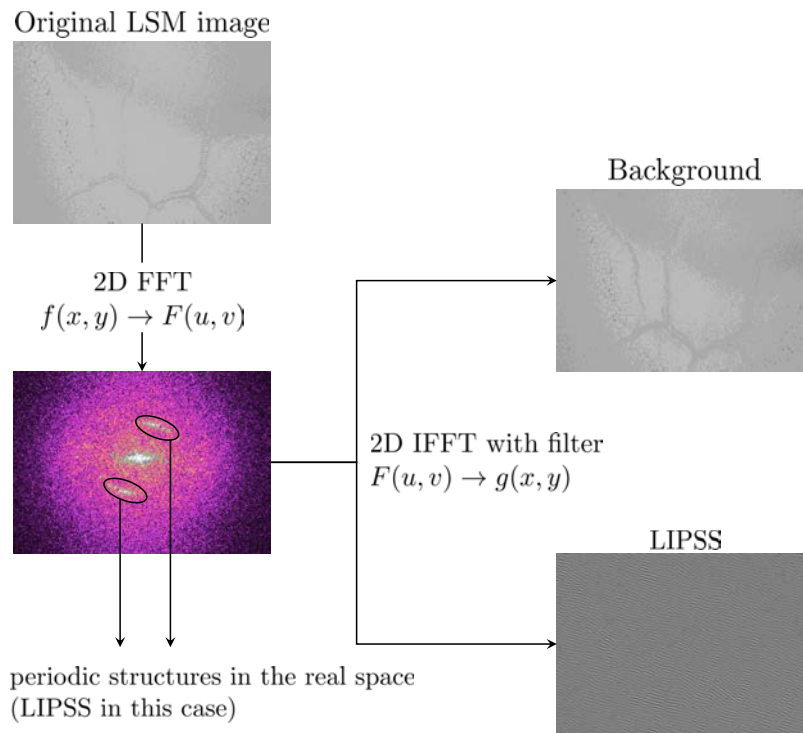


**Figure 5.4.** Exemplary scheme of the analysis of the surfaces via a 2d FFT. First the image of the surface in real space is transformed into the frequency space via a 2d FFT. By filtering certain frequency peaks in the Fourier space the periodic LIPSS structures can be separated from the background in order to get more detailed view of the periodic induced patterns.

choice is simply to plot the grey values of the image along the LIPSS on the image and identify the peaks next to each other and simply calculate the distance. This method, however, yields only local information about the LIPSS at the very spot the distance between the peaks of the grey values is evaluated.

### 5.3.2 LIPSS on substrates under $\theta_i = 0^\circ$ incident irradiation

With the afore mentioned techniques the periodicities of the LIPSS induced on the surfaces by the laser can be analyzed. Here different materials with different thicknesses have been irradiated, namely Ti (20, 60 and 100 nm), Cr (20 and 60 nm) and Cu (20 nm). The energy of the laser pulse for the different materials was chosen in a such way that the area of the induced structures on the surface was as large and homogeneous as possible. Here the energy ranged from 3.5 mJ for Ti samples up to 8 mJ for Cr samples. The substrates

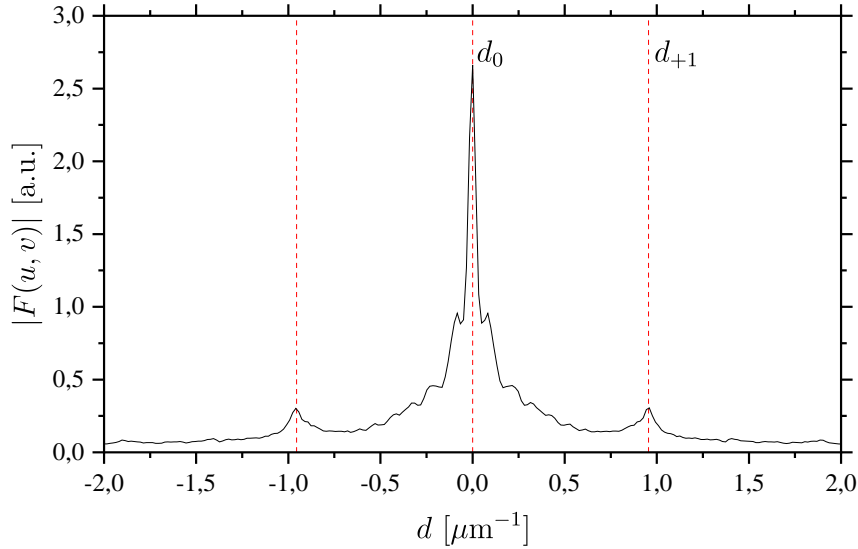


**Figure 5.5.** Magnitude spectrum in the Fourier space through the origin and the distinct peaks that represent the LIPSS. By taking the relative distance between the peaks the periodicity can be calculated.

are irradiated under an angle of  $\theta_i = 0^\circ$ . The results of the LIPSS periodicity can be seen in image 5.6. The dotted line represents the predictions by the different theories according to  $\Lambda_{\text{LIPSS}}(\theta_i = 0^\circ) = \lambda_L$ . As can be seen the measurement data from the experiment show good agreement with theory. One of the main difficulties performing the laser-surface experiments is the shape of the laser-beam showing strong deviations from the Gaussian profile. This leads to an inhomogeneous intensity distribution of the irradiated area on the surface. Two examples of the induced LIPSS on a 20 nm thick Ti film on a Si wafer for  $\theta_i = 0^\circ$  is shown in figure 5.7. The top row shows SEM measurements while the bottom row shows the same sample measured by the LSM. The LSM images show a larger overview of the irradiated spot over a surface area of  $(86.2 \times 64.8) \mu\text{m}^2$ , while the SEM images show a smaller area of  $(19.6 \times 13.3) \mu\text{m}^2$ . From the LSM images it can be seen that the LIPSS are not only induced on a small area as visible by the SEM images but a much larger area is affected by the laser irradiation and the proper energy is deposited to induce the nanostructures. Furthermore, on the LSM images the inhomogeneity of the laser profile can be seen by the sharp edges of the LIPSS regions, as indicated by the dashed red lines in the respective images. Here the two surfaces were irradiated by the fundamental ( $\lambda_L = 1064 \text{ nm}$  and the

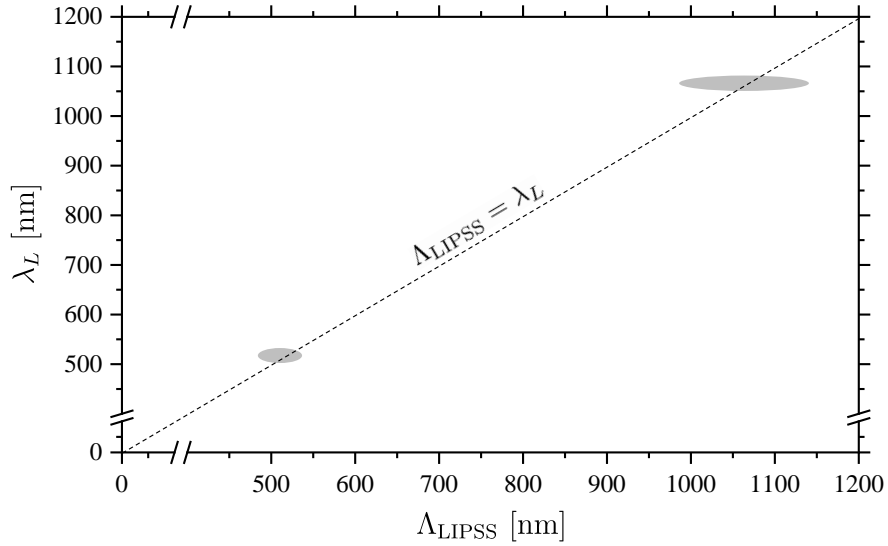


**Figure 5.6.** Periodicity of LIPSS induced on different metal surfaces (Ti, Cr, Cu) under an incident angle of  $\theta_i = 0^\circ$ . The orientation of the LIPSS is perpendicular to the polarization of the laser  $LIPSS \perp \vec{E}_L$ , that was operated at  $f_L = 20$  Hz and a pulse energy of  $E_p = 3.8 - 5$  mJ. The dotted line is the periodicity predicted by the theory according to  $\Lambda_{LIPSS} = \lambda_L$ .

SHG  $\lambda_L = 532$  nm) that also represent the periodicity of the induced patterns in the respective images. The orientation of the electric field vector of the laser is indicated by the white arrow in the bottom left corner of the single images. It can be seen that the orientation of the LIPSS is perpendicular to the electric field vector of the laser,  $LIPSS \perp \vec{E}_L$ . According to figure 2.7 those are LIPSS of the type LSFL-I. Although the intensity at the surface has a very inhomogeneous distribution, it can be concluded that LIPSS of the same type are induced at spots of same energy deposition. These spots, where a similar amount of energy has been deposited on the surface show a similar morphology and colour on the LSM images. An example of the laser spot on the surface is shown in figure 5.3. In that way several samples of different material and different thicknesses have been irradiated by the two different wavelengths and the results of the LIPSS periodicities, as well as the experimental parameters, are shown in table S1. The treatment duration and the pulse energies were experimentally chosen in such a way that the induced LIPSS covered the largest possible area on the surface while at the same time being homogeneous and nicely pronounced. It can be seen that the periodicity is in the order of the laser wavelength within the measurement errors.

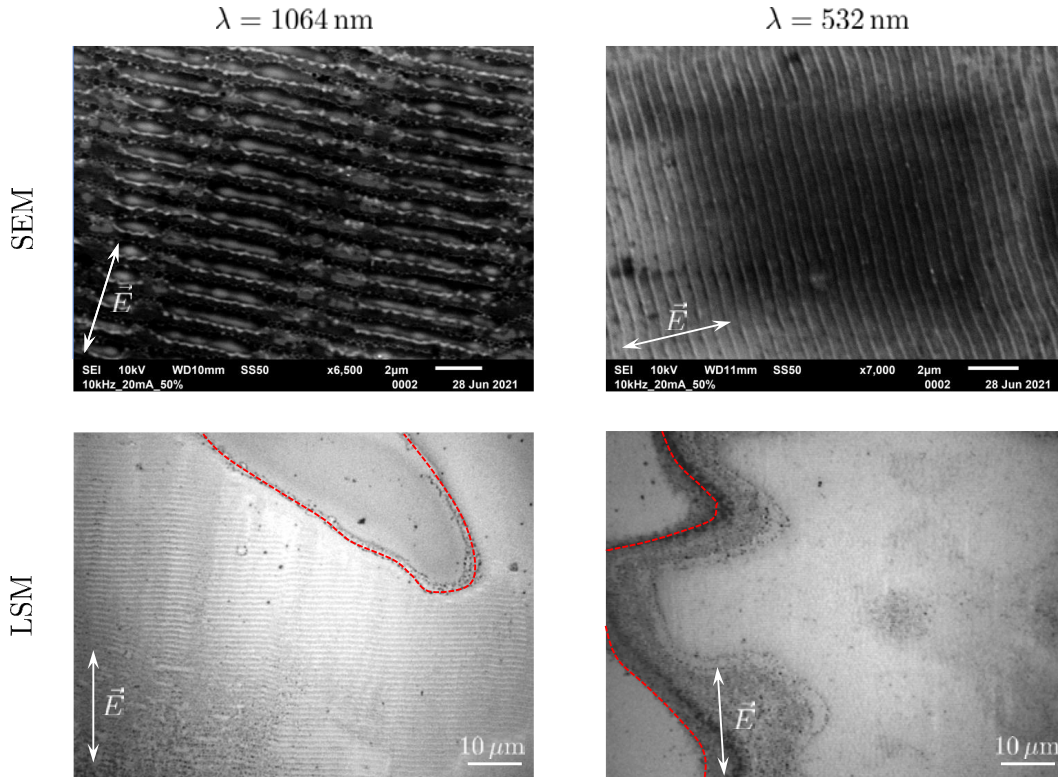


**Figure 5.7.** Top row: SEM images and bottom row: LSM images of LIPSS induced by laser irradiation under  $\theta_i = 0^\circ$  and  $\lambda_L = 1064$  nm and  $\lambda_L = 532$  nm on a 20 nm thick Ti layer on a Si wafer.

Furthermore the LIPSS are all oriented perpendicular to the electric field vector of the laser. This finding is independent of the target material, as well as the target thickness. This is different to the findings of Nürnbergger et al. who investigated the thickness dependency on a SiO<sub>2</sub> on Si substrate to the LIPSS formation. They investigated different SiO<sub>2</sub> thicknesses ranging from 1.7 nm up to 184 nm and found out that not only the LIPSS periodicity decreases with increasing film thickness, but also the orientation of the LIPSS aligns with the electric field vector that rotates around 90° from perpendicular to parallel. For average thicknesses at around 90 nm, even superimposed LIPSS perpendicular and parallel were observed [124].

The experimentally observed periodicities of the LIPSS induced on different surface materials can now be compared to the different introduced theories according to classical interference, Surface Plasmon Polaritons (SPPs)

TABLE S1: LIPSS periodicities  $\Lambda_{\text{LIPSS}}$  on different surface materials induced by perpendicular irradiation ( $\theta_i = 0^\circ$ ) of the fundamental  $\lambda_L = 1064$  nm and the SHG  $\lambda_L = 532$  nm.

mat.	$d$ [nm]	$\lambda_L$	$\Lambda_{\text{LIPSS}}$ [nm]	$E_p$ [mJ]	$t_{\text{rad}}$ [s]	$\Lambda_{\text{LIPSS}}$ to $\vec{E}_L$
Ti	20	532	523±9	3.8	21	⊥
	20	1064	1054±16	3.8	7	⊥
	60	532	519±16	3.4	7	⊥
	60	1064	1067±8	3.8	4	⊥
	100	532	512±21	3.4	6	⊥
	100	1064	1054±32	4.2	3	⊥
Cr	20	532	520±42	5.3	12	⊥
	60	532	518±18	8.4	5	⊥
Cu	20	532	512±27	6.2	2	⊥

and Sipe's theory. To evaluate the theories, the dielectric constants for the different materials according to the excitation wavelength are needed. They are listed in table S2.

Here the wavelength dependent refractive index of the materials is given by

$$n(\lambda) = \tilde{n}(\lambda) + i\kappa(\lambda) \quad (5.3)$$

where  $n$  is the refractive index,  $\tilde{n}$  is the real part of the refractive index and  $\kappa$  is the imaginary part also called the extinction coefficient which is responsible for the attenuation of the electromagnetic wave inside the material. The dielectric function is then given as the square of the refractive index and therefore

$$\epsilon_r(\lambda) = \epsilon_r'(\lambda) + i\epsilon_r''(\lambda) = n(\lambda)^2 = [\tilde{n}(\lambda) + i\kappa(\lambda)]^2 \quad (5.4)$$

$$\Rightarrow \epsilon_r'(\lambda) = n(\lambda)^2 - \kappa(\lambda)^2 \quad (5.5)$$

$$\Rightarrow \epsilon_r''(\lambda) = 2\tilde{n}(\lambda)\kappa(\lambda)i. \quad (5.6)$$

With these optical constants the theoretical values for the LIPSS periodicity can be calculated.  $\text{Si}_m$  denotes molten silicon. It is observed on the LSM

TABLE S2: Optical constants of the investigated materials. The refractive index of a material is given by  $n(\lambda) = \tilde{n}(\lambda) + i\kappa(\lambda)$  and  $\epsilon_r(\lambda) = \epsilon_r(\lambda)' + i\epsilon_r(\lambda)'' = n(\lambda)^2$ .

mat.	$\lambda_L$ [nm]	$\tilde{n}$	$\kappa$	$\epsilon_r'$	$\epsilon_r''$	Ref
Ti	521	2.44	3.3	-4.94	16.1	[119]
	1088	3.5	4.02	-3.91	28.14	[119]
Cr	521	2.94	3.33	-2.45	19.58	[119]
Cu	521	1.18	2.608	-5.41	6.15	look up
Si <sub>m</sub>	515	3.11	4.89	-14.2	30.4	look up

images that the surface is partially melted, hence the temperatures rise near or partially above the melting point. Due to the fact that the thin layer on the silicon wafer have a thickness in the order of a couple nm, it is possible that even the silicon of the bulk material is melted. The real part of the refractive index of molten silicon is highly negative and therefore a plasmonic active material that might lead or enhance the formation of SPPs. The theoretical values are calculated according to the following equations, as presented in section 2.4.1:

$$\text{Classical Interference (CI):} \quad \Lambda(\lambda, \theta_i) = \begin{cases} \frac{\lambda}{1 \pm \sin(\theta_i)} & (\pi\text{-pol}) \quad (5.7) \\ \frac{\lambda}{\cos(\theta_i)} & (\sigma\text{-pol}) \quad (5.8) \end{cases}$$

$$\text{Surface Plasmons (SPP):} \quad \Lambda(\lambda, \theta_i) = \begin{cases} \frac{\lambda_L}{\chi \pm \sin(\theta_i)} & (\pi\text{-pol}) \quad (5.9) \\ \frac{\lambda}{\sqrt{\zeta^2 - \sin^2(\theta_i)}} & (\sigma\text{-pol}) \quad (5.10) \end{cases}$$

Sipe's theory (Sipe): numerical calculation (eq. 2.55-2.58)

TABLE S3: Comparisons of the theoretical calculated values of the LIPSS periodicities,  $\Lambda_t$ , with the experimental observed values,  $\Lambda_{exp}$ . The last column shows the deviations between the experimental and the theoretical value of the respective theory  $\Delta\Lambda = |\Lambda_{exp} - \Lambda_t|$ . Different theories are evaluated here, according to the Classical Interference theory (CI), the Surface Plasmon Polariton theory (SPP) and Sipe's theory (Sipe).

Theory	mat.	$\lambda_L$ [nm]	$\Lambda_t$ [nm]	$\Lambda_{exp}$ [nm]	$\Delta\Lambda$ [nm]
CI	Ti	1064	$\lambda_L$	1054	10.00
CI	Ti	532	$\lambda_L$	523	9.00
CI	Cr	532	$\lambda_L$	519	13.00
CI	Cu	532	$\lambda_L$	512	20.00
Sipe	Ti	1064	1053.98	1054	0.02
Sipe	Ti	532	521.57	523	1.43
Sipe	Cr	532	523.70	519	4.70
Sipe	Cu	532	506.67	512	5.33
SPP	Ti	1064	917.91	1054	136.09
SPP	Ti	532	475.11	523	47.89
SPP	Cr	532	409.27	519	109.73
SPP	Cu	532	480.23	512	31.77
SPP	Si <sub>m</sub>	532	512.98		

The results of the different theories and the comparison to the experimental measured values are shown in table S3.

The classical interference theory predicts the laser wavelength as the LIPSS periodicity for perpendicular irradiation. This is independent from the surface material. Applying Sipe's theory, as well as the SPPs, the periodicity is slightly below the excitation wavelength. However, the possibility of the influence and formation of SPPs at the surface can be excluded in those experiments. This becomes obvious from the strong deviations between the experimental observed values and the theoretical ones. This is also an indication for the fact that the molten silicon as a lossy material has no strong

influence on the LIPSS formation itself, although the thicknesses of the metal layers on the silicon wafer is only in the nm range. The most accurate predictions for the periodicities are obtained by Sipe's model. This is also the most common and most accepted theory in the field.

In Sipe's theory the so called efficacy factor describes the response function of the surface roughness leading to an inhomogeneous energy absorption and therefore potential LIPSS formation. The efficacy maps for the three investigated materials are calculated and shown in figure 5.10. To evaluate the orientation of the LIPSS with respect to the electric field vector of the excitation laser, a given coordinate system is crucial. The orientation of the  $x$  and  $y$ -axes that is used to analyze the efficacy factor maps is shown in figure 5.8.

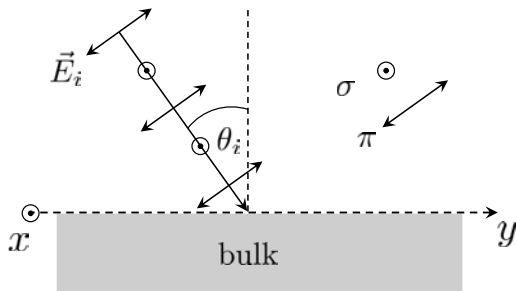


**Figure 5.8.** Coordinate system for the orientation of the efficacy maps according to Sipe's theory.

In this coordinate system it is chosen that the electric field vector of the laser,  $\vec{E}_L$ , is oriented parallel to the  $x$ -direction for  $\sigma$ -polarized laser light, hence perpendicular to the  $y$ -axis. It should be noted that when evaluating the efficacy maps, the  $\kappa$ -vector is the normalized grating vector of the LIPSS itself,  $\kappa = \Lambda_{\text{LIPSS}}/2\pi$ . If the LIPSS are oriented parallel to the electric field vector, this means that the grating

vector is oriented perpendicular to it, meaningly  $\vec{\kappa} \perp \vec{E}_L$ .

Two of the surface properties that are needed to calculate the efficacy factor maps are the filling factor and the geometrical shape factor,  $F$  and  $s$ , respectively. These factors characterize the surface roughness, as for example a relatively flat "pancake" or slab structure for  $\lim s \rightarrow \infty$ , to a "banana" or spike shape for  $\lim s \rightarrow 0$  [74]. Contrary to the other surface parameters, such as the dielectric function or the refraction index, those geometrical factors are nowhere to be looked up, but have to be assumed. In most publications it was found that the best parameter-pair to describe LIPSS was setting  $(F, s) = (0.1, 0.4)$ , that is considered to be spherical shaped islands on a bulk

material [74]. However, the influence of the shape factors in the near vicinity of the mostly used parameter-pair is studied here. Therefore the factors  $F$  and  $s$  are varied according to  $F, s \in [0, 1]$  and a matrix is calculated to obtain the calculated LIPSS periodicity according to the different  $(F, s)$ . The result is shown in figure 5.9. The pair that is taken for the calculation in this thesis is

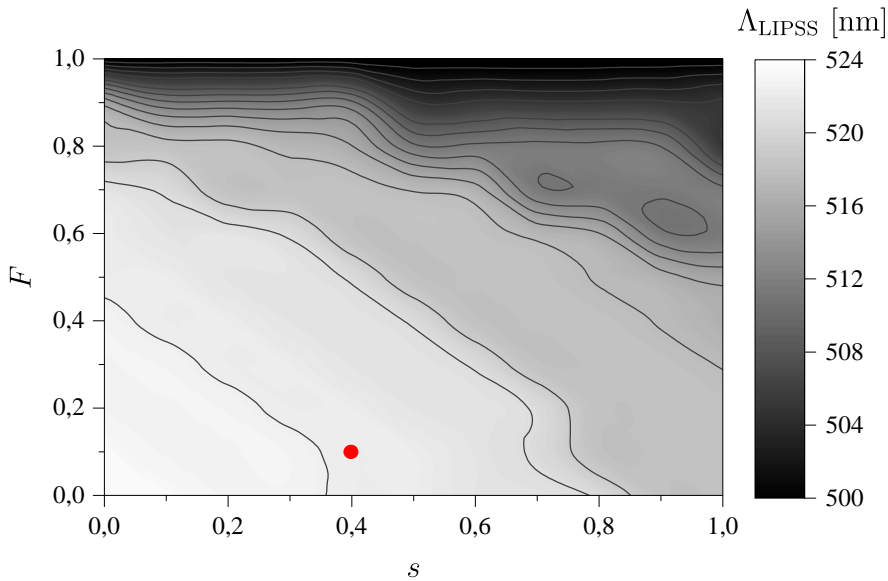


**Figure 5.9.** The position of the maximum of the efficacy factor depending on the filling factor  $F$  and the geometrical shape factor  $s$ . Here the map is calculated for perpendicular irradiation, according to  $\theta_i = 0^\circ$ , onto a Ti layer with a laser wavelength of  $\lambda_L = 532$  nm. The pair, according to  $(F, s) = (0.1, 0.4)$  that is used for the calculations in this thesis is marked via the red dot.

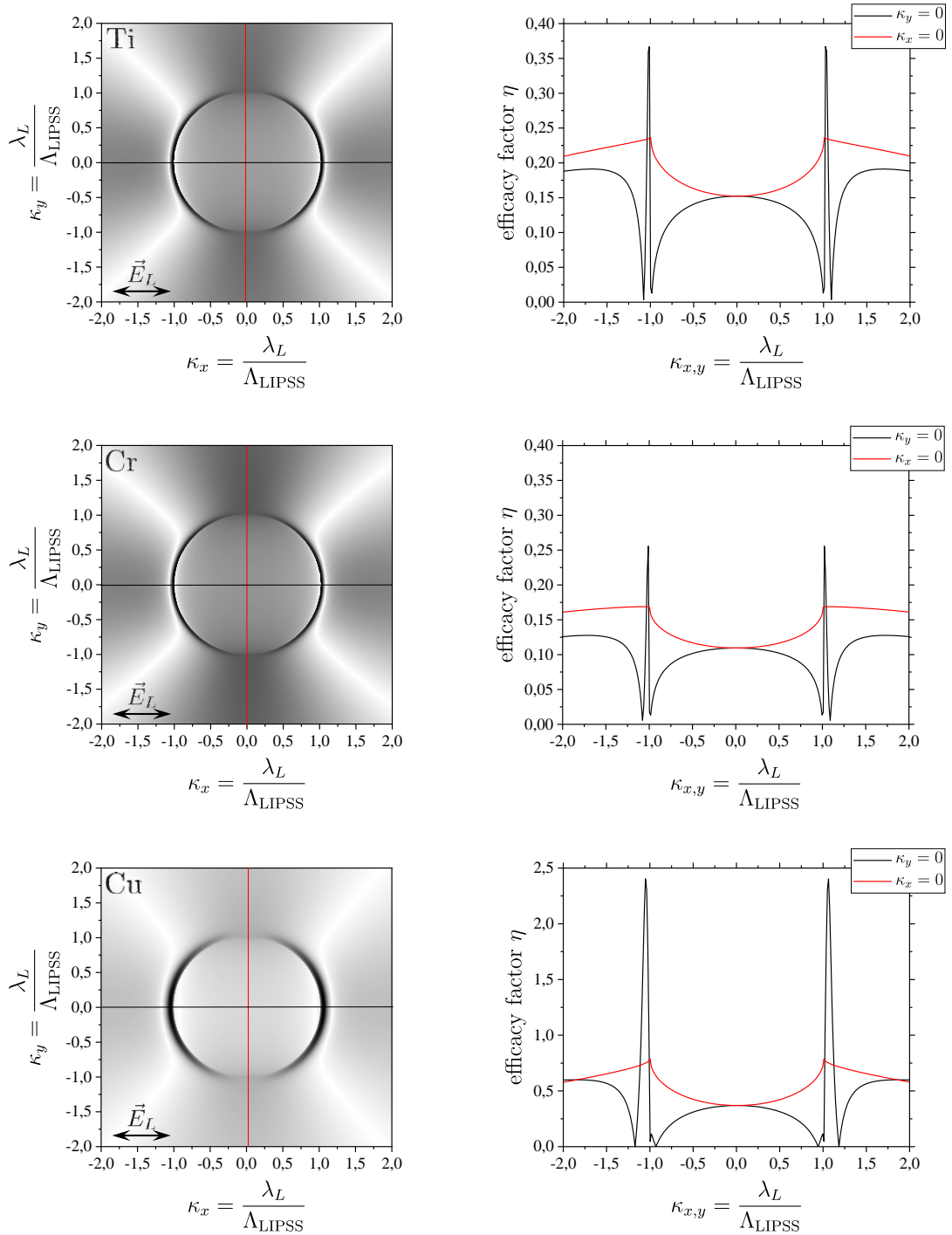
marked by the red dot in the figure. However, from the map it can be seen that the LIPSS periodicity varies only to a small degree when varying the filling and shape factor, especially in the vicinity of the applied values. Only in the limit  $F \rightarrow 1$  that refers to a "full" selvedge, the values more significantly change. In this region the periodicity is also independent from the geometric shape factor  $s$  due to the entirely filled selvedge and therefore, this region is most likely not meaningful in a physical sense. In the other regions, as already stated, the position of the maximum of the efficacy factor is more or less insensitive to the  $F$  and  $s$  factors. This in turn means that the formation and periodicity is not a strong function of the original and initial shape of the morphology and the roughness. For the whole parameter range of  $F$  and  $s$  studied here the variation is only about  $\Delta\Lambda_{\text{LIPSS}} \sim 5\%$ .

Figure 5.10 shows the efficacy factor maps for the investigated materials (Ti, Cr and Cu) for perpendicular laser irradiation of the surface according to  $\theta_i = 0^\circ$ . The orientation of the polarization vector of the laser is along the  $x$ -direction in this case, according to  $\vec{E}_L(t) = \hat{E} \sin(\omega_L t) \vec{e}_x$ . From the figure it can be seen that the general shape in Fourier space looks quite similar for all three materials. For the component parallel to the polarization vector ( $\kappa_y = 0$ ) a sharp and very narrow peak can be found at values slightly above  $\kappa_x = 1$  ( $\kappa = 1 \Rightarrow \Lambda_{\text{LIPSS}} = \lambda_L$ ), that corresponds to the LIPSS periodicities listed in table S3. The narrow nature of the peak indicates a well defined periodicity of the LIPSS perpendicular to the polarization vector. This was also found in the experiments. Hence it can be deduced, that the LIPSS can be well described by the theory of Sipe et al.. It should be noted that the scale for Cu is different from the scale for Ti and Cr and the amplitude of the efficacy factor is about 9 times higher as compared to the respective other ones. This means that the LIPSS should be formed much more efficient on the Cu surface. For the orientation parallel to the polarization ( $\kappa_x = 0$ ) no such pronounced narrow peaks are observed in the calculations. In this direction rather broad bands are present with a maximum at around  $\kappa_y = 1$ . However, the amplitude of the efficacy factor in this direction is significantly smaller as compared to the parallel component. Structures that are oriented in this direction are not observed in the experiments.

### 5.3.3 Dependence of the LIPSS orientation on the polarization vector

As found from the experiments and the numerical calculations of Sipe's model, the most effective and most likely formation of LIPSS for perpendicular irradiation of the surface is of the kind LSFL-I ( $\Lambda_{\text{LIPSS}} \approx \lambda_L; \perp \vec{E}_L$ ). To verify this assumption the polarization vector of the laser was rotated and the LIPSS were recorded and evaluated with respect to their orientation.

To do so, the polarization of the laser was rotated via a  $\lambda/2$  wave-plate. As seen in figure 5.11 the perpendicular orientation of the polarization vector (hence the horizontal orientation of the LIPSS) was defined as the zero position,  $\varphi = 0^\circ$ . The angle which represents the orientation of the LIPSS in



**Figure 5.10.** Efficacy factor maps for perpendicular irradiation according to  $\theta_i = 0^\circ$  for different materials (Ti, Cr, Cu). The colormaps are chosen as an inverse gray scale where black values represent high factors and white vice versa low. The 1-dimensional profiles for the single components of  $\kappa$ , according to  $\kappa_x = 0$  (red) and  $\kappa_y = 0$  (black) are shown in the graphs on the right. Special attention should be paid to the different scale in the case of Cu.

relation to the horizontal line is defined as  $\psi$ . The evaluation of the orientation of the LIPSS is performed in two ways: (i) in the filtered back transformed Fourier spectrum, to isolate the LIPSS from the background noise (see workflow in figure 5.4), the lines in real space were evaluated by the software Gwyddion. And (ii) the angle of the positions of the maxima in the Fourier space is evaluated. These methods are chosen, since both methods deliver global information, where all the LIPSS that are present in the images are taken into account, rather than a local information, when evaluating only a couple of LIPSS in real space. The rotation of the polarization is performed

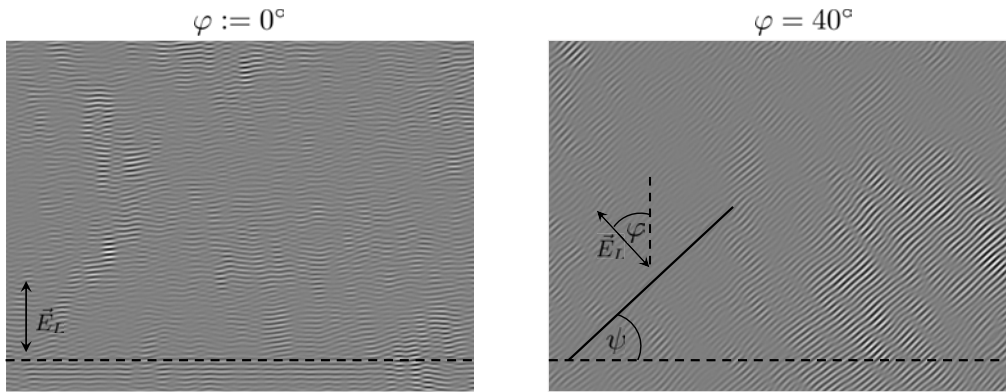


**Figure 5.11.** Evaluation of the orientation of the LIPSS with respect to the polarization vector  $\vec{E}_L$ . The images show the filtered back transformation of the Fourier spectra, in order to isolate the LIPSS from the background.  $\varphi = 0^\circ$  is defined as the horizontal line.

in  $\Delta\varphi = 5^\circ$  steps from  $\varphi = 0^\circ$  to  $80^\circ$ . The measurements were performed on a 100 nm thick Ti layer on a silicon substrate with an irradiation angle of  $\theta_i = 0^\circ$ . The results can be seen in figure 5.12. It is observed that the orientation of the LIPSS is indeed dependent on the orientation of the polarization vector. As the polarization is rotated the orientation of the LIPSS rotates as well. All angles measured within the experiments are lying inside the error interval around the dashed identity line. This behaviour was found for all investigated materials, independent on substrate thickness. From those measurements it can be concluded that the LIPSS are coupled to the polarization vector and are oriented perpendicular to it. Hence, this is one of the laser parameters to tailor the laser induced structures on the surface, as it is also predicted by Sipe's theory.

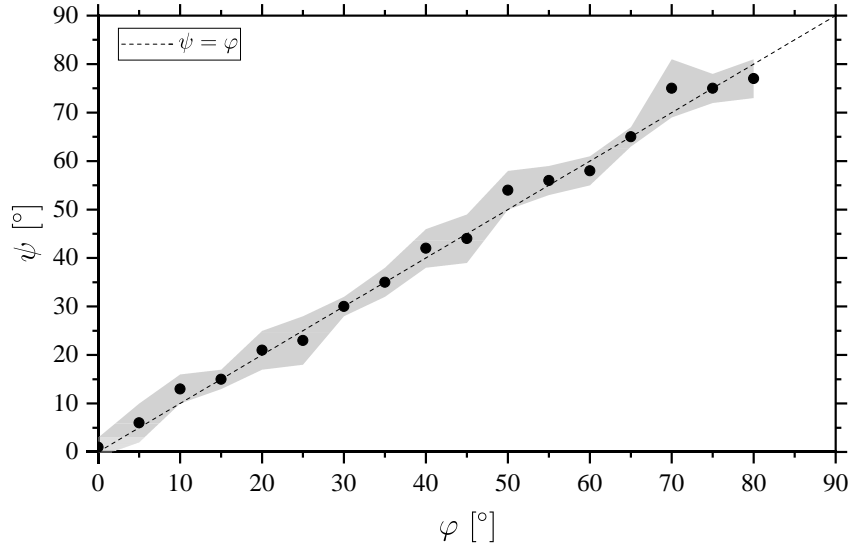


**Figure 5.12.** Orientation of the LIPSS against the orientation of the polarization vector of the laser. The definition of the angles  $\psi$  and  $\varphi$  can be seen in figure 5.11. The dotted line represents the identity  $\psi = \varphi$  and the gray shaded area indicates the error interval.

### 5.3.4 LIPSS on substrates for $\theta_i \neq 0^\circ$ incident irradiation

According to the theories presented in section 2.4.1, the incident angle,  $\theta_i$  is one of the parameters to tailor the periodicity of the LIPSS. To further investigate this correlation, experiments have been performed, where the incident angle was varied up to  $\theta_i = 75^\circ$  in  $\Delta\theta_i = 5^\circ$  steps. The experiments were performed for both wavelengths,  $\lambda_L = 1064 \text{ nm}$  and  $\lambda_L = 532 \text{ nm}$  and also for both polarizations,  $\sigma$ - and  $\pi$ -polarization (see figure 5.8).

Since the LIPSS are very pronounced on Ti surfaces, the results shown here are for a 20 nm thick Ti layer on a silicon substrate. However, the experiments have been performed on other materials with different thicknesses as well and the same trend has been observed for all variations. Hence, the results shown here represent the trend for all other materials as well. For all investigated materials it was found, that the LSFL-I are present and can be accurately described by Sipe's theory for all investigated angles (see figure 5.16). However, it was found, that for angles  $\theta_i > 50^\circ$  another type of LIPSS are present that are, contrary to the LIPSS observed before, parallel to the polarization vector of the laser. Young et al. denoted the different types of LIPSS as  $c$ -type LIPSS that follow a  $\Lambda_{\text{LIPSS}} = \lambda_L / \cos(\theta_i)$  relation and are oriented parallel to

$\vec{E}_L$ , while the LIPSS that already occurred under perpendicular irradiation as  $s^-$  and  $s^+$ -type LIPSS depending on the "+" or "-" sign in the denominator of the analytical expression  $\Lambda_{\text{LIPSS}} = \lambda_L / (1 \pm \sin(\theta_i))$  [76]. An LSM image of a

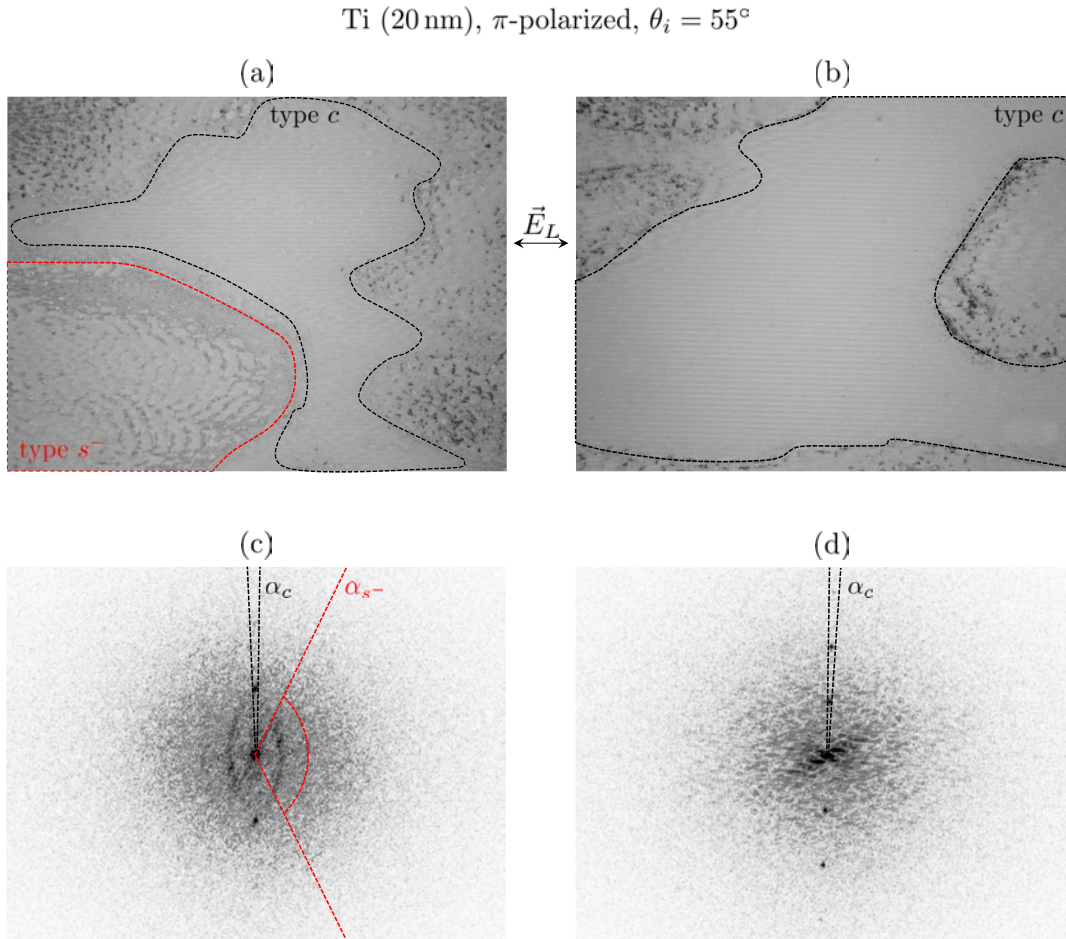


**Figure 5.13.** Type  $c$  and type  $s^-$  LIPSS induced on a 20 nm thick Ti substrate with  $\theta_i = 55^\circ$  irradiation. (a) shows the coexistence of type  $c$  (black dotted area) and the type  $s^-$  (red dotted area) LIPSS. (b) shows a larger area of type  $c$  LIPSS. The polarization vector is shown in between the images and the area of the LSM images is  $(94 \times 70) \mu\text{m}^2$ . (c) and (d) show the (centre zoomed) power spectra of the 2dFFT of (a) and (b), respectively.

20 nm thick Ti layer that was irradiated with laser-light of  $\lambda_L = 532$  nm under an angle of  $\theta_i = 55^\circ$  can be seen in figure 5.13 (a) and (b). In (a) it can be seen that a coexistence of the different LIPSS types is observed on the Ti substrate. The type  $s^-$  are oriented perpendicular to the polarization, whereas the type

$c$ -LIPSS form parallel to it. Also when zooming into the images, a superposition of the two types can be seen. In (b) solely type  $c$  fringes are visible on a large area. It can be seen how accurate these LIPSS form with a very well defined periodicity. This can also be seen in the corresponding power spectra in the 2dFFT that are shown in figure 5.13 (c) and (d). Those images show a zoomed view of the FFT corresponding to the images above (a) and (b) respectively. In both power spectra, distinct peaks along a very narrow angle  $\alpha_c$  can be seen. The fact that the opening angle is so small is a direct evidence of the high quality of the induced  $c$ -type LIPSS as being judged by their orientation and their periodicity. The ring shaped frequencies in figure 5.13 (c) are generating the  $s^-$  type LIPSS in the real image (a). Here it can be seen that the opening angle  $\alpha_{s^-}$  is very big and therefore, orientation and periodicity are very noisy and irregular. These features can be clearly seen comparing the red and black dotted regions.

These features can also be seen in the efficacy factor maps calculated by Sipe's theory for angles  $\theta_i \neq 0^\circ$ . Different maps calculated for a Ti target, according to the images shown in figure 5.13 (a) and (b) are shown in figure 5.14. The left column shows the efficacy factor maps for different incidence angles according to  $\theta_i \in \{0^\circ, 30^\circ, 60^\circ\}$ .

Here it is observed that as the incidence angle is increased, several distinct peaks are formed in Fourier space. Contrary to the perpendicular irradiance case ( $\theta_i = 0^\circ$ ), for larger angles it can be seen that these peaks are not only formed parallel to the polarization vector (hence the LIPSS are perpendicular to it) but peaks with significant efficacy factors are also created perpendicular to it. In the experiments, the type  $c$  LIPS were only observed for angles  $\theta_i \geq 50^\circ$ . This can be explained by extracting the profiles for  $\kappa_y = 0$  from figure 5.14. Those profiles for different angles are shown in figure 5.15. It can be seen that not only the position of the maximum shifts along the wave-vector axis but also the absolute amount of the efficacy factor increases steeply. For an angle of  $\theta_i = 10^\circ$  a peak can barely be seen and the amount is  $\eta < 1$ , while the factor increases up to about  $\eta \approx 7$  for  $\theta_i = 50^\circ$ . Due to the fact that these types of LIPSS are only observed for angles larger than this there must be a critical efficacy factor  $\eta_c$  for the given experimental conditions and the structures are only induced, if  $\eta > \eta_c$ .

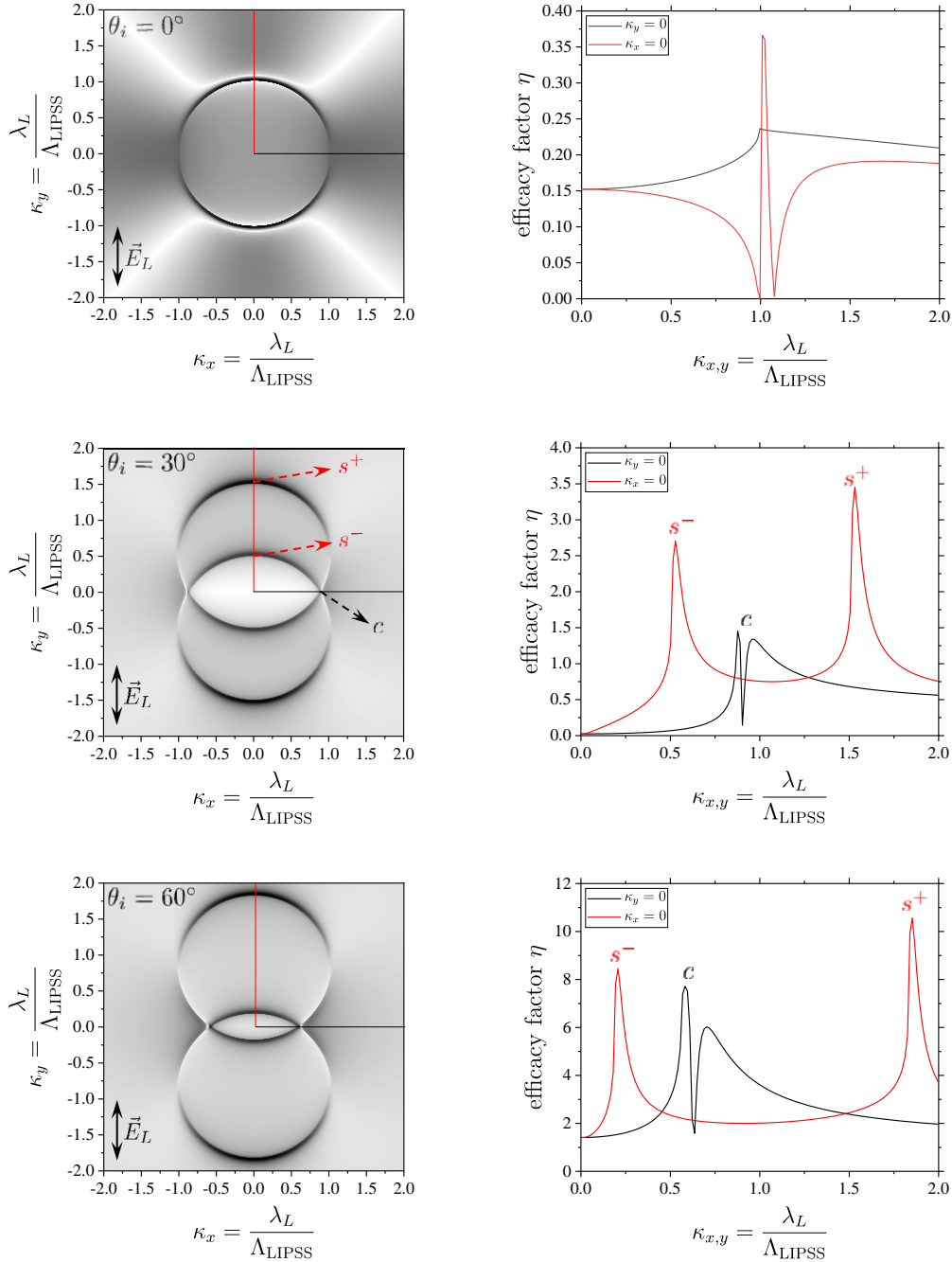


**Figure 5.14.** Efficacy factor maps for non-perpendicular irradiation according to  $\theta_i \neq 0^\circ$  for a Ti layer and  $\pi$ -polarized laser. The colormaps are chosen as an inverse gray scale where black values represent high factors and white vice versa low. The 1-dimensional profiles for the single components of  $\kappa$ , according to  $\kappa_x = 0$  (red) and  $\kappa_y = 0$  (black) are shown in the graphs on the right. Special attention should be paid to the different scale.

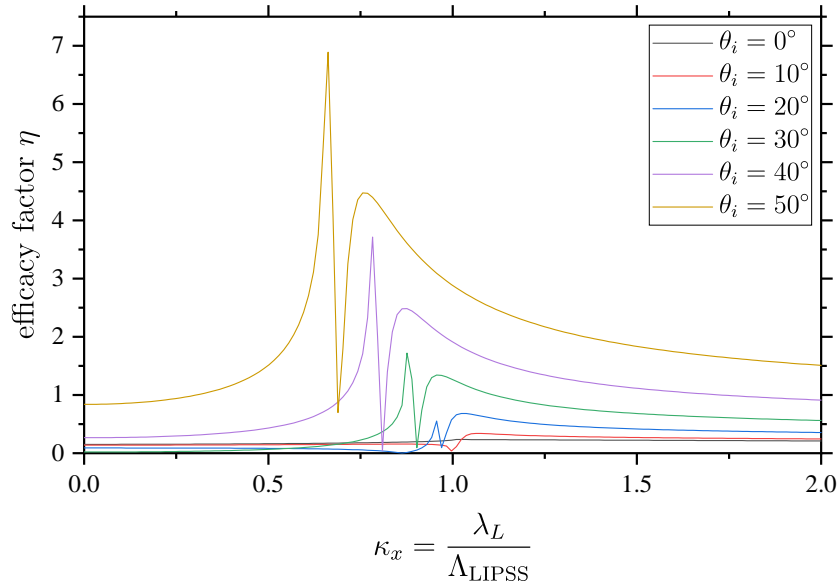


**Figure 5.15.** Efficacy factor  $\eta$  of the  $c$ -type LIPSS for different incidence angles  $\theta_i$  onto a 20 nm thick Ti layer.

As seen from figure 5.14 Sipe's theory can not only explain the  $s^-$ -type LIPSS that are induced on the Ti layer, but also the  $c$ -type. This becomes also clear by looking at figure 5.16. This figure shows the incident angle variation for  $\pi$ - and  $\sigma$ -polarized laserlight of the wavelength  $\lambda_L = 532$  nm.

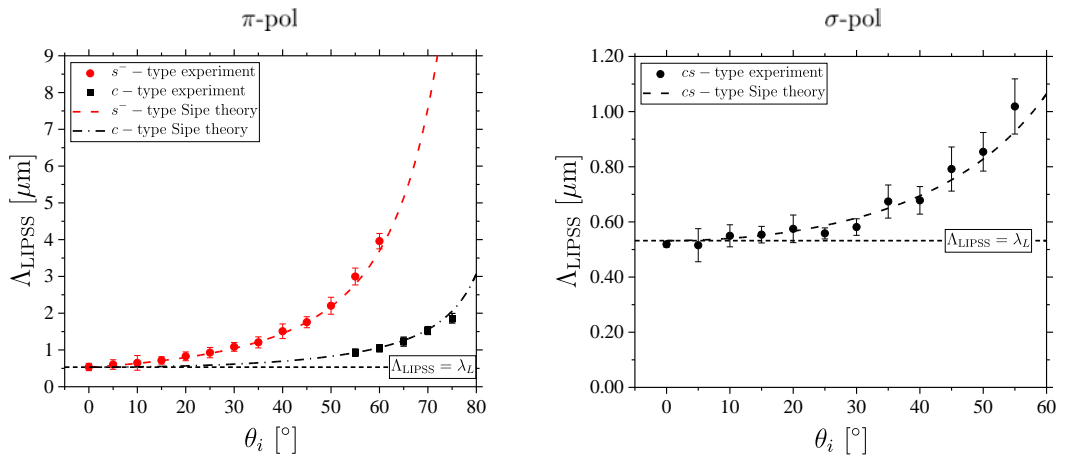


**Figure 5.16.** LIPSS periodicities for different incident angles,  $\theta_i$  and different polarizations of the laser. It can be seen that all the induced structures are adequately described by Sipe's theory, as seen by the match of experimental and calculated values. The plots shown here are for  $\lambda_L = 532$  nm.

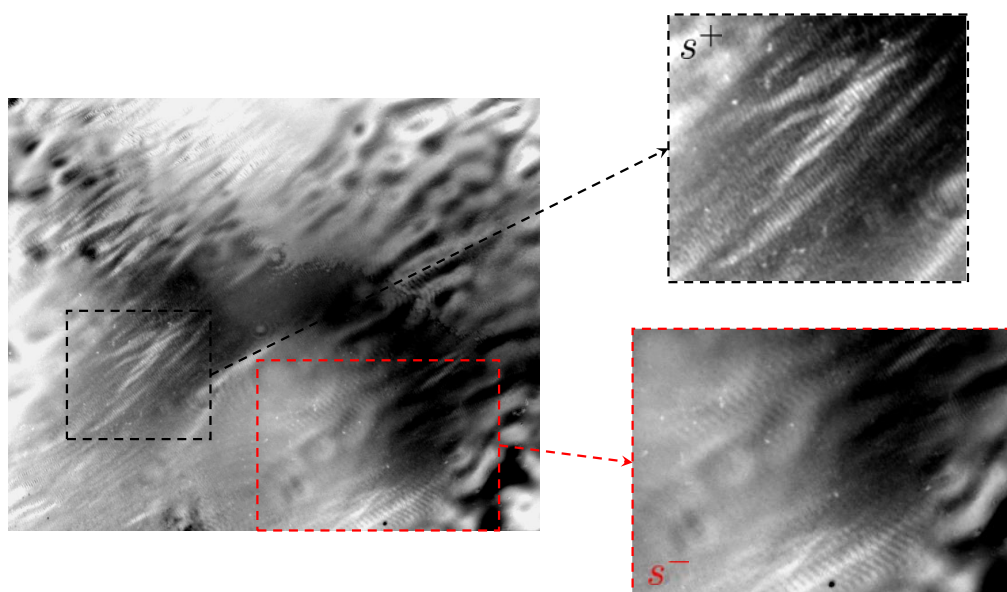


**Figure 5.17.** LSM image of a Si wafer irradiated by  $\pi$ -polarized laserlight of the wavelength  $\lambda_L = 532$  nm. The woven structures indicate partially molten silica and two different types of LIPSS can be seen according to  $s^+$ -types (black dotted area) and  $s^-$ -types (red dotted area).

It can be seen that the induced  $s^-$ ,  $c$  and  $cs$ -type LIPSS are adequately described by Sipe's theory for the whole angle range that was investigated. It is striking how clean the  $c$ -type LIPSS are induced on the Ti layer in the case of  $\pi$ -polarized light, due to the error bars that are negligible small. For  $\sigma$ -polarized light the error bars are considerably larger, hinting for less reproducible structures in this case. The same trend, that all the induced structures can be described by Sipe, is not only valid in the  $\lambda_L = 532$  nm case, but also holds for the fundamental wavelength of  $\lambda_L = 1064$  nm, which is not shown here.

For irradiance on a Si wafer without a metallic coating another feature is observed that has not been observed on the other materials. The simultaneous creation of  $s^+$  and  $s^-$ -type LIPSS. An example LSM image that shows a Si wafer irradiated with  $\lambda_L = 532$  nm can be seen in figure 5.17. It is observed that in different areas of the sample different types of LIPSS have been induced. In some parts even a superposition of the structures is observed. The orientation with respect to the polarization vector is similar,  $\text{LIPSS} \perp \vec{E}_L$ , the periodicity however is different. Due to the fact that these patterns have been

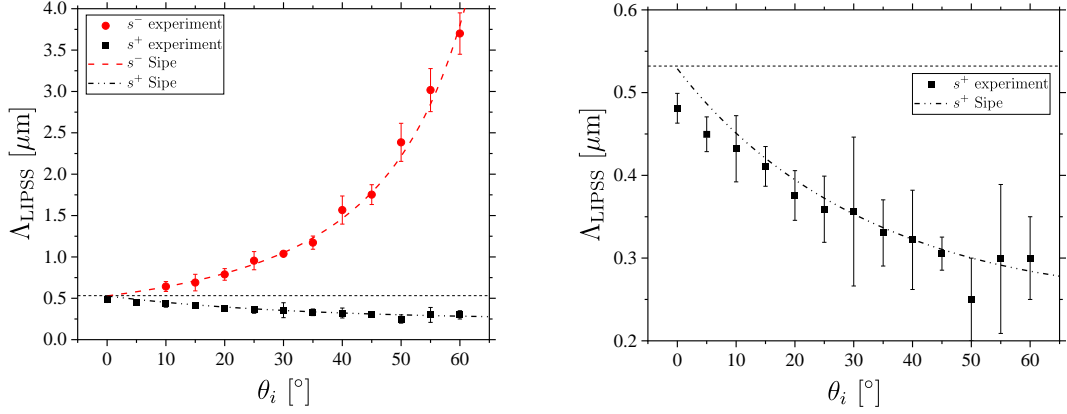


**Figure 5.18.** Periodicity of the induced LIPSS,  $\Lambda_{\text{LIPSS}}$ , depending on the incident angle  $\theta_i$ . The results shown here are for a  $\pi$ -polarized laser of the wavelength  $\lambda_L = 532$  nm. The wavelength is depicted by the dashed horizontal line.

induced with  $\pi$ -polarized light and the orientation those LIPSS must be of the type  $s^-$  and  $s^+$ . An evaluation of the periodicities for varying incident angles onto a Si wafer is shown in figure 5.18.

From the experimental obtained data and the numerical calculations by Sipe's theory it is found that the induced LIPSS can as well be described by Sipe's theory. For the  $s^+$  type LIPSS a decent deviation from the model can be seen for angles  $\theta_i < 10^\circ$  and for large angles  $\theta_i \geq 50^\circ$ . This deviation might be due to the fact that the silica has been partially molten. The theory by Sipe requires that the roughness of the surface,  $l$ , must be much smaller than the used excitation wavelength. If the surface is molten the inequality  $l/\lambda_L \ll 1$  might not be fulfilled locally and therefore the theory might not predict the exact periodicity.

In the case of molten silica the development of SPPs is most likely, due to the high imaginary part of the dielectric function ( $\epsilon_r(521 \text{ nm}) = 14.2 + 30.4i$ ) that characterizes it as a lossy material, prone to SPP formation. However, evaluating the SPP theory, a strong deviation from the experimental data was found and no correlation between SPPs and the observed data can be deduced.

### 5.3.5 Summary of the LIPSS experiments

In this thesis it was shown that LIPSS could be induced on all the investigated materials (Ti, Cu, Cr, Si) to great extent. This is possible for different wavelengths of  $\lambda_L = 1064 \text{ nm}$  and also  $\lambda_L = 532 \text{ nm}$ . The correlation between different laser and experimental parameters, namely the polarization of the laser, the orientation of the polarization itself and the angle of incidence was investigated and all three have shown to be tuning parameters to vary either the periodicity or the orientation of the LIPSS.

It was shown that the alignment of the LIPSS is perpendicular to the polarization of the laser,  $\text{LIPSS} \perp \vec{E}_L$  for  $s^+$ -, and  $s^-$ -type LIPSS and parallel in the case of  $c$ -types. By rotating the polarization plane of the laser the LIPSS rotated by the same angle, as seen in figure 5.12.

The periodicity of the LIPSS could be tuned by the variation of the angle of incidence. Furthermore the types and also the periodicity is adequately described by Sipe's theory and the according efficacy factor maps. SPPs seem not to play an important role, since the calculations do not match the experimental data. Since the physical origin of LIPSS is still a controversy in the field, this is an important finding to note.

## 5.4 PLiD on Cu substrates

Another effect that is induced when irradiating thin metallic layers are small nanoparticles. Those nanoparticles can be catalytic active sites. The activity of particles is strongly dependent on their surface to volume ratios, reacting more active for smaller particles [125]. Those particles have only been observed on Cu targets, while on the other materials none of those structures are created. In the literature this mechanism is described as Pulsed Laser Induced Dewetting, abbreviated PLiD.

In the experiments, PLiDs were effectively created throughout the whole laser spot on the surface. Figure 5.19 shows an SEM image with a zoomed view into the interaction region where single nanoparticles are visible. The experiments are performed with a 10 nm thick Cu layer coated onto a silicon wafer. However, when zooming into the interaction region a lot of different

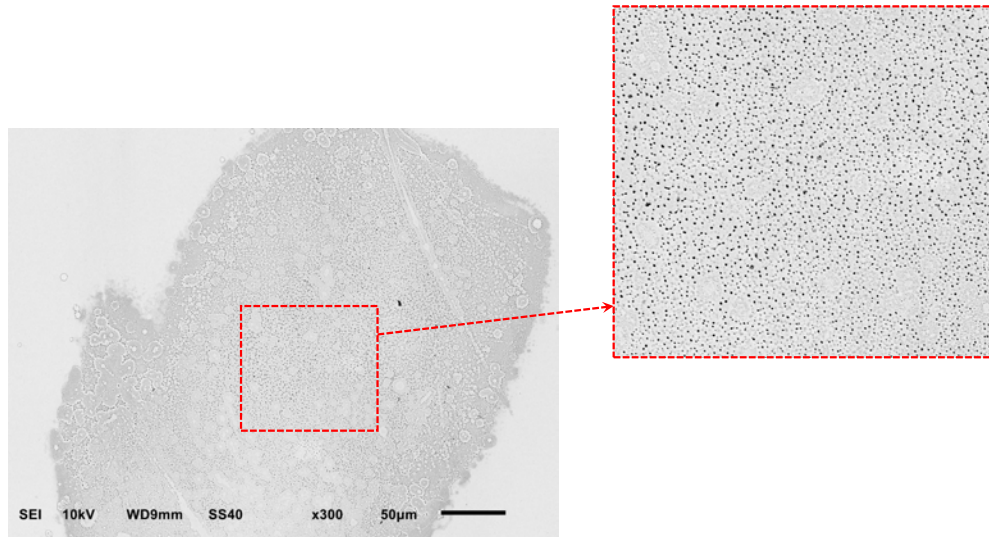


**Figure 5.19.** SEM image of the PLiD induced by laser irradiation of a 10 nm thick Cu layer. The right image shows a zoomed view of the centre of the laser spot marked by the red square. Here the single nanoparticles are visible homogeneously distributed.

features become visible. These features can be described as a chronological pathway in order to create nanoparticles according to thin film hydrodynamic instabilities (TFH). This theory predicts the initiation of non-linear dewetting due to the melting of the surface by laser irradiation and eventually the creation of nanopatterns when the stabilizing interfacial tension is dominated by attractive intermolecular forces, such as van der Waals interaction or steric forces [126, 127, 128]. The formation of these patterns is dependent on many material properties. The initial stage of the instability is partial dewetting and the formation of polygons that eventually break up and form the spheric nanoparticles. LSM images of the first stages are shown in figure 5.20. Two different regimes are observed within the same laser spot and the same number of subsequent pulses. Figure 5.20 (a) shows the characteristic polygon net structure. An interesting feature is the fact that in between those structures LSFL-I LIPSS are induced on the Si wafer. It can be seen that the Cu is completely removed in between those structures. In (b) the net structure is already mostly broken and single particles have already formed. However, there are still filaments visible that are remnants from the earlier net structure.

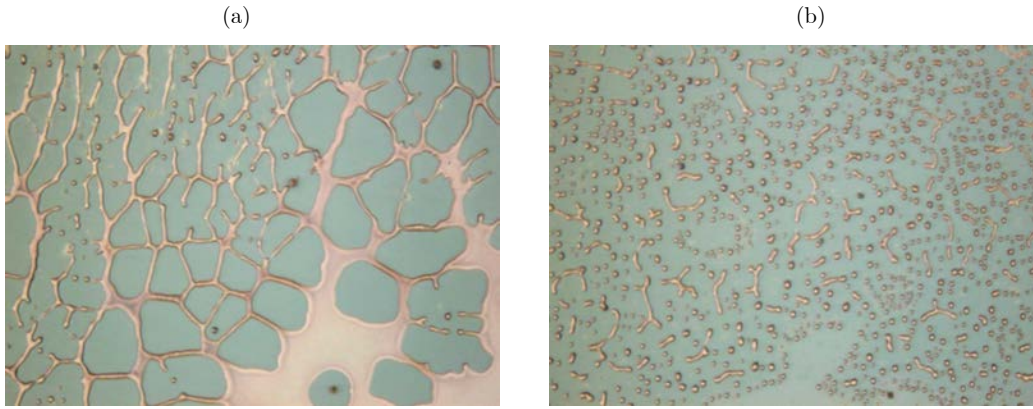


**Figure 5.20.** LSM images of the initial stages of the dewetting process on a 10 nm thick Cu layer on a Si wafer after  $n = 200$  laser pulses. (a) shows a region where the polygons are still present and (b) shows a later stage where the net structure is already partially broken and single nanoparticles start to form. Images show areas of  $90 \times 66 \mu\text{m}^2$ .

Interestingly in the literature it is found that those structures are a chronological procedure with increasing laser pulses from (a)  $\rightarrow$  (b), meaningly increased deposited energy [129, 130, 131]. In the experiments presented here, the structures have been formed within the same laser spot, hence the same amount of subsequent pulses. However, it is observed that the structures induced for lower energy input, hence earlier stages of the PLiD formation, (5.20 (a)) are mostly found at the edges of the laser spot, where the deposited energy is lower. Furthermore this could also be an effect of the inhomogeneous laser profile shown in figure 5.2.

According to the TFH model the polygons and particles do not arbitrarily form on the surface with random sizes and distributions but they follow certain analytical solutions to the instability theory. The characteristic spinodal length, hence the spacings between the polygons can be written as:

$$\Lambda(h, T) = \sqrt{\frac{16\pi^3\gamma(T)}{A(T)}} \cdot h^2 \quad (5.11)$$

where  $\gamma(T)$  is the surface tension,  $A(T)$  is the Hamaker constant and  $h$  is the film thickness on the Si wafer. For the final stage, when the nanoparticles

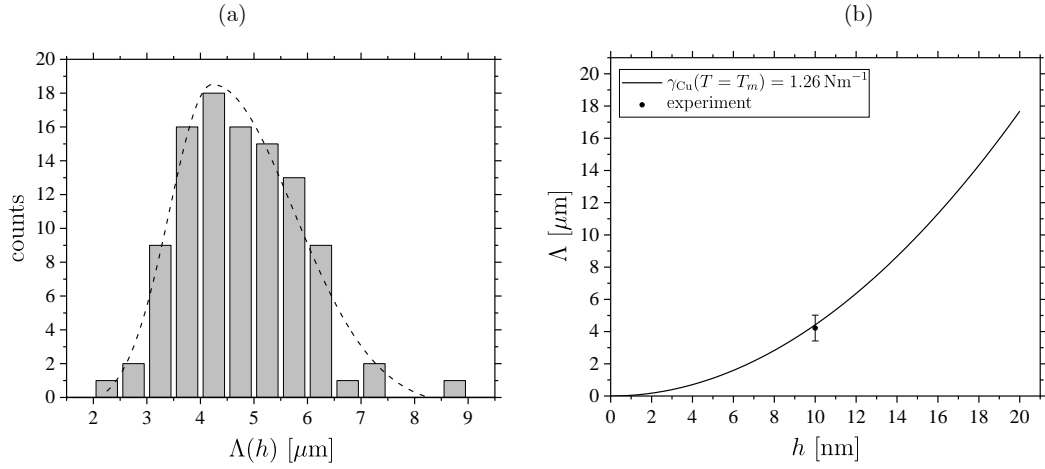


**Figure 5.21.** Evaluation of the average spacings between the spinodal net structure observed in the experiments. (a) shows the experimental data, meaningly the histogram evaluated from 5.20 (a) and (b) shows the theoretical values obtained from the linear TFH theory.

have formed, their mean diameter is described by:

$$\bar{D}_{\text{PLiD}}(h, T) = \left( \frac{24\pi^3\gamma(T)}{A(T)f(\theta)} \right)^{1/3} \cdot h^{5/3} \quad (5.12)$$

where  $f(\theta)$  is a geometric function depending on the contact angle of the droplets on the surface. The density of the nanoparticles can eventually be described in terms of the spinodal length as

$$N_{\text{PLiDS}}(h, T) = \frac{A(T)}{4\pi^4\gamma(T)} \cdot h^{-4} = \left( \frac{1}{4}\pi\Lambda(h)^2 \right)^{-1}. \quad (5.13)$$

Those properties can be calculated using the material constants and the film thickness of the Cu layer. For the surface tension at the melting point the data found in the literature vary between 1.26 N/m and 1.40 N/m. Here the data are taken from Passerone et al. as  $\gamma_{\text{Cu}}(T = T_m) = 1.4 \text{ N/m}$  [132]. The Hamaker constant of Copper is taken from [133] as  $A_{\text{Cu}} = 32 \times 10^{-20} \text{ J}$ . Figure 5.21 (a) shows the histogram of the spinodal length evaluated from figure 5.20 (a), hence a 10 nm Cu layer. after  $n = 200$  laser pulses. A bi-Gaussian function is fitted and the centre value is deduced to be  $\bar{\Lambda}(h = 10 \text{ nm}) = (4.22 \pm 0.8) \mu\text{m}$ . the analytical expression from equation 5.11 with the according spacing calculated from the histogram is plotted in (b). It can be seen that the experimental data fit the linear TFH within the error range.

As can be seen from equations 5.11, 5.12 and 5.13 (which is a function of  $(\Lambda)$ ) the respective properties are functions not only of the film thickness  $h$  but also on the temperature,  $T$ . Due to the inhomogeneity of the laser-profile and other parameters it is not straight forward to solve the heat equation and determine a temperature profile across the laser-spot. It can be seen that the analytical expressions for the different parameters,  $\Lambda$  and  $\bar{D}_{\text{PLiD}}$ , (in the following generalized as  $\chi$ ) follow a  $(\gamma(T)/A(T))^{1/n}$  law.

The sensitivity of the quantities on the temperature can be derived by differentiating equations 5.11-5.13 with respect to  $T$ . In general it is:

$$\chi(T, h) = C_j(h) \left[ \frac{\gamma(T)}{A(T)} \right]^{\frac{1}{n}} \begin{cases} C_j = \left( \frac{24\pi^3}{f(\theta)} \right)^{1/3} h^{5/3} & \text{and } n = 3 \text{ for } \chi = \bar{D} \\ C_j = \sqrt{16\pi^3} h^2 & \text{and } n = 2 \text{ for } \chi = \Lambda \end{cases} \quad (5.14)$$

Then the temperature sensitivity can be written as

$$\frac{\partial \chi(T, h)}{\partial T} = C_j(h) \left( \frac{\partial}{\partial T} \frac{\gamma(T)}{A(T)} \right)^{\frac{1}{n}} \quad (5.15)$$

$$= C_j(h) \left[ \frac{\gamma(T)}{A(T)} \right]^{\frac{1}{n}-1} \left[ \frac{\partial \gamma(T)}{\partial T} \frac{1}{nA(T)} - \frac{\partial A(T)}{\partial T} \frac{\gamma(T)}{nA(T)^2} \right]. \quad (5.16)$$

This can be simplified using the work of French et al. who have shown that the Hamaker constant is a very weak function of the temperature in the case of metals [134]. Then  $\partial A/\partial T \approx 0$  and the equation reads as follows:

$$\frac{\partial \chi(T, h)}{\partial T} = C_j(h) \left[ \frac{\gamma(T)}{A(T)} \right]^{\frac{1}{n}-1} \frac{\partial \gamma(T)}{\partial T} \frac{1}{nA(T)} \quad (5.17)$$

$$= C_j(h) \left[ \frac{\gamma(T)}{A(T)} \right]^{\frac{1}{n}} \frac{\partial \gamma(T)}{\partial T} \frac{1}{n\gamma(T)} \quad (5.18)$$

$$= \chi(T, h) \frac{\partial \gamma(T)}{\partial T} \frac{1}{n\gamma(T)}. \quad (5.19)$$

The linear temperature dependence of the surface tension for Cu is calculated from [132] as  $\partial \gamma/\partial T = -2.3 \times 10^{-4} \text{ N m}^{-1} \text{ K}^{-1}$ . From equation 5.19 it can be seen that the deviation of the properties with respect to the temperature is proportional to the quantity itself multiplied with a factor depending on the temperature gradient of the surface tension. Inserting the values and

changing from a continuous to a discrete description for a temperature rise  $\Delta T$  above the melting temperature  $T_m$  for a Cu layer with a given thickness  $h$  we get:

$$\Delta\chi(\Delta T) \approx -3.2 \times 10^{-4} \cdot \frac{\chi(T_m, h)}{n} \frac{\Delta T}{[\text{K}]} \quad (5.20)$$

From this equation it can be seen that even for a temperature rise  $\Delta T = 500$  K above the melting point the deviation is small in the range of  $\sim 7\%$ . This is within the error range of the experimental determined values.

As the dewetting process further moves on the polygon structure, seen in figure 5.20, breaks and single nanoparticles start to form. SEM images of the resulting particle formation on the Cu layer is shown in figure 5.22. It can be seen that almost all the polygons are broken up and the single particles are homogeneously distributed throughout the whole area. For the quantitative evaluation, the images are pre-processed in the software Gwyddion via a 2-dimensional continuous wavelet transformation to get rid of pixel artifacts and subsequently the nanoparticles are detected via a threshold algorithm and the diameter of the particles is calculated. The histogram in figure 5.22 shows the particle diameter distribution with the according fit function. However, it can be seen that the distribution of the particles is not a Gaussian or Voigt like distribution but rather asymmetric and the fitting procedure for the histogram is inaccurate. Nevertheless, from this distribution the mean diameter can be calculated and compared with the TFH instability. In this case the distribution shows a mean diameter of  $\bar{D}_{\text{PLiD}} = (641 \pm 22)$  nm. The particles with radius  $\bar{D}_{\text{PLiD}} < 250$  nm are cut off due to a lack of resolution of the used SEM. Furthermore the results of the nanoparticle formation concerning the particles diameter varied from probe to probe under otherwise similar irradiation conditions. Quantitatively the diameter varied from  $\bar{D}_{\text{PLiD}} \in [482, 676]$  nm. This might be due to the inhomogeneity of the laser itself. Another fact that needs to be taken into account is the fact that the linear TFH theory is based on the assumption that temperature gradients in the axial direction of the Cu layer are neglected and the heat loss is primarily through conduction across the layer. This requires the following inequation for the film thickness  $h < \alpha_{\text{Cu}}^{-1}$ , where  $\alpha_{\text{Cu}}$  is the absorptivity of copper. Depending on different sources in the literature the 10 nm layers studied in this thesis are right at the edge to fulfill the inequation and therefore the assumptions in the analytical model.

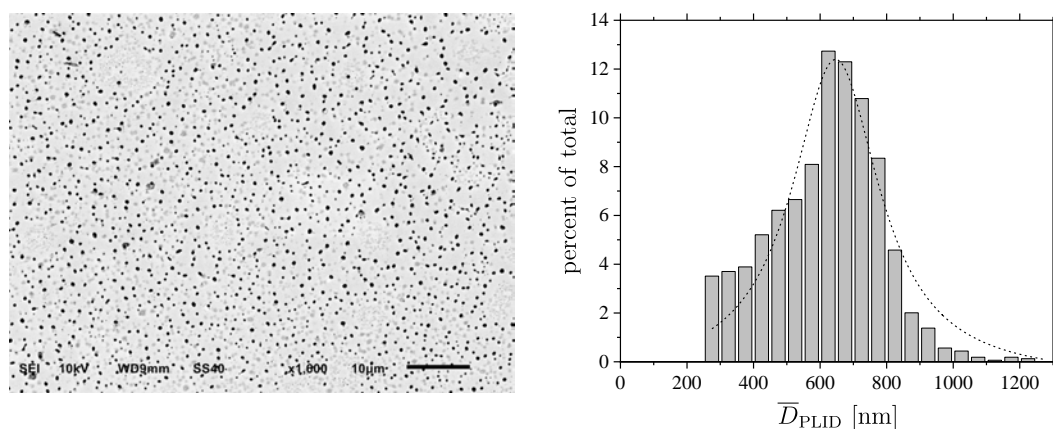


**Figure 5.22.** SEM image of the nanoparticles created by laser irradiation of a 10 nm thick Cu layer. the histogram shows the mean diameter distribution of the particles with a fitted Gaussian function. The image covers a region of  $(80 \times 60 \mu\text{m}^2)$ .

Therefore deviations from probe to probe may also originate from the degree of applicability of the model depending on the layer conditions.

Another interesting feature was observed by incidence when investigating different samples. Figure 5.23 shows another, slightly larger, SEM image of a sample that was irradiated under the same conditions as the image shown in figure 5.22. Here, it can be seen by eye that two different regions with two different morphologies have formed. While the majority of the image shows the same nanoparticles, as already observed in figure 5.22, the bottom right part (red encircled) shows different properties. The nanoparticles are smaller and also denser in this area. This is also obvious, when evaluating the histogram of the image of the mean diameters. Two distinct peaks can be seen. The first higher peak, with a high density of nanoparticles, shows a mean diameter of  $\bar{D}_{\text{PLiD}} = (322 \pm 15) \text{ nm}$ . This peak belongs to the red encircled area. the second peaks shows a similar mean diameter as the one before. The fit function gives  $\bar{D}_{\text{PLiD}} = (524 \pm 17) \text{ nm}$ . As shown by equation 5.20, the diameter is not very sensitive to temperature fluctuations. Therefore the smaller diameter is not likely to be an effect of the laser inhomogeneity. According to the TFH theory the determined diameter of  $\sim 322 \text{ nm}$  would match a film thickness of  $h \sim 7 \text{ nm}$ . Therefore this might rather be an effect of a fluctuating film thickness during the coating process.

Figure 5.24 shows the properties, mean diameter, density, and inter spinodal

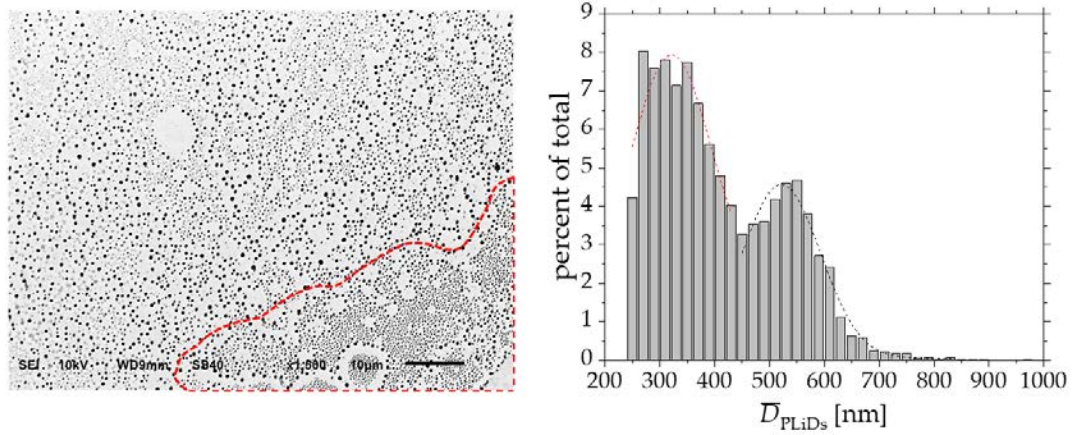


**Figure 5.23.** SEM image of PLiDs induced by laser irradiation of a 10 nm thick Cu layer. On the SEM image two distinct morphologies with nanoparticles of different sizes is observed. This can also be seen by the two separated peaks in the histogram.

spacing, as calculated by the TFH theory compared with the experiments in this study. The experimental data are gathered from different irradiated samples and the range of data is shown in the plots as a shaded area with the respective color. It can be seen that the results for the inter spinodal spacings and the mean diameter fit well to the theory, although the deviations from the different measurements are rather large and only contingently reproducible. Nevertheless, this gives rise to the fact that a dewetting process is induced by the pulsed laser irradiation. Interestingly, despite the fact that the inter spinodal spacings are well represented by the theory the density of particles,  $N_{\text{PLiD}}$ , shows large deviations (note the logarithmic scale). This is interesting considering the fact that they are functions of each other,  $N_{\text{PLiDs}} = f(\Lambda)$ . According to the theory the nanoparticles are created due to the breakup of the polygonal structure owing to either a Rayleigh instability or capillary effects [135]. Following this physical mechanism the particles are created at the junctions of the polygons and hence  $\Lambda$  is connected to  $N_{\text{PLiDs}}$ . The fact that the density is significantly lower in the experiments shows that here not at every junction a particle is formed.

Furthermore, areas with different characteristic were observed on many irradiated samples. After the irradiation of the Cu samples in certain areas circular pattern of Cu PLiDs have formed. Those circular structures are formed

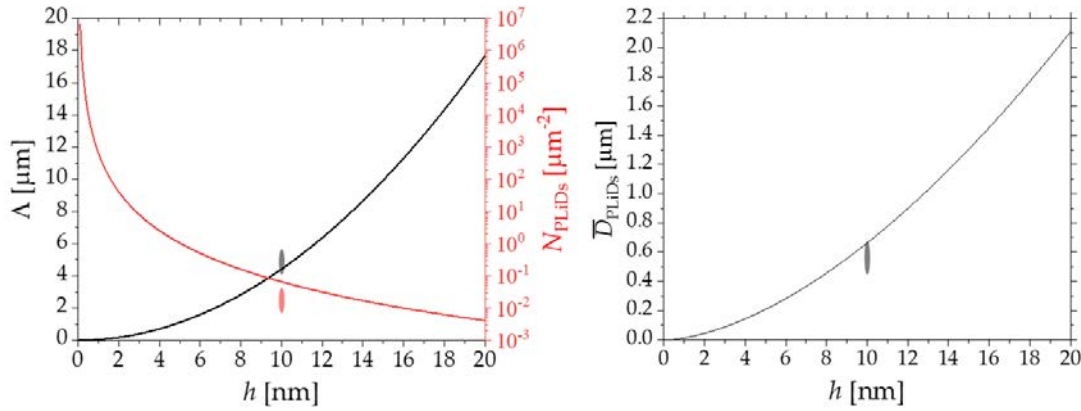


**Figure 5.24.** Comparisons of the linear TFH model against the experimental data. Displayed here are the interspinodal spacing,  $\Lambda$ , the density of particles,  $N_{\text{PLiD}}$  and the mean diameter  $D_{\text{PLiD}}$ . The range of experimental results from different probes is shown as filled areas in the according color. The surface tension taken from [136] and used for the model is  $\gamma_{\text{Cu}} = 1.26 \text{ N/m}$

by smaller nanoparticles and are surrounded by larger radii structures of nanoparticles with a bigger diameter. An example of such structures is seen in figure 5.25 Similar findings have been observed by the group of Wu et al.. They reported on a certain type of breakup of these structures on a Cu sample, where they first induced narrow rings with a narrow radial profile. They attributed these types of structures to a Rayleigh-Plateau instability. For rings with a greater radius of  $r > 265 \text{ nm}$  they ascribed the formation to thin film instability [137]. The rings observed in this study have large diameters in the range  $r \sim \mu\text{m}$ . This potentially supports the thesis that he induced nanoparticles are a phenomenon caused by the thin film hydrodynamic instability.

However, these ring like structures are randomly distributed across the samples and no real scheme of laser or surface parameters can be deduced that correlate with the orientation or position of these structures. Furthermore, they are not induced on every irradiated sample but partially observed. Therefore, these structures are not really a controllable inducible feature, nevertheless an interesting formation mechanism that can be further investigated and tried to be controlled.

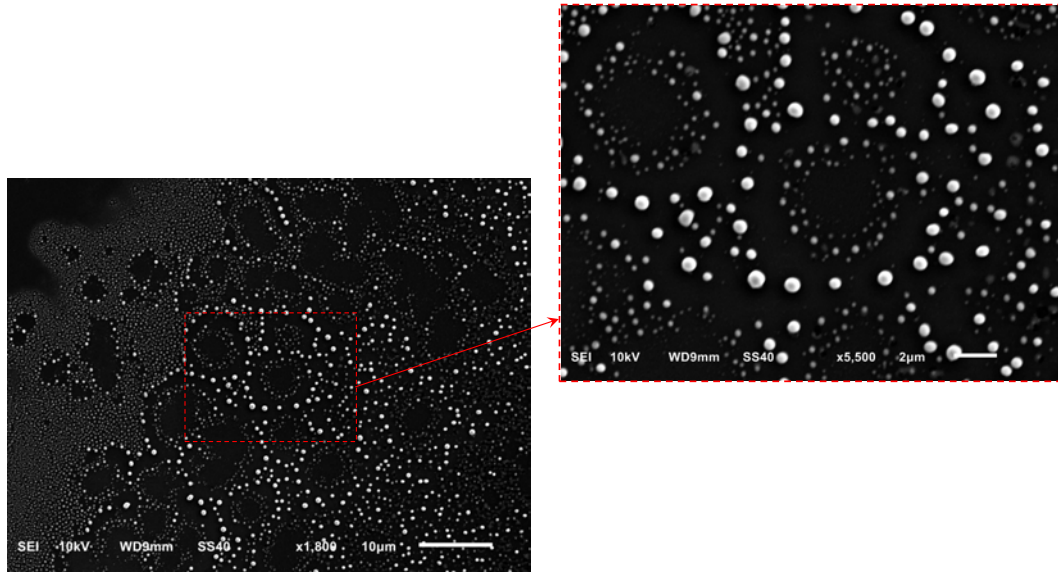


**Figure 5.25.** Circular structures induced on a 10 nm thick Cu layer irradiated by a  $\pi$ -polarized laser of the wavelength of  $\lambda_L=532$  nm.

#### 5.4.1 Summary of PLiDs experiments

Pulsed Laser induced Dewetting structures have been observed on 10 nm thick Cu layers on a Si substrate and are compared to the thin film hydrodynamic dewetting theory (TFH).

The nanoparticles were induced on almost every irradiated sample. In the center of the laser spot a large area of homogeneous particles is induced as seen in figure 5.19. The induction of the particles is reproducible even on a large scale, however, the mean diameter and density of the particles varied from probe to probe with otherwise similar irradiation and surface parameters. Furthermore on different probes several structures like polygons, which are the early stages of PLiD formation, nanoparticles with different size distributions or ring like structures formed from nanoparticles and also LIPSS are observed at the same time. This might be an effect of laser inhomogeneities or small fluctuations in the film thickness. The experimental data fit the TFH model partially when it comes to the inter spinodal spacings,  $\Lambda$  and the mean diameter of the particles  $\bar{D}_{\text{PLiDS}}$ , which supports the theory of induced dewetting effects by the pulsed laser irradiation. However, concerning the density of nanoparticles deviations from the theory are observed. Due to the fact that the density is a function of the inter spinodal spacing here the explanation of

capillary effects and the creation of nanoparticles at the junctions of the polygons does not hold and other effects might (additionally) be responsible for the formation.

## Chapter 6

# Summary and Further Research

The main aim of the B2 project is to investigate the simultaneous interaction between three main components: a plasma source, a laser and a solid state, the sample. To fully understand the complex interactions during all the processes, it is crucial to investigate the interaction between the single components beforehand. These component independent measurements, that are crucial to eventually decipher and understand the simultaneous processes, were performed in this work.

The first main question that this thesis addressed was the density distribution of reactive species that are generated inside the active plasma region of the COST-Jet and are eventually transported into the effluent region, towards a potential sample to be treated. In this case the reactive species of choice was set to be nitric oxide. This decision was made, based on the fact that nitric oxide is an important extracellular messenger and an important molecule to trigger different biological processes, hence its fundamental importance for applications involving biological samples.

In this work, this was done first by the investigation of distributions of nitric oxide in the free effluent i.e. without any sample being placed in front of the jet. This was done by means of Laser Induced Fluorescence Spectroscopy (LIF).

Prior to the distribution measurements, the main plasma parameters for the most effective production of NO, such as used gas mixture ratio, absolute gas mixture or plasma power were investigated. Here it was found, that an admixture of 0.5 % of synthetic air ( $N_2/O_2 = 4$ ) to the helium feed gas flow is the most efficient way to create NO, although higher absolute values of NO can

be achieved by adding 5 sccm of  $N_2$  and  $O_2$  each, which is owed to higher applicable powers as compared to the synthetic air admixture. By normalizing the NO density to the dissipated power it was found, that indeed synthetic air admixture is most efficient.

Subsequently, the NO distributions with 3-dimensional spatial resolution were measured in different atmospheres, namely in air and controlled He+0.5 % air. From the time resolved LIF measurements, the lifetime of the upper NO(A) state was measured and from the reduction of its lifetime, the quenching rate coefficient of different quenchers were deduced. It was found that quenching by helium is negligible, while the quenching in air is very fast and efficient. This is solely due to the oxygen content, while quenching by nitrogen is negligible. Furthermore, it was possible to calculate the intrusion of the surrounding air into the helium gas stream. Here it was revealed that the reactive species are well shielded from their surrounding up to  $z \approx 15$  mm, while at greater distances large amount of air intrudes and disturbs the NO distribution.

It was also found that NO particles are closely coupled to the helium feed gas flow. This was found by the buoyancy character of the NO distribution, although  $\rho_{NO} > \rho_{air}$ . The trajectory of helium particles in air was then calculated by a single particle approach taking into account Stokes friction. Excellent agreement was found, verifying the assumption of the NO-He coupling. From the spatial resolved NO distributions it was found that the NO tends to form turbulence like behavior in air. This is not due to an excess of the critical Reynolds number, but is induced by quenching and momentum transfer from the surrounding air particles, hence elastic and inelastic collisions. In the helium atmosphere it was found that NO propagates laminar even at great axial distances. The radial transport of NO is solely driven by free diffusion, as was shown by the excellent agreement of the measured distributions and the solution of the diffusion equation, without any chemical reactions. Those findings are a central aspect for applications of the jet, where typically a sample is placed in the effluent to be treated. As further research, it would be interesting to establish a model, when the jet is operated in air, that includes

the reaction term in the reaction diffusion equation, as follows:

$$\frac{\partial}{\partial t} n_{\text{NO}}(\vec{r}, t) = D\Delta n_{\text{NO}}(\vec{r}, t) + \underbrace{f(n_1 \dots n_{i-1}, n_i)}_{\text{reaction term}}. \quad (6.1)$$

However, this is challenging, since the absolute numbers of constituents of the atoms and molecules in air and the impurities ( $n_1 \dots n_i$ ) are usually not known and a very complex plasma chemistry of coupled kinetics take place. Therefore, either more data about the reaction partners need to be collected, or the initial values need to be assumed by the modelers.

The second question that was addressed is the density distribution in front of different samples and how they affect the density distributions, when comparing them to the ones measured in the free effluent. This is a crucial point, because the density must not exceed certain critical values, to ensure that e.g., biological system remains intact and are not damaged. To do so, different samples of different materials have been placed in the effluent to investigate the influence of those samples on the density distribution as compared to the ones measured in the free effluent. Here it was found that a distinct maximum develops in front of the surface for several materials, which is most pronounced in the case of aluminum. This is on the one hand an effect of the reflection of the fluorescence signal from the surface into the detection system, on the other hand it was found by simulation taking into account the geometry of the setup that the back reflection cannot be the sole reason for this effect. To appropriately understand the observations from the experiments, a detailed surface kinetics model would be needed. By simulations of the helium gas flow towards the surface and a comparison to the measured distributions it was found that the coupling of NO to helium is not only valid in the free effluent but also holds in front of the surface as well. Here further research should focus on the solution of the (reaction) diffusion towards the surface. Close to the surface, in the stationary layer, the transport of particles is solely driven by diffusion. hence, equation 6.1 also holds. At the surface the following boundary conditions can be applied:

$$\Phi^- = (1 - \gamma_j)\Phi^+ \quad (6.2)$$

where  $\Phi^\pm$  are the reflected flux (-) and the flux towards the wall, respectively.  $\gamma_j$  is the wall loss probability of particles that arrive at the surface. Furthermore from fundamental kinetic theory it is in the 1-dimensional case:

$$\Phi^\pm = \frac{n_{\text{NO}} \langle v \rangle}{4} \Big|_{x=S_b} \pm \frac{D}{2} \frac{\partial n_{\text{NO}}}{\partial x} \Big|_{x=S_b}, \quad (6.3)$$

where  $\langle v \rangle$  is the average velocity of the particles and  $S_b$  the position of the surface. Combining equations 6.2 and 6.3, one eventually gets the boundary condition to be

$$D \frac{\partial n_{\text{NO}}}{\partial x} \Big|_{x=S_b} = -\frac{2\gamma_j}{2-\gamma_j} \frac{n_{\text{NO}} \langle v \rangle}{4} \Big|_{x=S_b} \approx \gamma_j \frac{n_{\text{NO}} \langle v \rangle}{4} \Big|_{x=S_b} \quad \text{for } \gamma_j \ll 1 \quad (6.4)$$

With these boundary conditions it is possible to deduce the wall loss probability coefficient  $\gamma_j$  that implicitly yields information about the chemical kinetics of NO at the surface and allows drawing conclusions about the dynamics.

The species that are transported from the jet into the effluent eventually arrive at the surface and are potentially incorporated into the chemical surface structure. This incorporation can be enhanced by macro- and microscopic surface structures. The inducement of these structures via short pulsed laser irradiation under suitable conditions for the operation of the jet needed to be investigated, afterwards. Here it was shown the Laser Induced Periodic Surface Structures (LIPSS) could be effectively induced on different materials with ns laser pulses. The LIPSS could further be tuned by several parameters, such as the incident angle, the polarization, and the wavelength of the laser. The results were compared to several theories in the field and it was found that the periodicity, as well as the orientation of the induced structures with respect to the electric field vector of the laser could be accurately described by Sipe's theory.

Beside the induced LIPSS, another feature was observed solely on 10 nm copper surfaces. Here nanoparticles were induced on large scales. Those nanoparticles are supposed to be induced by Pulsed Laser induced Dewetting (PLiD). This is assumed by a typical chronological evolution of the morphological

structures, where first a characteristic polygon structure is formed on the surface that eventually breaks up into single particles. The spinodal spacing between the polygons and the average diameter of the PLiDs as well as the areal density were compared to a theory according to a thin film hydrodynamic instability (TFH), which is induced by the dewetting effect. The results of the experiment are consistent with the theory, which supports the assumption of a laser induced dewetting effect and the resulting nanoparticle formation.

From the LIPSS and the PLiDs formation it was shown that a variety of different surface structures could be induced on surfaces made of material with catalytic properties, under conditions suitable for the operation of the jet. This is an important finding and the subsequent simultaneous interaction with the reactive species needs to be investigated in the future. In the future, the COST-Jet will be further used for the treatment and modification of biological and non-biological samples. In this context, the density distributions in front and at the surfaces are crucial. Here it will be necessary to figure out the reflection issue of the surface and to reveal the chemical kinetics by a detailed surface kinetic model.

Concerning the PLiDs formation on the surface, only 10 nm copper samples were available at the times of the experiments. The TFH theory mainly holds for layers that are in the sub 10 nm range. Here it would be necessary to perform a layer thickness variation, to compare the results in this parameter space with the theory, to see how the mean diameter and the areal density vary with layer thickness.

Furthermore, the simultaneous interaction of both, the reactive species coming from the jet and the induced structures on the surface needs to be investigated. Here, the plasma source needs to be synchronized with the laser source. XPS measurements need to be performed in order to investigate the influence of the laser induced structures on the chemical bondings on the surface and potential synergisms concerning the incorporation of species into the surface concerning the catalytic activity.

In conclusion, the findings in this thesis are of central importance towards further research. The investigation of the interaction and the unveiling of

the physical mechanisms of the single components form the foundation towards further experiments and understanding of the complex laser-plasma-solid system.

## Bibliography

- [1] Mick Donegan, Vladimir Milosavljević, and Denis P. Dowling. “Activation of PET Using an RF Atmospheric Plasma System”. In: *Plasma Chemistry and Plasma Processing* 33.5 (2013), pp. 941–957. ISSN: 1572-8986. DOI: [10.1007/s11090-013-9474-4](https://doi.org/10.1007/s11090-013-9474-4).
- [2] Zhi Fang et al. “Hydrophobic surface modification of epoxy resin using an atmospheric pressure plasma jet array”. In: *IEEE Transactions on Dielectrics and Electrical Insulation* 23.4 (2016), pp. 2288–2293. ISSN: 1070-9878. DOI: [10.1109/tdei.2016.7556505](https://doi.org/10.1109/tdei.2016.7556505).
- [3] A. J. Knoll et al. “Real time characterization of polymer surface modifications by an atmospheric-pressure plasma jet: Electrically coupled versus remote mode”. In: *Applied Physics Letters* 105.17 (2014), p. 171601. ISSN: 0003-6951. DOI: [10.1063/1.4900551](https://doi.org/10.1063/1.4900551).
- [4] Aline C. Borges et al. “Applications of Cold Atmospheric Pressure Plasma in Dentistry”. In: *Applied Sciences* 11.5 (2021), p. 1975. ISSN: 2076-3417. DOI: [10.3390/app11051975](https://doi.org/10.3390/app11051975). URL: <https://www.mdpi.com/1009388>.
- [5] Hiromitsu Yamazaki et al. “Microbicidal activities of low frequency atmospheric pressure plasma jets on oral pathogens”. In: *Dental Materials Journal* 30.3 (2011), pp. 384–391. ISSN: 1881-1361. DOI: [10.4012/dmj.2010-190](https://doi.org/10.4012/dmj.2010-190). URL: [https://www.jstage.jst.go.jp/article/dmj/30/3/30\\_2010-190/\\_article/-char/ja/](https://www.jstage.jst.go.jp/article/dmj/30/3/30_2010-190/_article/-char/ja/).
- [6] Andrei Vasile Nastuta et al. “Stimulation of wound healing by helium atmospheric pressure plasma treatment”. In: *Journal of Physics D: Applied Physics* 44.10 (2011), p. 105204. ISSN: 0963-0252. DOI: [10.1088/0022-3727/44/10/105204](https://doi.org/10.1088/0022-3727/44/10/105204).
- [7] Gui-Min Xu et al. “Dual effects of atmospheric pressure plasma jet on skin wound healing of mice”. In: *Wound Repair and Regeneration* 23.6 (2015), pp. 878–884. ISSN: 1524-475X. DOI: [10.1111/wrr.12364](https://doi.org/10.1111/wrr.12364).

- [8] Abdel-Aleam H. Mohamed et al. "Atmospheric pressure plasma jet for bacterial decontamination and property improvement of fruit and vegetable processing wastewater". In: *Journal of Physics D: Applied Physics* 49.19 (2016), p. 195401. ISSN: 0963-0252. DOI: [10.1088/0022-3727/49/19/195401](https://doi.org/10.1088/0022-3727/49/19/195401).
- [9] María C. García et al. "Microwave atmospheric pressure plasma jets for wastewater treatment: Degradation of methylene blue as a model dye". In: *Chemosphere* 180 (2017), pp. 239–246. DOI: [10.1016/j.chemosphere.2017.03.126](https://doi.org/10.1016/j.chemosphere.2017.03.126).
- [10] Jaime Wisniak. "The History of Catalysis. From the Beginning to Nobel Prizes". In: *Educación Química* 21.1 (2010), pp. 60–69. ISSN: 0187893X. DOI: [10.1016/S0187-893X\(18\)30074-0](https://doi.org/10.1016/S0187-893X(18)30074-0).
- [11] Jöns-Jakob Berzelius. *Théorie des proportions chimiques, et table synoptique des poids atomiques, des corps simples, et de leurs combinaisons les plus importantes*. Didot, 1835.
- [12] NobelPrize.org. *The Nobel Prize in Chemistry 1909*. 4.05.2022. URL: <https://www.nobelprize.org/prizes/chemistry/1909/ostwald/biographical/>.
- [13] A. Gicquel, S. Cavadias, and J. Amouroux. "Heterogeneous catalysis in low-pressure plasmas". In: *Journal of Physics D: Applied Physics* 19.11 (1986), pp. 2013–2042. ISSN: 0963-0252. DOI: [10.1088/0022-3727/19/11/003](https://doi.org/10.1088/0022-3727/19/11/003). URL: <https://iopscience.iop.org/article/10.1088/0022-3727/19/11/003>.
- [14] Akira Mizuno, A. Chakrabarti, and Ken Okazaki. "Application of Corona Technology in the Reduction of Greenhouse Gases and other Gaseous Pollutants". In: *Non-Thermal Plasma Techniques for Pollution Control*. Ed. by Bernie M. Penetrante and Shirley E. Schultheis. NATO ASI Series, Series G. Berlin and Heidelberg: Springer, 1993, pp. 165–185. ISBN: 978-3-642-78478-1. DOI: [10.1007/978-3-642-78476-7\\_{\\\_}14](https://doi.org/10.1007/978-3-642-78476-7_{\_}14).
- [15] Ludwig Boltzmann. "On the nature of gas molecules". In: *The London, Edinburgh, and Dublin Philosophical Magazine and Journal of Science* 3.18 (1877), p. 320. ISSN: 1941-5982. DOI: [10.1080/14786447708639243](https://doi.org/10.1080/14786447708639243).

- [16] Annemie Bogaerts et al. “The 2020 plasma catalysis roadmap”. In: *Journal of Physics D: Applied Physics* 53.44 (2020), p. 443001. ISSN: 0963-0252. DOI: [10.1088/1361-6463/ab9048](https://doi.org/10.1088/1361-6463/ab9048). URL: <https://iopscience.iop.org/article/10.1088/1361-6463/ab9048/meta>.
- [17] Christopher Dawes. *Laser welding: A practical guide*. Cambridge: Abington Publ, 1992. ISBN: 9781855730342.
- [18] V. Senthilkumar. *Laser cutting process-A review*. 2014. URL: [https://www.researchgate.net/profile/senthilkumar-vagheesan/publication/305385939\\_laser\\_cutting\\_process\\_-\\_a\\_review/links/57fa48d108ae8da3ce5ba61laser-cutting-process-a-review.pdf](https://www.researchgate.net/profile/senthilkumar-vagheesan/publication/305385939_laser_cutting_process_-_a_review/links/57fa48d108ae8da3ce5ba61laser-cutting-process-a-review.pdf).
- [19] Milton Birnbaum. “Semiconductor Surface Damage Produced by Ruby Lasers”. In: *Journal of Applied Physics* 36.11 (1965), pp. 3688–3689. ISSN: 0021-8979. DOI: [10.1063/1.1703071](https://doi.org/10.1063/1.1703071).
- [20] Jorn Bonse et al. “Laser-Induced Periodic Surface Structures— A Scientific Evergreen”. In: *IEEE Journal of Selected Topics in Quantum Electronics* 23.3 (2017). ISSN: 1077-260X. DOI: [10.1109/JSTQE.2016.2614183](https://doi.org/10.1109/JSTQE.2016.2614183).
- [21] Karsten Lange, Malte Schulz-Ruhtenberg, and Jürgen Caro. “Platinum Electrodes for Oxygen Reduction Catalysis Designed by Ultrashort Pulse Laser Structuring”. In: *ChemElectroChem* 4.3 (2017), pp. 570–576. ISSN: 21960216. DOI: [10.1002/ce1c.201600630](https://doi.org/10.1002/ce1c.201600630).
- [22] Alex R. Neale et al. “Electrochemical performance of laser micro-structured nickel oxyhydroxide cathodes”. In: *Journal of Power Sources* 271 (2014), pp. 42–47. ISSN: 0378-7753. DOI: [10.1016/j.jpowsour.2014.07.167](https://doi.org/10.1016/j.jpowsour.2014.07.167).
- [23] Fabio Raimondi et al. “Nanoparticles in energy technology: examples from electrochemistry and catalysis”. In: *Angewandte Chemie (International ed. in English)* 44.15 (2005), pp. 2190–2209. ISSN: 1433-7851. DOI: [10.1002/anie.200460466](https://doi.org/10.1002/anie.200460466).
- [24] Andrzej Wieckowski, Elena R. Savinova, and Constantinos G. Vayenas. *Catalysis and electrocatalysis at nanoparticle surfaces*. New York: Marcel Dekker, 2003. ISBN: 9780203912713.
- [25] J. Golda et al. “Concepts and characteristics of the ‘COST Reference Microplasma Jet’”. In: *Journal of Physics D: Applied Physics* 49.8 (2016), p. 084003. ISSN: 0963-0252. DOI: [10.1088/0022-3727/49/8/084003](https://doi.org/10.1088/0022-3727/49/8/084003).

- [26] Y. Gorbanev et al. "Combining experimental and modelling approaches to study the sources of reactive species induced in water by the COST RF plasma jet". In: *Physical Chemistry Chemical Physics* 20.4 (2018), pp. 2797–2808. ISSN: 1463-9084. DOI: [10.1039/C7CP07616A](https://pubs.rsc.org/en/content/articlehtml/2018/cp/c7cp07616a). URL: <https://pubs.rsc.org/en/content/articlehtml/2018/cp/c7cp07616a>.
- [27] N. Knake et al. "Absolute atomic oxygen density distributions in the effluent of a microscale atmospheric pressure plasma jet". In: *Journal of Physics D: Applied Physics* 41.19 (2008), p. 194006. ISSN: 0963-0252. DOI: [10.1088/0022-3727/41/19/194006](https://doi.org/10.1088/0022-3727/41/19/194006).
- [28] Gert Willems, Jan Benedikt, and Achim von Keudell. "Absolutely calibrated mass spectrometry measurement of reactive and stable plasma chemistry products in the effluent of a He/H<sub>2</sub>O atmospheric plasma". In: *Journal of Physics D: Applied Physics* 50.33 (2017), p. 335204. ISSN: 0963-0252. DOI: [10.1088/1361-6463/aa77ca](https://doi.org/10.1088/1361-6463/aa77ca). URL: <https://iopscience.iop.org/article/10.1088/1361-6463/aa77ca/meta>.
- [29] J. Waskoenig et al. "Atomic oxygen formation in a radio-frequency driven micro-atmospheric pressure plasma jet". In: *Plasma Sources Science and Technology* 19.4 (2010), p. 045018. ISSN: 0022-3727. DOI: [10.1088/0963-0252/19/4/045018](https://doi.org/10.1088/0963-0252/19/4/045018).
- [30] I. Langmuir. "Oscillations in Ionized Gases". In: *Proceedings of the National Academy of Sciences of the United States of America* 14.8 (1928), pp. 627–637. ISSN: 0027-8424. DOI: [10.1073/pnas.14.8.627](https://doi.org/10.1073/pnas.14.8.627).
- [31] Youfan He et al. "Zero-dimensional and pseudo-one-dimensional models of atmospheric-pressure plasma jets in binary and ternary mixtures of oxygen and nitrogen with helium background". In: *Plasma Sources Science and Technology* 30.10 (2021), p. 105017. ISSN: 0022-3727. DOI: [10.1088/1361-6595/ac278d](https://doi.org/10.1088/1361-6595/ac278d).
- [32] A. Tejero-del Caz et al. "The LisbOn KInetics Boltzmann solver". In: *Plasma Sources Science and Technology* 28.4 (2019), p. 043001. ISSN: 0022-3727. DOI: [10.1088/1361-6595/ab0537](https://doi.org/10.1088/1361-6595/ab0537).
- [33] M. Capitelli et al. "On the relaxation of electron energy distribution function in LIBS plasmas". In: *Chemical Physics Letters* 316.5-6 (2000), pp. 517–523. ISSN: 00092614. DOI: [10.1016/S0009-2614\(99\)01318-4](https://doi.org/10.1016/S0009-2614(99)01318-4).

- [34] Mario Capitelli et al. "Coupling of Plasma Chemistry, Vibrational Kinetics, Collisional-Radiative Models and Electron Energy Distribution Function Under Non-Equilibrium Conditions". In: *Plasma Processes and Polymers* 14.1-2 (2017), p. 1600109. ISSN: 16128850. DOI: [10.1002/ppap.201600109](https://doi.org/10.1002/ppap.201600109).
- [35] Marlous Hofmans et al. "Characterization of a kHz atmospheric pressure plasma jet: comparison of discharge propagation parameters in experiments and simulations without target". In: *Plasma Sources Science and Technology* 29.3 (2020), p. 034003. ISSN: 0022-3727. DOI: [10.1088/1361-6595/ab6d49](https://doi.org/10.1088/1361-6595/ab6d49).
- [36] B. F. Gordiets et al. "Kinetic model of a low-pressure N<sub>2</sub>/O<sub>2</sub> flowing glow discharge". In: *IEEE Transactions on Plasma Science* 23.4 (1995), pp. 750–768. ISSN: 00933813. DOI: [10.1109/27.467998](https://doi.org/10.1109/27.467998).
- [37] Vasco Guerra et al. "Modelling N<sub>2</sub>/O<sub>2</sub> plasmas: volume and surface kinetics". In: *Plasma Sources Science and Technology* 28.7 (2019), p. 073001. ISSN: 0022-3727. DOI: [10.1088/1361-6595/ab252c](https://doi.org/10.1088/1361-6595/ab252c).
- [38] V. Guerra and J. Loureiro. "Self-consistent electron and heavy-particle kinetics in a low-pressure - glow discharge". In: *Plasma Sources Science and Technology* 6.3 (1997), pp. 373–385. ISSN: 0022-3727. DOI: [10.1088/0963-0252/6/3/014](https://doi.org/10.1088/0963-0252/6/3/014).
- [39] V. Guerra and J. Loureiro. "Non-equilibrium coupled kinetics in stationary N<sub>2</sub>/O<sub>2</sub> discharges". In: *Journal of Physics D: Applied Physics* 28.9 (1995), pp. 1903–1918. ISSN: 0963-0252. DOI: [10.1088/0022-3727/28/9/018](https://doi.org/10.1088/0022-3727/28/9/018).
- [40] D. Marinov et al. "Production of molecules on a surface under plasma exposure: example of NO on pyrex". In: *Journal of Physics D: Applied Physics* 43.11 (2010), p. 115203. ISSN: 0963-0252. DOI: [10.1088/0022-3727/43/11/115203](https://doi.org/10.1088/0022-3727/43/11/115203).
- [41] K. Niemi et al. "Diagnostics on an atmospheric pressure plasma jet". In: *Journal of Physics: Conference Series* 71 (2007), p. 012012. ISSN: 0963-0252. DOI: [10.1088/1742-6596/71/1/012012](https://doi.org/10.1088/1742-6596/71/1/012012).

- [42] S. Reuter et al. "Generation of atomic oxygen in the effluent of an atmospheric pressure plasma jet". In: *Plasma Sources Science and Technology* 18.1 (2009), p. 015006. ISSN: 0022-3727. DOI: [10.1088/0963-0252/18/1/015006](https://doi.org/10.1088/0963-0252/18/1/015006).
- [43] N. Knake et al. "Absolute atomic oxygen density distributions in the effluent of a microscale atmospheric pressure plasma jet". In: *Journal of Physics D: Applied Physics* 41.19 (2008), p. 194006. ISSN: 0963-0252. DOI: [10.1088/0022-3727/41/19/194006](https://doi.org/10.1088/0022-3727/41/19/194006).
- [44] Gert Willems et al. "Corrigendum: Characterization of the effluent of a He/O<sub>2</sub> micro-scaled atmospheric pressure plasma jet by quantitative molecular beam mass spectrometry (2010 New J. Phys.12 013021)". In: *New Journal of Physics* 21.5 (2019), p. 059501. ISSN: 0022-3727. DOI: [10.1088/1367-2630/ab1dfc](https://doi.org/10.1088/1367-2630/ab1dfc).
- [45] I. A. Kossyi et al. "Kinetic scheme of the non-equilibrium discharge in nitrogen-oxygen mixtures". In: *Plasma Sources Science and Technology* (1992). ISSN: 0022-3727.
- [46] M. Capitelli, ed. *Plasma Kinetics in Atmospheric Gases*. 31st ed. Springer Series on Atomic, Optical, and Plasma Physics. Springer-Verlag Berlin Heidelberg, 2000.
- [47] L. G. Piper, G. E. Caledonia, and J. P. Kennealy. "Rate constants for deactivation of N<sub>2</sub>A<sup>3</sup>Σ<sub>u</sub><sup>+</sup>, v' = 0, 1 by O". In: *The Journal of Chemical Physics* 75.6 (1981), pp. 2847–2852. ISSN: 0021-9606. DOI: [10.1063/1.442357](https://doi.org/10.1063/1.442357).
- [48] Lawrence G. Piper. "The excitation of O( 1S ) in the reaction between N<sub>2</sub>A<sup>3</sup>Σ<sub>u</sub><sup>+</sup> and O( 3P )". In: *The Journal of Chemical Physics* 77.5 (1982), pp. 2373–2377. ISSN: 0021-9606. DOI: [10.1063/1.444158](https://doi.org/10.1063/1.444158).
- [49] Joseph M. Thomas and Frederick Kaufman. "An Upper Limit on the Formation of NO(X<sup>2</sup>Π<sub>r</sub>) in the reactions N<sub>2</sub>(A<sup>3</sup>Σ<sub>u</sub><sup>+</sup>)+O(<sup>3</sup>P) and N<sub>2</sub>(A<sup>3</sup>Σ<sub>u</sub><sup>+</sup>)+O<sub>2</sub>(X<sup>3</sup>Σ<sub>g</sub><sup>-</sup>) at 298 K". In: *The Journal of Physical Chemistry* 100.21 (1996), pp. 8901–8906. ISSN: 0022-3654. DOI: [10.1021/jp960164v](https://doi.org/10.1021/jp960164v).
- [50] S. de Benedictis and G. Dilecce. "Rate constants for deactivation of N<sub>2</sub>(A) v = 2 – 7 by O, O<sub>2</sub>, and NO". In: *The Journal of Chemical Physics* 107.16 (1997), pp. 6219–6229. ISSN: 0021-9606. DOI: [10.1063/1.474287](https://doi.org/10.1063/1.474287).

- [51] Ivan Shkurenkov et al. "Kinetics of excited states and radicals in a nanosecond pulse discharge and afterglow in nitrogen and air". In: *Plasma Sources Science and Technology* 23.6 (2014), p. 065003. ISSN: 0022-3727. DOI: [10.1088/0963-0252/23/6/065003](https://doi.org/10.1088/0963-0252/23/6/065003).
- [52] Elise Vervloessem et al. "Plasma-Based N<sub>2</sub> Fixation into NO<sub>x</sub> : Insights from Modeling toward Optimum Yields and Energy Costs in a Gliding Arc Plasmatron". In: *ACS Sustainable Chemistry & Engineering* 8.26 (2020), pp. 9711–9720. ISSN: 2168-0485. DOI: [10.1021/acssuschemeng.0c01815](https://doi.org/10.1021/acssuschemeng.0c01815).
- [53] David Park. *Introduction to the Quantum Theory: Third Edition*. Newburyport: Dover Publications, 2012. ISBN: 9780486441375. URL: <http://gbv.ebib.com/patron/FullRecord.aspx?p=1894509>.
- [54] Kari Niemi. *Nachweis leichter Atome in reaktiven Plasmen mittels Zweiphotonen laserinduzierter Fluoreszenzspektroskopie unter besonderer Berücksichtigung der Absolutkalibrierung*. 1st ed. Göttingen: Cuvillier Verlag, 2003. ISBN: 9783898738323. URL: <https://ebookcentral.proquest.com/lib/gbv/detail.action?docID=5021527>.
- [55] K. Huber. *Molecular Spectra and Molecular Structure: IV. Constants of Diatomic Molecules*. New York, NY: Springer, 1979. ISBN: 9781475709612. URL: <https://ebookcentral.proquest.com/lib/kxp/detail.action?docID=6572918>.
- [56] Percival Lewis. "The Afterglow of Metallic Vapors in Nitrogen - a New Band Spectrum". In: *The Astrophysical Journal* 20 (1904), p. 49. ISSN: 0004-637X. DOI: [10.1086/141135](https://doi.org/10.1086/141135).
- [57] R. Engleman et al. *Beta and Gamma band Systems of Nitric Oxide*. Office of Scientific and Technical Information (OSTI), 1969. DOI: [10.2172/4128104](https://doi.org/10.2172/4128104).
- [58] Horace A. Ory. "Franck—Condon Factors and Electronic Oscillator Strengths for Nitric Oxide Ultraviolet Band Systems". In: *The Journal of Chemical Physics* 40.2 (1964), pp. 562–566. ISSN: 0021-9606. DOI: [10.1063/1.1725155](https://doi.org/10.1063/1.1725155).

- [59] A. B. Callear and I. W. M. Smith. "Fluorescence of nitric oxide. Part 1. Determination of the mean lifetime of the  $A^2\Sigma^+$  state". In: *Trans. Faraday Soc.* 59.0 (1963), pp. 1720–1734. ISSN: 0014-7672. DOI: [10.1039/tf9635901720](https://doi.org/10.1039/tf9635901720).
- [60] Wolfgang Demtröder. *Atoms, Molecules and Photons: An Introduction to Atomic-, Molecular- and Quantum Physics*. 2. ed. Graduate Texts in Physics. Berlin, Heidelberg: Springer-Verlag Berlin Heidelberg, 2010. ISBN: 978-3-642-10297-4. DOI: [10.1007/978-3-642-10298-1](https://doi.org/10.1007/978-3-642-10298-1). URL: [http://www.ifuap.buap.mx/~omeza/assets/atoms%2C\\_molecules\\_and\\_photons.pdf](http://www.ifuap.buap.mx/~omeza/assets/atoms%2C_molecules_and_photons.pdf).
- [61] Reginald W. Pearse and A. G. Gaydon. *The identification of molecular spectra*. 4. ed., repr. London: Chapman and Hall, 1984. ISBN: 041214350X.
- [62] George W. Bethke. "Oscillator Strengths in the Far Ultraviolet. I. Nitric Oxide". In: *The Journal of Chemical Physics* 31.3 (1959), pp. 662–668. ISSN: 0021-9606. DOI: [10.1063/1.1730443](https://doi.org/10.1063/1.1730443).
- [63] D. C. Emmony, R. P. Howson, and L. J. Willis. "Laser mirror damage in germanium at 10.6  $\mu\text{m}$ , pages = 598–600, volume = 23, number = 11, issn = 0003-6951, journal = Applied Physics Letters, doi = 10.1063/1.1654761," in: (1973).
- [64] H. M. van Driel, J. E. Sipe, and Jeff F. Young. "Laser-Induced Periodic Surface Structure on Solids: A Universal Phenomenon". In: *Physical Review Letters* 49.26 (1982), pp. 1955–1958. ISSN: 0031-9007. DOI: [10.1103/physrevlett.49.1955](https://doi.org/10.1103/physrevlett.49.1955).
- [65] Dieter Bäuerle, ed. *Laser Processing and Chemistry: Fourth Edition*. 4th ed. Heidelberg: Springer, 2011. ISBN: 978-3-642-17612-8.
- [66] David Pines and David Bohm. "A Collective Description of Electron Interactions: II. Collective vs Individual Particle Aspects of the Interactions". In: *Physical Review* 85.2 (1952), pp. 338–353. ISSN: 0031-899X. DOI: [10.1103/PhysRev.85.338](https://doi.org/10.1103/PhysRev.85.338).
- [67] R. H. Ritchie. "Plasma Losses by Fast Electrons in Thin Films". In: *Physical Review* 106.5 (1957), pp. 874–881. ISSN: 0031-899X. DOI: [10.1103/PhysRev.106.874](https://doi.org/10.1103/PhysRev.106.874).

- [68] Dror Sarid. *Modern Introduction to Surface Plasmons: Theory, Mathematica Modeling, and Applications*. Cambridge: Cambridge University Press, 2010. ISBN: 9781139638579. URL: <https://ebookcentral.proquest.com/lib/kxp/detail.action?docID=1182925>.
- [69] Thibault J-Y Derrien, Jörg Krüger, and Jörn Bonse. “Properties of surface plasmon polaritons on lossy materials: lifetimes, periods and excitation conditions”. In: *Journal of Optics* 18.11 (2016), p. 115007. ISSN: 2040-8978. DOI: [10.1088/2040-8978/18/11/115007](https://doi.org/10.1088/2040-8978/18/11/115007).
- [70] J. M. Pitarke et al. “Theory of surface plasmons and surface-plasmon polaritons”. In: *Reports on Progress in Physics* 70.1 (2007), pp. 1–87. ISSN: 0034-4885. DOI: [10.1088/0034-4885/70/1/r01](https://doi.org/10.1088/0034-4885/70/1/r01).
- [71] Junxi Zhang, Lide Zhang, and Wei Xu. “Surface plasmon polaritons: physics and applications”. In: *Journal of Physics D: Applied Physics* 45.11 (2012), p. 113001. ISSN: 0963-0252. DOI: [10.1088/0022-3727/45/11/113001](https://doi.org/10.1088/0022-3727/45/11/113001).
- [72] S. A. Akhmanov et al. “Interaction of powerful laser radiation with the surfaces of semiconductors and metals: nonlinear optical effects and nonlinear optical diagnostics”. In: *Soviet Physics Uspekhi* 28.12 (1985), pp. 1084–1124. ISSN: 0038-5670.
- [73] J. E. Sipe, H. M. van Driel, and Jeff F. Young. “Surface electrodynamics: radiation fields, surface polaritons, and radiation remnants”. In: *Canadian Journal of Physics* 63.1 (1985), pp. 104–113. ISSN: 0008-4204. DOI: [10.1139/p85-017](https://doi.org/10.1139/p85-017).
- [74] J. E. Sipe et al. “Laser-induced periodic surface structure. I. Theory”. In: *Physical Review B* 27.2 (1983), pp. 1141–1154. ISSN: 1098-0121. DOI: [10.1103/PhysRevB.27.1141](https://doi.org/10.1103/PhysRevB.27.1141).
- [75] Jeff F. Young, J. E. Sipe, and H. M. van Driel. “Laser-induced periodic surface structure. III. Fluence regimes, the role of feedback, and details of the induced topography in germanium”. In: *Physical Review B* 30.4 (1984), pp. 2001–2015. ISSN: 0163-1829. DOI: [10.1103/PhysRevB.30.2001](https://doi.org/10.1103/PhysRevB.30.2001).
- [76] Jeff F. Young et al. “Laser-induced periodic surface structure. II. Experiments on Ge, Si, Al, and brass”. In: *Physical Review B* 27.2 (1983), pp. 1155–1172. ISSN: 0163-1829. DOI: [10.1103/PhysRevB.27.1155](https://doi.org/10.1103/PhysRevB.27.1155).

- [77] Jeff F. Young et al. "Laser-induced periodic surface damage and radiation remnants". In: *Applied Physics Letters* 41.3 (1982), pp. 261–264. ISSN: 0003-6951. DOI: [10.1063/1.93494](https://doi.org/10.1063/1.93494).
- [78] A. Schutze et al. "The atmospheric-pressure plasma jet: a review and comparison to other plasma sources". In: *IEEE Transactions on Plasma Science* 26.6 (1998), pp. 1685–1694. ISSN: 00933813. DOI: [10.1109/27.747887](https://doi.org/10.1109/27.747887).
- [79] P. A. C. Beijer et al. "Multiplying probe for accurate power measurements on an RF driven atmospheric pressure plasma jet applied to the COST reference microplasma jet". In: *Journal of Physics D: Applied Physics* 49.10 (2016), p. 104001. ISSN: 0963-0252. DOI: [10.1088/0022-3727/49/10/104001](https://doi.org/10.1088/0022-3727/49/10/104001). URL: <https://iopscience.iop.org/article/10.1088/0022-3727/49/10/104001>.
- [80] D. Wright et al. "Laser beam width, divergence and beam propagation factor — an international standardization approach". In: *Optical and Quantum Electronics* 24.9 (1992), S993–S1000. ISSN: 0306-8919. DOI: [10.1007/BF01588600](https://doi.org/10.1007/BF01588600).
- [81] Marcos A. C. de Araújo et al. "Measurement of Gaussian laser beam radius using the knife-edge technique: improvement on data analysis". In: *Applied Optics* 48.2 (2009), pp. 393–396. ISSN: 0003-6935. DOI: [10.1364/AO.48.000393](https://doi.org/10.1364/AO.48.000393).
- [82] Michael A. Lieberman and Allan J. Lichtenberg, eds. *Principles of Plasma Discharges and Materials Processing: Second Edition*. 2nd. New Jersey: John Wiley & Sons, Inc, 2005. ISBN: 0-471-72001-1.
- [83] Judith Golda. "Cross-correlating discharge physics, excitation mechanisms and plasma chemistry to describe the stability of an RF-excited atmospheric pressure argon plasma jet". PhD thesis. URL: <https://hss-opus.ub.ruhr-uni-bochum.de/opus4/frontdoor/index/index/docId/5737>.
- [84] J. Danielak et al. "Reinvestigation of the Emission  $\gamma$  Band System  $A^2\Sigma^+ - X^2\Pi$  of the NO Molecule". In: *Journal of Molecular Spectroscopy* 181.2 (1997), pp. 394–402. ISSN: 00222852. DOI: [10.1006/jmsp.1996.7181](https://doi.org/10.1006/jmsp.1996.7181).

- [85] D. Ellerweg et al. "Characterization of the effluent of a He/O<sub>2</sub> microscale atmospheric pressure plasma jet by quantitative molecular beam mass spectrometry". In: *New Journal of Physics* 12.1 (2010), p. 013021. ISSN: 0022-3727. DOI: [10.1088/1367-2630/12/1/013021](https://doi.org/10.1088/1367-2630/12/1/013021). URL: <https://iopscience.iop.org/article/10.1088/1367-2630/12/1/013021/meta>.
- [86] S. Kelly and M. M. Turner. "Generation of reactive species by an atmospheric pressure plasma jet". In: *Plasma Sources Science and Technology* 23.6 (2014), p. 065013. ISSN: 0022-3727. DOI: [10.1088/0963-0252/23/6/065013](https://doi.org/10.1088/0963-0252/23/6/065013). URL: <https://iopscience.iop.org/article/10.1088/0963-0252/23/6/065013/pdf>.
- [87] A. V. Pipa et al. "Absolute production rate measurements of nitric oxide by an atmospheric pressure plasma jet (APPJ)". In: *Journal of Physics D: Applied Physics* 41.19 (2008), p. 194011. ISSN: 0963-0252. DOI: [10.1088/0022-3727/41/19/194011](https://doi.org/10.1088/0022-3727/41/19/194011).
- [88] A. V. Pipa et al. "Controlling the NO production of an atmospheric pressure plasma jet". In: *Journal of Physics D: Applied Physics* 45.8 (2012), p. 085201. ISSN: 0963-0252. DOI: [10.1088/0022-3727/45/8/085201](https://doi.org/10.1088/0022-3727/45/8/085201).
- [89] I. Korolov et al. "Control of electron dynamics, radical and metastable species generation in atmospheric pressure RF plasma jets by Voltage Waveform Tailoring". In: *Plasma Sources Science and Technology* 28.9 (2019), p. 094001. ISSN: 0022-3727. DOI: [10.1088/1361-6595/ab38ea](https://doi.org/10.1088/1361-6595/ab38ea).
- [90] D. R. Boris et al. "Controlling the electron energy distribution function of electron beam generated plasmas with molecular gas concentration: I. Experimental results". In: *Plasma Sources Science and Technology* 22.6 (2013), p. 065004. ISSN: 0022-3727. DOI: [10.1088/0963-0252/22/6/065004](https://doi.org/10.1088/0963-0252/22/6/065004).
- [91] L. Bischoff et al. "Experimental and computational investigations of electron dynamics in micro atmospheric pressure radio-frequency plasma jets operated in He/N<sub>2</sub> mixtures". In: *Plasma Sources Science and Technology* 27.12 (2018), p. 125009. ISSN: 0022-3727. DOI: [10.1088/1361-6595/aaf35d](https://doi.org/10.1088/1361-6595/aaf35d).

- [92] H. Bubert and F. W. Froben. "Direct lifetime measurements of NO ( $A^2\Sigma^+$ )". In: *Chemical Physics Letters* 8.2 (1971), pp. 242–244. ISSN: 00092614. DOI: [10.1016/0009-2614\(71\)80027-1](https://doi.org/10.1016/0009-2614(71)80027-1).
- [93] J. Brzozowski, N. Elander, and P. Erman. "Direct Measurements of Lifetimes of Low-lying Excited Electronic States in Nitric Oxide". In: *Physica Scripta* 9.2 (1974), pp. 99–103. ISSN: 0031-8949.
- [94] Thomas B. Settersten, Brian D. Patterson, and Campbell D. Carter. "Collisional quenching of NO  $A^2\Sigma^+(v' = 0)$  between 125 and 294 K". In: *The Journal of Chemical Physics* 130.20 (2009), p. 204302. ISSN: 0021-9606. DOI: [10.1063/1.3138178](https://doi.org/10.1063/1.3138178).
- [95] I. Stuart McDermid and James B. Laudenslager. "Radiative lifetimes and electronic quenching rate constants for single-photon-excited rotational levels of NO ( $A^2\Sigma^+, v' = 0$ )". In: *Journal of Quantitative Spectroscopy and Radiative Transfer* 27.5 (1982), pp. 483–492. ISSN: 0022-4073. DOI: [10.1016/0022-4073\(82\)90100-5](https://doi.org/10.1016/0022-4073(82)90100-5). URL: <http://www.sciencedirect.com/science/article/pii/0022407382901005>.
- [96] Michael C. Drake and John W. Ratcliffe. "High temperature quenching cross sections for nitric oxide laser-induced fluorescence measurements". In: *The Journal of Chemical Physics* 98.5 (1993), pp. 3850–3865. ISSN: 0021-9606. DOI: [10.1063/1.465047](https://doi.org/10.1063/1.465047).
- [97] Gary D. Greenblatt and A. R. Ravishankara. *Collisional quenching of NO( $A, v' = 0$ ) by various gases*. Vol. 136. 1987. DOI: [10.1016/0009-2614\(87\)80506-7](https://doi.org/10.1016/0009-2614(87)80506-7). URL: <https://www.sciencedirect.com/science/article/pii/0009261487805067>.
- [98] Micha Asscher and Yehuda Haas. "The quenching mechanism of electronically excited Rydberg states of nitric oxide". In: *The Journal of Chemical Physics* 76.5 (1982), pp. 2115–2126. ISSN: 0021-9606. DOI: [10.1063/1.443306](https://doi.org/10.1063/1.443306).
- [99] Takashi Imajo et al. "Energy Transfer and Electronic Quenching of the Low-Lying Rydberg States of NO in NO/N<sub>2</sub> Mixtures". In: *J. Phys. Chem.* 1986.90 (1986), pp. 6006–6011. URL: <https://pubs.acs.org/doi/pdf/10.1021/j100280a109>.

- [100] George A. Raiche and David R. Crosley. "Temperature dependent quenching of the  $A^2\Sigma^+$  and  $B^2\Pi$  states of NO". In: *The Journal of Chemical Physics* 92.9 (1990), pp. 5211–5217. ISSN: 0021-9606. DOI: [10.1063/1.458604](https://doi.org/10.1063/1.458604).
- [101] Rong Zhang and David R. Crosley. "Temperature dependent quenching of NO  $A^2\Sigma^+$  + NO between 215 and 300 K". In: *The Journal of Chemical Physics* 102.19 (1995), pp. 7418–7424. ISSN: 0021-9606. DOI: [10.1063/1.469054](https://doi.org/10.1063/1.469054).
- [102] Thomas B. Settersten, Brian D. Patterson, and Jeffrey A. Gray. "Temperature- and species-dependent quenching of NO  $A^2\Sigma^+(v' = 0)$  probed by two-photon laser-induced fluorescence using a picosecond laser". In: *The Journal of Chemical Physics* 124.23 (2006), p. 234308. ISSN: 0021-9606. DOI: [10.1063/1.2206783](https://doi.org/10.1063/1.2206783).
- [103] R. L. Renka and A. K. Cline. "A triangle-based  $C^1$  interpolation method". In: *Rocky Mountain Journal of Mathematics* 14.1 (1984), pp. 223–238. ISSN: 0035-7596. DOI: [10.1216/RMJ-1984-14-1-223](https://doi.org/10.1216/RMJ-1984-14-1-223).
- [104] John T. Herron and David S. Green. "Chemical Kinetics Database and Predictive Schemes for Nonthermal Humid Air Plasma Chemistry. Part II. Neutral Species Reactions". In: *Plasma Chemistry and Plasma Processing* 21.3 (2001), pp. 459–481. ISSN: 1572-8986. DOI: [10.1023/A:1011082611822](https://doi.org/10.1023/A:1011082611822). URL: <https://link.springer.com/article/10.1023/A:1011082611822>.
- [105] C. Douat et al. "Production of nitric/nitrous oxide by an atmospheric pressure plasma jet". In: *Plasma Sources Science and Technology* 25.2 (2016), p. 025027. ISSN: 0022-3727. DOI: [10.1088/0963-0252/25/2/025027](https://doi.org/10.1088/0963-0252/25/2/025027).
- [106] S. Iseni et al. "Nitric oxide density distributions in the effluent of an RF argon APPJ: effect of gas flow rate and substrate". In: *New Journal of Physics* 16.12 (2014), p. 123011. ISSN: 0022-3727. DOI: [10.1088/1367-2630/16/12/123011](https://doi.org/10.1088/1367-2630/16/12/123011).
- [107] Stephan Reuter, Thomas von Woedtke, and Klaus-Dieter Weltmann. "The kINPen—a review on physics and chemistry of the atmospheric pressure plasma jet and its applications". In: *Journal of Physics D: Applied Physics* 51.23 (2018), p. 233001. ISSN: 0963-0252. DOI: [10.1088/0963-0252/51/23/233001](https://doi.org/10.1088/0963-0252/51/23/233001).

- 1361-6463/aab3ad. URL: <https://iopscience.iop.org/article/10.1088/1361-6463/aab3ad/meta>.
- [108] Garry M. Barrow, ed. *Introduction to molecular spectroscopy*. McGRAW-HILL Book Company, Inc, 1962.
- [109] J. K. Badenhoop and F. Weinhold. "Natural steric analysis: Ab initio van der Waals radii of atoms and ions". In: *The Journal of Chemical Physics* 107.14 (1997), pp. 5422–5432. ISSN: 0021-9606. DOI: [10.1063/1.475149](https://doi.org/10.1063/1.475149).
- [110] David Steuer et al. "2D spatially resolved O atom density profiles in an atmospheric pressure plasma jet: from the active plasma volume to the effluent". In: *Journal of Physics D: Applied Physics* 54.35 (2021), p. 355204. ISSN: 0963-0252. DOI: [10.1088/1361-6463/ac09b9](https://doi.org/10.1088/1361-6463/ac09b9). URL: <https://iopscience.iop.org/article/10.1088/1361-6463/ac09b9/meta>.
- [111] Samira Bagheri, Nurhidayatullaili Muhd Julkapli, and Sharifah Bee Abd Hamid. "Titanium dioxide as a catalyst support in heterogeneous catalysis". In: *TheScientificWorldJournal* 2014 (2014), p. 727496. DOI: [10.1155/2014/727496](https://doi.org/10.1155/2014/727496). URL: <https://www.hindawi.com/journals/tswj/2014/727496/>.
- [112] Hemma Mistry et al. "Highly selective plasma-activated copper catalysts for carbon dioxide reduction to ethylene". In: *Nature Communications* 7.1 (2016), p. 12123. ISSN: 2041-1723. DOI: [10.1038/ncomms12123](https://doi.org/10.1038/ncomms12123). URL: <https://www.nature.com/articles/ncomms12123?origin=ppub>.
- [113] Zixian Jia et al. "Plasma catalysis application of gold nanoparticles for acetaldehyde decomposition". In: *Chemical Engineering Journal* 347 (2018), pp. 913–922. ISSN: 1385-8947. DOI: [10.1016/j.cej.2018.04.106](https://doi.org/10.1016/j.cej.2018.04.106). URL: <https://www.sciencedirect.com/science/article/pii/S1385894718306806>.
- [114] Mohammad S. AlQahtani et al. "Plasma-assisted catalytic reduction of SO<sub>2</sub> to elemental sulfur: Influence of nonthermal plasma and temperature on iron sulfide catalyst". In: *Journal of Catalysis* 391 (2020), pp. 260–272. ISSN: 0021-9517. DOI: [10.1016/j.jcat.2020.08.013](https://doi.org/10.1016/j.jcat.2020.08.013). URL: <https://www.sciencedirect.com/science/article/pii/S0021951720303249>.

- [115] B. L. Jiang and Y. M. Wang. "Plasma electrolytic oxidation treatment of aluminium and titanium alloys". In: *Surface Engineering of Light Alloys* (2010), pp. 110–154. DOI: 10.1533/9781845699451.2.110. URL: <https://www.sciencedirect.com/science/article/pii/B9781845695378500051>.
- [116] John W. Harris and Horst Stocker. *Handbook of mathematics and computational science*. New York et al.: Springer, 1998. ISBN: 0387947469. URL: <http://www.loc.gov/catdir/enhancements/fy0818/98020290-d.html>.
- [117] Augustin Jean Fresnel. *Cœuvres complètes d'Augustin Fresnel: Théorie de la lumière*. TOMES DEUXIÈME. Paris, 1866.
- [118] A. D. Rakić. "Algorithm for the determination of intrinsic optical constants of metal films: application to aluminum". In: *Applied Optics* 34.22 (1995), pp. 4755–4767. ISSN: 0003-6935. DOI: 10.1364/AO.34.004755.
- [119] P. Johnson and R. Christy. "Optical constants of transition metals: Ti, V, Cr, Mn, Fe, Co, Ni, and Pd". In: *Physical Review B* 9.12 (1974), pp. 5056–5070. ISSN: 1098-0121. DOI: 10.1103/PhysRevB.9.5056.
- [120] Xiaoning Zhang et al. "Complex refractive indices measurements of polymers in visible and near-infrared bands". In: *Applied Optics* 59.8 (2020), pp. 2337–2344. ISSN: 0003-6935. DOI: 10.1364/AO.383831.
- [121] Xiaoning Zhang et al. "Complex refractive indices measurements of polymers in infrared bands". In: *Journal of Quantitative Spectroscopy and Radiative Transfer* 252 (2020), p. 107063. ISSN: 0022-4073. DOI: 10.1016/j.jqsrt.2020.107063.
- [122] T. Yi-Ting and S. Wei-Fang. *Ray Optics Simulation*. 2016. DOI: 10.5281/zenodo.6386611. URL: <https://ricktu288.github.io/ray-optics/>.
- [123] B. Gordiets et al. "Surface kinetics of N and O atoms in discharges". In: *Journal of Physics D: Applied Physics* 29.4 (1996), pp. 1021–1031. ISSN: 0963-0252. DOI: 10.1088/0022-3727/29/4/012. URL: [https://iopscience.iop.org/article/10.1088/0022-3727/29/4/012/meta?casa\\_token=45vnpfyxricaaaaa:yzqzwhzev-hulbumsc-uixoitycbn0w-rzszru9juff-par6pup3bhtheyu4pe6ifrfms19rzsg](https://iopscience.iop.org/article/10.1088/0022-3727/29/4/012/meta?casa_token=45vnpfyxricaaaaa:yzqzwhzev-hulbumsc-uixoitycbn0w-rzszru9juff-par6pup3bhtheyu4pe6ifrfms19rzsg).

- [124] Philipp Nürnberger et al. "Orthogonally superimposed laser-induced periodic surface structures (LIPSS) upon nanosecond laser pulse irradiation of SiO<sub>2</sub>/Si layered systems". In: *Applied Surface Science* 425 (2017), pp. 682–688. ISSN: 01694332. DOI: [10.1016/j.apsusc.2017.06.316](https://doi.org/10.1016/j.apsusc.2017.06.316).
- [125] A. Z. Moshfegh. "Nanoparticle catalysts". In: *Journal of Physics D: Applied Physics* 42.23 (2009), p. 233001. ISSN: 0963-0252. DOI: [10.1088/0022-3727/42/23/233001](https://doi.org/10.1088/0022-3727/42/23/233001).
- [126] A. Vrij. "Possible mechanism for the spontaneous rupture of thin, free liquid films". In: *Discussions of the Faraday Society* 42 (1966), p. 23. ISSN: 0366-9033. DOI: [10.1039/df9664200023](https://doi.org/10.1039/df9664200023).
- [127] Eli Ruckenstein and Gersh Osievich Berim. *Wetting theory*. Boca Raton, London, and New York: CRC Press, 2019. ISBN: 9780429687051. DOI: [10.1201/9780429401848](https://doi.org/10.1201/9780429401848). URL: <https://www.taylorfrancis.com/books/9780429401848>.
- [128] Rabibrata Mukherjee. "Liquid Thin Film Hydrodynamics: Dewetting and Pattern Formation". In: *Mechanics over micro and nano scales*. Ed. by Suman Chakraborty. New York, NY: Springer, 2011, pp. 193–215. ISBN: 978-1-4419-9600-8. DOI: [10.1007/978-1-4419-9601-5\\_{6}](https://doi.org/10.1007/978-1-4419-9601-5_{6}).
- [129] J. Trice et al. "Pulsed-laser-induced dewetting in nanoscopic metal films: Theory and experiments". In: *Physical Review B* 75.23 (2007). ISSN: 1098-0121. DOI: [10.1103/PhysRevB.75.235439](https://doi.org/10.1103/PhysRevB.75.235439).
- [130] Sagar Yadavali, Mikhail Khenner, and Ramki Kalyanaraman. "Pulsed laser dewetting of Au films: Experiments and modeling of nanoscale behavior". In: *Journal of Materials Research* 28.13 (2013), pp. 1715–1723. ISSN: 0884-2914. DOI: [10.1557/jmr.2013.90](https://doi.org/10.1557/jmr.2013.90).
- [131] H. Krishna et al. "Pulsed laser induced self-organization by dewetting of metallic films". In: *Journal of Materials Research* 26.2 (2011), pp. 154–169. ISSN: 0884-2914. DOI: [10.1557/jmr.2010.17](https://doi.org/10.1557/jmr.2010.17).
- [132] A. Passerone et al. "Thermodynamics and surface properties of liquid Cu–B alloys". In: *Surface Science* 603.17 (2009), pp. 2725–2733. ISSN: 00396028. DOI: [10.1016/j.susc.2009.07.011](https://doi.org/10.1016/j.susc.2009.07.011).

- [133] Jacob N. Israelachvili. *Intermolecular and surface forces*. 3rd ed. Burlington, MA: Academic Press, 2011. ISBN: 9780123751829. URL: <http://www.sciencedirect.com/science/book/9780123751829>.
- [134] Roger H. French. "Origins and Applications of London Dispersion Forces and Hamaker Constants in Ceramics". In: *Journal of the American Ceramic Society* 83.9 (2000), pp. 2117–2146. ISSN: 00027820. DOI: [10.1111/j.1151-2916.2000.tb01527.x](https://doi.org/10.1111/j.1151-2916.2000.tb01527.x).
- [135] C. Favazza, R. Kalyanaraman, and R. Sureshkumar. "Robust nanopatterning by laser-induced dewetting of metal nanofilms". In: *Reviews of Modern Physics* 78.6 (2006), pp. 4229–4234. ISSN: 0957-4484. DOI: [10.1088/0957-4484/78/6/038](https://doi.org/10.1088/0957-4484/78/6/038). URL: <https://iopscience.iop.org/article/10.1088/0957-4484/78/6/038/meta>.
- [136] Taihei Matsumoto et al. "Measurement of surface tension of molten copper using the free-fall oscillating drop method". In: *Measurement Science and Technology* 16.2 (2005), pp. 432–437. ISSN: 0957-0233. DOI: [10.1088/0957-0233/16/2/014](https://doi.org/10.1088/0957-0233/16/2/014).
- [137] Yueying Wu et al. "On the breakup of patterned nanoscale copper rings into droplets via pulsed-laser-induced dewetting: competing liquid-phase instability and transport mechanisms". In: *Langmuir* 26.14 (2010), pp. 11972–11979. ISSN: 0743-7463. DOI: [10.1021/la1013818](https://doi.org/10.1021/la1013818).

# Lebenslauf

## Persönliche Daten

Name Patrick Preissing  
Geboren 04.10.1989 in Essen

## Schulische Ausbildung

1996 - 2000 Waldschule Bochum  
2000 - 2009 Goethe Gymnasium Bochum

## Studium

2009 - 2011 Bachelor of Science Bauingenieurwesen, Ruhr-Universität Bochum  
2011 - 2014 Bachelor of Science Physik, Ruhr-Universität Bochum  
2014 - 2016 Master of Science Physik, Ruhr-Universität Bochum

## Berufliche Laufbahn

2016 - 2017 Wissenschaftlicher Mitarbeiter, Heinrich-Heine Universität Düsseldorf  
2017-2018 Lehrer für Physik, Märkisches Gymnasium Schwelm  
2018 - 2022 Wissenschaftlicher Mitarbeiter, Ruhr-Universität Bochum  
2022 - heute Prozessentwickler strahlbasierte Optikbearbeitung, Carl Zeiss SMT